

# **Step and island dynamics at solid/vacuum and solid/liquid interfaces**

**Margret Giesen**\*

*Institut für Grenzflächenforschung und Vakuumphysik, Forschungszentrum Jülich,  
52425 Jülich, Germany*

## **Abstract**

The investigation of step and island dynamics on surfaces has enormously contributed to the microscopic understanding of mass transport processes in equilibrium, during growth and coarsening of surface structures. From the scaling behavior of step fluctuations as well as of the ripening of mono- and multilayer islands, the atomic diffusion processes may be unambiguously determined even when single atom motion cannot be observed directly. This is the case for metal surfaces at high temperatures and, in particular, for metal electrodes in electrochemical environment. In the case of the latter, the analysis of step and island dynamics is the only method available to date to learn about the dynamics at the solid liquid interface on the atomic scale. Here, we review the basic theoretical principles and the experimental contributions on step and island dynamics performed in ultra-high vacuum as well as (more recently) in electrolyte. It focuses also on the comparison between experimental results obtained at the solid/vacuum and at the solid/liquid interface.

*Keywords:* Step dynamics, island decay, coarsening, step-step interactions, diffusion, metal surfaces, solid/vacuum interface, metal electrodes, solid/liquid interface

---

\* Electronic address: [m.giesen@fz-juelich.de](mailto:m.giesen@fz-juelich.de); Fax: (+49) 2461 / 61-3907



**Contents:**

Acronyms .....	5
1. Introduction .....	6
2. Defects on metal surfaces .....	9
2.1 Structure of defects and their notation .....	9
2.2 Vicinal surfaces .....	10
2.3 Adatom and vacancy islands .....	13
2.4 Stability of surfaces .....	13
2.5 Equilibrium dynamics of defects and their influence on STM recording .....	15
3. Step fluctuations .....	20
3.1 Energy of fluctuating step .....	20
3.2 Langevin equation .....	22
3.3 Step correlation function $G(y,t)$ .....	25
3.3.1 Spatial step correlation function $G(y,t=0)$ .....	25
3.3.2 Time dependence of step fluctuations: Time correlation function $G(y=0,t)$ .....	28
3.3.3 Temperature dependence of time correlation function .....	43
3.3.4 Transition in dominant mass transport regimes .....	47
3.4 Influence of tunneling tip on measurement of $G(t)$ .....	49
3.5 Step fluctuations in Fourier space .....	52
4. Step-step interactions .....	56
4.1 Mean-field approximation .....	56
4.2 Fermion description .....	59
4.3 Generalized Wigner surmise .....	60
4.4 Experimental results on metal surfaces .....	61
5. Step fluctuations at solid/liquid interfaces .....	69
5.1 Step fluctuations on Ag(111) electrodes .....	70
5.2 Step fluctuations on Cu(100) and (111) electrodes .....	78
5.3 Step fluctuations on Au(111) electrodes .....	85
5.4 Influence of tunneling tip .....	97
5.5 Step-step interactions on metal electrodes .....	98

6. Islands on metal surfaces .....	101
6.1 Equilibrium shape of islands .....	102
6.1.1 Wulff construction .....	102
6.1.2 Island equilibrium shape in Ising-model .....	111
6.1.3 Determination of kink and step energy by analyzing curvature of quasi-straight edge segments of islands .....	115
6.1.4 Determination of absolute step energies from aspect ratio of islands .....	118
6.1.5 Brownian motion of islands .....	121
6.2 Coarsening of monolayer island structures .....	123
6.2.1 Ostwald ripening of islands .....	123
6.2.2 Island coalescence .....	139
6.3 Coarsening of multilayer island structures .....	140
6.3.1 Barrier limited decay of multilayer islands .....	141
6.3.2 Rapid interlayer mass transport .....	153
7. Islands on metal electrodes in liquid environment .....	159
8. Conclusion .....	169
Appendix A .....	173
Appendix B .....	175
Appendix C .....	177
References .....	179

**Acronyms**

CEM	Corrected Effective Medium
DFT	Density Functional Theory
DLA	Diffusion Limited Aggregation
EAM	Embedded Atom Method
ECT	Equivalent Crystal Theory
EMT	Effective Medium Theory
ES	Ehrlich-Schwoebel
FIM	Field Ion Microscopy
GGA	Generalized Gradient Approximation
KMC	Kinetic Monte Carlo
LDA	Local Density Approximation
LEEM	Low Energy Electron Microscopy
MC	Monte Carlo
MC-CEM	Monte Carlo-Corrected Effective Medium
MD	Molecular Dynamics
NHE	Normal Hydrogen Electrode
REM	Reflection Electron Microscopy
RHE	Reversible Hydrogen Electrode
SCE	Saturated Calomel Electrode
SOS	Solid-on-solid
STM	Scanning Tunneling Microscopy
UHV	Ultra High Vacuum
UPD	Under potential deposition

## 1. Introduction

Studies of the physics and chemistry of solid surfaces in *ultra high vacuum* (UHV) have a long tradition. Spectroscopy techniques, such as *electron energy loss spectroscopy* [1, 2], *photoemission spectroscopy* or *infrared spectroscopy* [3-5], provide information about the chemistry of surfaces and the kinetics of chemical reactions. The investigation of the local surface structure has become possible by the use of microscopy techniques as for example *scanning* and *reflection electron microscopy* (REM), as well as *low energy electron microscopy* (LEEM) [6, 7] and more recently *scanning tunneling microscopy* (STM) [8] and other scanning probe techniques such as *atomic force microscopy* [9].

In electrochemistry, classical experiments using *cyclic voltammetry*, *chronopotentiometry* or the *capillary technique* [10] are integral methods and provide no local information about the electrode surface. Local imaging techniques using particles as a surface probe, however, are not applicable on metal electrodes in contact with a liquid. In the early years, the influence of electrochemical reactions on the electrode surface was therefore frequently investigated using ex-situ studies where the electrode was transferred into a UHV system [11, 12]. In ex-situ studies, however, many problems remain unsolved. In particular, concern is raised in how far the transfer of the electrode from the liquid into the UHV environment influences the surface structure. By using light as a surface probe (e.g., in *fourier transform infrared spectroscopy* [13, 14] and *second harmonic generation* [15]), in-situ studies of some aspects of the surfaces structure have become possible. *X-ray scattering* has become applicable to in-situ investigations, since synchrotron sources are accessible [16]. Considerable progress is owed to the invention of in-situ electrochemical STMs [17, 18], which are capable of atomic resolution on metal surfaces in contact with a liquid.

The availability of local structure information from surfaces in UHV, as well as in liquid environment, has stimulated the interest of experimentalists and theorists in the characteristic similarities and differences of surface reactions and dynamical processes on solid surfaces in UHV and in electrolyte. This review focuses on studies of the defect dynamics on metal surfaces<sup>1</sup> in UHV and in electrochemical environment.

Surface defects serve as preferred binding and reaction sites for chemically or physically adsorbed particles. The dynamical behavior and the stability of such defect sites may influence the surface reaction kinetics. Studies of the dynamics of defects are therefore important for the understanding of chemical reactions at the solid/vacuum as well as at the solid/liquid interface. To learn about the kinetics of surface defects, local information on the

---

<sup>1</sup> For a recent review on UHV studies on semiconductor surfaces see [19].

surface structure is necessary. The first mile stone in the analysis of the local atomic structure of surfaces and the kinetics of adatoms in UHV was the invention of the *field ion microscope* (FIM) [20]. There, a high voltage is applied to a sharp metal tip. Atoms of a surrounding noble gas are ionized in the strong electrical field at the tip and accelerated to a screen. The impacting ions create a atomically resolved image of the metal tip. FIM is capable of direct observation of free adatoms on the sharp metal tip. Due to the possibility of high and low temperature measurements, diffusion constants and activation barriers can be determined. Although the tip used in FIM is restricted to relatively few metals due to the high electrical fields, this method has contributed substantially to the understanding of surface diffusion until today. Real space imaging techniques using electron diffraction (e.g., REM, LEEM [6, 7]) are not restricted to specific materials but can be used for any metallic and semiconducting sample. In addition, they combine the advantage of real images of a large surface area up to several 10th of a micron with real time recording capability. In contrast to FIM, however, atomic resolution is provided merely perpendicular to the surface.

A breakthrough in the investigation of the local atomic structure and in particular in studies of local defects and their kinetics in UHV as well as at the solid/liquid interface was achieved by the application of the STM [8, 17]. In recent years, the STM has been increasingly used to obtain quantitative information about the equilibrium and growth kinetics on surfaces. Although the scanning technique of the STM does not permit real time observations of the surface, relatively high time resolution is achieved by the use of high speed equipment, which is capable of recording with video frequency [21]. Depending on the temperature, on the studied material and on the electrode potential (for surfaces in electrolyte), surface diffusion may be (i) slow or (ii) fast compared to the STM recording speed. In case (i), single STM images represent snap shots of the surface structure. Motion of atoms, kinks or steps may then be studied by analyzing the changes in successive images. In case (ii), however, the structure changes during recording of a single image and even between successive scan lines. Then, the images include time as well as spatial information. Here, information on atomic diffusion processes can be extracted only by resorting to theoretical models which are capable to relate macroscopic changes in the surface structure to individual atomic processes.

It is our goal to provide an overview of STM studies on the kinetics of defects. The review focuses on studies of the equilibrium and non-equilibrium fluctuations of monatomic steps and the investigation of island mobility and island ripening on metal surfaces in UHV as well

as in an electrochemical environment and is organized as follows: In the next section, the reader is provided with the basic information on defects on surfaces as discussed here: Adatoms, vacancies, monatomic steps, adatom and vacancy single-layer and multilayer islands. Section 3 deals with the theoretical background of fluctuations of (isolated) steps together with the experimental studies performed in UHV. In Section 4, interactions between steps are considered and an overview over studies on the step-step interaction energy on metal surfaces is given. Next, we present experimental investigations of step fluctuations and step-step interactions on metal electrodes in contact with an electrolyte. Section 6 deals with the dynamics of non-equilibrium island structures on metal surfaces. The basic theory, as well as an overview over experimental data obtained from metal surfaces in UHV, is presented and extended to metal electrodes in contact with an electrolyte in Section 7.

## 2. Defects on metal surfaces

### 2.1. Structure of defects and their notation

Studies of the statistical mechanics of defects on crystal surfaces are mostly based on the *solid-on-solid (SOS) model*. In this model, the surface is represented by a square lattice of positions  $(x_i, y_j)$  spanned in the  $x$ - $y$ -plane, with atoms in lattice positions represented by cubes. The third dimension is measured by the height  $h_{ij}$  at each position  $(x_i, y_j)$ . The height describes the roughness of the interface which is introduced by defects. In the SOS-model, energetically unfavorable overhangs are forbidden so that a column of cubes at a site  $(x_i, y_j)$  with a height  $h_{ij}$  includes no vacant positions. Since overhangs on real surfaces are rare at low temperatures, the SOS model is appropriate in this temperature range to describe the surface morphology. In this review, the SOS model is exclusively used to illustrate the notation. Fig. 1 shows an SOS-model of a surface with various defects, which give rise to a certain roughness of the interface: A pair of steps with step adatoms, kink sites of monatomic and multiple length, as well as adatoms and vacancies on the terraces and isolated adatom and vacancy islands. The distance between step 1 and 2 at a distinct  $y_j$  is denoted as  $L_j$ . Depending on the real surface structure, the various defects have different coordinations as shown in Fig. 2: Free adatoms on the surface are denoted as "1", kinks as "2", vacancies and atoms in the surface layer as "3" and "4", respectively. On the (100)-surface, an adatom has 4 nearest neighbors, while on the (111)-surface its coordination is 3. Surface atoms and vacancies have 8 and 9 nearest neighbor

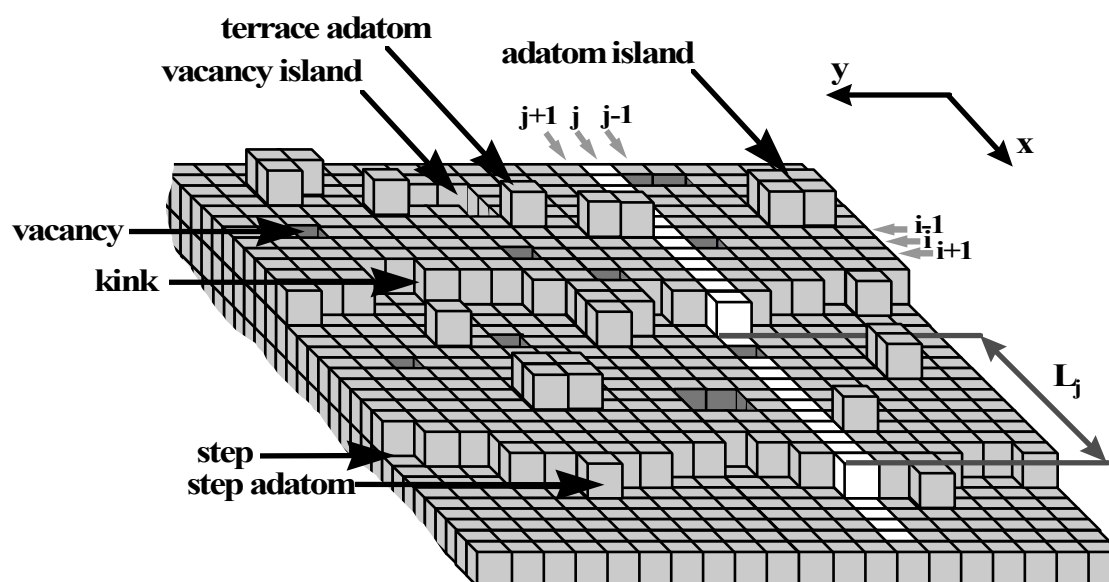
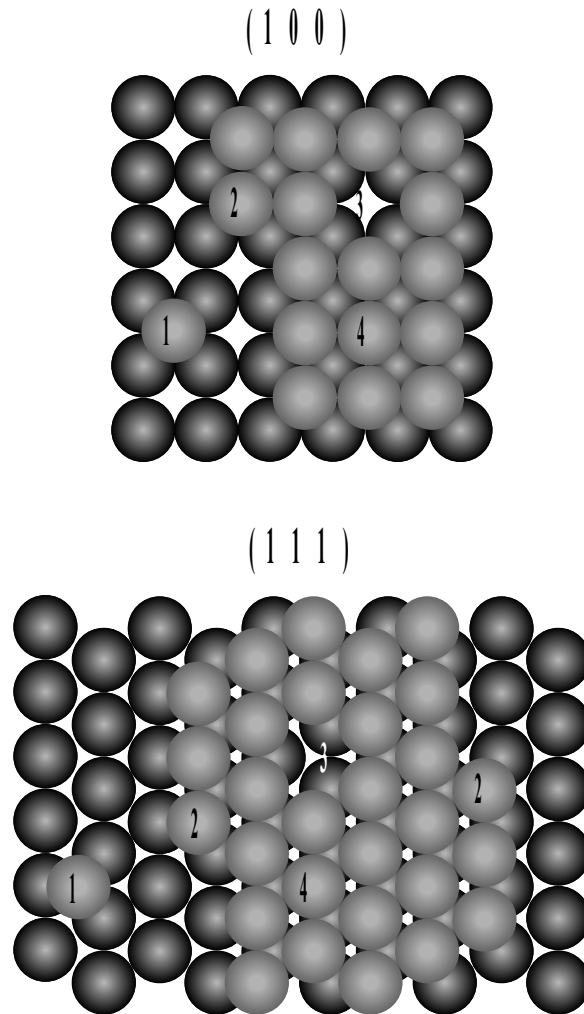


Fig. 1. SOS-model of surface defects.



**Fig. 2.** Ball model of atomic configurations on fcc (100)- and (111)-surfaces. Atoms in deeper layers have a darker shading. Atom 1 is a free adatom on the surface, 2 is a kink atom, 3 is a mono-vacancy in the surface and 4 is a surface atom.

atoms for the (100)- and the (111)-surface, respectively. On both surfaces, the kink atom is 6-fold coordinated. At room temperature, the concentration of free adatoms and mono-vacancies on Cu and Ag surfaces in equilibrium is of the order of  $10^{-9}$ . It increases to the order of  $10^{-5}$  around 500K. The concentration of kinks of monatomic length on metal surfaces is of the order of  $10^{-2}$  at room temperature and about  $10^{-1}$  at 400K.

## 2.2. Vicinal surfaces

The defects discussed before are formed due to thermal activation. Defects as steps and kinks are also germane to the particular kind of surfaces discussed in this paragraph usually referred to as *vicinal surfaces*. Vicinal surfaces have a slight miscut with respect to a low index surface along a high- or low-symmetry direction. This report focuses on vicinal surfaces

of face centered cubic (fcc) metals. In particular, merely those vicinal surfaces are considered which have a miscut with respect to the low index orientations (001) and (111).

Fig. 3 shows a model of a such a surface with a polar angle  $\theta$  and an azimuth  $\Phi$  with respect to the low index surface whose orientations are indicated as (001) and (111) by their surface normals. When the azimuth  $\Phi$  is non-zero, as shown in Fig. 3, the geometrically ideal vicinal surface has equidistant, parallel steps with a regular array of kinks. In contrast to this case, surfaces with no azimuthal miscut reveal no geometric kink sites. Whereas, in the Fig. 3 model all steps are monatomic, real vicinal surfaces may also consist of multilayer high steps.

The (001) surface has four-fold symmetry and therefore includes a set of four equivalent high symmetry directions in the  $\langle 110 \rangle$ -zone<sup>2</sup>. Vicinal surfaces to the (001)-plane with the same miscut angle  $\theta$  and azimuth  $\Phi$  with respect to the  $\langle 110 \rangle$ -zone axis are equivalent. All of these surfaces, reveal steps of the (111)-type, i.e., the microfacet formed at the step edge has a  $\{111\}$ -orientation. The (111)-surface of fcc metals has a three-fold symmetry (if the next atomic layer is considered) and therefore contains two sets of non-equivalent high-symmetry zones,  $\langle 11\bar{2} \rangle$  and  $\langle \bar{1}\bar{1}2 \rangle$ , each including three equivalent crystallographic directions. Hence, vicinal surfaces with the same azimuth  $\Phi$  and miscut angle  $\theta$  which belong, however, to non-equivalent sets, have a different geometrical structure (Fig. 4): Surfaces with miscuts along

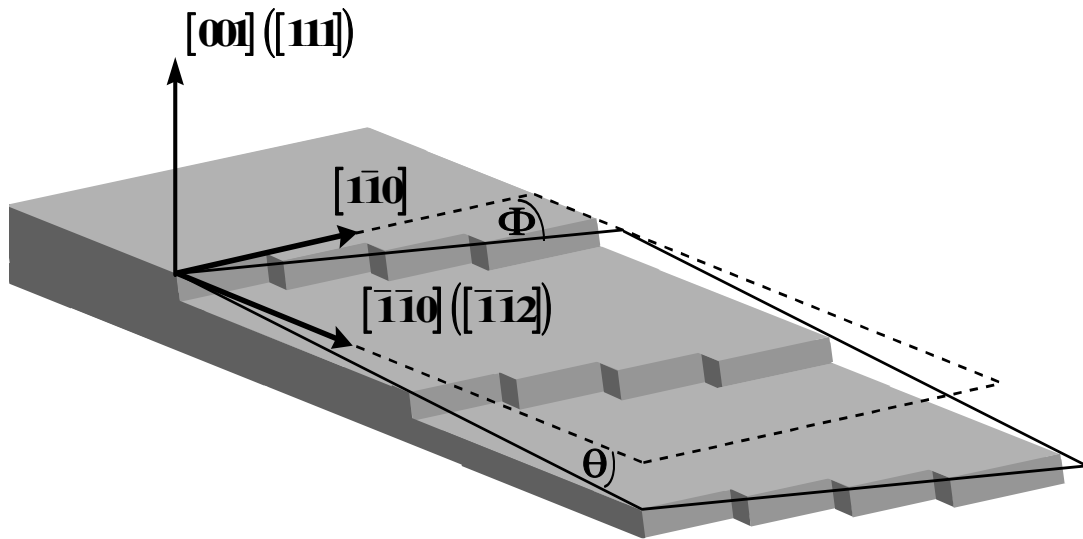


**Fig. 3.** Model of a surface vicinal to the (001)- and the (111)-surface orientation. The vicinal surface may have a miscut with respect to the polar angle  $\theta$  and the azimuth  $\Phi$ . If the azimuth  $\Phi$  is zero, the geometrically ideal vicinal surface consists of parallel, equidistant steps, while for finite azimuth  $\Phi$  the steps have "forced" kinks. The mean distance between steps and kinks depends on the polar angle and the azimuth, respectively.

<sup>2</sup> Note, that crystallographic directions which belong to the same crystallographic zone are indicated by " $\langle hkl \rangle$ " and specific directions within this zone are indicated by " $[hkl]$ ".

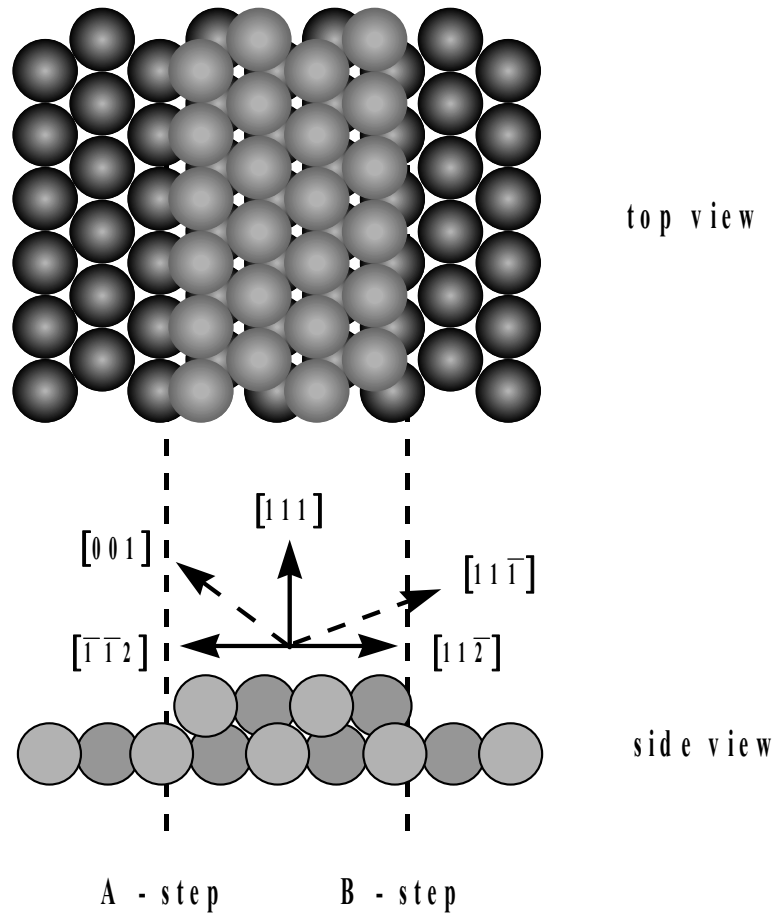


**Fig. 4.** Model of the two step types on the (111)-surface of fcc metals. The so-called A-step forms a (100)-microfacet with the atomic layer below. The B-step forms a (111)-microfacet. Atoms in deeper layers are depicted by a darker shading.

$\langle \bar{1} \bar{1} 2 \rangle$  have (100)-steps (also called A-steps) and for  $\Phi \neq 0$  (111)-oriented kinks. If  $\theta$  is measured with respect to the  $\langle 11\bar{2} \rangle$ -zone, (111)-steps (B-steps) are formed and the kink orientation is (100). In Appendix A, the relation between the Miller indices and the miscut angle  $\theta$  is described for some vicinal surfaces to (001) and (111) with  $\Phi=0$ . The geometrical structure around kinks at A- is similar to that at B-steps, as can be seen from Fig. 2. In the nearest-neighbor model, a kink in an A-step is equivalent to a B-step segment of one atomic length and vice versa.

### 2.3. Adatom and vacancy islands

Entire adatom and vacancy islands are thermally generated only close to the roughening temperature of a surface [22] which may be close to the melting temperature. At lower temperatures, adatom and vacancy islands are created by deposition or removal of material. Fig. 5 shows ball models of adatom and vacancy islands on fcc (100)- and (111)-surfaces. On (100)-surfaces, the island periphery is formed by monatomic step segments, which belong to the  $\langle 110 \rangle$ -zone. Hence, the microfacets formed at the island edge segments are (111)-oriented. On (111)-surfaces, the island edges may belong to the  $\langle \bar{1}01 \rangle$ - or the  $\langle 0\bar{1}1 \rangle$ -zone. Due to the three-fold symmetry of the (111)-plane, the step segments of adatom and vacancy islands are an alternating sequence of A- and B-steps. As isolated infinite steps on surfaces, step segments of islands may have free adatoms (1) and kinks (2) which are included in the model.

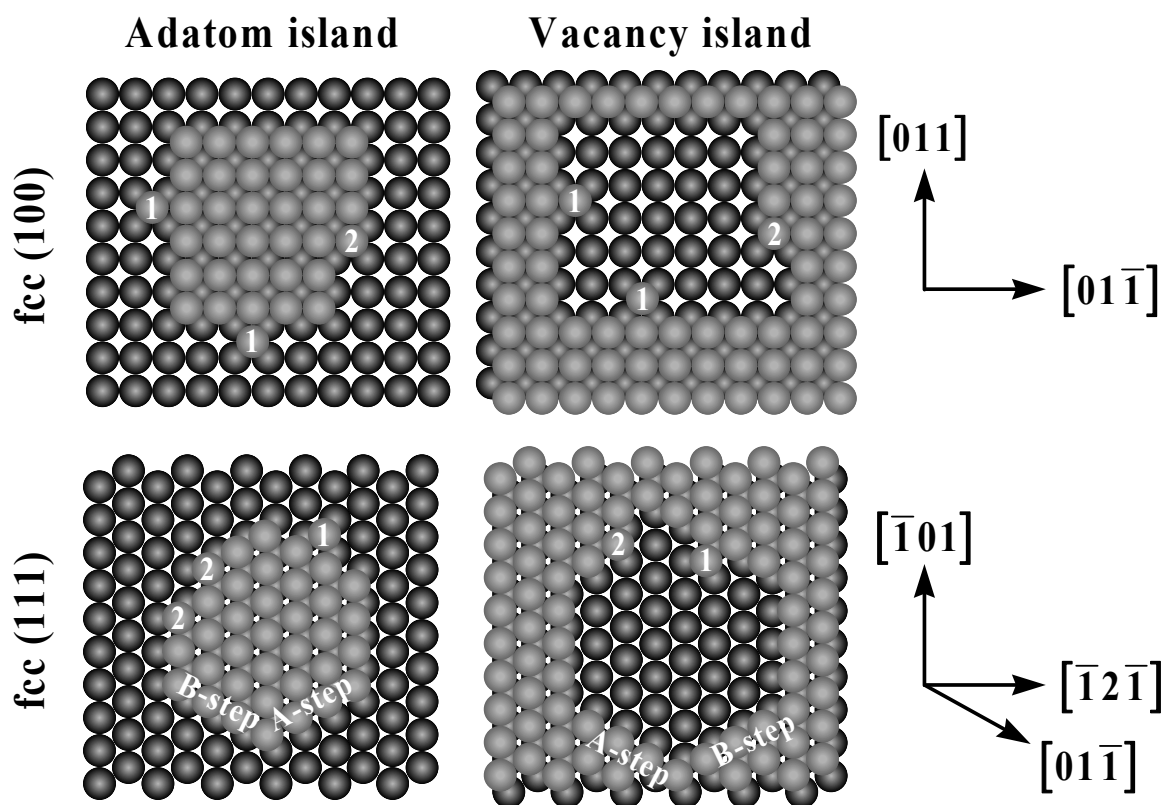


Fig. 5. Model of adatom and vacancy islands on fcc (100)- and (111)-surfaces. Adatoms and kinks at the island edges are indicated by numbers (1) and (2), respectively.

### 2.4. Stability of vicinal surfaces

The spontaneous creation of defects as steps and islands at high temperatures may render vicinal surfaces unstable such that the surface height at two points on the surface are no longer correlated. Then, the vicinal facet orientation is not defined and the surface is in a state

above its *roughening transition* [22]. Energetic instabilities of a vicinal surface may arise either by step-step interactions (see Section 4) or by high step energies. In both cases, the formation of large step bunches and step-free terraces may be energetically favorable over a regular step array. The difference in step free energies between A- and B-steps on fcc (111)-surfaces may likewise be the driving force for the restructuring of vicinal surfaces. For reconstructed surfaces, where the surface unit cell is larger than that of the unreconstructed substrate, vicinal surfaces may restructure towards the energetically favorable *magic* vicinal orientations proposed by Bartolini et al. [23]. The magic vicinal orientations correspond to terrace widths between the steps of integer multiple length of the reconstructed surface unit cell.

In experiment, a restructuring of vicinal surfaces was observed for some fcc metals on surfaces vicinal to the (111)-plane. Klas et al. [24] concluded from *low energy electron diffraction* studies that Cu(545) ( $\theta=5.77^\circ$  with respect to the  $\langle 1\bar{2}1 \rangle$ -zone, B-steps) restructures and forms an irregular zig-zag pattern of A-steps. The zig-zag pattern was later observed in STM measurements on Cu(997) ( $\theta=6.45^\circ$  with respect to the  $\langle 11\bar{2} \rangle$ -zone, B-steps) by our group [25]. The surface restructures into  $\{445\}$ - and  $\{212\}$ -facets, which both consist

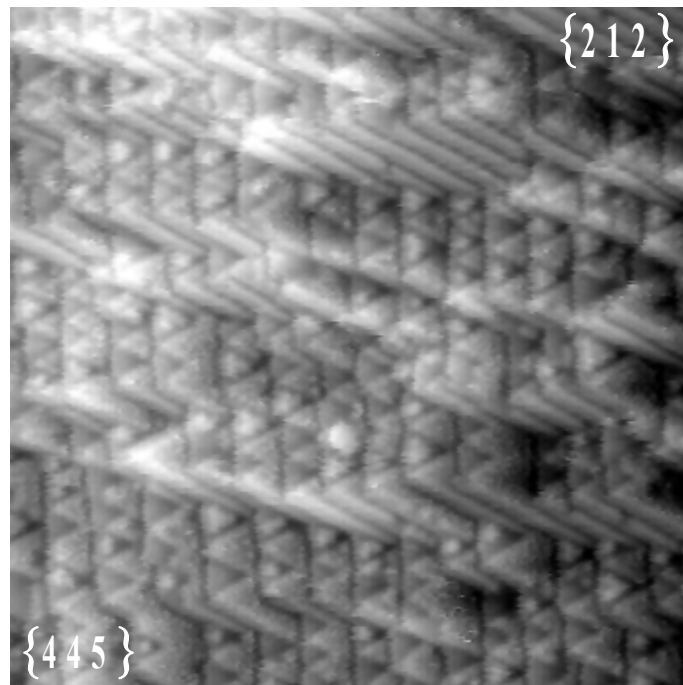


**Fig. 6.** Room temperature STM image of the Cu(997) surface, which restructures into  $\{445\}$ - and  $\{212\}$ -facets [25]. The scan width is 44nm.

exclusively of A-steps and the  $\{445\}$ -oriented areas reveal a zig-zag structure of the steps (Fig. 6). A parallel step structure of B-steps may be temporarily established for Cu(997) by low annealing temperatures during sample preparation [26]. This step structure, however, is unstable and the steps fluctuate stronger than A-steps in equilibrium as will be discussed in Section 3.3.5. We interpreted this observation as an enhanced mass transport on the (997)-plane after preparation at low temperatures, which drives the surface from a non-equilibrium state to a faceted equilibrium structure [26]. The terrace width on such a surface should be broader and steps may not be found in discrete lattice positions in STM images.

Bönicke et al. [27] observed no faceting on Cu(111) vicinal surfaces with B-steps when the terrace width is smaller than that of the (997)-plane in contradiction to the results of Klas et al. [24]. We showed that Cu(779), a vicinal surface with about the same terrace width as the (997) plane, however with A-steps is stable [25]. Likewise, no restructuring is found on all other Cu vicinal surfaces with A-steps investigated so far [28]. A restructuring was observed for stepped Ni(111) surfaces with Miller indices (221) and (331) by Benndorf et al. [29]. Hahn et al. [30] showed that Pt(997) undergoes a faceting transition at higher temperatures. A temperature dependent instability was furthermore observed for stepped surfaces of Pt(111) by Yoon et al. [31], Ni(111) by Shen et al. [32], Pb(111) by Pinxteren et al. [33] and Au(111) by Bonzel et al. [34].

### ***2.5. Equilibrium dynamics of defects and their influence on STM recording***

In equilibrium, a thermodynamic system fluctuates around the state of minimum free energy. The fluctuations are caused by diffusion of atoms on the surface and mass transport between defects like steps and islands. The net flux between two arbitrary points on the surface vanishes on the time average, because the chemical potential of the surface is constant by definition in equilibrium. The continuous mass transport, the creation and the annihilation of defects lead to a defect mobility that is observable in STM studies of solid surfaces. Special interest has been focused on the mobility of steps in equilibrium and on the wandering of adatom and vacancy islands, due to edge fluctuations, in the past as discussed in detail in the following sections.

The problem in studying dynamic processes on surfaces by STM is that the STM does not genuinely provide the experimentalist with snap shot images, due to the finite speed of the tunneling tip. When the mobility is comparable to or even faster than the scan speed, the STM image includes spatial as well as time information. The contribution of time information becomes significant, in particular, by the *frizzy* appearance of step edges in STM images.

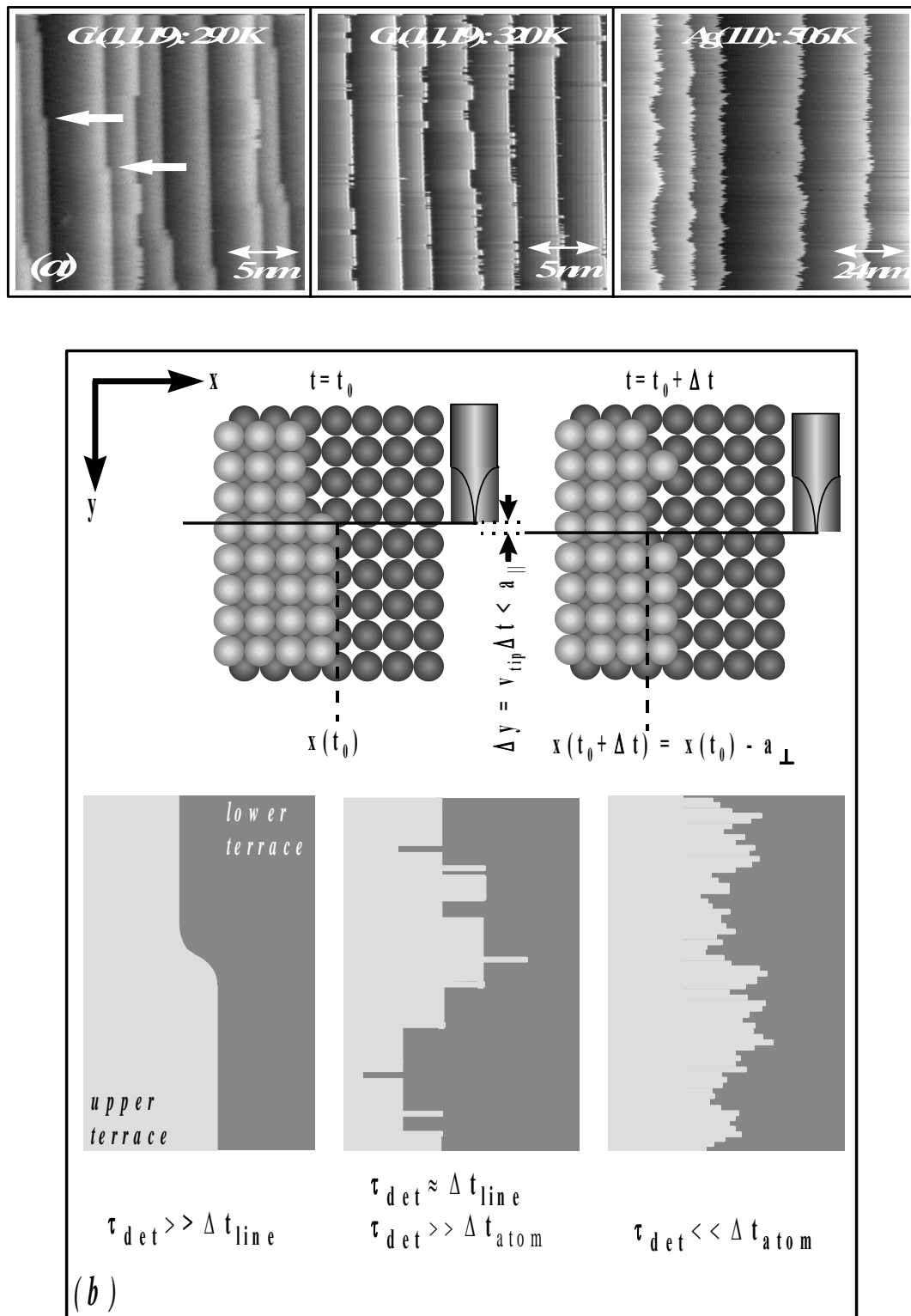


**Fig. 7.** (a) STM images of the Cu(1,1,19) surface (vicinal to the (001)-plane) at 290 and 320K and of a stepped area on Ag(111) at 506K. Note the different scan widths. (b) The frizzy appearance of steps is caused by kink motion along the steps during the scanning process and depends on the scan rate (see text for discussion).

First observations of frizzy steps were reported by Kuk et al. on rough steps on clean Cu(110), which straightened after oxygen chemisorption [35]. The roughness manifested itself by sudden jumps in the step position and was interpreted as mobile copper atoms detaching and attaching at the steps. The same phenomena was later also observed by Wintterlin et al. for the same system [36]. Concern was raised that the step frizziness may be due to noise of the tunneling tip. By studying subatomic high steps in Shockley partial dislocations on Ag(111), Wolf et al. [37] showed that the frizzy appearance of steps cannot be explained by simple tip noise but is rather attributed to kinks crossing the scan line during STM recording. The first quantitative study of this effect was performed by our group on Ag(111) and Cu(100) [38, 39]. In the following, the physics of frizzy steps is explained with the help of Fig. 7.

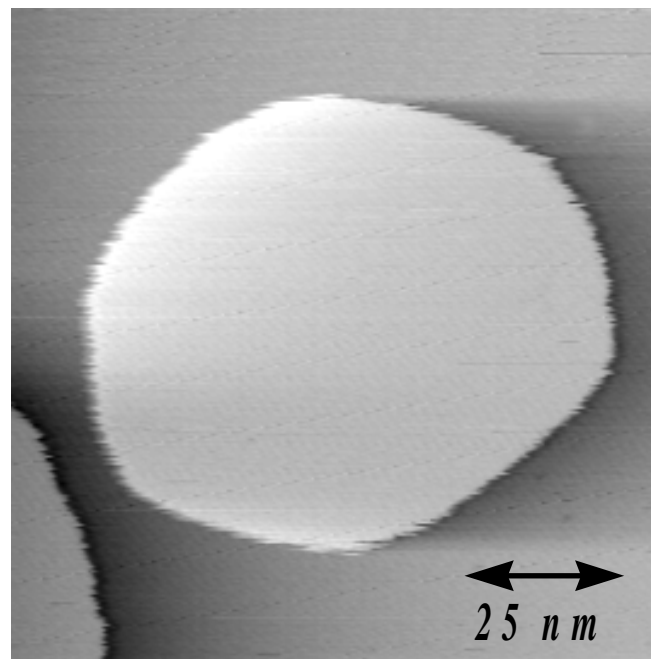
Fig. 7(a) shows STM images of stepped Cu(001) surfaces at 290 and 320 K [40, 41] and also a stepped area on Ag(111) at 506K [42]. The copper steps are almost straight at 290 K despite some kink sites (arrow) which have a round shape, due to the finite resolution of the tunneling tip. At 320 K, steps on Cu(001) display sudden jumps of atomic length in step position perpendicular to the step. Parallel to the step, however, some of the protrusions concern only a single scan line, which corresponds to a length below the diameter of one atom. In addition, the kink-like features at the steps are sharp rather than rounded. Steps on Ag(111) at 506 K are very frizzy and the displayed step positions no longer correspond to atomic lattice sites.

Fig. 7(b) shows a model explaining how kink motion along steps causes sudden jumps in the step position: The tunneling tip scans across a kink site at the step edge at  $t = t_0$  and the step position is displayed at  $x(t_0)$  (top panel). When the tip returns to the same step in the next scan line after an additional time  $\Delta t$ , the kink atom has detached from the kink to the step edge and the step position is shifted by one atomic unit  $a_{\perp}$  to the left. Hence, the step position is displayed at  $x(t_0 + \Delta t) = x(t_0) - a_{\perp}$ , which in turn gives rise to a sudden sharp jump in the step in the STM image. In most cases, the adatom returns to the kink site after having performed a random walk along the step edge and the tip finds the step again in the original position, which gives rise to the finite length of protrusions. According to this interpretation, it is clear that the statistics of the step jumps of defined atomic length such as in Fig. 7(a) is due to adatom detachment kinetics and the random walk of the adatom. A quantitative analysis has been performed by our group [41]. We found that the probability to find a protrusion of a certain length obeys a return statistics [43]. From the detailed temperature dependent study of the return statistics of adatom at kinks, we determined the activation barrier for emission of an adatom from a kink site to a step site ( $E_{em} = 0.53 \pm 0.08 \text{ eV}$ ) and the activation barrier for adatom

diffusion along a straight step ( $E_d=0.47\pm 0.08\text{eV}$ ) [41]. Both values are in good agreement with STM investigations by Girard et al. [44], who analyzed the fluctuations of steps on Cu(1,1,1) off the dense  $\langle 110 \rangle$ -direction (i.e., steps with "forced" kinks) and found  $E_d\sim 0.45\text{eV}$  and  $E_{em}=0.65\text{eV}$ .

Steps are straight and reveal real, rounded kink sites in STM images, when the mean time  $\tau_{det}$  between detachments/attachment processes at kink sites is much larger than the time  $\Delta t_{line}$  needed to scan one line (Fig. 7(b), bottom panel). For stepped Cu(001), this is found only for temperatures below room temperature (Fig. 7(a)). When  $\tau_{det}$  is of the same order of  $\Delta t_{line}$  but still much larger than the time  $\Delta t_{atom}$  to scan across one atom, the steps are frizzy, however, reveal straight segments and the step position is found at discrete lattice sites. This scenario is observed for stepped Cu(001) at 320 K (Fig. 7(a)). Steps appear completely frizzy, when atoms detach from kink sites while the tip is scanning across an atomic site ( $\tau_{det}\ll\Delta t_{atom}$ ), which is observed for copper surfaces above 340 K [40] and for Ag(111) already at room temperature.

When steps appear frizzy in STM images, the coordinate  $y$  along the step edges is also a time axis and the STM images include spatial as well as time information, as was demonstrated for stepped Cu(001) surfaces [40, 45, 46]. For metal surfaces, diffusion may be fast already around room temperature. Hence, cooling of the sample may become necessary in order to obtain exclusively spatial information from STM images. As will be discussed in the next



**Fig. 8.** Monatomic high Ag island on Ag(111) at 393 K. Island edges appear frizzy, due to edge fluctuations.

section, the latter is very important to determine the kink energy.

Step frizziness is also well known from STM images of mobile islands on metal surfaces. Fig. 8 shows a monolayer high adatom island on Ag(111) at 393 K. The island edges appear frizzy, due to atomic diffusion around the island periphery and/or exchange of atoms with the surrounding terrace. The mass transport at the island edges gives rise to a Brownian motion of islands as recently described by Morgenstern et al. [47].

Frizzy steps are also observed on metal electrodes in liquid environment. Dietterle et al. [48] showed that steps on Ag(111) electrodes in sulfuric acid appear frizzy and that the frizziness depends on the electrode potential. Meanwhile, frizzy steps have been qualitatively and quantitatively discussed in quite a number of studies in UHV [37, 41, 42, 44, 49-54] and in an electrolyte [55-62]. Details concerning these studies are given in Sections 3 and 5.

### 3. Step fluctuations

#### 3.1. Energy of a fluctuating step

The total energy of a surface configuration is often modeled by an Hamiltonian, which depends only on the height difference  $|h_{ij} - h_{i+n,j+m}|$  at sites  $(i,j)$  and  $(i+n,j+m)$  (where  $n,m$  are integers) with a coupling constant  $J$ :

$$H = J \sum_{i,j,m,n} |h_{ij} - h_{i+n,j+m}|^p. \quad (3.1)$$

Note, that the energy is normalized with respect to the energy of the flat surface. In the SOS-model, the total energy  $H$  is a linear function of the energy differences between different heights  $h_{ij}$  and  $h_{i+n,j+m}$  and in (3.1) the exponent becomes  $p=1$ . In the *discrete Gaussian model*,  $H$  depends quadratically on the energy difference, and hence,  $p=2$ . For  $p=1$  and nearest-neighbor interactions, (3.1) is analog to the Hamiltonian of a two-dimensional spin-distribution as described by the Ising model [63]. The coupling constant  $J$  corresponds to twice the coupling strength between nearest neighbor sites in the Ising model. In the case of a step on the surface of length  $Na_{\parallel}$  ( $a_{\parallel}$  the atomic unit parallel to the step), (3.1) is rewritten to

$$H = J \sum_{j=1}^N \frac{|x_j - x_{j+1}|}{a_{\perp}}, \quad (3.2)$$

where  $x$  is the direction perpendicular to the step as denoted in Fig. 1 and  $a_{\perp}$  is the atomic distance perpendicular to the step<sup>3</sup>.

A transition from the discrete description in the SOS-model to a continuum approach is based on the continuum model for the kinetics of faceting and surface relaxation by Mullins [64-66]. His two-dimensional problem can be reduced to the one-dimensional case of a fluctuating step profile. Within such an approach, the total free energy  $f$  of a fluctuating step can be expressed in terms of the line tension  $\gamma$ , which is the specific free step energy (per unit length):

---

<sup>3</sup> Note, that in the SOS-model, as shown in Fig. 1,  $a_{\perp}$  and  $a_{\parallel}$  are identical and are measured with respect to nearest-neighbor sites on the square lattice. For real surfaces with steps along the high-symmetry  $\langle 110 \rangle$ -direction of fcc metals,  $a_{\parallel}$  denotes the nearest-neighbor distance parallel to the step which is  $a_{\parallel} = a_0/\sqrt{2}$  ( $a_0$  being the lattice constant) for all surface orientations.  $a_{\perp}$  is the perpendicular distance between atomic rows along  $\langle 110 \rangle$ . In the case of the (100) surface orientation,  $a_{\perp}=a_{\parallel}$ , and for (111) surfaces,  $a_{\perp}=a_0\sqrt{3}/(2\sqrt{2})$ .

$$f = \int \gamma ds = \int \gamma \left( \frac{\partial x}{\partial y} \right) \sqrt{1 + \left( \frac{\partial x}{\partial y} \right)^2} dy. \quad (3.3)$$

Here,  $x$  is again the coordinate perpendicular to the mean orientation of the step and  $y$  is the coordinate parallel to it, as denoted in Fig. 9<sup>4</sup>. The last term in (3.3) corresponds to the small step segment  $ds$  along the step profile (Fig. 9). Variation of the step position  $x(y)$  is accompanied by a variation in the total step length, and hence, leads to a variation in the step free energy  $f$ . This variation is given by the chemical potential  $\mu$ , since moving the step by  $\delta x$  over a step length  $dy$  changes the number of atoms by  $dN = \delta x \cdot dy / \Omega$ , where  $\Omega = a_{||} a_{\perp}$  is the area of an atom:

$$\delta f = \frac{1}{\Omega} \int (\delta x \mu) dy, \quad (3.4)$$

with the chemical potential

$$\mu = -\Omega \frac{\partial}{\partial y} \frac{\partial}{\partial \left( \frac{\partial x}{\partial y} \right)} \left( \gamma \left( \frac{\partial x}{\partial y} \right) \sqrt{1 + \left( \frac{\partial x}{\partial y} \right)^2} \right). \quad (3.5)$$

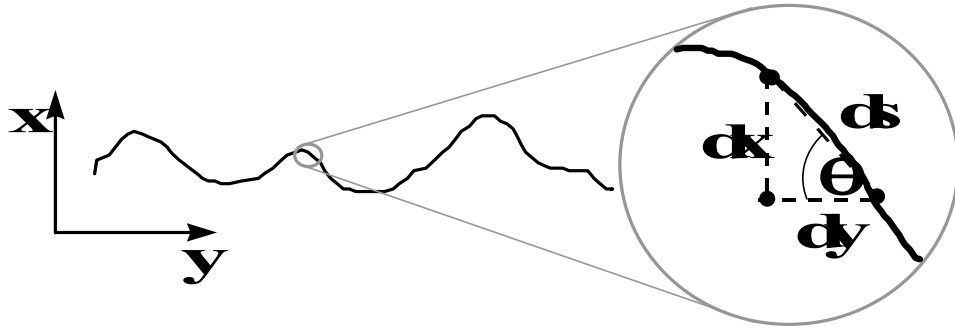


**Fig. 9.** The profile of a fluctuating step may be interpreted as the sum of many small step segments  $ds$ . The step free energy can then be expressed in terms of the local slope of the step profile, i.e., the local curvature and the line tension.

<sup>4</sup> This notation is frequently referred to as "*Maryland notation*", since it has been introduced by the group at the University of Maryland, College Park [67] and is, meanwhile, used by many experimentalists and theorists.

As can be seen from Fig. 9,  $\partial x/\partial y$  can be substituted by  $\tan\theta$ , where  $\theta$  is the local slope at the step profile. When using this substitution in the differential equation in (3.5), the chemical potential can be expressed in terms of the local curvature  $K = -\partial^2 x/\partial y^2 \left[1 + (\partial x/\partial y)^2\right]^{-3/2}$

(For a derivation of (3.5) and (3.6), see Appendix B.):

$$\mu = \Omega K \left( \gamma + \frac{\partial^2 \gamma}{\partial \theta^2} \right). \quad (3.6)$$

For low temperatures, the curvature  $K$  is small and can be approximated by  $K \approx -\partial^2 x/\partial y^2$ .

Then, (3.6) becomes (with  $\Omega = a_{\perp} a_{\parallel}$ )

$$\mu = -a_{\perp} a_{\parallel} \frac{\partial^2 x}{\partial y^2} \left( \gamma + \frac{\partial^2 \gamma}{\partial \theta^2} \right). \quad (3.7)$$

The last term in (3.6) and (3.7) is the step-edge stiffness:

$$\tilde{\gamma} = \gamma + \frac{\partial^2 \gamma}{\partial \theta^2}. \quad (3.8)$$

For (a) the SOS- and (b) the Ising-model, the stiffness can be calculated exactly, as demonstrated by Fisher and Forgacs et al. [68-70]:

$$\tilde{\gamma} = 2k_B T a_{\parallel} / a_{\perp}^2 \sinh(J/2k_B T). \quad (3.9a)$$

$$\tilde{\gamma} = k_B T a_{\parallel} / a_{\perp}^2 \sinh(J/k_B T). \quad (3.9b)$$

### 3.2. Langevin equation

In non-equilibrium, the driving force for the relaxation of the system towards equilibrium is the gradient in the chemical potential  $\mu$ . The relaxation rate depends on the kinetics of the dominant atomic processes, which mediate the mass transport associated with the relaxation of the system. In addition, thermal noise introduces random fluctuations to the system. In the

case of the one-dimensional system of step fluctuations, the thermodynamics may be described by a *Langevin equation* as established by Kardar [71]:

$$\frac{\partial x(y,t)}{\partial t} = \frac{\Gamma_h}{k_B T} \Lambda(x,t) + \eta(x,t). \quad (3.10)$$

$\Lambda(x,t)$  is a to be determined function of  $x$  and  $t$  and the last term in (3.10),  $\eta(x,t)$ , is a noise term.  $\Gamma_h = a_{\perp}^2 a_{\parallel} / \tau_h$  is the *friction coefficient* as defined by Bartelt et al. [72], which involves the time  $\tau_h$  between two detachment processes from a step site.  $\Gamma_h$  depends on the sticking probability of an atom at a distinct step site and is therefore a function of the activation barriers relevant for the dominant mass transport processes. Blagojevic and Duxbury [73] presented a systematic derivation of the friction coefficient for different mass transport situations.

To provide an example for the atomic processes involved in the fluctuations, we consider step motion by detachment/attachment of atoms from the step onto the terrace. Fig. 10 shows the relevant energy barriers: Approaching the step edge from the lower terrace, an atom may

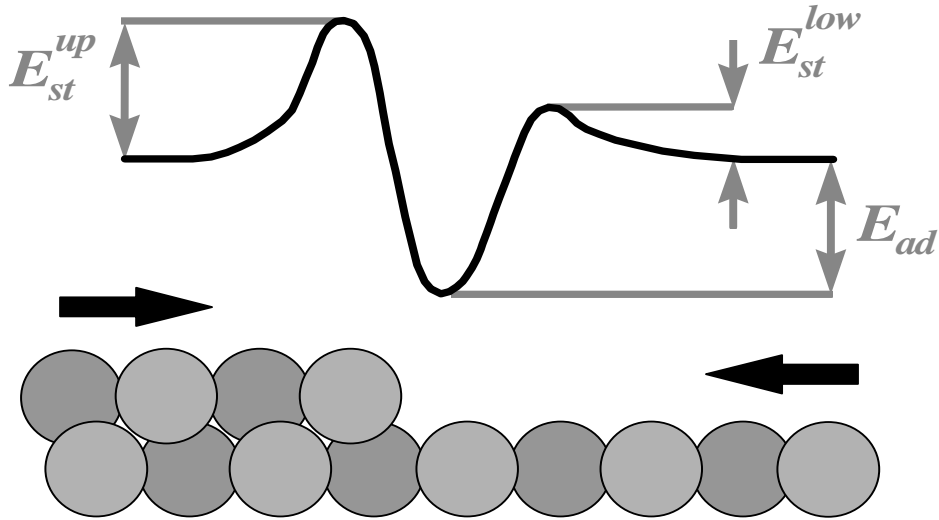


**Fig. 10.** The sticking probability of an atom approaching a step edge from the upper or the lower terrace is given by the activation barriers for crossing the step edge  $E_{st}^{up}$  and the extra energy barrier  $E_{st}^{low}$  for being attached from the lower terrace. In the upper panel, the energy potential of an atom approaching the step edge is shown. The lower panel is a side view of a surface with a step. The potential corrugation associated with terrace diffusion is not included (after Blagojevic and Duxbury [73]).

have to overcome an additional sticking barrier  $E_{st}^{low}$ . When the atom attaches from the upper terrace, sticking to the lower step edge may be hindered by the energy barrier  $E_{st}^{up}$ <sup>5</sup>. The formation energy of an atom on the terrace from a step site is  $E_{ad}$ . In this special case of step fluctuations, mediated by attachment/detachment from step sites onto terrace sites, the jump rate is given by<sup>6</sup> [73]

$$\Gamma_{EC} = a_{\perp}^2 a_{\parallel} \nu e^{-E_{ad}/k_B T} \left( e^{-E_{st}^{low}/k_B T} + e^{-E_{st}^{up}/k_B T} \right), \quad (3.11)$$

where  $\nu$  is the attempt frequency. When the step fluctuations are due to motion of atoms along the steps,  $\Gamma_{PD} = a_{\perp}^2 a_{\parallel} \nu_d e^{-E_d/k_B T}$  with  $E_d$  being the diffusion barrier along the step edge. The detailed microscopic meaning of the hopping coefficients and the attempt frequencies are later discussed in Section 3.3.2.

The function  $\Lambda(x, t)$  in (3.10) depends also on the dominant mass transport and can be expressed in terms of the chemical potential  $\mu(x, t)$  and the *diffusion kernel*  $P(\ell)$  [73]:

$$\Lambda(x, t) = \int_0^{L/2} P(\ell) \frac{\partial^2 \mu}{\partial x^2} d\ell, \quad (3.12)$$

with  $L$  the length of the step. The diffusion kernel describes the probability that an atom at site A reaches site B at distance  $\ell$ . When the step fluctuations are mediated by edge diffusion, the diffusion kernel is given by the probability that an atom at the step edge in one atomic distance to the site  $\ell$  reaches site  $\ell$ , hence [73],

$$P(\ell) = \frac{1}{2} \left[ \delta(\ell - a_{\parallel}) + \delta(\ell + a_{\parallel}) \right], \quad (3.13)$$

---

<sup>5</sup> This extra barrier is also known as *Ehrlich-Schwoebel (ES-) barrier* [74, 75] or *step edge barrier*. The ES-barrier is an extra energy barrier for hopping of atoms down a step. For large ES-barriers, atoms on the upper terrace which approach the step edge are most probably reflected and interlayer mass transport is significantly reduced. The ES-barrier is discussed in detail in Section 6.

<sup>6</sup> In the following, the friction coefficient is denoted with different indices as a reminder that the friction coefficient varies with the various mass transport situations. The case discussed in (3.11) is also known in the literature as "*evaporation/condensation*", and hence, " $\Gamma_{EC}$ " is used for this case. Step edge diffusion is usually denoted as "*periphery diffusion*", and hence,  $\Gamma_h$  becomes " $\Gamma_{PD}$ ". A third important case is called "*terrace diffusion*" and the sticking coefficient is therefore " $\Gamma_{TD}$ ". The different mass transport situations are discussed in detail later.

where  $\delta(x)$  is the delta-function. In the case of evaporation/condensation, the atom detaches from the step site onto the terrace site and surface diffusion is fast. In addition, the correlation length  $\xi$  between atomic sites is assumed to be much larger than the step length  $L$ ,  $\xi \gg L$ . Then, the diffusion kernel is constant and is given by [73]

$$P(\ell) = L^{-1}. \quad (3.14)$$

In the case of slow terrace diffusion, the situation is more complex. Here, the attachment/detachment at step sites is fast compared to the surface diffusion. Hence, an adatom concentration profile is built up on the terrace. For details see [73] (Section 2.3 and Appendix C), [76] (Section III) and [19] (Section 3.3.4.1).

### 3.3. Step correlation function $G(y,t)$

For a step in equilibrium, the step fluctuations are measured by means of a step correlation function  $G(y,t)$ <sup>7</sup>

$$G(y,t) = \left\langle \left( x(y,t) - x(y_0,t_0) \right)^2 \right\rangle, \quad (3.15)$$

where the notation for  $x$  and  $y$  is as before (Fig. 9). Steps on surfaces in equilibrium fluctuate (around their mean position if there is one), and hence,  $x$  is a function of the time  $t$ . The reference values  $y_0$  and  $t_0$  are usually set to zero.  $G(y,t)$  measures the fluctuation amplitude of a wandering step in space and time.

As an alternative to (3.15), one may also consider the case in which an initially straight step reaches equilibrium due to its fluctuations. In the latter case, the fluctuation width at a distinct position  $y$  is denoted as  $w(t)$ , where  $w(t)$  is related to  $G(y=0,t)$  by  $w^2(t) = G(y=0,2t)$  [72, 73].

#### 3.3.1. Spatial correlation function $G(y,t=0)$

Here, the step structure is analyzed for a fixed time  $t=0$ , i.e., snap shot images of the surface are considered. In experiment, snap shot images are recorded, if surface diffusion is slow. Then, the step correlation function depends only on the spatial coordinate along the step. When neighboring step sites move uncorrelatedly, the motion of a step position  $x(y)$  is a

<sup>7</sup> In some of the experimental work, this correlation function is denoted as "F(y,t)" [40, 50, 59, 60, 77, 78],  $\sigma_x^2(y,t)$  [51, 52] or " $\sigma_f^2$ " [38].

*random walk* [43], and consequently,  $G(y)$  is a linear function of the distance  $y$  along the step<sup>8</sup> [67]:

$$G(y) = \langle (x(y) - x(0))^2 \rangle = \frac{b^2}{a_{\parallel}} |y|. \quad (3.16)$$

In the nearest-neighbor model, the energy of a kink of length  $na_{\perp}$  is  $n\varepsilon$ , where  $\varepsilon$  is the energy of a monatomic kink. The *diffusivity*  $b^2$  is then expressed by

$$b^2 = \frac{2a_{\perp}^2}{\sinh^2(\varepsilon/2k_{\text{B}}T)}. \quad (3.17)$$

For low temperatures, where kinks are exclusively of monatomic length, (3.17) reduces to

$$b^2 = \frac{2a_{\perp}^2}{2 + e^{\varepsilon/k_{\text{B}}T}}. \quad (3.18)$$

From (3.18) one finds the relation between the diffusivity  $b^2$  and the *kink concentration*  $P_k$  for  $\varepsilon \gg k_{\text{B}}T$  to be

$$b^2 \approx P_k a_{\perp}^2 = 2e^{-\varepsilon/k_{\text{B}}T} a_{\perp}^2. \quad (3.19)$$

From (3.9), (3.17) and (3.19) comes the step edge stiffness

$$\tilde{\gamma} = \frac{k_{\text{B}}T}{b^2} a_{\parallel} \approx \frac{k_{\text{B}}T}{2e^{-\varepsilon/k_{\text{B}}T}} \frac{a_{\parallel}}{a_{\perp}^2}. \quad (3.20)$$

Note that (3.19), (3.20) are model independent and valid for steps with a mean orientation along close-packed directions.

---

<sup>8</sup> When  $y_0 \neq 0$ ,  $G(y)$  is linear in the distance  $|y - y_0|$ . In the following, however,  $y_0$  is set to zero.

By measuring  $G(y)$ , one can determine the kink energy  $\varepsilon$  ((3.16), (3.17) and (3.19)). In most of the experimental work on metal surfaces [38-41, 45, 46, 77-80], the kink creation energy was determined by the analysis of  $G(y)$ . Fig. 11 shows  $G(y)$  measured on (a) a Cu(001) vicinal surface with a mean step separation of about  $17\text{\AA}$  (corresponding to a (1,1,13) surface orientation) at 290K [40] and (b) for Pt(111) between 530 and 550K [78]. For Cu(1,1,13), a kink energy  $\varepsilon=126\pm 3\text{meV}$  (per atom) is found. This value is in agreement with measurements on Cu(1,1,11) (mean step separation  $14\text{\AA}$ ) by Barbier et al. and our group on Cu(1,1,19) (mean step separation  $24\text{\AA}$ ), where  $\varepsilon=123\text{meV}$  [79] and  $\varepsilon=128\pm 3\text{meV}$  [40] were obtained, respectively. On Pt(111), the kink energy was experimentally determined for A- and B-steps to be about 170 meV [78]. The experimental results for both Cu and Pt surfaces are larger than what is found from *Effective Medium Theory* (EMT)-calculations by Stoltze [81]:  $\varepsilon=107\text{meV}$  and  $104\text{meV}$  for Cu(100) and Pt(111), respectively. Calculations using the *Embedded Atom Method* (EAM) by Nelson et al. [82] for Pt(111), on the other hand, are in good agreement with the experimental results. These authors calculate  $178\text{meV}$  for a (111)-oriented kink at a B-step. Very recent ab-initio calculations by Feibelman [Feibelman, 2000 #1276] show, however, that the kink energies for A- and B-steps should differ significantly (A-step:  $\varepsilon=0.25\text{eV}$ ; B-step:  $\varepsilon=0.18\text{eV}$ ). Tian and Rahman [83] performed EAM calculations for kink formation energies on Cu(001) vicinal surfaces. Their results are in good agreement with our experimental values: For stepped Cu(001) with mean step separations of about  $6.4$  and  $37\text{\AA}$ , they obtain  $\varepsilon=135\text{meV}$  and  $137\text{meV}$ , respectively.

Hoogeman et al. and Chang et al. [84, 85] analyzed the kink distribution probability to

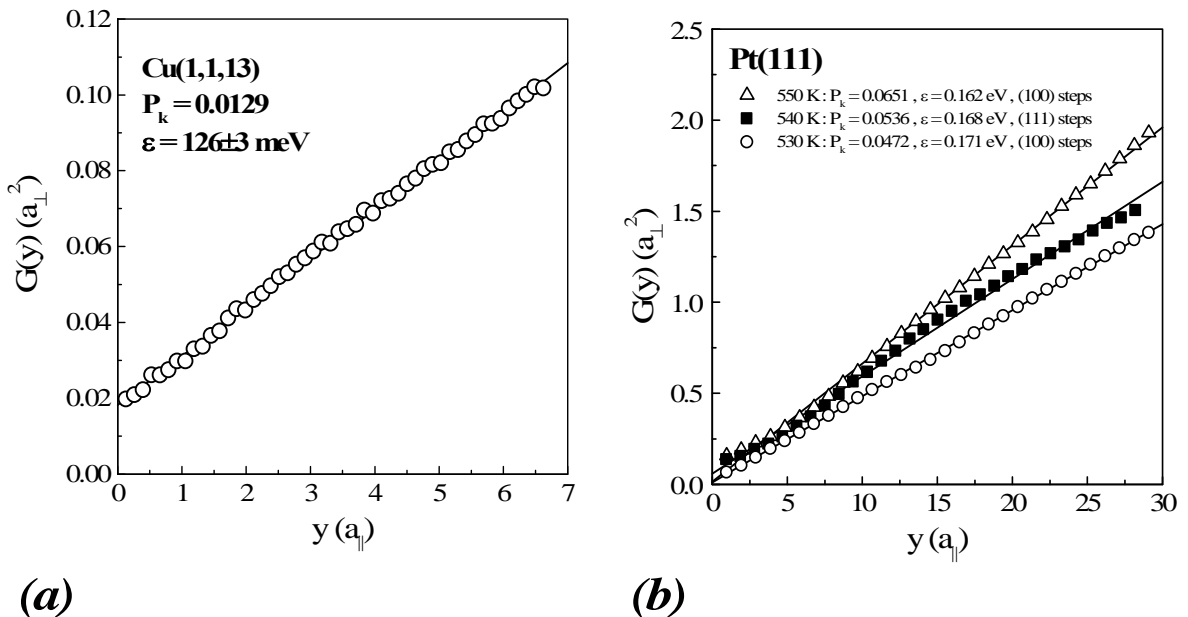


Fig. 11. Spatial correlation function  $G(y)$  ((3.16)) for (a) Cu(1,1,13) [41] and (b) Pt(111) [78].

measure the kink formation energy on stepped Ag(001). They find a kink energy of  $\varepsilon=114\pm 1\text{meV}$  and  $\varepsilon=110\pm 2\text{meV}$  for surfaces with a mean step separation of about 7 and  $4\text{\AA}$ , respectively. Both values are in reasonable agreement with EAM calculations by Nelson et al. [82], who obtain  $\varepsilon=102\text{meV}$ , but are significantly larger than the EAM calculations by Stoltze ( $\varepsilon=82\text{meV}$ ) [81]. *Equivalent Crystal Theory* (ECT) calculations for Ag, Cu and Pt by Khare et al. [86] yield generally too high values for the kink energy.

In order to examine the kink energy on Ag(110), Ozcomert et al. [93] studied the curvature of a pinned step at room temperature whose nominal orientation is along the  $[1\bar{1}0]$ -direction. From the curvature they determined the step edge stiffness  $\tilde{\gamma}$  which is directly related to the step diffusivity  $b^2$  via (3.20). They find  $\tilde{\gamma} = 5.2\text{meV}\text{\AA}^{-1}$ , and hence,  $\varepsilon=43\text{meV}$ . In Table 1, theoretical and experimental values for the kink formation energy on fcc metal surfaces<sup>9</sup> are listed including experimental studies [88], where  $\varepsilon$  has been determined from the equilibrium shape of islands [96, 97]. This method will be discussed later in Section 6. From Table 1 one finds, that the EMT results by Stoltze [81] are generally much too low compared to the experimental values. In general, good agreement between experiment and theory is provided by the EAM calculations by Nelson et al. [82] and by ab-initio calculations by Feibelman [Feibelman, 1999 #989; Feibelman, 2000 #1276]. EAM calculations by Liu et al. are of the right order of magnitude [95].

### 3.3.2. Time dependence of step fluctuations: Time correlation function $G(y=0,t)$

For a fixed value of  $y$  (e.g.,  $y=0$ ), the step correlation function has the form

$$G(t) = \left\langle (x(t) - x(0))^2 \right\rangle. \quad (3.21)$$

In Section 3.2, it was mentioned that the Langevin equation for a one-dimensional fluctuating step (3.10) is a function of the diffusion kernel  $P(\ell)$ , which depends on the mass transport involved in the step fluctuations (3.12)-(3.14). Therefore, the solution of the partial differential equation as given by the Langevin expression depends on the details of the atomic

---

<sup>9</sup> Results for semiconductor surfaces are given in [19]. There, however, experimental results for the diffusivity  $b^2$  are listed instead, which is related to the kink energy via (3.17)-(3.19). Note, that the diffusivity is temperature dependent and in order to obtain the kink energy  $\varepsilon$ , the actual equilibrium temperature has to be considered.

Table 1.

Surface	Vicinal and step orientation	Terrace width (Å)	$\epsilon_{\text{exp}}$ (meV)	$\epsilon_{\text{calc}}$ (meV)	Ref.
<i>Cu(001)</i>				107 <sup>(10)</sup>	[81]
				139 <sup>(11)</sup>	[87]
			129±9 <sup>(12)</sup>		[88]
				163 <sup>(13)</sup>	[89]
	(115) (111)-steps    $\langle 110 \rangle$	6.4		135 <sup>(11)</sup>	[83]
	(1,1,11) (111)-steps    $\langle 110 \rangle$	14	123 <sup>(14)</sup>		[79]
	(1,1,13) (111)-steps    $\langle 110 \rangle$	16.6	126±3 <sup>(14)</sup>		[40]
	(1,1,19) (111)-steps    $\langle 110 \rangle$	24.2	128±3 <sup>(14)</sup>		[40, 41]
	(1,1,29) (111)-steps    $\langle 110 \rangle$	37		137 <sup>(11)</sup>	[83]
<i>Cu(111)</i>			A-step: 113±8 <sup>(12)</sup> B-step: 121±8		[88, 90]
				A-step: 92 <sup>(13)</sup> B-step: 117	[91]
				107 <sup>(10)</sup>	[81]
<i>Cu(110)</i>			step    $\langle 110 \rangle$ : 44 <sub>(11)</sub> step    $\langle 100 \rangle$ : 133	[87]	
<i>Ag(111)</i>			101±5 <sup>(12)</sup>		[88]
				79 <sup>(10)</sup>	[81]
				99 <sup>(11)</sup>	[87]
				B-step: 74 <sup>(13)</sup>	[89]
				A-step: 102 <sup>(11)</sup> B-step: 99	[82, 86]
<i>Ag(001)</i>				82 <sup>(10)</sup>	[81]
				102 <sup>(11)</sup>	[82, 86]
	(113) (111)-steps    $\langle 110 \rangle$	4.3	110±2 <sup>(15)</sup>		[85]
	(115) (111)-steps    $\langle 110 \rangle$	7.2	114±1 <sup>(15)</sup>		[85, 92]

<sup>10</sup> EMT calculations (no distinction is made between A- and B-steps on (111) surfaces).

<sup>11</sup> EAM calculations.

<sup>12</sup> Determined from the equilibrium shape of monolayer islands.

<sup>13</sup> LDA first principles calculations.

<sup>14</sup> Determined from the spatial correlation function  $G(y)$  (3.16), (3.19).

<sup>15</sup> Evaluation of the kink probability distribution.

**Table 1 (cont.).**

Surface	Vicinal and step orientation	Terrace width (Å)	$\epsilon_{\text{exp}}$ (meV)	$\epsilon_{\text{calc}}$ (meV)	Ref.
<i>Ag(110)</i>			43 <sup>(16)</sup>		[93]
			29 <sup>(17)</sup>		[94]
				step    $\langle 110 \rangle$ : 3 <sup>(10)</sup> step    $\langle 100 \rangle$ : 79	[81]
<i>Au(001)</i>			70 <sup>(10)</sup>	[81]	
<i>Au(111)</i>				74 <sup>(10)</sup>	[81]
<i>Au(110)</i>				step    $\langle 110 \rangle$ : -8 <sup>(10)</sup> step    $\langle 100 \rangle$ : 75	[81]
				step    $\langle 110 \rangle$ : 2 <sup>(11)</sup> step    $\langle 100 \rangle$ : 24	[95]
<i>Pt(001)</i>				102 <sup>(10)</sup>	[81]
<i>Pt(111)</i>			A-step: 171±5 <sup>(14)</sup> B-step: 168±5		[78]
				A-step: 316 <sup>(13)</sup>	[89]
				A-step: 161 <sup>(11)</sup> B-step: 178	[82, 86]
				104 <sup>(10)</sup>	[81]
				A-step: 250 <sup>(13)</sup> B-step: 180	[Feibelman, 2000 #1276]

**Table 1.**

Overview over experimental and theoretical values of the kink formation energy  $\epsilon$  on various fcc metal surfaces in UHV. If the measurements were performed on vicinal surfaces to the low-index planes given in column 1, the Miller indices are given in column 2 (to calculate the corresponding miscut angle see Appendix A).

<sup>16</sup> Evaluation of the step curvature at pinning sites. Note, that the kink energy given here is an average over both step types on a  $\{110\}$ -surface.

<sup>17</sup> Analysis of Fourier representation of  $G(t)$ .

processes involved in the step fluctuations. Pimpinelli et al. [98], Blagojevic and Duxbury [73] as well as Khare and Einstein [76] have discussed multiple solutions of (3.10) for different mass transport situations. Here, a summary of the various solutions is given, which can be found in great detail also in a review by Jeong and Williams [19].

(i) *Equilibrium with gas phase.*

This case corresponds to "Case A" in the paper of Pimpinelli et al. [98] and "3d-Evaporation condensation" in the work of Khare and Einstein [76]. Atoms from the step edge are emitted onto the terrace and exchanged with the gas phase, after a mean diffusion time on the terrace. If the mean diffusion path on the terrace is much smaller than the mean terrace width  $L$  of the stepped surface and the surrounding gas phase is the reservoir for atoms desorbing from the surface and vice versa (left panel of Fig. 12(i)), the time correlation function is

$$G(t) = (P_k c_t)^{1/2} \left( \frac{D_t}{\tau_{sg}} \right)^{1/4} t^{1/2}. \quad (3.22)$$

Here,  $c_t$  and  $P_k$  are the adatom concentration on the terraces and the kink density at the steps per site. The diffusion constant for adatoms on the terraces is denoted as  $D_t$ , and  $\tau_{sg}$  is the average time of an atom on the surface before it desorbs into the gas phase, likewise, it is emphasized that (3.22) and the following equations contain atomic unit parameters  $a_{\perp}$  and  $a_{\parallel}$ . In order to extract the physical relevant tracer diffusion coefficients and pre-exponential factors, the scaling has to be taken into account. As shown in Appendix C, the kink and adatom concentration can be considered as dimensionless and tracer diffusion constants as to have units  $s^{-1}$  (hopping rate), if  $G(t)$  is plotted in units of  $a_{\perp}^2$  and the step-step distance  $L$  in units of  $a_{\perp}$ .

If the diffusion length is of the order of the mean terrace width or even larger (right panel of Fig. 12(i)), neighboring steps serve also as a sink or source for atoms. Then, the time correlation function depends also on the mean terrace width  $L$ :

$$G(t) = \left( P_k \frac{c_t}{\tau_{sg}} \right)^{1/2} L^{1/2} t^{1/2}. \quad (3.23)$$

(ii) *Rapid exchange of atoms between steps.*

This case corresponds to "Case D" of Pimpinelli et al. [98] and to "Diffusion from step to step" of Khare and Einstein [76]. Here, the terrace diffusion is fast and the atom reservoir are the neighboring steps (Fig. 12 (ii)), then,

$$G(t) = (c_t D_t P_k)^{1/2} L^{-1/2} t^{1/2}. \quad (3.24)$$

Whereas the time dependence remains a  $t^{1/2}$ -law as in the previous case, the dependence on the mean terrace width is with the inverse power in  $L$  compared to (3.23). Therefore, the dependence of the time correlation function  $G(t)$  on the mean step-step distance  $L$  allows to discriminate between different mass transport situations which cause the same time exponent.

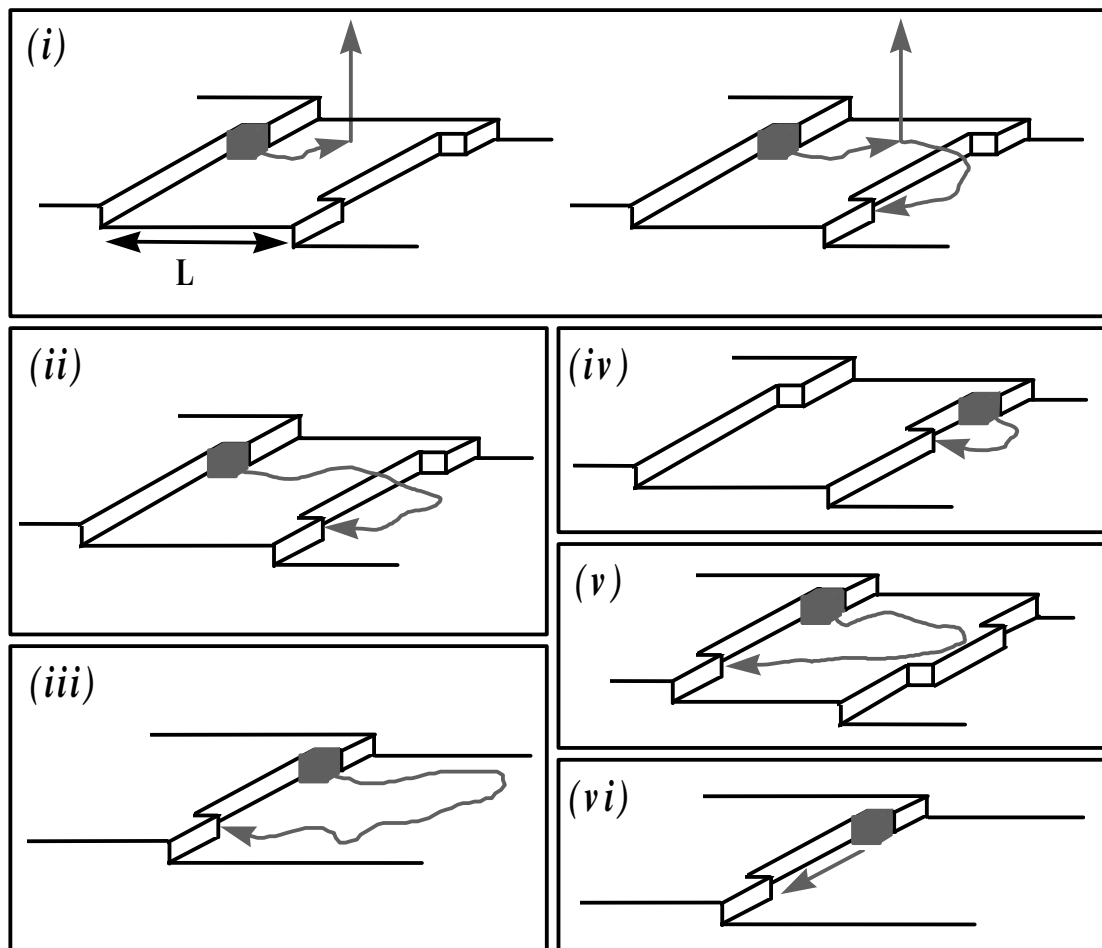


**Fig. 12:** Different mass transport situations may mediate step fluctuations and give rise to different time dependencies of the time correlation function  $G(t)$  (see text for discussion).

(iii) *Exchange of atoms with terrace, fast terrace diffusion.*

This case corresponds to "Case B" in the work of Pimpinelli et al. [98], to the case "Isolated-step evaporation-condensation" of Khare and Einstein [76] and to the "Attachment-detachment model" of Blagojevic and Duxbury [73]. The case has been discussed earlier by Bartelt et al. [72] in the continuum model and by our group by considering the detachment of individual atoms from kink sites [40]. The attachment/detachment kinetics of atoms from step sites onto terrace sites is assumed to be slow compared to the diffusion of atoms on the terraces. Atoms are emitted from a step and, after rapid terrace diffusion, captured by the same step at a different site (Fig. 12(iii)). When  $\tau_a$  is the mean time between two detachment processes of atoms from a step site onto the terrace, the time correlation function is

$$G(t) = \left( \frac{P_k}{\tau_a} \right)^{1/2} t^{1/2}. \quad (3.25)$$

In the atomistic picture, the detachment and attachment process of atoms are from the kink sites, giving rise to a random walk and uncorrelated hopping of kinks. If  $\Gamma_a$  denotes the hopping rate of kinks via emission and capture of atoms, the correlation function is [40, 72]:

$$G(t) = \sqrt{2/\pi} P_k^{1/2} \Gamma_a^{1/2} t^{1/2}. \quad (3.26)$$

$\Gamma_a$  is equal to the inverse of the mean time between two detachment processes of atoms from kink sites onto the terrace [72]. Equations (3.25) and (3.26) are therefore identical except for the scaling factor.

(iv) *Exchange of atoms with terrace, slow terrace diffusion.*

This case corresponds to "Case C" of Pimpinelli et al., to the "Isolated step terrace diffusion, diffusion limited case" by Khare and Einstein and to the "Terrace diffusion" by Blagojevic and Duxbury. In contrast to case (iii), where the time constant of the step fluctuations is dominated by the detachment/attachment kinetics, the time limiting step is diffusion on the terrace. As a consequence, the adatom concentration on the terrace close to the step edge differs from the equilibrium concentration far away from the steps (Fig. 12(iv)).  $G(t)$  is then given by [73, 76, 98-100]

$$G(t) = 4 / \left( \sqrt{3} \Gamma(1/3) \right) P_k^{2/3} (2c_t D_t)^{1/3} t^{1/3}, \quad (3.27)$$

$c_t$  and  $D_t$  being the equilibrium adatom concentration per site and the tracer diffusion constant on the terrace, respectively.

(v) Rapid exchange of atoms with terrace in the presence of large Ehrlich-Schwoebel barrier at step edge.

This case corresponds to "Case E" of Pimpinelli et al. and to "Perfect Schwoebel effect terrace diffusion" by Khare and Einstein. The basic assumptions are the same as in (ii), except the difference that the fluctuating step itself is the reservoir. Atom attachment to the neighboring step is forbidden due to an infinitely high ES-barrier [74, 75]: Atoms approaching the neighboring step from the upper terrace are reflected (Fig. 12(v)). Then,  $G(t)$  is [76, 98]

$$G(t) = P_k^{3/4} (c_t D_t)^{1/4} L^{1/4} t^{1/4}. \quad (3.28)$$

The existence of the step-edge barrier is reflected in the  $L$ -dependence of the time correlation function.

(vi) *Atom hopping alongside steps.*

The last case, which is mentioned here, corresponds to "Case F" in the paper of Pimpinelli et al., to the case "Periphery or edge diffusion" by Khare and Einstein and to the case "Step-edge diffusion" by Blagojevic and Duxbury. Here again, the step itself is the reservoir, but exchange of atoms with the terrace is forbidden (Fig. 12(vi)). Therefore, the time correlation function is independent of  $L$ :

$$G(t) = P_k^{3/4} (c_{st} D_{st})^{1/4} t^{1/4}, \quad (3.29)$$

where  $c_{st}$  and  $D_{st}$  denote the equilibrium adatom concentration per step site and the tracer diffusion constant for atoms moving along the step, respectively. Bartelt et al. [72] have calculated this case under the assumption of initially straight steps and subsequent equilibration of the step profile, and

$$G(t) \approx 0.464 P_k^{3/4} \Gamma_h^{1/4} t^{1/4}, \quad (3.30)$$

where  $\Gamma_h$  is the hopping coefficient, which is the inverse of the mean time between two hopping processes along the step and can be interpreted as the product of the adatom

concentration  $c_{st}$  and the tracer diffusion coefficient  $D_{st}$  as used in (3.29). Under the assumption of an initially equilibrated step, Masson et al. [45, 46] and Ihle et al. [100] find the same time dependence of  $G(t)$ , however, with a slightly different prefactor:

$$G(t) = 2/\pi \Gamma(3/4) P_k^{3/4} \Gamma_h^{1/4} t^{1/4}. \quad (3.31)$$

The value of the gamma function  $\Gamma(3/4)$  is about 1.225, hence (3.30) and (3.31) differ by a factor of about 1.7.

### ***3.3.3. Time dependence of step fluctuations: Time correlation function $G(t)$ (experimental results in UHV)***

Quite a number of experimental results on metal surfaces in UHV [38, 40, 42, 45, 46, 50-53, 77-80, 101] as well as *Monte-Carlo (MC) simulations* [67, 72, 99, 102-105] have been published on the time dependence of equilibrium step fluctuations and the mass transport processes involved. As an input into the simulations, the relative activation energies of the various mass transport situations were set such that a distinct mass transport process was dominant. The time dependence of the step correlation function was then studied in detail. The experimental studies of  $G(t)$  were performed on various metal surfaces, such as Cu(001) [38, 40, 45, 46, 77, 80], Cu(111) [50], Ag(111) [38, 42, 101], Au(110) [51, 52], Pb(111) [52, 53], Pb(110) [53] and Pt(111) [78]. These studies deal partly [38, 40, 45, 46, 53, 77, 79, 80] with the determination of the time exponent and conclude on the mass transport, which dominates the equilibrium step fluctuations at room temperature. An unambiguous identification on the dominating mass transport, however, can be made only by additionally analyzing the step-step distance dependence of  $G(t)$ . This is because different mass transport situations may obey the same time dependence, albeit with different dependencies on the step-step distance  $L$ . The problem has been theoretically well understood for several years now [73, 76, 98]. In most of the experimental studies of  $G(t)$  in UHV, however, the  $L$ -dependence have not been considered in detail. The only quantitative investigations of the  $L$ -dependence of  $G(t)$  has been recently performed by our group for Cu(111) [50] and Ag(111) [42].

Additional information may be obtained from the measurement of  $G(t)$  beyond the time dependence and the dominant mass transport involved. The effective activation energy of the temperature dependent pre-factors can be extracted by temperature dependent studies [42, 50-52, 78]. By measuring  $G(t)$  in the low and in the high temperature limit one may also find a change in the time exponent, and hence, a transition in the dominant mass transport [42, 50].

A  $t^{1/4}$ -dependence of  $G(t)$  was found for Cu(001) between 290 and 600K by our group and Masson et al. [40, 45, 46, 77], for Pb(111) by Kuipers et al. [52] and Speller et al. [53] and for Pb(110) by Speller et al. [53] at room temperature. A time exponent 1/4 was also measured for stepped Cu(111) with A-steps below 500 K [50]. We found a  $t^{1/4}$ -law on Ag(111) below 450 K [42] and on Pt(111) below 800 K [78]. A  $t^{1/4}$ -dependence of  $G(t)$  may be caused a priori by two different mass transport mechanisms, namely the case of rapid exchange of atoms with the terraces in presence of a large ES-barrier (case (v)) and the case of mass transport restricted to the step edges (case (vi)). The first scenario may be excluded for Cu(001) [40, 45, 46, 77], however. By investigation of multilayer island decay on Cu(001), we showed that no ES-barrier is present at the step edges [106] (see also Section 6.3). Hence, a  $t^{1/4}$ -dependence of  $G(t)$  is indicative of dominant step edge diffusion. For the (111) surfaces of fcc metals as Cu, Ag, Pb and Pt, interlayer mass transport is frequently hindered by a ES-barrier and hence, reflection of atoms at neighboring steps may become important. Kalff et al. [107] studied multilayer growth on Pt(111) and measured an extra barrier for interlayer mass transport of  $E_{ES}=0.08$  eV. FIM studies by Kyuno and Ehrlich on the same surface yielded 0.06 eV [108] and first principles calculations by Feibelman 0.02 eV for A-steps and 0.35 eV for B-steps [109]<sup>18</sup>. Nevertheless for Pt(111) below 800K, the  $t^{1/4}$ -dependence is indicative of edge diffusion rather than terrace exchange and reflection at the neighboring step. This was demonstrated by Bott et al. [110], who showed that Pt islands on Pt(111) have a dendritic shape up to 425K and are compact at 625K. The compact shape of islands arises from the onset of diffusion along the island perimeter. A further argument that the  $t^{1/4}$ -dependence of  $G(t)$  corresponds to edge diffusion (case (vi)) rather than to terrace exchange and reflection at the neighboring down-step (case(v)) is the small ES-barrier on Pt(111): If atoms were exchanged with the terrace, the small ES-barrier would not be an effective reflecting barrier for atoms approaching the down-step. One may expect that a considerable amount of atoms cross the neighboring step edge at 800K. Then, exchange of atoms with the neighboring step would cause  $G(t)$  to obey a  $t^{1/2}$ - rather than a  $t^{1/4}$ -law according to case (ii) (3.24), at variance with experiment. In the STM studies on Pb(111) by Kuipers et al. [52] and Speller et al. [53], the possibility of exchange with the terrace combined with reflection at the neighboring step was not considered.

It is emphasized at this point that statistical relevant experimental data on both, spatial as well as time fluctuations require a very large data set. A smooth looking shape of the

---

<sup>18</sup> Note that in experimental studies, FIM measurements or multilayer island decay studies, an average over the step barriers of both step types is obtained. If the activation barrier differs significantly for both steps (as seems

correlation function alone is not indicative of statistical significance of the measured  $G(y,t)$ : The kink density may locally vary substantially, in particular, on nominal flat surfaces, where steps have no preferential orientation and may be pinned to be oriented off the high symmetry direction. These steps have a large number of "forced" kinks. But even for vicinal surfaces, where steps are nominally oriented along a distinct crystallographic direction, the kink concentration varies in different surface areas. Small variations in the kink density, however, produce large errors in the step correlation function (3.16), (3.20)-(3.31). These errors are more pronounced at low temperatures, where the kink density at a step along the atomic dense direction is small. As a rule of thumb, statistically relevant data on the step correlation function is achieved if several  $\mu\text{m}$  step length are analyzed.

So far, an unambiguous identification of the dominant mass transport mechanism by measuring the step-step distance dependence of  $G(t)$  was performed only for stepped Cu(111) [50] and Ag(111) [42]<sup>19</sup> surfaces by our group. We showed that for both surfaces  $G(t)$  obeys a  $t^{1/4}$ -law and that  $G(t)$  is independent on the step-step distance  $L$ . Hence, the fluctuations of A-steps on Cu(111) below 500 K and on Ag(111) below 450 K are mediated by dominant

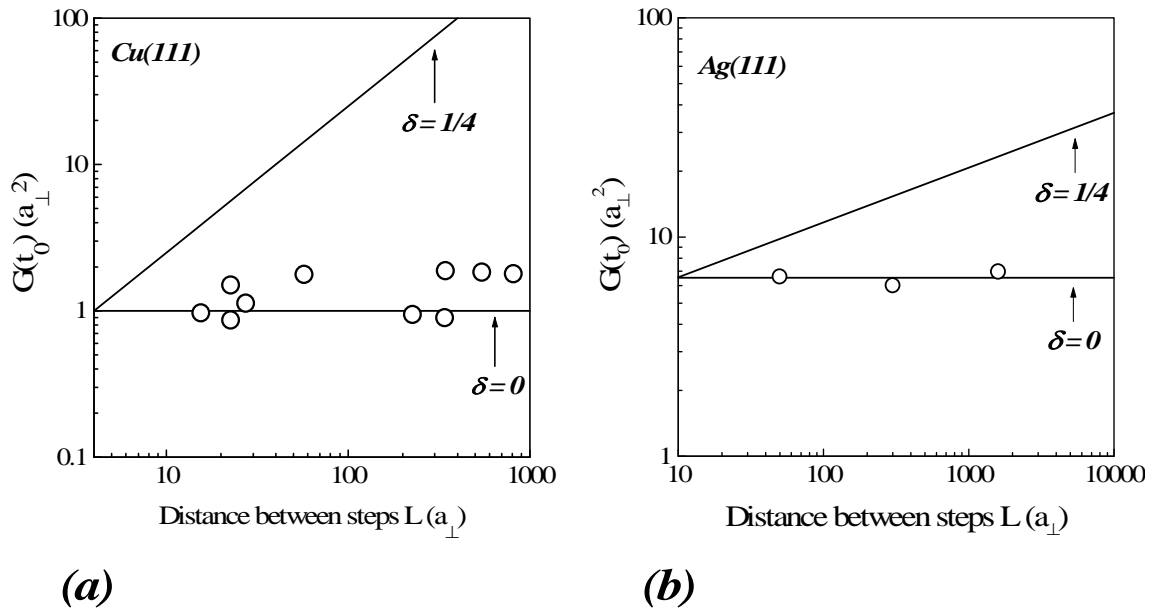


**Fig. 13.** Step-step distance dependence of  $G(t)$  at a fixed time  $t_0=2\text{s}$  for (a) Cu(111) below 500K [50] and (b) Ag(111) at 350K [42]. In the case of Cu(111), the correlation value  $G(t_0)$  is scaled by a temperature dependent prefactor such that data measured at different temperatures may be plotted on the same scale.

to be the case for Pt(111) [109]), the experimental values are closer to the smaller step barrier, since the probability for crossing of steps is higher at steps with the lower barrier.

<sup>19</sup>Mugele et al. [101] measured a  $t^{1/4}$  dependence of  $G(t)$  for Ag(111) at 300K and concluded that mass transport occurs along the steps. They suggested, however, that for steps in a step bunch this time dependence may also belong to the case of terrace exchange in presence of a large ES-barrier (case (v), (3.28)). Nevertheless, no systematic investigation of the step-step distance dependence was performed.

edge diffusion. Fig. 13 (a) and (b) show the time correlation values  $G(t_0=2s)$  vs. the step-step distance  $L$  in a log-log plot as measured for stepped Cu(111) revealing A-steps only [50] and Ag(111) [42], respectively. The data for Cu(111) were taken from measurements between 300 and 500K and the data for Ag(111) were measured at 350K. In Fig. 13 (a) and (b), the solid lines correspond to theoretical solutions of  $G(t)$  as expected for a  $L^\delta$ -dependence with  $\delta=0$  or  $1/4$ . For both, Cu(111) and Ag(111), the experimental data points (open circles) are obviously in agreement with the solution  $\delta=0$ , i.e.,  $G(t)$  is independent on the step-step distance<sup>20</sup>. As will be discussed in Section 5, an  $L$ -dependence of  $G(t)$  has been found for Ag(111) and Cu(001) electrodes in electrolyte [59, 60].

A  $t^{1/2}$ -dependence of  $G(t)$  has been observed for  $\langle 110 \rangle$ -oriented steps on Au(110) between room temperature and 590 K by Kuipers et al. [51, 52]. Pai et al. [94] measured a  $t^{1/2}$ -law for almost  $\langle 110 \rangle$ -oriented steps<sup>21</sup> on Ag(110) at room temperature. The same time dependence of  $G(t)$  was observed for A-steps on Cu(111) at 600K [50] and for B-steps on Ag(111) above 450 K [42] by our group. A  $t^{1/2}$ -law is indicative of either one out of three different mass transport mechanisms, namely, case (i), where the surface is in equilibrium with the gas phase (3.22) and (3.23), case (ii), where atoms are rapidly exchanged between steps (3.24) and case (iii), where atoms are exchanged with the terrace and terrace diffusion is fast compared to the detachment/attachment of atoms at the steps (3.25) and (3.26). As discussed before, one can distinguish between the cases by the dependence of  $G(t)$  on  $L$ . For Au(110) and Cu(111), no systematic studies of the step-step distance dependence in the  $t^{1/2}$ -regime have been performed. Kuipers et al. [52] concluded from a detailed analysis of the kink motion that the  $t^{1/2}$ -dependence of  $G(t)$  on Au(110) arises from uncorrelated kink motion. This conclusion would be in agreement with either of the three mass transport cases (i)-(iii), in which the kink motion is uncorrelated. While one can exclude exchange with the gas phase (case(i)), the unambiguous distinction between case (ii) and (iii) is impossible.

In the case of stepped Cu(111) (with A-steps), we proposed that the  $t^{1/2}$ -dependence measured at 600K is indicative of case (iii) [50], which is confirmed by more recent studies. There, we showed by investigating the temperature dependence of the long-time behavior of step fluctuations (see Section 3.3.5) that the  $t^{1/2}$ -regime on Cu(111) is caused by atomic exchange with the terraces [111]. Pai et al. [94] studied the fluctuations of isolated steps on

<sup>20</sup> It is noted in passing that in order to distinguish between a  $L^0$ - and a  $L^{1/4}$ -dependence of  $G(t)$ , one has to consider several orders of magnitudes of step-step distances  $L$ . To verify a possible  $L^{1/2}$ - or  $L^{-1/2}$ -dependence (case (i) and (ii) in Section 3.3.2), one order of magnitude in the step-step distance  $L$  is sufficient to reliably distinguish an exponent  $\delta=\pm 1/2$  from an exponent  $\delta=0$ .

<sup>21</sup> Pai et al. [94] remark that the step direction was less than  $30^\circ$  off  $\langle 110 \rangle$ .

Ag(110) with neighboring steps at least in 300 nm distance. Thus, one may expect that exchange of atoms with neighboring steps (case(ii), (3.24)) is negligible. The authors therefore concluded that the  $t^{1/2}$ -dependence of  $G(t)$  on Ag(110) at 300K is indicative of mass exchange with the terrace and fast terrace diffusion (case(iii), (3.25) and (3.26)). For Ag(111) (with B-steps) above 450 K, we found that  $G(t)$  is independent of the step-step distance [42]. Hence, the dominant mass transport mechanism is clearly identified as exchange of atoms with the terrace (case (iii)).

Table 2 summarizes the time exponents  $\alpha$  and the step-step distance exponents  $\delta$  for the various systems studied. So far, no  $t^{1/3}$ -dependence has been observed for metal surfaces in UHV. As is discussed in Section 5, such a time dependence of  $G(t)$  was, however, found for Cu(111) electrodes in HCl [112].

At the end of this section, it is emphasized that the time contribution to STM images may introduce errors in the determination of the kink energy as discussed in Section 3.3.1. The spatial correlation function  $G(y)$  can be determined strictly only from snap shot images of the surface, i.e., from exclusively spatial STM images. For spatial step fluctuations, the chemical potential  $\mu$  is constant and so is the step line tension  $\gamma$ . Hence, no net mass transport along the step occurs and the time evolution of the step profile can be described as an uncorrelated motion of kinks. Time fluctuations occur due to local distortions of the step profile which give rise to local gradients in the chemical potential along the step. Local gradients in the chemical potential give rise to mass transport in order to relax the step profile into equilibrium. The dominant mass transport determines the time dependence of the step fluctuations as discussed before. The narrower the transport channel (e.g., edge diffusion against terrace diffusion) the longer is the relaxation time and the smaller is the time exponent of  $G(t)$ . When a step correlation function containing significant time information is fitted to a linear function according to (3.16), the kink formation energy  $\varepsilon$  is underestimated by far. This is the reason why in earlier STM studies [38] of the kink energies on Cu(001) and Ag(111) by our group, the kink energies were much lower ( $\varepsilon_{\text{Cu}}=100\pm 3\text{meV}$  and  $\varepsilon_{\text{Ag}}=75\pm 2\text{meV}$ ) than what is reported later in refs. [40] and [88] ( $\varepsilon_{\text{Cu}}=128\pm 3\text{meV}$  and  $\varepsilon_{\text{Ag}}=90\pm 7\text{meV}$ , respectively. See also Table 1).

Table 2.

Surface	Temperature range (K)	Time exponent $\alpha$	Step distance exponent $\delta$ <sup>(22)</sup>	$E_d$ (eV)	$E_{em}$ (eV)	$E_{st}^{ad}$ (eV)	$E_{ad}$ (eV)	Ref.
Cu(100) <sup>(23)</sup>				0.26	0.53	0.27 <sup>(24)</sup>		[83]
Cu(100) <sup>(25)</sup>				0.247			0.507	[81]
Cu(100) <sup>(23)</sup>				0.27				[114]
Cu(100) <sup>(23)</sup>				0.38	0.75	0.37 <sup>(24)</sup>	0.45	[115]
Cu(100) <sup>(23)</sup>				0.25			0.35	[116]
Cu(100) <sup>(26)</sup>				0.24±0.02				[117]
Cu(100) <sup>(23)</sup>				0.24	0.48	0.24 <sup>(24)</sup>	0.35	[118]
Cu(119) <sup>(25)</sup>				0.258	0.518	0.279	0.36	[113, 119]
Cu(1,1,11) <sup>(‡)</sup>	293			~0.45	~0.65	~0.20 <sup>(24)</sup>		[44]
Cu(1,1,11) <sup>(‡)</sup>	300	1/4	---	---				[45, 46]
Cu(1,1,13) <sup>(‡)</sup>	300-370	1/4	---	0.53±0.03				[40]
Cu(1,1,19) <sup>(‡)</sup>	310-360	1/4	---	0.53±0.03				[40, 77, 80]
Cu(1,1,19) <sup>(‡)</sup>	290-370			0.45±0.08	0.53±0.08			[41]
Cu(1,1,79) <sup>(‡)</sup>	390-600	1/4	---	0.53±0.03				[40]
Cu(111) <sup>(25)</sup>				0.228			0.714	[81]
Cu(111) <sup>(23)</sup>				0.29			0.56	[116]
Cu(17,17,19) <sup>(‡)</sup>	300-500	1/4	---	~0.30 <sup>(27)</sup>				[50]
Cu(21,21,23) <sup>(‡)</sup>	300-500 600	1/4 1/2	0 ---	~0.30 <sup>(27)</sup> ---				[50]

<sup>22</sup> The step-step distance dependence of  $G(t)$  can be expressed in terms of a power law  $L^\delta$ , where  $\delta$  can be 0, 1/4,  $\pm 1/2$  (compare also (3.22)-(3.31)).

<sup>23</sup> EAM calculations.

<sup>24</sup> This value is estimated from the activation energy  $E_{em}$  for adatom emission from a kink site to a step site assuming  $E_{em} \sim E_{st}^{ad} + E_d$  (this assumption is reasonable, as becomes obvious from the calculated values of  $E_{em}$  and  $E_{st}^{ad} + E_d$  [113]).

<sup>25</sup> EMT calculations.

<sup>26</sup> GGA first principles calculations.

<sup>27</sup> If one uses  $\epsilon=117\text{meV}$  [88] instead of  $\epsilon=128\text{meV}$  [50].

Table 2 (cont.).

Surface	Temperature range (K)	Time exponent $\alpha$	Step distance exponent $\delta$ <sup>(22)</sup>	$E_d$ (eV)	$E_{em}$ (eV)	$E_{st}^{ad}$ (eV)	$E_{ad}$ (eV)	Ref.
Ag(100) <sup>(25)</sup>				0.224			0.364	[81]
Ag(100) <sup>(26, 28)</sup>				0.27				[120, 121]
Ag(100) <sup>(23)</sup>				0.23	0.45	0.22 <sup>(24)</sup>	0.25	[118]
Ag(119) <sup>(25)</sup>				0.224	0.412	0.205	0.21	[113, 119]
Ag(111) <sup>(‡)</sup>	300	1/4	---	---				[38]
Ag(111) <sup>(‡)</sup>				A-step: 0.222 B-step: 0.300				[122]
Ag(111) <sup>(‡)</sup>	300	1/4	---	---				[101]
Ag(111) <sup>(‡)</sup>	310-390 440-590	1/4 1/2	0 0	---				[42]
Ag(111) <sup>(25)</sup>				0.22			0.555	[81]
Ag(110) <sup>(‡)</sup>	300	1/2	---					[94]
Au(100) <sup>(25)</sup>				0.303			0.307	[81]
Au(100) <sup>(23)</sup>				0.36	0.61	0.25 <sup>(24)</sup>	0.29	[118]
Au(111) <sup>(25)</sup>				0.311			0.568	[81]
Au(110) <sup>(‡)</sup>	300-590	1/2	---					[51, 52]
Ni(111) <sup>(25)</sup>				0.296			1.002	[81]
Ni(100) <sup>(25)</sup>				0.330			0.749	[81]
Ni(100) <sup>(25)</sup>				0.357	0.701	0.379	0.415	[113]
Ni(100) <sup>(23)</sup>				0.31	0.63	0.32 <sup>(24)</sup>	0.41	[118]

---

<sup>28</sup> LDA first principles calculations.

**Table 2 (cont.).**

Surface	Temperature range (K)	Time exponent $\alpha$	Step distance exponent $\delta$ <sup>(22)</sup>	$E_d$ (eV)	$E_{em}$ (eV)	$E_{st}^{ad}$ (eV)	$E_{ad}$ (eV)	Ref.
Pt(100) <sup>(25)</sup>				0.438			0.435	[81]
Pt(111) <sup>(‡)</sup>	530-800	1/4	---	$\sim 1.00 \pm 0.16$				[78]
Pt(111) <sup>(29)</sup>				A-step: 0.46 B-step: 0.40				[123]
Pt(111) <sup>(30)</sup>				$0.40 \pm 0.02$				[124]
Pt(111) <sup>(25)</sup>				0.456			0.806	[81]
Pt(111) <sup>(23)</sup>				A-step: 0.60 B-step: 0.43				[125]
Pt(111) <sup>(28)</sup>				A-step: 0.84 B-step: 0.90				[126]
Pt(331) <sup>(‡)</sup>	$\sim 80-300$			$0.84 \pm 0.10$				[127]
Pb(111) <sup>(‡)</sup>	300	1/4	---					[52]

**Table 2.**

Time and step-step distance exponents  $\alpha$  and  $\delta$  measured on various fcc metal surfaces from the analysis of the time correlation function  $G(t)$  (3.21),  $G(t) \propto L^\delta t^\alpha$ . In columns 5,6 and 7, experimental and theoretical values for the diffusion barrier  $E_d$  along a straight step and the adatom formation energies from a kink to a step site  $E_{st}^{ad}$  and onto the terrace  $E_{ad}$  are given.  $E_{em}$  denotes the activation energy for emission of an adatom from a kink site to the step edge. The index "(‡)" marks experimental data while theoretical results are indicated by numbers explained in the footnotes.

---

<sup>29</sup> KMC simulations.

<sup>30</sup> DLA simulations.

### 3.3.4. Temperature dependence of time correlation function

Activation energies of the mass transport processes have been determined by temperature dependent studies of the time correlation function for Au(110) [52], Cu(111) [50], Ag(111) [42] and Pt(111) [78]. For Au(110), Kuipers et al. [52] found an activation energy of  $E_{\text{act}}=0.72\text{eV}$  for the uncorrelated kink motion at steps along the dense  $[1\bar{1}0]$  direction. Since they could not distinguish between different mass transport cases, the activation energy of  $0.72\text{eV}$  cannot be assigned to a specific process. The interpretation of the measured activation energy is difficult, because the kink motion on the Au(110) surface involves the concerted motion of two atoms, due to the missing-row reconstruction of Au(110), which is illustrated in Fig. 14. The arrows and the white line indicate a monatomic high step on the reconstructed surface. A kink position in the step is denoted by the numbering of the two atoms forming the kink. Here, MC-simulations could be particular useful.

A detailed analysis of the activation energy of  $G(t)$  was performed for Cu(111) below  $500\text{K}$  (in the  $t^{1/4}$ -regime) [50] and for Ag(111) below  $450\text{K}$  (in the  $t^{1/4}$ -regime) and above  $450\text{K}$  (in the  $t^{1/2}$ -regime) [42] by our group. Fig. 15 shows the Arrhenius plot of  $G(t_0)$  at  $t_0=1\text{s}$  measured for A-steps on Cu(111) [50] and for B-steps on Ag(111) [42]. The data for Cu(111) were measured on a (21,21,23)-oriented surface which consists of parallel steps along the

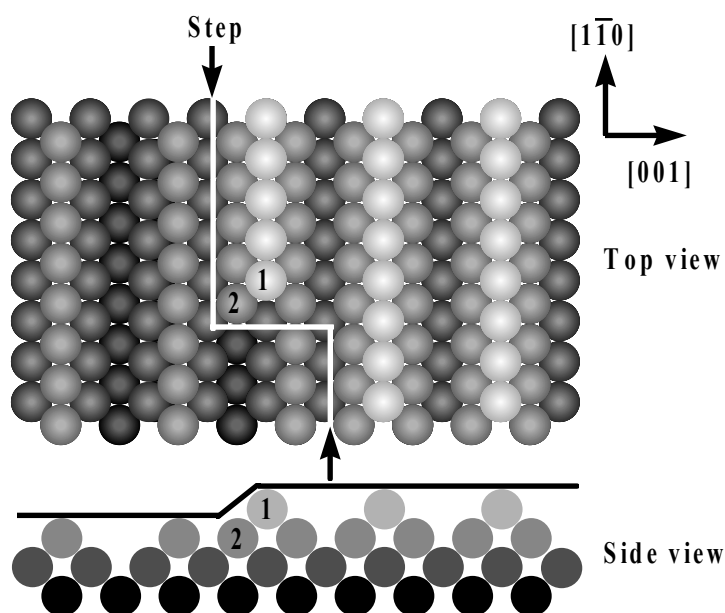


**Fig. 14.** Model of the fcc (110) surface with a missing row reconstruction. Deeper atomic layers are indicated by a darker shading. The arrows and the white line indicate a monatomic high step on the surface. The atoms depicted as "1" and "2" are kink atoms. These atoms have to move concertedly in order to move the kink along the step.

dense atomic direction. The activation energy of the mass transport is  $E_t=0.25\pm 0.01\text{eV}$  between 300 and 500K and the pre-exponential factor is  $D_0=2\times 10^{14\pm 1}\text{s}^{-1}$ . In this temperature range, edge diffusion is the dominant mass transport on Cu(111).

As can be seen from (3.29), the activation energy  $E_t$  contains the kink energy  $\varepsilon$  ( $P_k \approx 2 \exp(-\varepsilon/k_B T)$ ), the adatom creation energy  $E_{st}$  at the step edge ( $c_{st} = \exp(-E_{st}/k_B T)$ ) and the diffusion energy  $E_d^k$  along the kinked step ( $D_{st} = D_0 \exp(-E_d^k/k_B T)$ ;  $D_0$  being the pre-exponential factor). Hence, one finds for the measured activation energy  $E_t$  the relation:  $4E_t = 3\varepsilon + E_{st} + E_d^k$ . Note, that  $E_d^k$  is the effective diffusion barrier along a kinked step, which can be expressed by the diffusion barrier  $E_d$  along a straight step [78], where we reduced the theoretical description of 2-dimensional diffusion

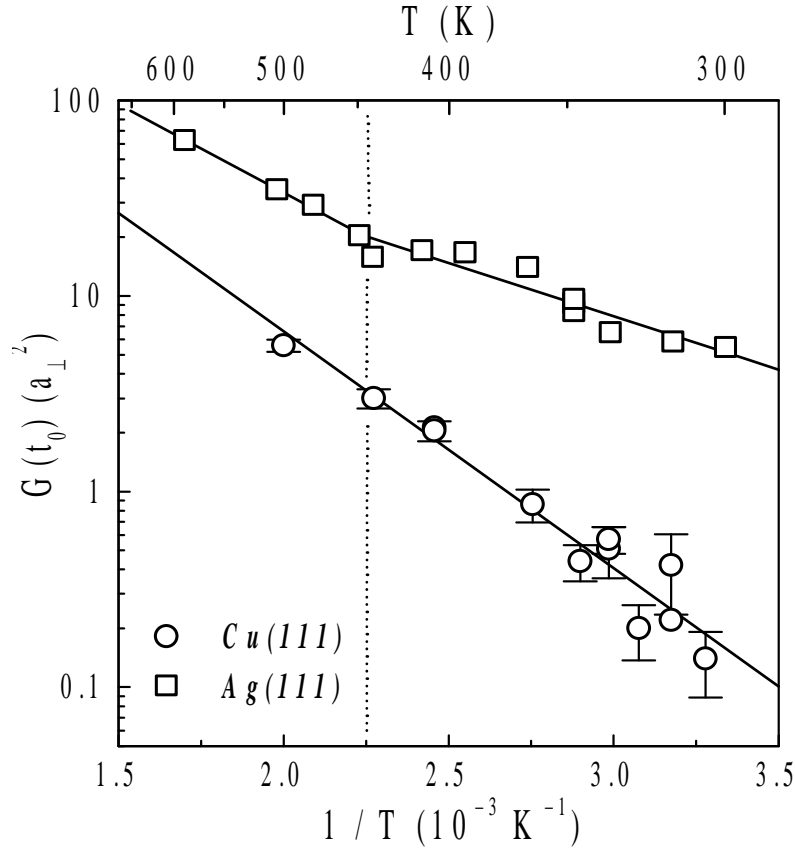


**Fig. 15.** Arrhenius-plot of the correlation function  $G(t)$  at fixed time  $t_0=1\text{s}$  for Cu(111) (circles) [50] and Ag(111) (squares) [42]. In the case of Cu(111), the data fall on a straight line. The activation energy is  $E_t=0.25\pm 0.01\text{eV}$ . The data for Ag(111) is fitted by two lines with different slopes corresponding to a crossover in the dominant mass transport. Below 450K, the activation energy is  $E_t=0.11\pm 0.01\text{eV}$  and between 450 and 600K,  $E_t=0.18\pm 0.01\text{eV}$ .

on a regularly stepped surface by Natori and Godby [128] to the 1-dimensional diffusion along a kinked step and found  $E_d^k = \varepsilon + E_d$ . This expression holds as long as a corner barrier<sup>31</sup> for diffusion across a kink site is small compared to the kink energy [128]. Making furthermore the reasonable assumption that  $E_{st} \approx 2\varepsilon$ , one finds  $4E_t \approx 6\varepsilon + E_d$ . Using this result and  $\varepsilon = 117 \text{ meV}$  [88], as determined from the analysis of the island equilibrium shape (see Section 6), we obtain for the diffusion barrier along straight A-steps on Cu(111)  $E_d = 0.30 \text{ eV}$  [50]<sup>32</sup>. A similar analysis for Pt(111) between 500 and 800K by our group yields  $E_d = 1.0 \text{ eV}$  for both A- and B-steps [78].

The data measured on Ag(111) (Fig. 15) were obtained from B-steps on a non-vicinal Ag(111) surface, where steps have no preferential orientation. The Arrhenius plot of  $G(t_0)$  at  $t_0 = 1 \text{ s}$  reveals two different regimes: Between 300 and 450K an activation energy of  $E_t = 0.11 \pm 0.01 \text{ eV}$  and a pre-exponential factor of  $3 \times 10^{11 \pm 1} \text{ s}^{-1}$  were measured. In this temperature range, edge diffusion is the dominant mass transport. The total activation barrier therefore contains the kink energy, the adatom creation energy at the step and the diffusion energy along a kinked step, analog to what has been discussed for Cu(111) before. Using again the ansatz  $E_d^k = \varepsilon + E_d$  [78] and  $E_{st} \approx 2\varepsilon$ , we find for the diffusion barrier along a straight B-step  $E_d = 0.04 \pm 0.06 \text{ eV}$ . Between 450 and 620K the effective mass transport energy is  $E_t = 0.18 \pm 0.01 \text{ eV}$ <sup>33</sup>. In this temperature range, the time correlation function obeys a  $t^{1/2}$ -law and no dependence on the step-step distance is found. According to (3.26), the total activation energy  $E_t$  contains the kink energy  $\varepsilon$  and the activation energy for adatom creation from a kink onto the terrace  $E_{ad}^\ddagger$ ,  $2E_t = \varepsilon + E_{ad}^\ddagger$ . Using  $\varepsilon = 117 \pm 6 \text{ meV}$  [88], one finds  $E_{ad}^\ddagger = 0.26 \pm 0.05 \text{ eV}$  [42]. One may compare these results with calculated values. In Table 2, diffusion barriers  $E_d$  are listed in column 5. Stoltze [81] and Karimi et al. [116] determine the diffusion barrier along steps on Cu(111) to 0.228 and 0.29eV, respectively, the latter in good agreement with our experimental value of 0.30eV. The diffusion barrier we find on Ag(111) (0.04±0.06eV) is much smaller than a theoretical value by Stoltze (0.22eV [81]), even if one considers the large error bars. The value we obtain for the activation energy for adatom creation from kink sites onto the terrace is also much too small. Merikoski et al. [113] calculated the activation barrier

<sup>31</sup> This corner energy is an additional barrier for diffusion across a kink and can be interpreted as an ES-barrier [74, 75] in one dimension.

<sup>32</sup> In [50], the kink energy on Cu(111) was assumed to be about equal to the kink energy on Cu(100). On Cu(100), the kink energy was measured to  $\varepsilon = 128 \text{ meV}$  [40, 41]. Hence, the diffusion barrier along a straight step on Cu(111) was found to be  $E_d = 0.24 \text{ eV}$  [50]. From the more recent analysis of the equilibrium shape of islands on Cu(111) we determine the kink energy to be, however, about 117meV [88] (see Section 6). Using this value, the diffusion barrier  $E_d$  becomes larger.

<sup>33</sup> In the high temperature range, the data set is not sufficiently large to determine the pre-exponential factor.

for the hopping of an adatom at a straight step onto the terrace to  $0.57\text{eV}$ . Although  $E_{\text{ad}}^{\ddagger}$  is the activation energy for adatom creation from kink sites, the number they obtained should be of the same order of magnitude. A possible explanation for the small values of  $E_{\text{d}}$  and  $E_{\text{ad}}^{\ddagger}$ , we determine on  $\text{Ag}(111)$ , is that we may have analyzed non-parallel steps with a misorientation with respect to the dense  $\langle 110 \rangle$  direction. These steps have forced kinks which contribute

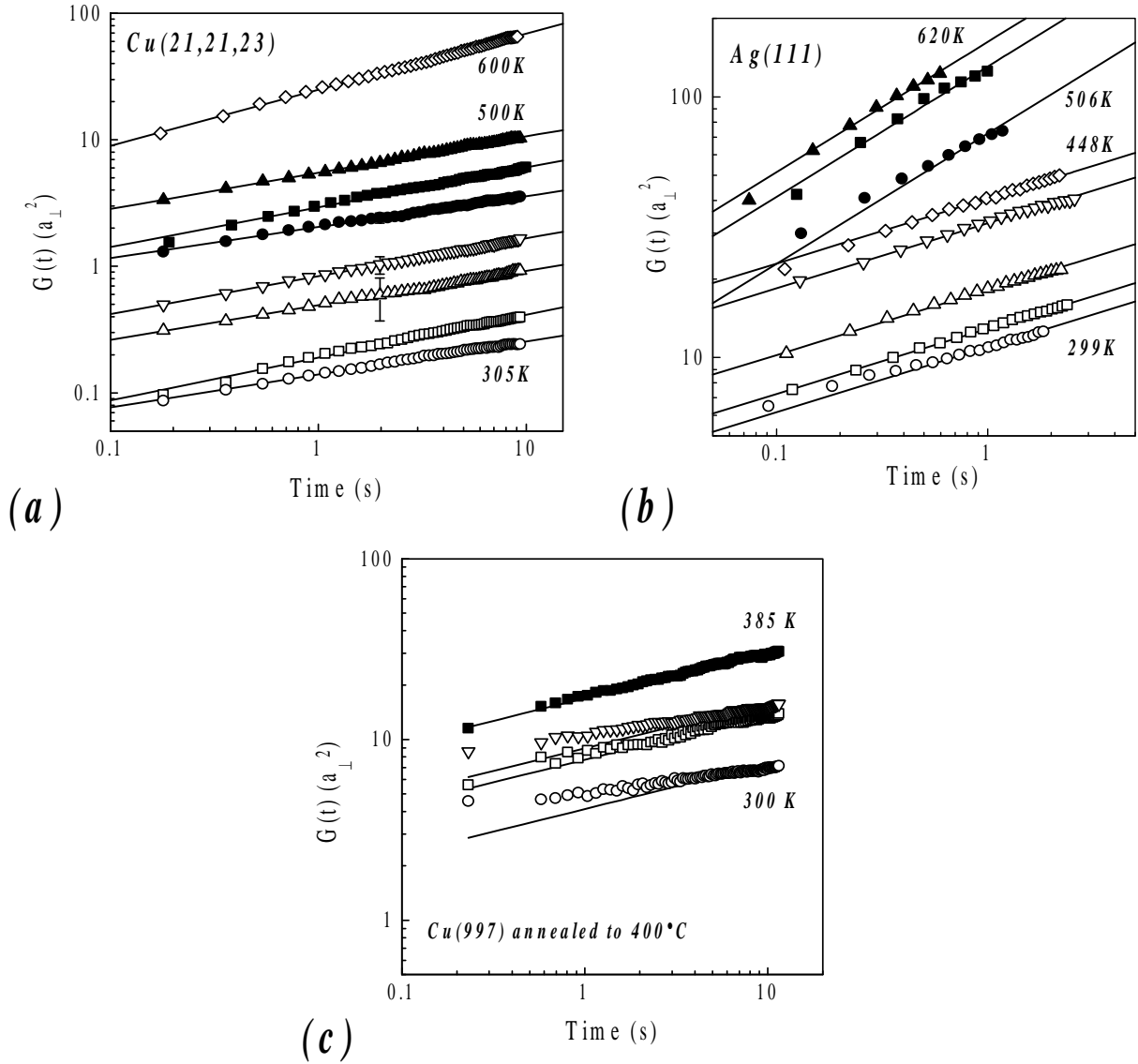


**Fig. 16.** Log-log plot of the time correlation function  $G(t) \propto t^{\alpha}$  for

(a)  $\text{Cu}(21,21,23)$  ( $\circ$  305K,  $\alpha=0.25$ ;  $\square$  325K,  $\alpha=0.32$ ;  $\triangle$  335K,  $\alpha=0.28$ ;  $\nabla$  363K,  $\alpha=0.30$ ;  $\bullet$  407K,  $\alpha=0.24$ ;  $\blacksquare$  440K,  $\alpha=0.30$ ;  $\blacktriangle$  500K,  $\alpha=0.28$ ;  $\diamond$  600K,  $\alpha=0.45$ ) and

(b)  $\text{Ag}(111)$  ( $\circ$  299K,  $\alpha=0.21$ ;  $\square$  335K,  $\alpha=0.25$ ;  $\triangle$  347K,  $\alpha=0.24$ ;  $\nabla$  392K,  $\alpha=0.25$ ;  $\diamond$  448K,  $\alpha=0.27$ ;  $\bullet$  506K,  $\alpha=0.41$ ;  $\blacksquare$  589K,  $\alpha=0.52$ ;  $\blacktriangle$  620K,  $\alpha=0.54$ ).

(c)  $\text{Cu}(997)$  ( $\circ$  300K,  $\alpha=0.15$ ;  $\square$  325K,  $\alpha=0.21$ ;  $\nabla$  355K,  $\alpha=0.15$ ;  $\blacksquare$  385K,  $\alpha=0.24$ ).

The solid lines are linear fits with fixed exponents 0.25 and 0.5 [42, 50].

considerably to  $G(t)$  at low temperatures, whereas the relative contribution is smaller at high temperatures. Therefore, the slope measured in the Arrhenius plot in Fig. 14 may be too small due to the influence of forced kinks on  $G(t)$ , and hence, the activation energy may be underestimated.

### 3.3.5. Transition in dominant mass transport regimes

In most cases, the time correlation function  $G(t)$  at a given temperature and for a given time scale is dominated by a particular mass transport mechanism. Nevertheless, in principle, *all* microscopic processes (as described in Section 3.3.2) contribute to the step fluctuations, albeit with *different weight!* The weight of the contribution of a specific transport process to  $G(t)$  is determined by the magnitude of its activation energy. For short times and low temperatures, the processes with lower activation energies have the highest contribution. On the long-time scale and at higher temperatures, the processes with higher activation energies dominate the time behavior of the step fluctuations. A crossover in the time exponent may therefore be observed in two different cases: First, a crossover in the time exponent as a function of *temperature*, because the weight of the contribution of different transport processes to  $G(t)$  changes with temperature. The temperature dependence of the time exponent was discussed in several theoretical papers in recent years [73, 76, 98-100]. Second, a crossover of the time exponent as a function of *time* because processes with higher activation energies prevail at long times. A crossover as a function of time was recently discussed in a theoretical paper by Khare and Einstein [76].

Experimentally, a transition of the time exponent in temperature from  $1/4$  to  $1/2$  was observed on Cu(111) around 500K [50] and for Ag(111) around 450 K [42]. Fig. 16 shows the results of the time correlation function  $G(t)$  for (a) stepped Cu(111) (with A-steps), (b) Ag(111) [42, 50] and (c) stepped Cu(111) (with B-steps) in a log-log plot. For the surfaces displayed in (a) and (b),  $G(t)$  was measured between approximately 300 and 600 K. For Cu(111) (Fig. 16(a)),  $G(t)$  reveals approximately the same slope between 300 and 500 K which on the average was found to be  $0.28 \pm 0.03$ . This slope is close to the theoretical value of  $1/4$ . The data points obtained at 600K, however, have a larger slope of  $0.45 \pm 0.01$ , close to a theoretical value of  $1/2$ . A similar result is found for Ag(111) (Fig. 16(b)). Here, the transition from an exponent close to  $1/4$  to  $1/2$  occurs around 450 K. The analysis of the step-step distance dependence of  $G(t)$  showed that the transition in the time exponent around 450 K is caused by a change in the dominant mass transport from edge diffusion (case (vi), (3.29)-(3.31)) to fast terrace diffusion (case (iii), (3.25) and (3.26)) [42]. The transition temperature found on Cu(111) (550K) is higher than on Ag(111) (450K), i.e., the activation energies for

atomic exchange with the terraces for Cu(111) is larger than for Ag(111). On Pt(111), the transition temperature must be even higher than for Cu and Ag(111), because no transition in the time exponent is observed up to 800K [78]. Hence, the activation energies for terrace exchange is highest on Pt(111). The increase of the activation energies on Cu, Ag and Pt(111) reflect the same trend as the cohesion energies on the various metal surfaces. The cohesion energy is lowest for Ag (2.95 eV/atom) and highest for Pt (5.84 eV/atom). For Cu (3.49 eV/atom), the cohesion energy is in between these two values, though closer to the value for Ag (values taken from [129]).

We have also measured the temperature dependence of  $G(t)$  for Cu(997), which is vicinal to the (111)-plane and reveals B-steps (Fig. 16(c)) [26]. As discussed in Section 2.4, this surface is unstable against restructuring into  $\{445\}$ - and  $\{212\}$ -facets upon annealing to 700°C [25]. As mentioned in [25], the surface may be temporarily stabilized, if the annealing temperature during sample preparation is reduced to about 400°C (it is noted in passing that this temperature is too low to reduce the sulfur content of the copper crystal and that the stabilization of the step structure may be due to a small sulfur amount on the surface). The step structure appears to be stable for about several days at room temperature. A closer inspection, however, shows that the steps tend to form arrangements of multiple steps in close distance leaving other parts of the surface free of steps. We interpret this step rearrangement as the beginning of the restructuring process, which is kinetically hindered at room

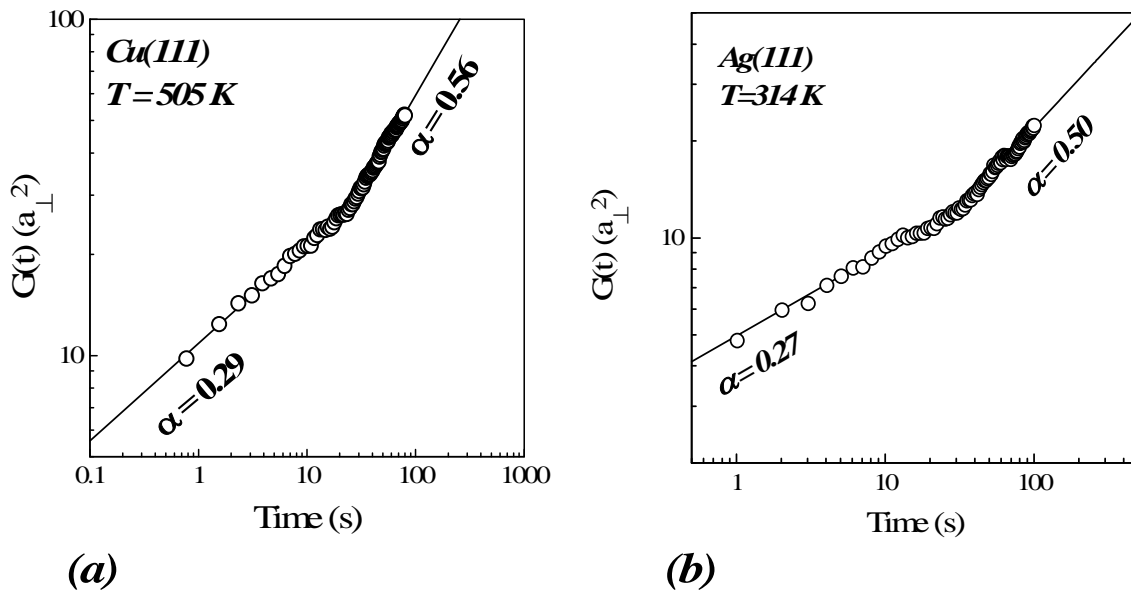


**Fig. 17:** Log-log plot of  $G(t)$  for very long times for (a) Cu(111) at 505K [111] and (b) Ag(111) at 314K [42]. Around  $t=30$ s, a change in the time exponent  $\alpha$  from a value close to 1/4 to 1/2 is observed.

temperature. This interpretation is confirmed by the measurement of the step correlation function  $G(t)$  shown in Fig. 16(c) [26]. The step mobility on the Cu(997) surface is higher than on the Cu(21,21,23)-surface in the same temperature regime, while the time dependence remains a  $t^{1/4}$ -law, which is evidence for dominant edge diffusion. Although  $G(t)$  is larger than for the Cu(21,21,23) surface, no transition in the time exponent is observed below 450 K.

We investigated the long-time behavior of the time exponent of  $G(t)$  for Cu(111) [111] and Ag(111) [42]. In both studies, the measurements were performed below the temperature, where the transition of the time exponent in temperature was observed. Fig. 17 shows  $G(t)$  for (a) Cu(111) at 505 K [111] and (b) Ag(111) at 314 K [42] in a log-log plot vs. the time as circles. In both data sets,  $G(t)$  displays a change in slope around 20-30 s from a value close to  $1/4$  at short times to a value close to  $1/2$  at long times. A comparison with temperature dependent data for Cu(111) [50] and Ag(111) [42] shows that the crossover in the time exponent is consistent with a transition in the dominant mass transport mechanism from edge diffusion to fast terrace diffusion. If one estimates the absolute contributions of the different mass transport processes to  $G(t)$  at different times, one can show [111] that the process with the higher activation energy prevails at long times, even for temperatures well below the temperature where the transition of the time exponent in temperature is found.

### ***3.4. Influence of tunneling tip on measurement of $G(t)$***

The tunneling tip of an STM has become an important tool to manipulate the morphology of metal surfaces on the atomic scale [130-134] (for a recent review see [135]). If the STM is capable of moving single atoms in a controlled way, it should be of concern whether the STM probe influences step fluctuations by tip-surface interactions and thereby alters the measurement of the step correlation function  $G(t)$ . A possible influence of the tunneling tip on  $G(t)$  is in particular of importance, if one wants to extract quantitative information on activation barriers. Several groups have therefore studied the influence of the tunneling tip on step fluctuations in recent years: A qualitative study was published by Thibaudau and Cousty [136], who observed an enhanced fluctuation amplitude for higher scan rates on Cu(11,10,9). The (11,10,9)-surface is vicinal to the (111) plane with parallel steps along  $\langle 121 \rangle$ . In contrast to the model in Fig. 4, these steps have a mean orientation perpendicular to the dense  $\langle 110 \rangle$ -direction and have therefore a high kink concentration. The latter becomes obvious from the zig-zag like pattern in the step profile as observed in the STM images [136]. The open character of these steps makes a manipulation of atoms by the tip more likely than for dense steps along  $\langle 110 \rangle$ . Speller et al. [53] observed a change in the step frizziness in STM images of Pb(110), when the scan direction is reversed. These authors, however, performed no

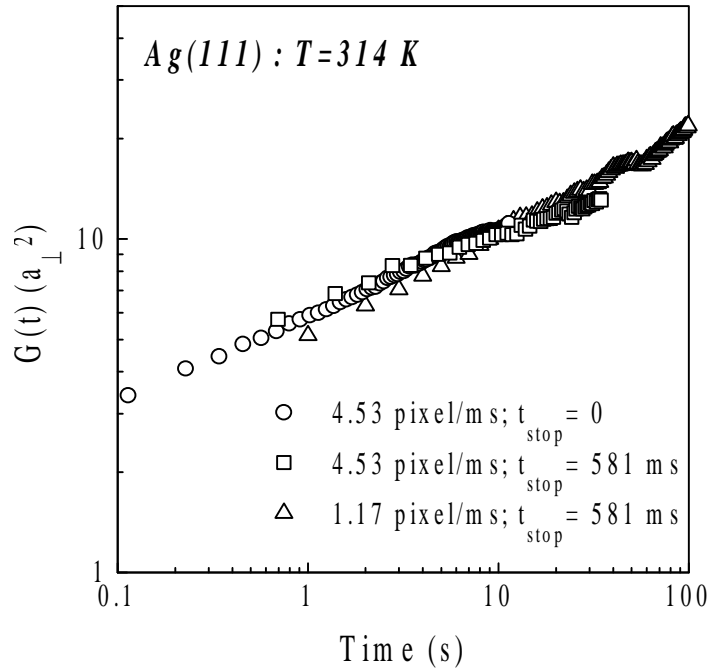


**Fig. 18.** Time correlation function  $G(t)$  measured on Ag(111) at 314K for different probe frequencies of the step edge and moderate tunneling conditions ( $I_T = 1.3$  nA,  $U_T = 0.6$  V) [42].

systematic analysis of  $G(t)$  as a function of the scan direction. A systematic study of  $G(t)$  for different scan directions across the steps was later performed by Mugele et al. [101] for Ag(111) at room temperature, who claimed that step fluctuations on Ag(111) would be tip assisted. In a more recent work, however, they corrected this result and showed for the same surface that  $G(t)$  is independent on the scan direction, and they find no evidence for tip assisted atomic motion at steps [137]. The latter result is consistent with our experiments on Ag(111) [42], which show that  $G(t)$  is independent on the probe frequency for tunneling currents of 1-3 nA and tunneling voltages around 600 mV (corresponding to a tunneling resistance of 0.2-0.6 G $\Omega$ ). Fig. 18 shows  $G(t)$  measured on Ag(111) at  $T=314$  K for three different scan rates [42]. The circles and squares refer to measurements of  $G(t)$  with a probe frequency of 4.53 pixel/ms in each scan line. The difference in the two measurements is that in one (squares) the tip was halted after each scan line for 581 ms, while the other data (circles) was obtained without a delay time between successive scan lines. Therefore, a total time of  $t=10$ s in both measurements corresponds to about 14 and 88 individual probe events of the step edge, respectively. In a third measurement (triangles), the scan frequency within each line was reduced to 1.17 pixel/ms while the delay time after each scan line was kept at 581 ms. Hence, the possible interaction time, when the tip crosses the step edge, is enhanced by a factor of 3.9 compared to the data plotted as squares. Obviously, there is no measurable difference between the three data sets within the statistical error. Thus, no influence of the tip

on the atomic motion at steps is observed. We found the same result for densely packed steps on Cu(111) [50] and Pt(111) [78].

For the more open Ag(110) surface though, Li et al. [54] showed that the tunneling tip may considerably influence the atomic diffusion. They found that the tip may create large bumps in the profile of steps misoriented with respect to the dense  $\langle 110 \rangle$ -direction even for a tunneling resistance of the order of  $4G\Omega$ . In a very recent STM study, Koch et al. [138] used a tunneling resistance of  $0.5G\Omega$  to scan parallel and perpendicular to steps along  $\langle 110 \rangle$  on Ag(110). These authors find that the steps appear frizzy at 300K, if the scan direction is perpendicular to the mean step orientation, whereas the steps are straight, if the scan direction is parallel to the steps. They concluded that the steps are straight at room temperature and that the frizziness is exclusively due to tip-surface interactions. From comparison of the STM data with MC-simulations, Koch et al. determine a tip-surface interaction energy of  $0.14\text{eV}$  [138]. An unresolved problem is whether a tip-surface interaction manifests itself in a change of the time dependence of  $G(t)$ . One may argue that tip-surface interactions contribute to  $G(t)$  exclusively at  $t=0$ , since a change in the step position caused by the tip at one time should be uncorrelated with the same effect at a later time. Then,  $G(t)$  only displays a constant offset while the time dependence remains unchanged [59, 60]. An answer to this question could be found, e.g., by a detailed analysis of  $G(t)$  for data similar to the one of Koch et al. [138]. As mentioned before, they showed that steps on Ag(110) at room temperature appear frizzy if the tip scans perpendicularly to the step edge. The steps seem to be straight if the scan direction is parallel to the steps. The authors concluded that in the case of a frizzy appearance of steps on Ag(110), the step frizziness is due to tip-mediated motion of adatoms, which is not induced if the tip scans parallel to the steps. Provided this conclusion is correct, the time exponent of  $G(t)$  should depend on the scan direction. In the other case, the time dependence of  $G(t)$  should remain the same save for a constant offset at  $t=0$ <sup>34</sup>.

In summary, one may say that for dense metal surfaces like Ag(111) [42], stepped Cu(111) with steps along  $\langle 110 \rangle$  [50] and Pt(111) [78], no evidence for tip-assisted mass transport at steps was found for moderate tunneling parameters ( $I \sim 1\text{-}3\text{nA}$ ,  $U \sim 0.6\text{-}1\text{V}$ ). For surfaces with reduced atom density like Ag(110) [54, 138], Pb(110) [53] or stepped Cu(111) with steps along  $\langle 121 \rangle$ , tip-assisted atomic motion may occur even under moderate tunneling conditions, but it is not clear yet whether the time dependence of  $G(t)$  is affected.

---

<sup>34</sup> It is noted in passing that the analysis of  $G(t)$  and in particular its time dependence must be performed rather carefully. The determination of the correct time dependence of  $G(t)$  in presence of a constant contribution to  $G(t)$

### 3.5. Step fluctuations in Fourier space

The step correlation function  $G(y,t)$  can be expressed in a Fourier representation by using the Fourier components  $x_q$  of the spatial coordinate  $x$ :

$$x(y,t) = \int_q x_q(t) e^{iqy} dy ; \quad q = \frac{2\pi n}{L_y}, \quad (3.32)$$

where  $q$  is the wave number and  $L_y$  the length of the step. The Fourier representation of the time correlation function  $G_q(t)$  is defined as [99]

$$G_q(t) = \left\langle \left| x_q(t) - x_q(0) \right|^2 \right\rangle. \quad (3.33)$$

By inserting (3.32) in (3.33),  $G_q(t)$  can be written in the general form [19, 73, 76, 99, 139]

$$G_q(t) = A(q) \left[ 1 - e^{-t/\tau(q)} \right]. \quad (3.34)$$

$A(q)$  is the amplitude of the fluctuations and  $\tau(q)$  is the relaxation time. One can show that  $A(q)$  decreases with increasing step stiffness  $\tilde{\gamma}$  according to [140]

$$A(q) = \frac{2k_B T}{L_y \tilde{\gamma} q^2}. \quad (3.35)$$

The relaxation time  $\tau(q)$  depends on the dominant mass transport mechanism involved in the fluctuations. The wave length dependence of  $\tau(q)$  has been theoretically discussed for three limiting cases: When atoms are exchanged with the terrace and terrace diffusion is either fast (case (iii)) or slow (case (iv)) and for the case of step edge diffusion (case (vi)) [19, 73, 99, 139] (and more generally in [76]). Terrace exchange with fast surface diffusion yields

$$\tau(q) = \frac{k_B T}{\Gamma_a \tilde{\gamma}} q^{-2}, \quad (3.36)$$

---

at  $t=0$  is difficult because the time exponent sensitively depends on  $G(t=0)$ . Hence, a large data base is necessary to unambiguously extract the contribution of tip-surface interactions to  $G(t)$ .

where the hopping coefficient  $\Gamma_a$  is the same as in (3.26). If terrace diffusion is slow, the relaxation time is

$$\tau(q) = \frac{k_B T}{2D_t c_t \tilde{\gamma}} |q|^{-3}. \quad (3.37)$$

$D_t$  is the terrace diffusion constant as used in (3.27) and  $c_t$  is the equilibrium adatom concentration on the terrace. If the fluctuations are dominated by edge diffusion, one has

$$\tau(q) = \frac{k_B T}{\Gamma_h \tilde{\gamma}} q^{-4}, \quad (3.38)$$

with  $\Gamma_h$  the hopping coefficient as in (3.30) and (3.31). In all cases,  $\tau(q)$  may be expressed in terms of the kink concentration  $P_k$  instead of  $\tilde{\gamma}$  by using (3.9) and (3.17)-(3.20). Since the characteristic wave vector  $q$  scales with the inverse of the linear size  $d$  of the decaying object, the characteristic time for the decay scales as  $d^2$ ,  $d^3$ ,  $d^4$  for fast terrace diffusion, slow terrace diffusion and edge diffusion, respectively. These scaling laws apply also to the reshaping of islands after a coalescence event (see Section 6.2.2).

In order to use the Fourier representation in the experimental analysis of step fluctuations, the sampling time must be much shorter than the relaxation time  $\tau(q)$ . The first experimental study was performed by Bartelt et al. [139] on Si(111) using REM. Later, Pai et al. [94] investigated the equilibrium fluctuations of isolated steps on Ag(110), which were less than  $30^\circ$  off the  $\langle 110 \rangle$ -direction. They found that  $\tau(q)$  is proportional to  $q^{-2}$  in agreement with the  $t^{1/2}$ -dependence of  $G(t)$  measured at room temperature. From the wave-number analysis of  $G_q(t)$ , they determine the step-edge stiffness to  $\tilde{\gamma} = 18 \text{ meV}/\text{\AA}$ , which corresponds to a diffusivity of  $b^2 = 0.664 a_\perp^2$  and a kink energy of about  $\varepsilon = 40 \text{ meV}$  consistent with their previous result  $\varepsilon = 43 \text{ meV}$  [93].

We analyzed the decay of a bump in a  $\langle 110 \rangle$ -oriented step on Cu(111) at 303K [50] and Fig. 19 shows STM images. After deposition of a submonolayer amount of Cu on a gently sputtered Cu(111) surface, quasi-hexagonal mono- and double-layer adatom and vacancy islands are formed (Fig. 19(a)). The islands migrate on the surface, due to edge fluctuations and engage in a Brownian motion, which has been extensively investigated by Morgenstern et al. [47] on Ag(111). Due to this motion, once in a while islands merge with steps (Fig. 19(a),

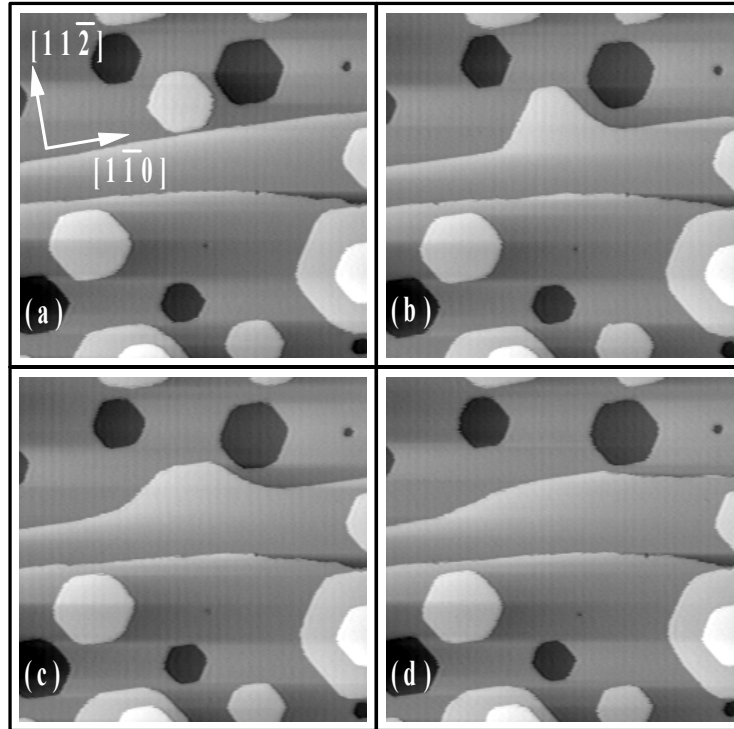


**Fig. 19.** STM images of Cu(111) at 303K. After gentle sputtering and subsequent Cu deposition, 2-dimensional adatom and vacancy islands are formed. (a) An adatom island in close vicinity to a step (b) merges with the step edge and a bump is formed. (c), (d) Due to rapid mass flux along the step edge, the bump broadens and the step straightens. The scan width in the images is 90 nm [50].

(b)). A bump is formed in the step profile (Fig. 19(b)), which causes locally a non-constant chemical potential along the step edge. Due to the gradient in the chemical potential, rapid mass flux along the step sets in, the bump decays, and the step eventually straightens (Fig. 19(c), (d)).

Fig. 20(a) shows the measured step profile for a set of 8 consecutive STM images [50]. In Fig. 20(b), the time dependence of the bump amplitude  $A(q)$  is plotted for different wave numbers  $q$ . For all values of  $q$ ,  $A(q)$  decays exponentially in time, albeit with different relaxation times  $\tau(q)$  (3.34). From an exponential fit to the data in (b) one obtains the relaxation time as a function of the wave number (Fig. 20(c)). As shown in (3.36)-(3.38),  $\tau(q)$  obeys a power law in  $q$ . From the slope in the log-log plot of  $\tau(q)$  vs.  $q$ , one obtains a  $q^{-4}$ -dependence, which corresponds to step edge diffusion (3.38), in agreement with the  $t^{1/4}$ -dependence of  $G(t)$  [50], as discussed in Section 3.3.3. Furthermore, using (3.38) one can calculate the hopping coefficient  $\Gamma_h$  from the data in Fig. 20(c). The number agrees well with what has been derived from the measurements of  $G(t)$  [50].

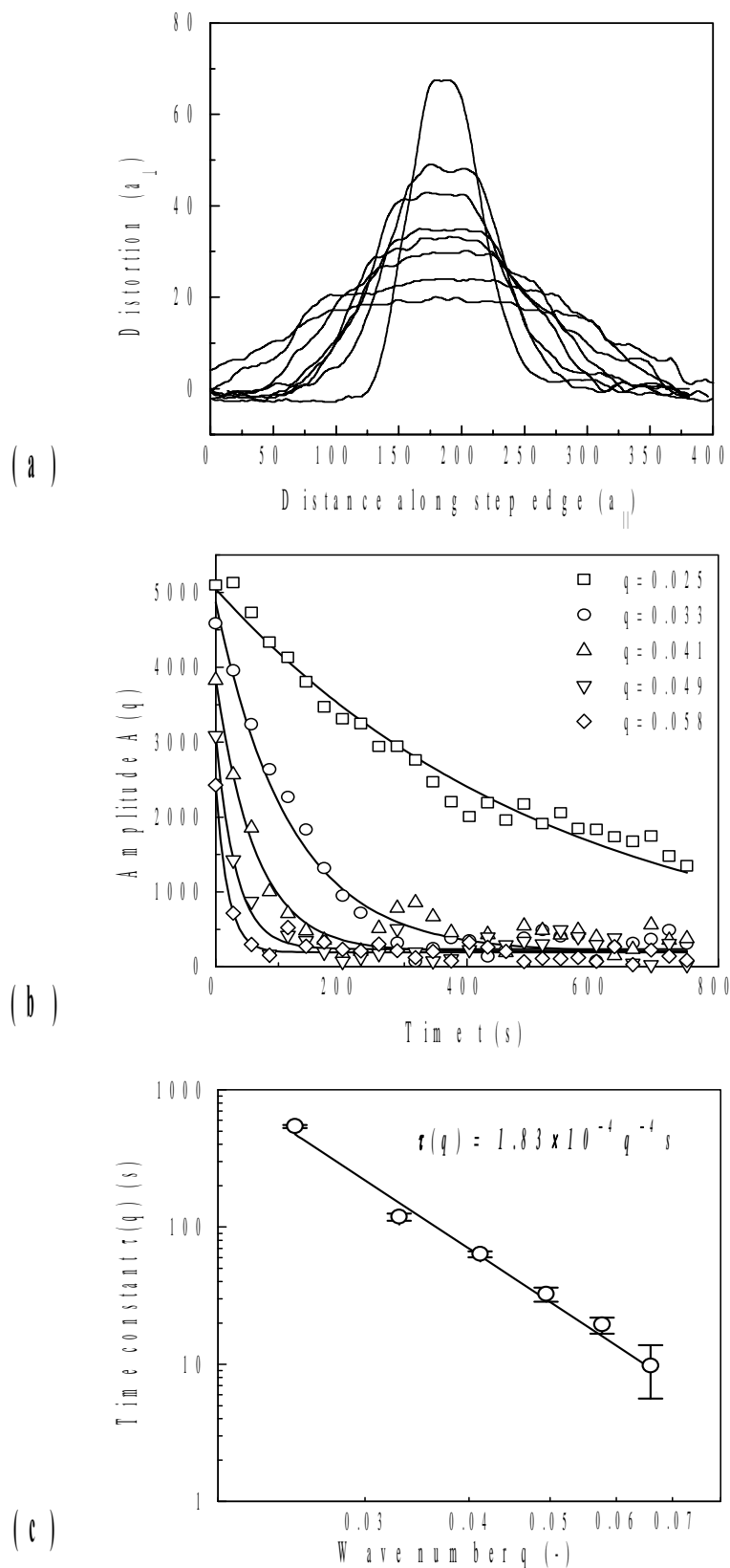


**Fig. 20.** (a) Profile of the step bump as measured from STM images as shown in Fig. 19. (b) Amplitude  $A(q)$  for different wave numbers  $q$  vs. time. (c) Relaxation time  $\tau(q)$  as determined from exponential fits to the data in (b) vs.  $q$  [49].

## 4. Step-step interactions

So far, steps on surfaces have been treated as non-interacting (isolated) steps. Many experimental investigations, however, have been performed on vicinal surfaces, which may have a high step density. In particular, vicinal surfaces with low Miller indices, e.g., surfaces of fcc metals vicinal to the (001) plane like (113), (115) and (117), or vicinal surfaces to the (111) plane like (997) or (779) have mean step-step separations between 1.5 and 8 atomic rows. Neighboring steps may have a considerable influence on step fluctuations, due to step-step interactions [141-144], in particular, when the step-step distance is small. Step-step interactions have attracted considerable interest in the past, because they have an influence on the wandering of steps and they play a crucial role in the equilibrium shape of crystals [145, 146], as well as in the roughening transition of surfaces [22, 147-149]. Step-step interactions may be purely *entropic*. Entropic interactions arise from the *non-crossing condition* of steps. The crossing of steps is forbidden, because it would lead to overhangs, which have a high energy. Examples for explicit *energetic* interactions are firstly elastic interactions, which arise from the lattice distortion at step edges and cause repulsive interactions [150]. Secondly, dipole-dipole forces arise from the electron distribution near step edges and may be of attractive or repulsive nature depending on the orientation of the dipole moment. In all three cases, the interaction potential  $V(x)$  decays with  $1/x^2$  [69, 140]. Other possible interactions have been proposed, which follow a different distance dependence. Oscillatory interactions were proposed by Redfield and Zangwill [151] and experimental evidence for such an interaction was found on Ag(110) by Pai et al. [152].

Early experimental studies on the step-step interaction were performed on metal surfaces using helium scattering (for an overview see [22]). In these studies, the roughening transition was determined from the decay of reflected helium intensity at higher temperature. The roughening temperature is related to the interaction energy between steps [153]. In STM studies by Frenken et al. [49], the roughening of stepped silver surfaces was observed and interpreted as the roughening transition. First explicit values of the interaction strength were determined by Wang et al. on Si(111) [154], who analyzed the step-step distance (or terrace width) distribution on stepped surfaces. (For an overview on other experimental work on semiconductor surfaces see [19].) The analysis of terrace width distributions is based on three basic theoretical models, which have been discussed controversially in the past.

### 4.1. Mean-field approximation

In the mean-field approximation, a step is considered to wander in the mean potential created by all other steps. Two explicit potentials have been discussed so far: In the Gruber-Mullins

picture [155], the potential  $V(x)$  is the classical potential well with  $V(x)=0$  for  $-\langle L \rangle < x < +\langle L \rangle$  and  $V(x)=\infty$  elsewhere, where  $2\langle L \rangle$  is the width of the well. In other words, a fluctuating step is fixed between two straight hard walls separated by twice the average step spacing  $\langle L \rangle$  (Fig. 21). In the following, the distance is normalized as  $s=x/\langle L \rangle$ . The probability distribution  $P(s)$  to find the step at a position  $s$  ( $-1 < s < +1$ ) is given by the ground state density [155]

$$P(s) = \sin^2\left(\frac{\pi s}{2}\right). \quad (4.1)$$

For explicit repulsive interactions, beyond the non-crossing condition, the potential is

$$V(s) = \frac{A}{\langle L \rangle^2} \sum_{n=1}^{\infty} \left[ \frac{1}{(n+s)^2} + \frac{1}{(n-s)^2} \right], \quad (4.2)$$

where the constant  $A$  is the *interaction strength*. The index  $n$  counts the steps forming the mean-field potential where  $n=1$  corresponds to the nearest-neighbor step.

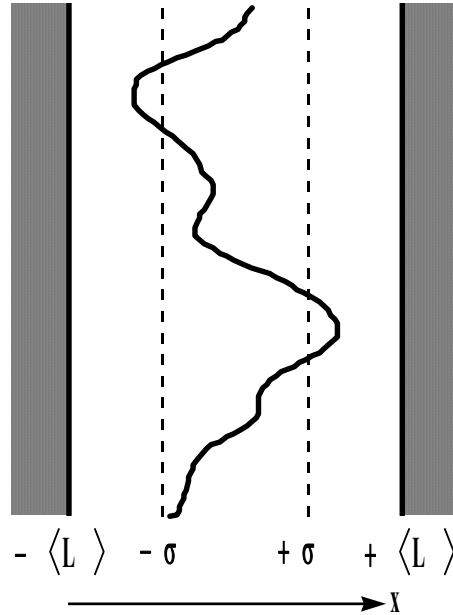


**Fig. 21.** Illustration of the mean-field model of a wandering step for two different potentials: If the potential is zero for  $-\langle L \rangle < x < +\langle L \rangle$  and infinitely large otherwise, the step wanders between two straight, rigid walls. The walls are located at twice the average step spacing  $\langle L \rangle$  [155]. If the potential is parabolic due to strong repulsive interactions, the width of the fluctuation is  $2\sigma$ , depending on the strength of the potential [67].

In the harmonic approximation around  $s=0$ ,  $V(s)$  is given by

$$V(s) = \frac{A}{\langle L \rangle^2} \left( \sum_{n=1}^{\infty} \frac{2}{n^2} \right) + \frac{\pi^4}{15} \frac{A}{\langle L \rangle^4} s^2 + \dots \quad (4.3)$$

The step-step distance distribution is then a Gaussian [67]

$$P(s) = \frac{1}{\sigma \sqrt{2\pi}} e^{-\frac{(s-1)^2}{2\sigma^2}}, \quad (4.4)$$

where the variance  $\sigma$  is given by

$$\sigma^2 = \sqrt{\frac{b^2(T) k_B T}{48 A a_{\parallel}}}, \quad (4.5)$$

when only nearest-neighbor interactions are taken into account ( $n=1$  in (4.2)) and

$$\sigma^2 = \sqrt{\frac{15 b^2(T) k_B T}{8 \pi^4 A a_{\parallel}}}, \quad (4.6)$$

when all steps are considered. Equations (4.5) and (4.6) differ by a factor of 1.04. Note that in the mean-field approximation it is assumed that the interaction potential is strictly 1-dimensional, i.e., interaction occurs only between segments of neighboring steps at constant  $y$ .

Misbah and coworkers [100, 156] claimed that the variance  $\sigma$  as determined in the mean-field approximation is underestimated for large step repulsion. They argue that the error is introduced into the mean-field model by the assumption that the neighboring steps are straight and rigid rather than wander independently. They found that the variance given in (4.5) and (4.6) should be larger by a factor 1.8 for nearest-neighbor interactions and by a factor 1.7 for all steps included. A similar argument was brought up by Barbier and coworkers [45, 46, 79, 105]: Step-step interactions contribute to the surface free energy. At the roughening transition [22], the surface free energy vanishes and the step-height correlation function diverges. On a vicinal surface, the divergence of the surface-height correlation function is directly related to

the step fluctuations. Hence, it was argued that the fluctuations of steps must be considered to determine the step-step interaction strength. Based on the roughening theory, they deduced a variance

$$\sigma^2 = \frac{4}{\pi^2} \left( 1 + \sqrt{1 + \frac{4A a_{\parallel}}{b^2(T) k_B T}} \right)^{-1}. \quad (4.7)$$

For large interactions, (4.7) has the same form as (4.5) and (4.6), however, the pre-factor obtained by Barbier and coworkers is somewhat different. The variance in (4.7) is about a factor of 1.46 larger than the variance in (4.6), where all steps are considered. Likewise, the interaction strength obtained from (4.7) by a given variance of the terrace width distribution is about a factor of 2 larger than the strength obtained based on (4.6). For small interactions, in particular for  $A=0$ , the variance becomes independent of temperature and  $\sigma^2=2/\pi^2$ . The case  $A=0$ , corresponds to non-interacting steps, which is also denoted as the case of *free fermions* [157].

#### 4.2. Fermion description

The more general one-dimensional *free-fermion* model makes use of the fact that steps do not start, end or cross. Step positions are interpreted as non-interacting free fermions evolving

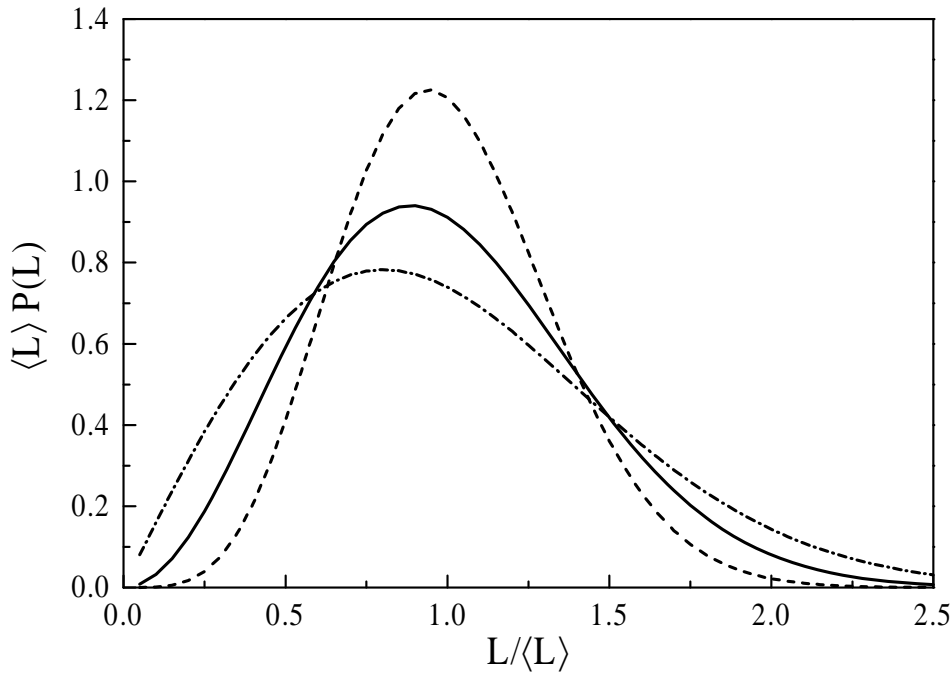


**Fig. 22.** Scaled terrace width distribution for repulsive interactions (dashed line), no interactions (solid line) and attractive interactions (dot-dashed line) between steps (after Joós et al. [157]).

in one spatial dimension. Within this picture, the configuration of a step profile is interpreted as a world line of the fermion. This model can be extended, so that energetic repulsive and attractive interactions are included [157]. In all cases, the terrace width distribution is asymmetric. Fig. 22 shows the scaled terrace width distribution as determined by Joós et al. [157] for the free-fermion case (solid line), repulsive interactions (dashed line) and attractive interactions (dot-dashed line). For entropic repulsion and energetic attraction, the terrace width distribution has a high skewness and the Gaussian approximation (4.4) obviously fails. In the case of strong repulsive interactions, however, the Gaussian description is a good approximation.

### 4.3. Generalized Wigner surmise

More recently, the application of *random matrix theory* [158, 159] provided a new insight into the ongoing controversy as to which of the various approaches is the most suitable to analyze terrace width distributions. Einstein and Pierre-Louis [160] showed that, according to the generalized Wigner surmise, the terrace width distribution of fluctuating steps can be approximated by

$$P_\rho(s) = a_\rho s^\rho e^{-b_\rho s^2}. \quad (4.8)$$

The parameter  $\rho$  is related to the interaction strength  $A$  via

$$A = \frac{b^2(T)k_B T}{a_\parallel} \frac{\rho(\rho-2)}{4}. \quad (4.9)$$

The constants  $a_\rho$  and  $b_\rho$  in (4.8) are determined by the normalization and the unit mean of the terrace width distribution and are given in terms of gamma functions [160, 161]<sup>35</sup>:

$$a_\rho = \frac{2b_\rho^{(\rho+1)/2}}{\Gamma\left(\frac{\rho+1}{2}\right)}; \quad b_\rho = \left( \frac{\Gamma\left(\frac{\rho+2}{2}\right)}{\Gamma\left(\frac{\rho+1}{2}\right)} \right)^2. \quad (4.10)$$

---

<sup>35</sup> For most applications, it is convenient to expand  $a_\rho$  and  $b_\rho$  in power laws around  $\rho=4$  [161].

Sutherland [162-164] showed that analytic solutions of (4.8) are available for  $\rho=1, 2$ , and 4. The cases  $\rho=1$  and 4 correspond to attractive and repulsive interactions, respectively. For  $\rho=2$ , the interaction strength  $A$  vanishes and  $P_2(s)$  is the distribution of non-interacting steps and is equal to the free-fermion distribution as shown in Fig. 22. An heuristic formula, which is identical to (4.8) in the case  $\rho=2$ , was proposed already several years ago by Ibach [165]<sup>36</sup>. For all other values of  $\rho$ , (4.8) serves as an extrapolation scheme between the exactly solvable cases  $\rho=1, 2$ , and 4 [160]. As emphasized by Einstein and Pierre-Louis [160], (4.8) should hold in the range from non-interacting steps ( $\rho=2$ ) to moderately strong interacting steps ( $\rho\sim 4$ ). Here, the terrace width distribution is considerably skewed and the Wigner model (4.8) should be a better approach than the Gaussian approximation (4.4). For strong interactions, the skewness of experimental terrace width distributions is almost zero. Then, the Wigner surmise fails and the symmetric Gaussian distribution yields excellent results on the step-step interaction strength. A detailed analysis [160, 161, 166] of the different interaction regimes shows that the mean-field model with all steps interacting (4.6) is closer to the exact solution of the Wigner surmise ( $\rho=4$ ) than the models used by Misbah and coworkers [100, 156] and Barbier and coworkers [45, 46, 79, 105] and should therefore be used to extract interaction strengths from experimental terrace width distributions.

#### 4.4. Experimental results on metal surfaces

The analysis of the terrace width distribution were performed on stepped Cu(001) and (111) surfaces. Most of the surfaces vicinal to (001) had Miller indices  $(11n)$ , i.e., the steps were oriented along the dense  $\langle 110 \rangle$ -direction. Rousset et al. [167] studied the Cu(810) surface, which is vicinal to the (001) plane, the steps are oriented, however, along the  $\langle 100 \rangle$ -direction. The vicinal surfaces to the (111) plane had Miller indices  $(n,n,n+m)$ . These surfaces consist of parallel A-steps along  $\langle 110 \rangle$ . The measured values of the interaction strength  $A$  from these surfaces are summarized in Table 3. Studies by Rousset et al. [167] of the terrace-width distribution on Cu(1,1,11) and Cu(810) at room temperature were found to fit a Gaussian and enabled the interaction strength to be determined via (4.5). For Cu(1,1,11),  $A=15.6 \text{ meV}\text{\AA}$  was obtained. In order to calculate this value from the variance  $\sigma$  of the distribution, the kink energy  $\varepsilon=67 \text{ meV}$ , measured in helium diffraction measurements [168] was used, which is much lower than the more precise values obtained by the analysis of

---

<sup>36</sup> In [165], the formula in (2) is misprinted and should read  $P(x) = \frac{4}{\sqrt{\pi}} \frac{x^2}{l_m^3} e^{-x^2/l_m^2}$  with  $l_m \equiv \sqrt{\pi/4} \langle L \rangle \approx 0.886 \langle L \rangle$ , where  $\langle L \rangle$  is the mean step-step distance as denoted in this review.

spatial step fluctuations ( $\varepsilon=128\text{meV}$  [40, 41]). If one recalculates the interaction strength, as determined by Rousset et al. using  $\varepsilon=128\text{meV}$ , one obtains  $A=2\text{meV}\text{\AA}$ . They also give a rough estimate for the interaction strength on Cu(810) ( $A=62\text{meV}\text{\AA}$ ). Using (4.7), Masson et al. [45, 46] find for Cu(1,1,11)  $A=5.9\pm 1.1\text{meV}\text{\AA}$ . Later, these authors presented a more detailed analysis on Cu(1,1,11) at room temperature and found  $A=6.0\text{meV}\text{\AA}$  [79]. They also compared their result with our previously published data on Cu(117) [169] and found good agreement. Subsequently, we reported a temperature variable study of Cu(117), Cu(1,1,11), Cu(1,1,13) and Cu(1,1,19) [165]. Following the mean-field approach, and using (4.6), an interaction strength of  $A=7.1\pm 3.8\text{meV}\text{\AA}$  on (117), (1,1,11) and (1,1,13) was obtained. Above room temperature, the terrace-width distributions measured on Cu(1,1,19) are in agreement with this interaction strength. For  $T=290\text{K}$ , however, the distribution is considerably broader than for higher temperatures and cannot be fitted by a Gaussian [165]. We reported a similar striking behavior of the distribution on Cu(1,1,19) at room temperature in an earlier study [169], where we found a double-peak distribution for the (1,1,19) surface at room temperature, which looks similar to the data shown in [165]. The unexpected broad distribution for Cu(1,1,19) at 300K and below was interpreted as evidence for attractive step-step interactions [169]. Another possible explanation, however, could also be a temperature dependent instability of vicinal metal surfaces, as discussed recently by Frenken and Stoltze [170].

Theoretical values for the step-step interaction energy by Tian and Rahman [83] are available for Cu(1,1,2m+1) vicinal surfaces. These authors use an EAM calculation to determine the step-step interaction energy as a function of the Miller index (2m+1). For (2m+1) between 7 and 19, they obtain step-pair interaction energies between 1.6 and 0.5meV/atom. According to (4.2), with  $n=1$ , these values correspond to values of the interaction strength  $A$  between 4 and 9meV $\text{\AA}$ , in reasonable agreement with experiment. Several investigations were performed on Cu(111) vicinal surfaces: Using the mean-field approximation, with all steps interacting (4.6), we determined the interaction strength on various A-step vicinal surfaces to  $A=6.1\pm 0.4\text{meV}\text{\AA}$  [28, 161].

Hoogeman et al. [92, 171] used a different ansatz to determine the interaction strength  $A$  on vicinal surfaces. Fig. 23 shows two models of three parallel steps with a mean step-step separation  $L$  and different kink configurations. The local step-step distance may be reduced or enhanced by the kink length  $a_{\perp}$  between two kinks on neighboring steps. In the kink configuration (a), the total length of the step segments with reduced step-step distance (indicated by bright shaded areas) remains unchanged, when the kink position  $y$  in the middle

Surface	T (K)	Model	A (meVÅ)	Step type	Ref.
Cu(117)	298	R	5.9±1.1	$\langle 110 \rangle$	[45, 169]
Cu(117)	298	all	7.1±3.8	$\langle 110 \rangle$	[165]
Cu(1,1,11)	298	NN	2 <sup>(37)</sup>	$\langle 110 \rangle$	[167]
Cu(1,1,11)	298	R	5.9±1.1	$\langle 110 \rangle$	[45]
Cu(1,1,11)	298	all	7.1±3.8	$\langle 110 \rangle$	[165]
Cu(1,1,13)	285-378	all	7.1±3.8	$\langle 110 \rangle$	[161, 165]
Cu(1,1,19)	290-370	all	7.1±3.8	$\langle 110 \rangle$	[161, 165]
Cu(810)	298	NN	62 <sup>(37)</sup>	$\langle 110 \rangle$	[167]
Ag(115)	298		9.5±1.0	$\langle 110 \rangle$	[92, 171]
Cu(7,7,11)	296-323	all	6.1±0.4	A-step    $\langle 110 \rangle$	[28, 161]
Cu(17,17,19)	305-353	all	6.1±0.4	A-step    $\langle 110 \rangle$	[28, 161]
Cu(21,21,23)	313-333	all	6.1±0.4	A-step    $\langle 110 \rangle$	[28, 161]
Pt(997)	298	NN	12.9 <sup>(38)</sup>	B-step    $\langle 110 \rangle$	[30]
Pb(111)	440		52	B-step    $\langle 110 \rangle$	[172, 173]

**Table 3.**

Interaction strength  $A$  measured on vicinal metal surfaces. If the interaction strength was determined by the analysis of terrace width distributions, the used models are denoted as "NN" and "all" for the nearest-neighbor approach (4.5) and if all steps are considered (4.6) in the mean-field model. "R" denotes the model based on roughening theory (4.7). If no model is indicated in column 3,  $A$  was not determined by the analysis of the terrace width distribution (see text).

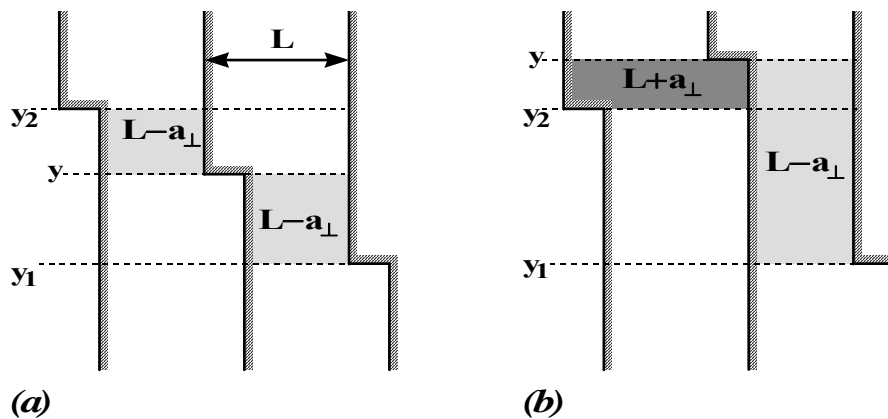


**Fig. 23.** Different kink configurations at parallel steps on a vicinal surface: (a) As long as the kink position  $y$  of the middle step is in between  $y_1$  and  $y_2$  the mean step-step interaction energy remains unchanged. In (b), the step-step interaction energy changes (after Hoogeman et al. [92, 171]).

<sup>37</sup> When  $\varepsilon=128\text{meV}$  [40, 41] is used as the kink energy.

<sup>38</sup> Hahn et al. [30] determined from the terrace width distribution  $A/b^2k_B T=21.5\text{\AA}^{-1}$ . Using  $\varepsilon=168\text{meV}$  [78] and (3.17)-(3.19) to determine the diffusivity  $b^2$ , an interaction strength of  $12.9\text{meV}\text{\AA}$  was obtained.

step wanders between the kink positions  $y_1$  and  $y_2$  of the outer steps. Hence, the wandering of the kink at the middle step between  $y_1$  and  $y_2$  does not change the mean step-step interaction energy. The situation is different for the kink configuration (b). Here, the position of the kink at the middle step  $y$  is outside the distance between  $y_1$  and  $y_2$ . Now, step segments with enhanced step-step distance occur (indicated by the dark shaded area) and the mean step-step interaction energy differs from that in the configuration in (a). Hoogeman et al. [92, 171] measured the probability to find a kink in position  $y$  for configurations as shown in (b) on Ag(115). From that they determine the step-step interaction strength on Ag(115) to  $A=9.5\pm 1\text{meV}\text{\AA}$ .

Two studies of the terrace width distribution were performed on Pt surfaces. Hahn et al. [30] measured the ratio  $A/b^2k_B T$  from the terrace width distribution on Pt(997) (B-steps along  $\langle 110 \rangle$ ) at room temperature and obtained  $21.5\text{\AA}^{-1}$ . One may calculate the diffusivity  $b^2(T)$  at 300K, using a kink energy of  $\varepsilon=168\text{meV}$ , as determined for B-steps on Pt(111) [78]. With (3.19), one finds a value for the interaction strength  $A=12.9\text{meV}\text{\AA}$ . Swamy et al. [174] analyzed the terrace width distribution on (1x2)-reconstructed Pt(110) at room temperature. As can be seen from Fig. 24, the distribution (gray columns) is highly asymmetric and cannot be fitted within the mean-field approximation for strong repulsive step-step interactions (dotted curve). The experimental result is neither in satisfactory agreement with the free-

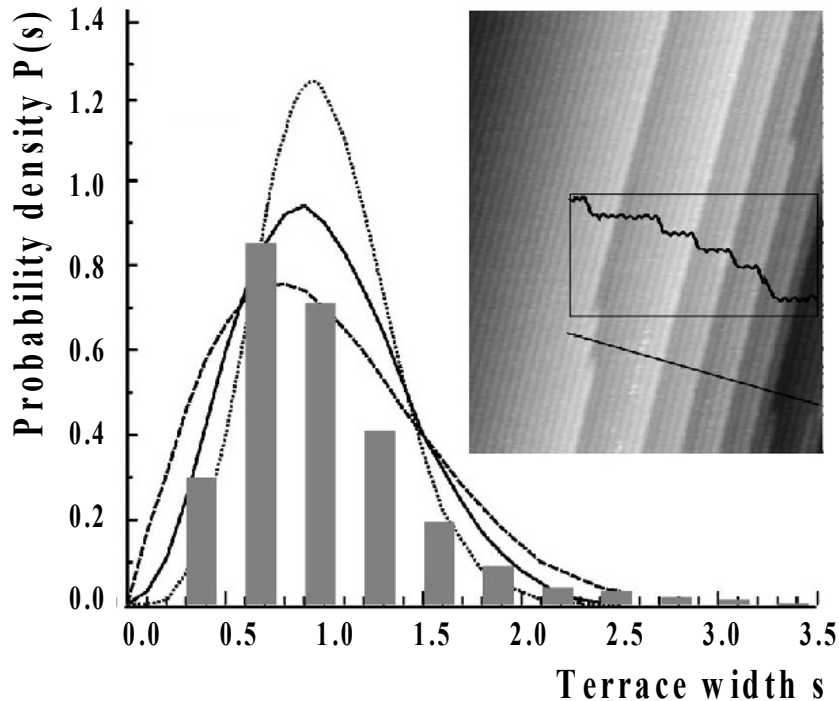


**Fig. 24.** Terrace-width distribution  $P(s)$  on Pt(110) (gray columns). The dotted, solid and dashed curves are theoretical distributions for repulsive, no and attractive interactions, respectively (after Swamy et al. [174]).

fermion distribution (solid curve) nor with attractive interactions (dashed curve). In collaboration with Einstein and coworkers, we used the data of these authors and fitted the distribution to the Wigner formula (4.8) and found  $\rho=2.06$  [166]. According to (4.9), this value corresponds to almost non-interacting ( $A\approx 0$ ) steps.

For small repulsive interactions, when the terrace-width distribution is obviously skewed, the Wigner surmise seems to be the most appropriate approach to analyze terrace width distributions. An extensive comparison of the fit quality using the different models was performed for Cu(001) and (111) vicinal surfaces by Giesen and Einstein [161]. Fig. 25 shows the terrace width distribution for Cu(1,1,13) for (a) 295K and (b) 348 K [161]. The experimental data points obtained from STM studies [161, 165] are plotted as circles. The solid lines are fits to the Wigner surmise (4.8). Note that the Wigner fit is a one-parameter fit

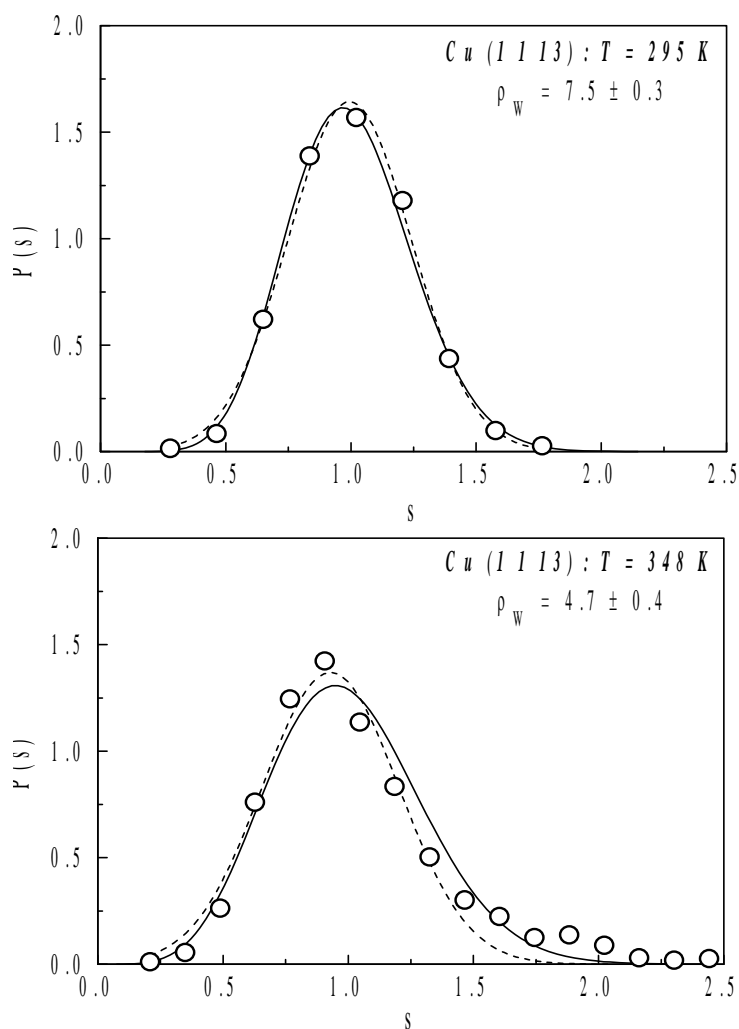


**Fig. 25.** Terrace width distributions as measured on Cu(1,1,13) at 295 and 348K. The dashed and solid curves correspond to a fit according to the mean-field model with strong repulsive interactions (4.4) and the Wigner approach (4.8), respectively. The values  $\rho_W$  were obtained from fitting the experimental data to (4.8) using (4.10) [161, 165].

because of (4.10). The dashed lines are Gaussian fits according to the mean-field model (4.4). At 295K, where the skewness is small, there is hardly no difference between the experimental data and both the Gaussian and Wigner distributions. With increasing temperature, the asymmetry of the experimental distribution increases and the Gaussian fit fails, in particular, for large step-step distances. This regime is far better reproduced by the Wigner model. The Gaussian model, however, is slightly superior than the Wigner fit in the peak area.

It was shown [161, 166] that for moderate step-step interactions ( $3 < \rho < 5$ ) the mean-field approximation and the Wigner surmise both give reasonable results. This may be demonstrated by plotting the dimensionless interaction strength  $\tilde{A}$ , which is defined as [160]

$$\tilde{A} = \frac{A\tilde{\gamma}}{(k_B T)^2}. \quad (4.11)$$

The product of  $\tilde{A}$  and  $T^2$  should obey the same temperature dependence as the step edge stiffness  $\tilde{\gamma}$  (3.20). One can show that [160]

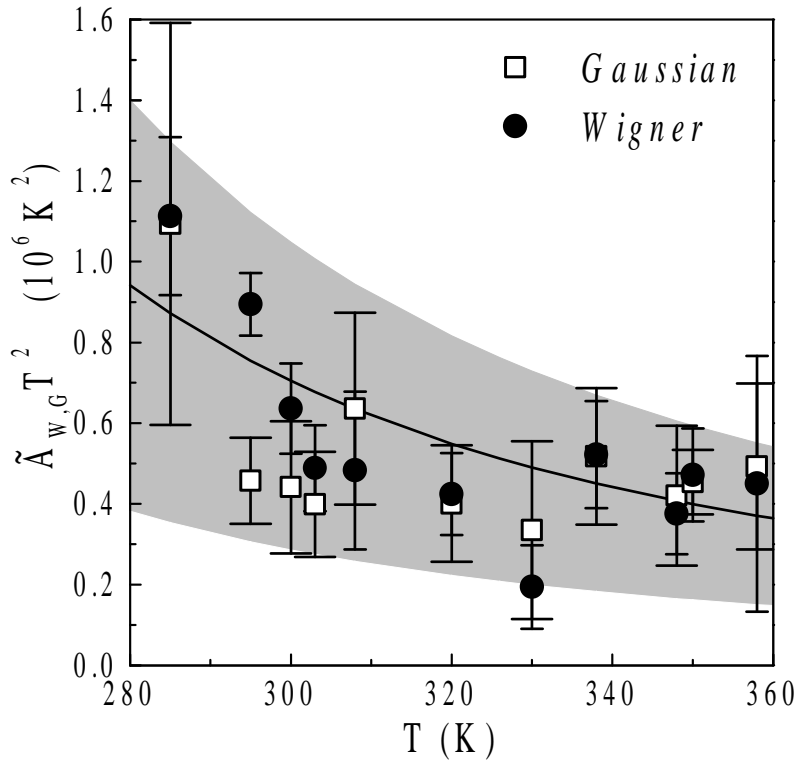


**Fig. 26.** Plot of the product of the dimensionless interaction constant  $\tilde{A}$  (4.11) and  $T^2$  measured for Cu(1,1,13), which should obey the same temperature dependence as the step stiffness (solid line). The indices "W" and "G" indicate that  $\tilde{A}$  was determined using the Wigner and the Gaussian approach, respectively [161].

$$\tilde{A}_W = \frac{\rho(\rho-2)}{4}, \quad (4.12)$$

where the subscript "W" serves as a reminder that  $\rho$  is determined from the Wigner surmise (4.8). In Fig. 26, the product of  $\tilde{A}$  and  $T^2$  measured for a Cu(1,1,13) surface is plotted for the Gaussian model (using (4.4), (4.6) and (4.11)) and for the Wigner surmise (using (4.8), (4.9) and (4.11)). The solid line is a theoretical curve using a kink energy of  $\varepsilon=128\pm 3\text{meV}$  [40, 41] and (3.20), (4.11). The gray shaded area reflects the error bars in the kink energy. The results obtained from both the Gaussian and the Wigner analysis reflect the general temperature dependence of the step stiffness within the error limits.

In the case of weak interactions ( $2 < \rho < 3$ ), the Wigner approach appears to be the best choice, as we demonstrated in collaboration with Einstein and coworkers [166] for the terrace width distribution measured by Swamy et al. [174] on Pt(110).

For completeness, we refer Arenhold et al. [173, 175], who used a different method to measure the step-step interaction strength on Pb(111). These authors analyzed the equilibrium facet shapes of small three-dimensional Pb particles. They find a step-step interaction strength on Pb(111) of  $A=52\text{meV}\text{\AA}$ .

At the end of this section, we mention that an effort has been made to determine the roughening temperature, as well as the surface stress of vicinal surfaces, by measuring the step-step interaction strength. According to the Villain-model [153], the roughening temperature  $T_R$  of a vicinal surface is given by

$$\frac{6A}{\langle L \rangle^4} \frac{e^{\frac{\varepsilon}{k_B T_R}}}{k_B T_R} = \frac{\pi^2}{2}. \quad (4.13)$$

Here,  $A$  is again the step-step interaction strength,  $\langle L \rangle$  is the mean terrace width and  $\varepsilon$  is the kink energy. In the Villain-model, it is assumed that  $\langle L \rangle$  is large compared to the nearest neighbor distance  $a_{||}$ . Therefore, (4.13) holds only for vicinal surfaces with small miscut angles to the low index surface. We found  $T_R$  for vicinal Cu(11n) surfaces to be between 220 and 140K for  $n$  between 7 and 19 [165]. The numbers of  $T_R$  obtained using (4.13) are in reasonable agreement with measurements of the roughening temperature using Helium diffraction [153, 168, 176-178], though our results are slightly smaller.

For an elastic isotropic medium, but with elastic constants pertinent to the crystallographic orientation of the surface, the step-step interaction potential  $V(s)$  for two parallel, equally oriented steps with distance  $x=s\langle L \rangle$  can be written as [179, 180]

$$V(s) = \frac{2(1 - \nu_{(hkl)}^2)}{\pi Y_{(hkl)}} \frac{D_x^2 + D_y^2}{\langle L \rangle^2} \frac{1}{s^2}, \quad (4.14)$$

where  $D_x^2, D_y^2$  are the parallel and perpendicular force dipoles arising from the mechanical strain field at the step edges.  $Y_{(hkl)}$  and  $\nu_{(hkl)}$  are the Youngs moduli and the Poisson ratios for the (hkl)-oriented surface. As shown in [28], the force dipoles can be expressed in terms of the step height and the surface stress of the respective surface plane (hkl). Comparing (4.2) with (4.14), one finds that for metal surfaces, the numbers for the surface stress estimated from the measured step-step interaction strength are considerably smaller than theoretical values [28, 165].

In summary, the analysis of terrace width distributions on vicinal surfaces yields numbers for the interaction strength between steps. It is noted, however, that the determination of the interaction strength requires a sufficient large data base measured at different temperatures. Even when this requirement is fulfilled, the error of the measured interaction strength is very large, as becomes obvious from the summary of the experimental results in Table 3.

The ongoing controversy, as to which of the different models described in Sections 4.1-4.3 is most suitable to analyze the terrace width distribution seems to come to a final conclusion: The mean-field approximation is an appropriate model for strong to moderate step-step interactions. For small interactions, the Wigner model seems to be the best choice.

## 5. Step fluctuations at solid/liquid interfaces

The most important difference between surfaces in UHV and surfaces in liquid environment is that, in the latter case, the surface is in equilibrium with the adjacent phase. In UHV, with no ambient vapor phase, desorption from the solid into the vacuum is negligible at the temperatures of interest. In electrolyte, dissolution from the solid into the liquid and deposition from the liquid onto the electrode surface are an integral part of the phenomena considered here. Deposition events include the deposition of metal cations, e.g., in *under potential deposition (UPD)*, or the specific adsorption of electrolyte anions. In contrast, dissolution events include the removal of metal cations or of specifically adsorbed anions. In most of the cases, deposition of metal atoms and specific adsorption (and vice versa) is correlated to structural changes of the electrode and -maybe even more important- to a change of formation energies of defects and of the energy barriers related to diffusion processes. Defects, such as monatomic steps and islands, are of special interest, because deposition and dissolution processes preferably start at defects as is similar to surfaces in UHV. Differences between surfaces in UHV and surfaces in an electrolyte may arise from both intrinsic differences, because of the absence, respectively, of the presence of the liquid and because of differences in the controlling extensive parameters. In UHV, the temperature is the only variable parameter, which may affect atomic processes. For solids in contact with an electrolyte, the electrode potential is an additional parameter, which controls the surface properties. The variation of the sample temperature (while the potential is held constant) is also possible, but is more difficult than in UHV. Changes in temperature of the metal electrode may introduce thermal drift, which is harder to control and to minimize in an electrochemical environment than in UHV, due to the heat capacity of the liquid. Furthermore, the use of aqueous electrolytes naturally restricts the temperature range to temperatures between about 280 and 330K. Therefore, temperature dependent investigations of metal electrodes in electrolyte are difficult, though not impossible.

For constant sample temperature, the electrode potential serves as an "electrochemical temperature". With increasing potential, the diffusion on the surface may be considerably enhanced and different mass transport processes may become dominant in different potential ranges.

A further parameter, which may be varied in studies of the dynamics of solid surfaces in contact with an electrolyte, is the nature and composition of the electrolyte. The chemical nature of the anions in the liquid have a strong influence on the interface dynamics. Chloride, e.g., is a well-known additive to aqueous electrolytes, which enhances the atom mobility

dramatically on metal surfaces. Rough surfaces are smoothed, if they are brought in contact with a chloride containing electrolyte - a process that is also known as *electrochemical annealing* [181-184].

While no analogue for the electrode potential exists in UHV, the surface dynamics may be studied in UHV at different temperatures, as well as under the influence of adsorption from the residual gas, although little is known about the latter. Despite the principle differences between studies in UHV and in electrolyte, some interesting similarities are found and discussed in the following section, which focuses on experimental studies of atomic mobility at steps.

### 5.1. Step fluctuations on Ag(111) electrodes

The first qualitative and semi-quantitative study of step fluctuations on metal electrodes was reported by Dietterle et al. [48] for Ag(111) in 0.05M H<sub>2</sub>SO<sub>4</sub>+0.1mM CuSO<sub>4</sub> at room temperature. These authors found that steps appear frizzy on Ag(111) and the frizziness increases with increasing potential. Fig. 27 shows in the left panel the STM images of a fluctuating silver step with atomic resolution in air (a) and in electrolyte at (b) -120mV vs. the *saturated calomel electrode* (SCE)<sup>39</sup>, (c) 0V vs. SCE, (d) +40mV vs. SCE and (e) +80mV vs. SCE [48]. At negative potentials, the fluctuations are comparable to what is found in air, which becomes apparent from the corresponding histograms for the step positions in the right panels. For positive electrode potentials, the step-edge mobility increases. In more detailed studies, by our group in collaboration with Kolb and coworkers, step fluctuations on Ag(111) electrodes were systematically investigated, as a function of the electrode potential [60]. More recently, we extended the investigation to the temperature dependence of G(t) [185]. Fig. 28(a) shows the time correlation function G(t) (3.21) as measured on a Ag(33,33,31) electrode (vicinal to the (111) plane with B-steps) at room temperature for different potentials<sup>40</sup> [60]. The step fluctuations and hence the correlation function G(t) increase with increasing potential. In contrast to the UHV-experiments on Ag(111) with B-steps, as discussed in Section 3, the time correlation function G(t) measured on the Ag(33,33,31) electrode is not a simple power law in the time t and the step-step distance L (3.22)-(3.31), but can be fitted to the function

<sup>39</sup> An electrode potential of -120 mV vs. SCE corresponds to -100 mV vs. Cu/Cu<sup>2+</sup> if the Cu<sup>2+</sup>-concentration is 0.1mM. At this potential, copper is deposited on the Ag(111) electrode. Dietterle et al. found, however, that Cu deposition is still slow at this potential and can be neglected in their measurements [48].

<sup>40</sup> The measurements were performed in two different electrolytes: For electrode potentials  $U_S < 0V$  and  $U_S \geq 0V$  vs. SCE, an electrolyte 0.05M Na<sub>2</sub>SO<sub>4</sub>+0.1mM H<sub>2</sub>SO<sub>4</sub> and 0.05M H<sub>2</sub>SO<sub>4</sub>+1mM CuSO<sub>4</sub> was used, respectively. Cu<sup>2+</sup>-cations improve the tip resolution [48] and the Cu<sup>2+</sup>-containing electrolyte is therefore used in the positive potential range. In order to avoid Cu deposition, a Na<sup>+</sup> containing electrolyte was used in the negative potential range.

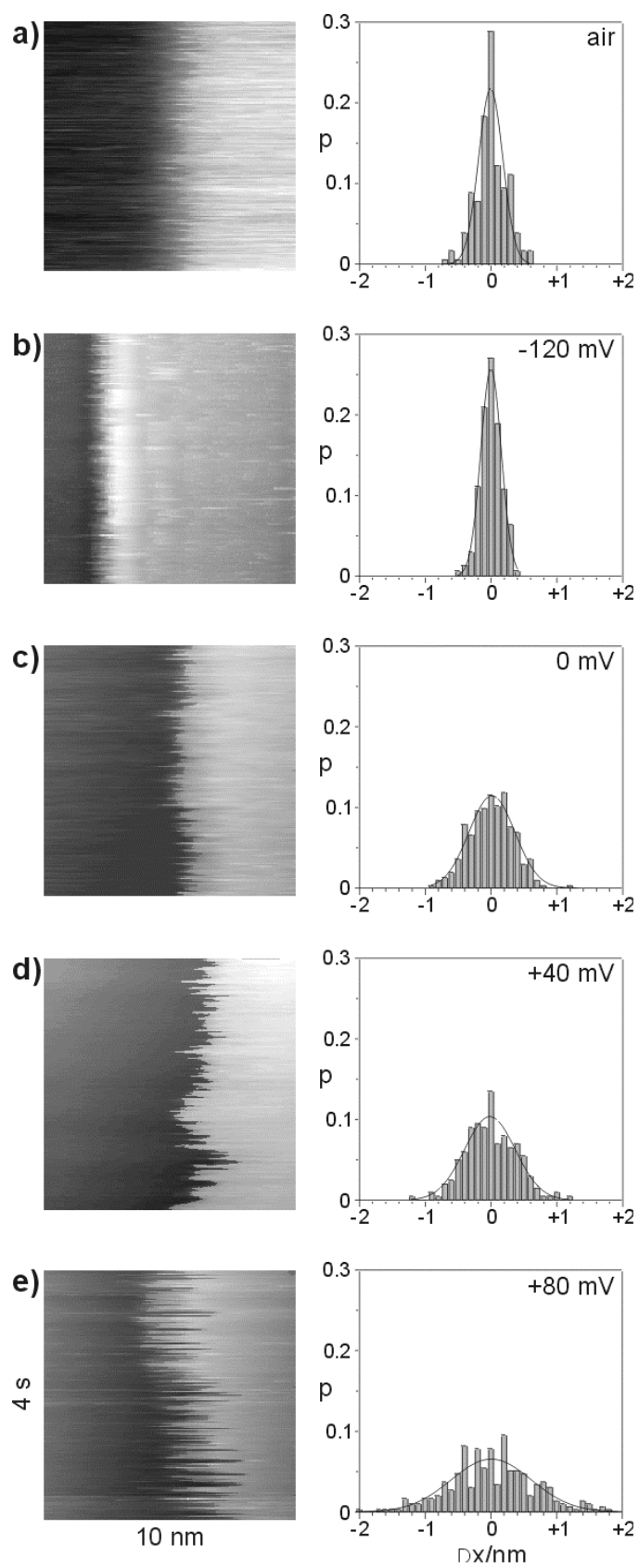


**Fig. 27:** Frizzy steps on a Ag(111) electrode in 0.05M H<sub>2</sub>SO<sub>4</sub>+0.1mM CuSO<sub>4</sub>. The frizziness increases with increasing electrode potential. The right panels show the probability distribution to find the step edge in a distance from the average step position in consecutive scan lines (after Dietterle et al. [48]).

$$G(t) = c_1 + c_2(U_S)t^\alpha. \quad (5.1)$$

Here,  $c_1$  is a constant independent of the electrode potential [60] and of temperature [185] (within the ranges investigated).  $c_2$  is a factor which depends on the electrode potential  $U_S$ . The physical origin of  $c_1$  is yet not understood. In addition to Ag(111) 1mM CuSO<sub>4</sub>+0.05 mM H<sub>2</sub>SO<sub>4</sub>, it has been observed also for Au(111) in 1mM KI + 50mM KClO<sub>4</sub> by McHardy et al. [186]. The constant contribution to  $G(t)$  may be due to tip-surface interactions, which is discussed at the end of this section. In the following, exclusively the time and potential dependent part of  $G(t)$  is discussed, i.e., the experimental data presented below are with the constant contribution  $c_1$  subtracted.

When (5.1) is fitted to the data in Fig. 28(a), time exponents  $\alpha=1/4$  for  $U_S < 0V$  vs. SCE and  $\alpha=1/2$  for  $U_S \geq 0V$  vs. SCE are found<sup>41</sup> [60]. For negative potentials, where  $G(t)$  obeys a  $t^{1/4}$ -law, the step fluctuations on the Ag(111) electrode at room temperature [60, 185] are of the same order of magnitude as on a Ag(111) surface in UHV at room temperature [42].

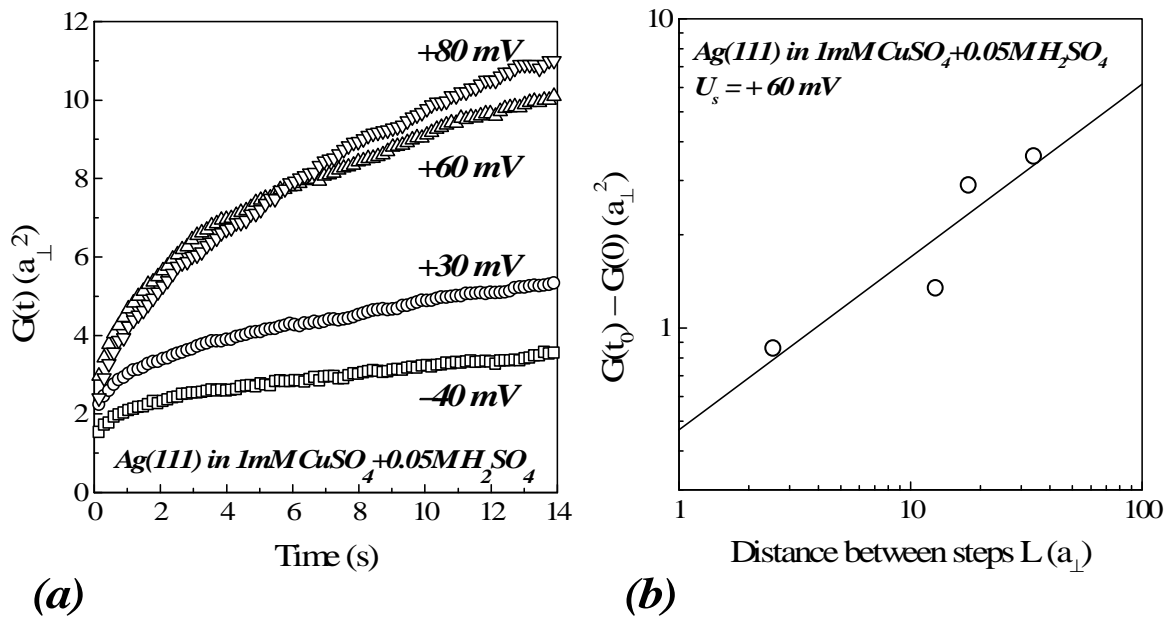


**Fig. 28:** (a) Time correlation function  $G(t)$  (3.21) as measured on a stepped Ag(111) electrode in 1mM CuSO<sub>4</sub>+0.05M H<sub>2</sub>SO<sub>4</sub> at various electrode potentials between  $-40$  and  $+80$ mV vs. SCE. (b) Step-step distance dependence of  $G(t)$  at constant time  $t_0=11$ s as measured at  $U_S=+60$ mV vs. SCE. The data is corrected for the constant contribution  $G(0)$  (5.1) at  $t=0$ . All data taken at room temperature [60].

<sup>41</sup> In order to obtain the time exponent from a fit according to (5.1), the fit to the experimental data must be performed very carefully. See [59, 60] for details.

The dominant mass transport involved in the step fluctuations for electrode potentials below and above  $U_S=0V$  vs. SCE, is unambiguously determined by measuring the dependence of  $G(t)$  on the step-step distance  $L$  [60]: In the  $t^{1/4}$ -regime below  $0V$  vs. SCE no dependence of  $G(t)$  on  $L$  was found. Hence, the dominant mass transport mechanism is edge diffusion (3.29)-(3.31). For  $U_S \geq 0V$  vs. SCE, the dependence of  $G(t)$  on the step-step distance  $L$  is shown in a log-log plot in Fig. 28(b).  $G(t)$  is  $L$ -dependent in this potential range and from the slope one finds a power law dependence with exponent  $\delta=1/2$  (solid line), which corresponds to case (i) (3.23). The electrode surface exchanges atoms with the surrounding liquid phase and the diffusion length is of the order of the mean terrace width. Although the data set as shown in Fig. 28(b) is small, one can safely discriminate the measured exponent from the other (possible) exponents  $\delta=0$  and  $-1/2$  (3.22), (3.24)-(3.26). Hence,  $G(t)$  obeys the correlation function

$$G(t) = \left( P_k \frac{c_t}{\tau_{sl}} \right)^{1/2} L^{1/2} t^{1/2}, \quad (5.2)$$

where  $P_k$  is the kink concentration (3.19),  $c_t$  is the adatom concentration on the terrace and  $\tau_{sl}$  is the average time of an atom on the surface before it dissolves into the liquid<sup>42</sup>. Comparison

of (5.1) and (5.2) yields  $c_2 = \left( P_k \frac{c_t}{\tau_{sl}} \right)^{1/2} L^{1/2}$ . The factor  $c_2$  can be expressed in Boltzmann

terms: It contains the kink concentration  $P_k \approx 2 \exp(-\varepsilon/k_B T)$  (3.19), and hence, the kink formation energy  $\varepsilon$ . Furthermore, the adatom concentration on the terrace is given by  $c_t \approx \exp(-E_{ad}/k_B T)$  ( $E_{ad}$  being the formation energy of an adatom from a kink site of a step onto the terrace). The average dissolution time  $\tau_{sl}$  of Ag atoms is given by  $\tau_{sl}^{-1} = v_0 \exp(-E^\ddagger/k_B T)$  ( $E^\ddagger$  being the activation enthalpy for Ag dissolution and  $v_0$  the pre-exponential factor). Hence, (5.2) can be rewritten as [60]

$$G(t) = (2v_0)^{1/2} e^{-\frac{E^\ddagger + E_{ad} + \varepsilon}{2k_B T}} L^{1/2} t^{1/2}. \quad (5.3)$$

---

<sup>42</sup> As a reminder, it is emphasized that all quantities are in atomic units (as in Section 3):  $G(t)$  is in units of  $a_\perp^2$ ,  $L$  in  $a_\perp$  and the kink and adatom concentration are dimensionless quantities. The tracer diffusion constant  $D_t$  and the pre-exponential factor  $v_0$  have the same unit  $s^{-1}$ .

In order to determine the activation energies of the dominant mass transport process, one may proceed via two different routes: Firstly, by measuring the temperature dependence of  $G(t)$  at constant electrode potential and secondly, by analyzing the potential dependence of  $G(t)$  at constant temperature. The latter procedure is, in particular, of interest if temperature dependent data is not available. In the following it is shown, that both methods provide consistent results.

We measured the temperature dependence of  $G(t)$  for Ag(19,19,17) (B-steps) in 1mM  $\text{CuSO}_4+0.05\text{M H}_2\text{SO}_4$  at +50mV vs. SCE [185]. At this potential, the system is close to the potential of rapid Ag dissolution into the electrolyte. Fig. 29 shows an Arrhenius plot of the correlation value  $G(t_0)$  at fixed time  $t_0=2\text{s}$ . In addition to the correction for the constant contribution of  $G(t)$  at  $t=0$ , the correlation value is scaled for the local step-step distance in the area where the measurements were performed. The activation energy of the dominant mass transport determined from the Arrhenius-plot in Fig. 29 is  $E_t=0.54\pm 0.11\text{eV}$  and the pre-exponential factor is  $6.3\times 10^{16\pm 4}\text{s}^{-1}$  [185]. According to (5.3), the activation energy  $E_t$  contains the kink formation energy  $\varepsilon$ , the adatom formation energy  $E_{\text{ad}}$  on the terrace and the activation enthalpy for dissolution  $E^\ddagger$ ; i.e.,  $2E_t=E^\ddagger+E_{\text{ad}}+\varepsilon$ . As described in Sections 6 and 7, the kink energy was experimentally determined by the comparison of the equilibrium shape of islands

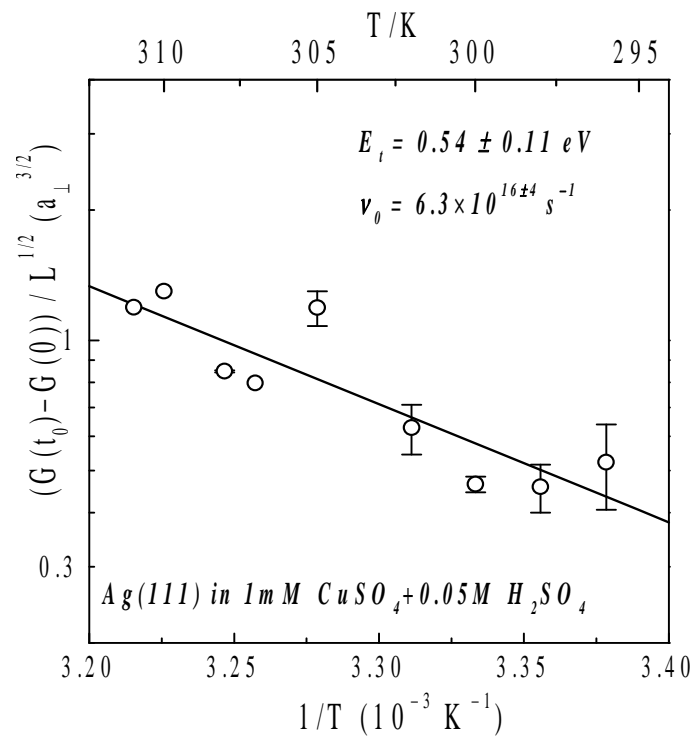


**Fig. 29.** Temperature dependence of the scaled time correlation value at  $t_0=2\text{s}$  on Ag(111) in 1mM  $\text{CuSO}_4+0.05\text{M H}_2\text{SO}_4$  at +50mV vs. SCE [185].

on the Ag(111) surface in 1mM CuSO<sub>4</sub>+0.05M H<sub>2</sub>SO<sub>4</sub> at +60mV vs. SCE to  $\varepsilon \approx 0.1\text{eV}$  [59]. Then, one finds for the sum of  $E^\ddagger$  and  $E_{\text{ad}}$  at  $U_S = +50\text{mV}$  vs. SCE [185]:

$$E^\ddagger(50\text{mV}) + E_{\text{ad}}(50\text{mV}) \approx 1.0 \pm 0.2\text{eV}. \quad (5.4)$$

The potential dependence of the time correlation value for Ag(111) in 1mM CuSO<sub>4</sub>+0.05M H<sub>2</sub>SO<sub>4</sub> is depicted in Fig. 30. There, the time correlation value  $G(t_0)$  at  $t_0=11\text{s}$  (circles) is plotted vs. the electrode potential [60, 61]. All data points were measured at room temperature. For negative potentials,  $G(t_0)$  is approximately potential independent within the (considerable) error bars. For positive potentials, however, below the potential of rapid Ag dissolution, a strong increase of  $G(t_0)$  is observed. The increase can be described by an exponential. From the detailed analysis of the exponential increase, one finds a second estimate for the sum of the activation enthalpy of Ag dissolution and the adatom formation energy, which is demonstrated in the following.

In the positive potential range, the measured time and step-step distance dependence of  $G(t)$  is indicative of exchange of atoms with the electrolyte (case (i), (3.23) and (5.3)). Haftel

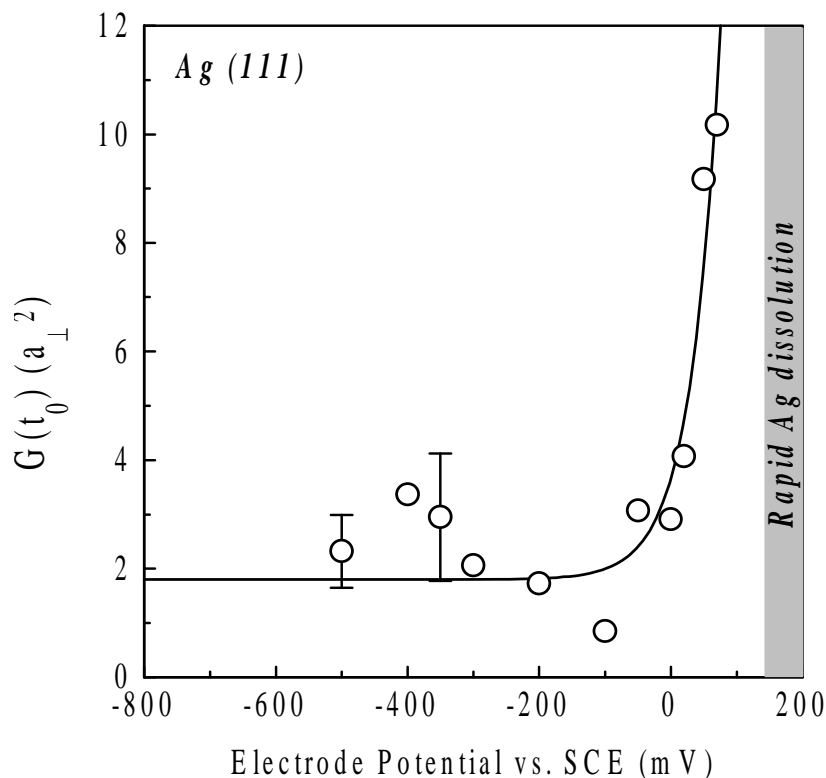


**Fig. 30.** Value of the time correlation function  $G(t)$  at  $t_0=11\text{s}$  vs. the electrode potential as measured on Ag(111) in 1mM CuSO<sub>4</sub>+0.05M H<sub>2</sub>SO<sub>4</sub> [60, 61].

and Einstein [187] used the *surface-embedded-atom-model* [188, 189] to determine the dependence of diffusion barriers on the charge deposited on the metal electrode by the electrical double layer. For Ag(111), they show that the diffusion barrier on the terrace is almost charge independent. The diffusion barrier along A-steps depends approximately linearly on the deposited charge. In the case of small variations in the charge (i.e., for small differences in the electrode potential), the functional dependence of the activation energies for atomic mass transport can be approximated by a linear function. In our experiments, the strong potential dependence of  $G(t)$  is limited to a small potential range of about 100mV. Therefore, we assume that the *activation* energies in (5.3) have a linear dependence on the potential  $U_S$ . Hence,

$$\begin{aligned} E^\ddagger(U_S) &= E^\ddagger(0) - \lambda_1 eU_S \\ E_{ad}(U_S) &= E_{ad}(0) - \lambda_2 eU_S \end{aligned} \quad (5.5)$$

The kink formation energy is assumed to be potential independent and of the same order as the kink energy measured on Ag(111) in UHV. This assumption is corroborated by the fact that in the  $t^{1/4}$ -regime of  $G(t)$  the fluctuations measured on Ag(111) in an electrolyte are of the same order of magnitude as measured on Ag(111) in UHV [42]. According to (3.29)-(3.31), the kink formation energy in electrolyte must therefore be approximately the same as in UHV ( $\varepsilon=90\text{meV}$  [88]). Since the kink energy at +60mV vs. SCE is  $\approx 100\text{meV}$  [59], it is reasonable to assume that  $\varepsilon$  is potential independent and about 100meV in the whole potential range.

Inserting (5.5) in (5.3) (with  $\varepsilon \approx 0.1\text{eV}$  [59] and  $\lambda = \lambda_1 + \lambda_2$ ) yields

$$G(t) = (2v_0)^{1/2} e^{-\frac{E^\ddagger(0)+E_{ad}(0)}{2k_B T} - \frac{\lambda eU_S - 0.1\text{eV}}{2k_B T}} L^{1/2} t^{1/2}. \quad (5.6)$$

In order to fit the experimental data in the positive potential range in Fig. 30 to (5.6), one has to consider also the contribution to  $G(t)$  in the negative potential range. There,  $G(t)$  is approximately constant. From the average of all data points for  $U_S < 0$  one obtains  $G(t) \sim 1.8 a_\perp^2$  in the negative potential range. The solid line in Fig. 30 is a fit to

$$G(t) = 1.8 + (2v_0)^{1/2} e^{-\frac{E^\ddagger(0)+E_{ad}(0)}{2k_B T} - \frac{\lambda eU_S - 0.1\text{eV}}{2k_B T}} L^{1/2} t^{1/2}. \quad (5.7)$$

The step-step distance was set to the nominal value of  $81(a_{\perp})$  for a Ag(33,33,31) plane and  $t=11$ s. For the pre-exponential factor, one may use the value of  $\nu_0=6.3\times 10^{16\pm 4}$  s<sup>-1</sup> as determined from the temperature dependent analysis<sup>43</sup>. Then, the fit parameters are  $\lambda$  and the sum  $E^{\ddagger}(0) + E_{\text{ad}}(0)$ . From the best fit, one finds

$$\begin{aligned}\lambda &= 1.08 \pm 0.28 \\ E^{\ddagger}(0) + E_{\text{ad}}(0) &= 1.0 \text{ eV}\end{aligned}\tag{5.8}$$

Note, that the sum of the energies  $E^{\ddagger}(0) + E_{\text{ad}}(0)$  at  $U_{\text{S}}=0$  merely serves as a reference point to define the linear relation between electrode potential and energy. If one had used another reference electrode, which is shifted by  $\Delta U$  with respect to SCE, one would have determined the same number for  $E^{\ddagger}(\Delta U) + E_{\text{ad}}(\Delta U)$  at an electrode potential  $\Delta U$  rather than at  $U_{\text{S}}=0$ <sup>44</sup>.

The value of the sum of the activation enthalpy for dissolution and the adatom creation energy at  $U_{\text{S}}=0$  ( $E^{\ddagger}(0) + E_{\text{ad}}(0) = 1.0$  eV [60]) is in good agreement with the value obtained from the temperature dependent analysis at +50mV vs. SCE ( $E^{\ddagger}(50\text{mV}) + E_{\text{ad}}(50\text{mV}) \approx 1.0 \pm 0.2$  eV [185]). Therefore, the potential dependent analysis of the time correlation function can be used to determine the activation energies of the dominant transport processes where temperature dependent studies are not available. However, in this case, the pre-exponential factor  $\nu_0$  must be chosen appropriately in order to determine the activation energies. Usually, one assumes  $\nu_0$  to be of the order of  $\nu_0 \sim k_{\text{B}}T/h$  ( $h$  being the Planck constant) [190], which corresponds to  $\nu_0 \sim 10^{13}$  s<sup>-1</sup>. Real pre-exponential factors, however, may considerably deviate from this value as does the value obtained here. The deviation may be caused by the higher number of degrees of freedom for the ions in solution due to the solvation shell [191].

It is still controversial, whether  $\lambda$  may be interpreted as the *cathodic transfer coefficient*, which is related to the difference in the Gibbs activation energies for cathodic and anodic processes at the electrodes, and hence, defines the relative contributions of the cathodic and anodic current to the electrochemical current (see [10]). The cathodic transfer coefficient lies

<sup>43</sup> In [60], a pre-exponential factor of  $\nu_0=10^{13}$  s<sup>-1</sup> was used. Therefore, the energies determined in [60] differ from the ones presented in this review.

<sup>44</sup> In other words, the sum of the energies is 1.0eV at 150mV below the dissolution potential of silver in this electrolyte.

in the range 0 to 1. For the two extreme cases,  $\lambda=0$  and  $\lambda=1$ , the cathodic and anodic current, respectively, is potential independent, whereas the other current depends on the electrode potential. In a real system, however,  $\lambda$  is in between these two extremes. In experiment,  $\lambda$  is often found to be of the 0.5, i.e., the Gibbs activation energies for cathodic and anodic processes are about equal. Hence, an experimental value of  $\lambda=1.08\pm 0.28$  (5.8) would indicate the contribution of two activated mass transport processes as was also assumed in (5.5). Concern is raised by the fact that the cathodic transfer coefficient is related to *activation* energies as discussed before. However,  $E_{ad}(0)$ , as used in (5.5), is a *formation* energy, which should, in a first approximation, not be affected by the electrode potential. On the other hand, it is reasonable to assume that a local dipole moment is associated with an adatom on the terrace, due to the change in the electron-charge distribution at the interface. The energy of such a dipole moment depends on the electric field of the double layer, and hence, the formation of an adatom should depend on the electrode potential.

Although there are still some difficulties to be solved, in order to obtain reliable values for activation energies from temperature and potential dependent measurements in the electrochemical cell, the recent experiments show that it is, in principle, possible to measure activation barriers for the mass transport at the solid/liquid interface.

### 5.2. Step fluctuations on Cu(100) and (111) electrodes

On Cu(100), we studied the potential dependence of step fluctuations in 0.05M H<sub>2</sub>SO<sub>4</sub> in collaboration with Kolb and coworkers [59]. The time dependence of the step correlation function is that of a  $t^{1/4}$ -law for electrode potentials between -590 and -490 mV vs. SCE and that of a  $t^{1/2}$ -law between -490 and -390 mV vs. SCE. In the more negative potential range, no dependence of  $G(t)$  on the step distance  $L$  is found. Hence, the dominant mass transport mechanism below -490 mV is edge diffusion. For higher potentials,  $G(t)$  depends on the terrace width  $L$ . Fig. 31(a) is a log-log plot of the correlation value  $G(t_0)$  at  $t_0=2s$  vs.  $L$  for an electrode potential  $U_s = -390mV$  vs. SCE. The step-step distance dependence is that of a  $L^{-1/2}$ -law. According to case (ii) in Section 3.3.2, the dominant mass transport on Cu(100) above -490mV vs. SCE is rapid exchange between neighboring steps (3.24). Fig. 31(b) shows  $G(t)$  as a function of the electrode potential for a reference time  $t_0=2s$  and a step-step distance  $L=50(a_{\perp})$  [59]. For comparison, the data is plotted on the same potential scale as for Ag(111) in Fig. 30. The increase of the fluctuations occurs well below the rapid dissolution of Cu into the electrolyte. The solid line is a fit with an exponential analog to what has been discussed for the Ag(111) electrode. According to case(ii), (3.24), the energy related quantities contributing to  $G(t)$  are the kink concentration (3.19)  $P_k \approx 2\exp(-\varepsilon/k_B T)$  and the equilibrium

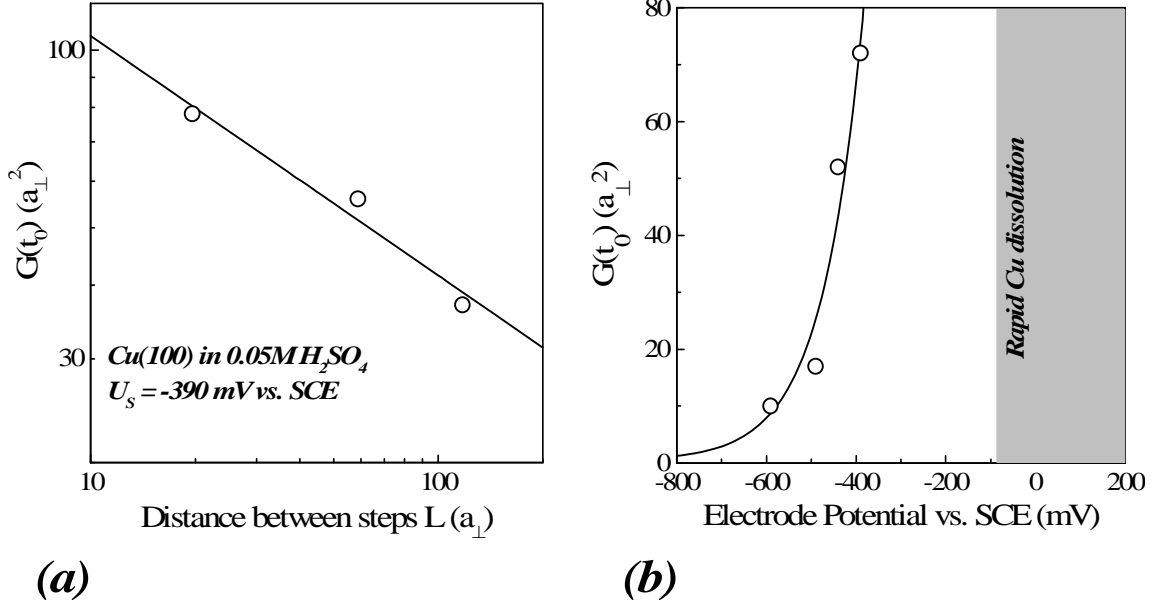


**Fig. 31.** (a) Step-step distance dependence of  $G(t)$  for  $t_0=2s$  on  $Cu(100)$  in  $0.05M H_2SO_4$  at  $-390mV$  vs. SCE. (b) Potential dependence of the corresponding data [59].

adatom concentration on the terrace which is given by  $c_t \approx \exp(-E_{ad}/k_B T)$ , where  $E_{ad}$  is the adatom formation energy from kink sites onto the terrace. The diffusion constant  $D_t$  contains the diffusion barrier on the terrace,  $D_t = v_0 \exp(-E_{diff}/k_B T)$ . As before, the kink energy is assumed to be independent on the electrode potential, while the diffusion barrier on the terrace and the adatom formation energy are assumed to be potential dependent. We use a linear ansatz for the potential dependence of the energies again:

$$\begin{aligned} E_{diff}(U_S) &= E_{diff}(0) - e\lambda_1 U_S \\ E_{ad}(U_S) &= E_{ad}(0) - e\lambda_2 U_S \quad . \\ \lambda &= \lambda_1 + \lambda_2 \end{aligned} \quad (5.9)$$

$E_{diff}(0)$  and  $E_{ad}(0)$  are the diffusion barrier on the terrace and the adatom formation energy from a kink site at  $U_S=0$ , respectively. Inserting (5.9) in (3.24), one obtains [59]

$$G(t) = \sqrt{\frac{2v_0 t}{L}} e^{-\frac{E_{diff}(0) + E_{ad}(0) + \varepsilon}{2k_B T}} e^{\frac{\lambda e U_S}{2k_B T}} \quad (5.10)$$

No temperature dependent data for  $Cu(100)$  in electrolyte is available. Hence, the pre-exponential factor  $v_0$  is assumed to be of the order of  $10^{13} s^{-1}$ . In order to fit (5.10) to the

experimental data, we determined the contribution to  $G(t)$  in the limit of very low potentials and find  $G(t) \sim 0.4(a_{\perp}^2)$ . Hence, the solid line in Fig. 31(b) is a fit to

$$G(t) = 0.4 + \sqrt{\frac{2v_0 t}{L}} e^{-\frac{E_{\text{diff}}(0) + E_{\text{ad}}(0) + \varepsilon}{2k_B T} - \frac{\lambda e U_S}{2k_B T}}, \quad (5.11)$$

where  $L=50(a_{\perp})$  and  $t=2s$ . From the best fit one finds  $\lambda=0.57$  and  $E_{\text{diff}}(0) + E_{\text{ad}}(0) + \varepsilon = 0.28\text{eV}$  [59]. So far, no measurements of the kink formation energy  $\varepsilon$  on Cu(001) in electrolyte has been performed. In UHV,  $\varepsilon$  has been determined to  $\varepsilon=0.128\text{eV}$  [40, 41]. A typical activation energy for diffusion on Cu(100) in UHV is  $\sim 0.3\text{-}0.5\text{eV}$  (see also Table 7). With  $\varepsilon=0.13\text{eV}$  [40, 41] and  $E_{\text{diff}}(0)$  between 0.3 and 0.5eV one obtains  $E_{\text{ad}}(0) < 0$ ! At first glance, this negative energy may appear surprising. One must remember, however, that  $E_{\text{ad}}(0)$  refers to the potential  $U_S=0\text{mV}$  vs. SCE. As seen from Fig. 31,  $U_S=0$  is well into the regime of rapid dissolution of Cu(100), which means that enthalpy is gained by creating  $\text{Cu}^{2+}$ -ions and, presumably, enthalpy is also gained in the intermediate process of forming adatoms on the terraces.

In contrast to Cu(001) in sulfuric acid, where the step dynamics increase with more positive electrode potential, on Cu(111) edge diffusion may be inhibited by the presence of sulfate, as discussed by Wilms et al. [192], who observed a decrease in step fluctuations, due to specific adsorption of sulfate and the formation of a  $(\sqrt{3} \times \sqrt{7})$  ordered sulfate overlayer.

Considerable attention was devoted recently to the dynamics of morphologic changes on Cu(001) and (111) surfaces in chloric acid solutions [56-58, 112, 192-194]. The special interest is, in particular, based on the restructuring of these surfaces during specific adsorption of chloride: For negative electrode potentials, steps are preferentially oriented along the dense  $\langle 110 \rangle$ -direction of fcc metals. Therefore, kinks in the equilibrium step structure are exclusively thermally excited kinks. For positive potentials, specific adsorption of chloride from the electrolyte occurs and  $(\sqrt{3} \times \sqrt{3})R30^\circ$  and  $c(2 \times 2)$  ordered structures are formed on Cu(111) [56, 195, 196] and Cu(100) [197-199], respectively. In both cases, the formation of the ordered structure is accompanied by a faceting of the steps, with facets preferentially oriented along  $\langle 211 \rangle$  and  $\langle 100 \rangle$ , respectively. These steps are 100% kinked, as illustrated in Fig. 32. During the process of step restructuring, rapid mass transport is observed in STM

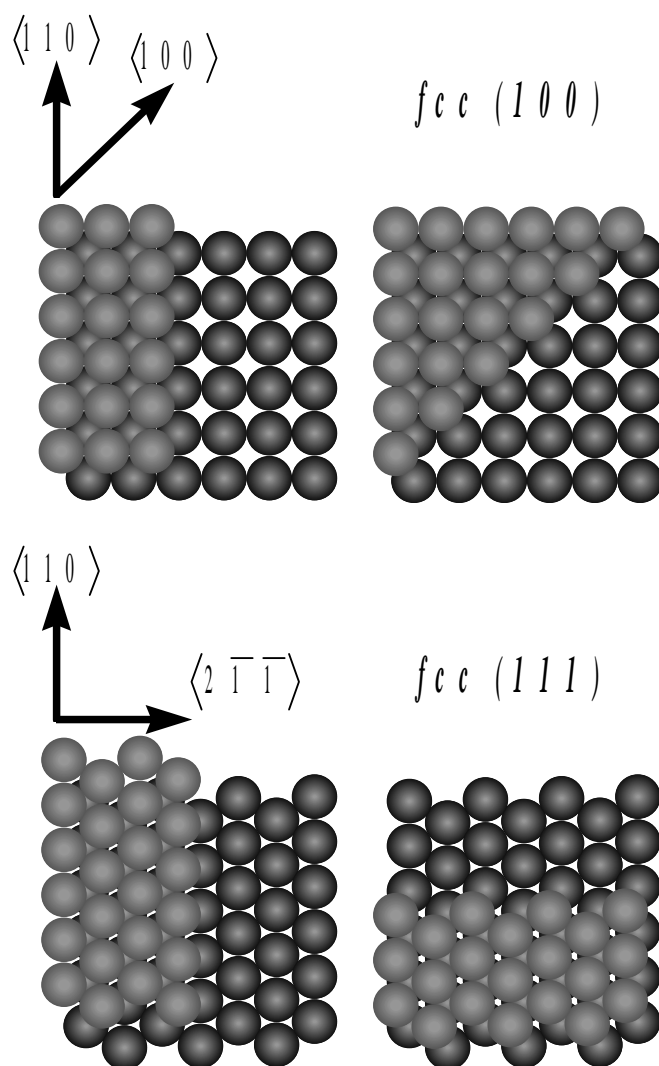


**Fig. 32.** Model of dense and 100% kinked steps on fcc (100) and (111) surfaces. For simplicity, the chloride superstructure is not included. The model displays merely the local step structure of the substrates before and after step facetting occurs.

images, which becomes evident from an enhanced fluctuation amplitude in the step profile and by a pronounced frizzy appearance of the steps [56, 193, 194]. Broekmann et al. [56] showed that for Cu(111) in 10mM HCl the step frizziness increases with increasing potential, when the surface is covered by a  $(\sqrt{3} \times \sqrt{3})R30^\circ$  chloride structure. In Fig. 33, STM images of a monatomic step along the dense direction of the  $(\sqrt{3} \times \sqrt{3})R30^\circ$  structure (corresponds to the  $\langle 2\bar{1}\bar{1} \rangle$ -direction with respect to the Cu substrate) at two different electrode potentials are shown. At (a) -650mV vs. Hg/Hg<sub>2</sub>SO<sub>4</sub> the step is almost straight despite some sudden jumps in the step position, due to kink motion. Increasing the potential to (b) -550mV vs. Hg/Hg<sub>2</sub>SO<sub>4</sub> gives rise to a significantly enhanced fluctuation amplitude [56]. We demonstrated recently that, for stepped Cu(111) in 1mM and 10mM HCl, the step fluctuations

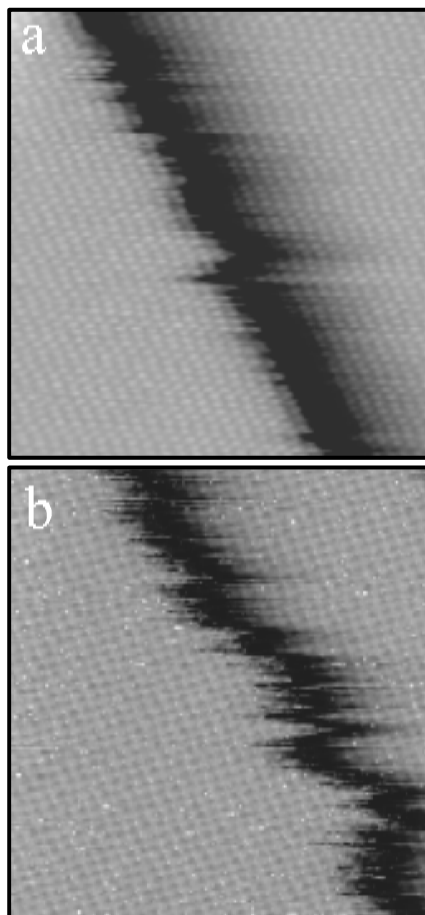


**Fig. 33.** STM images ( $10.5 \times 10.5 \text{ nm}^2$ ) of a monatomic high frizzy step on Cu(111) in 10mM HCl at (a)-650mV and (b)-550mV vs. Hg/Hg<sub>2</sub>SO<sub>4</sub> (after Broekmann et al. [56]).

are independent of  $U_S$  in the potential range, where chloride is specifically adsorbed, but does not form an ordered overlayer [112]. Fig. 34 shows the value of the time correlation function  $G(t)$  at  $t_0=2\text{s}$  for Cu(39,39,37) in 1mM HCl at 305K as a function of the electrode potential. The (39,39,37) plane is vicinal to the (111) surface with B-steps and the mean terrace width is  $84.7\text{\AA}$  (corresponding to  $38.3 a_{\perp}$ ). The step fluctuations are independent of the electrode potential. On the vicinal Cu(111) surface, facetting of the steps started between around  $-100\text{mV}$  vs. SCE. At  $-120\text{mV}$ , the steps remained unfaceted during the experimental observation. Hence, the data point at  $-120\text{mV}$  vs. SCE was measured without an ordered chloride layer on the Cu(111) terraces. No experimental results on the potential dependence of  $G(t)$  for more positive potentials are available, because statistical relevant results for the faceted steps are rather difficult to obtain<sup>45</sup>. Measurements of  $G(t)$  on stepped Cu(111) in

<sup>45</sup> When the steps are faceted, the step edges reveal a zig-zag structure and neighboring step segments have different orientations. Therefore, to obtain statistical relevant data on  $G(t)$ , the data must correspond to one and only one segment of the faceted step. Hence, the thermal drift of the microscope must be practically zero. If the

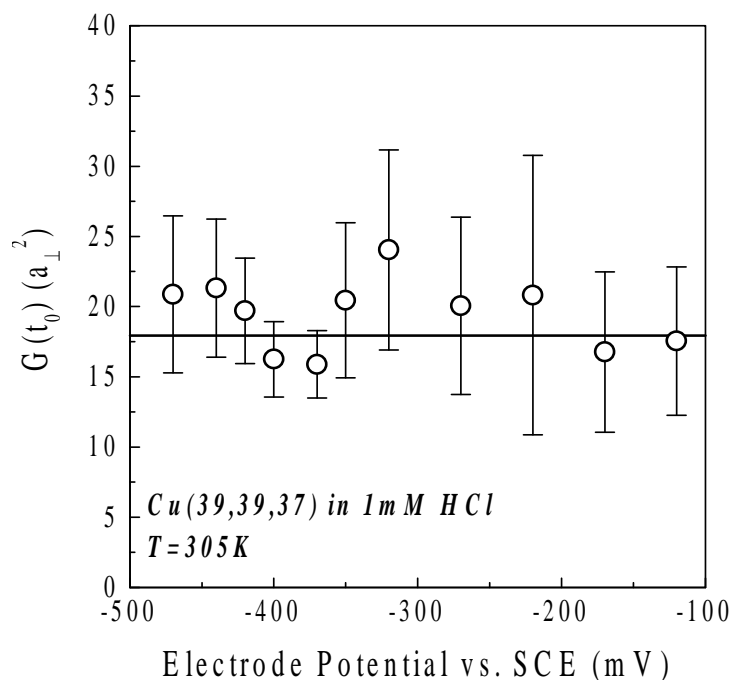


**Fig. 34.** Potential dependence of the time correlation value  $G(t)$  at  $t_0=2s$  measured on stepped Cu(111) (with B-steps) in 1mM HCl at 305K [112].

10mM HCl showed that  $G(t)$  is also independent on the electrode potential below -250mV vs. SCE for higher chloride concentrations. Here, faceting of the steps occurred at around -250mV, such that no data at higher potentials were obtained in this case.

The presence of chloride on the Cu(111) surface, which is specifically adsorbed from the electrolyte (in 1mM HCl for electrode potentials above -500mV vs. SCE), affects the dominant mass transport mechanism on Cu(111) surfaces. Fig. 35 shows the time correlation function  $G(t)$  measured on Cu(39,39,37) at 298K and  $U_S = -420mV$  vs. SCE as circles [112]. The time dependence of  $G(t)$  is that of a power law (with no constant contribution at  $t=0$ ). The solid curve is a fit to a power law with time exponent  $1/3$ . For comparison, least square fits with time exponents  $1/2$  (dotted) and  $1/4$  (dashed) are shown. Obviously, the experimental data is in excellent agreement with a time exponent  $1/3$ . The time exponent  $1/3$  is found for the electrode potential range between -500 and -100mV vs. SCE. According to (3.27), a  $t^{1/3}$ -dependence of  $G(t)$  is evidence for a dominant mass transport mechanism, where atoms are exchanged between steps and terraces and detachment/attachment at steps is fast compared to the diffusion on the terrace (case(iv)). Cu(111) in HCl is the only experimental system where a time exponent  $1/3$  has been observed so far.

---

drift is non-zero, a shift of the scan area to an adjacent step segment with different orientation may occur which introduces large errors into the analysis of  $G(t)$ .

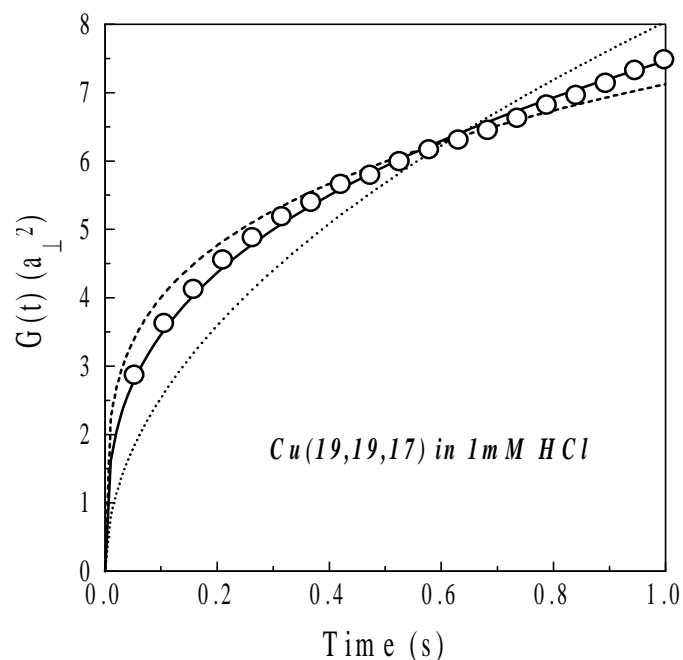


**Fig. 35.** Time correlation function  $G(t)$  measured on stepped Cu(111) (with B-steps) in 1mM HCl at -420mV vs. SCE and 298K. The solid curve is a fit with a time exponent 1/3. The dashed and dotted curves are fits with time exponents 1/4 and 1/2, respectively [112].

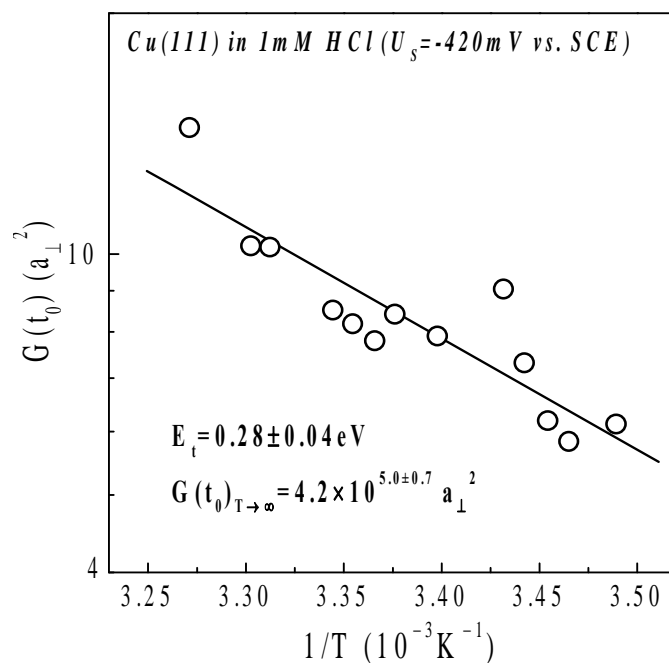


**Fig. 36.** Arrhenius-plot of the time correlation value  $G(t_0)$  at  $t_0=1$ s for Cu(111) in 1mM HCl. The electrode potential was set to -420mV vs. SCE [112].

The activation energy of the mass transport is determined from temperature dependent studies of  $G(t)$ . Fig. 36 shows an Arrhenius-plot of the time correlation value  $G(t_0)$  at fixed time  $t_0=1$ s and constant electrode potential  $U_s = -420$ mV vs. SCE. The total activation energy

$E_t$  and the value of  $G(t_0)$  for  $T \rightarrow \infty$  are  $E_t = 0.28 \pm 0.04 \text{ eV}$  and  $G(t_0) \Big|_{T \rightarrow \infty} = 4.2 \times 10^{5.0 \pm 0.7} a_{\perp}^2$ , respectively. The activation energy contains the kink energy  $\varepsilon$ , the activation energy for adatom creation from kink sites onto the terrace  $E_{\text{ad}}$  and the surface diffusion barrier  $E_{\text{diff}}$  (3.27). Assuming the kink energy on a Cu(111) electrode in chloric acid to be of the same order than in UHV (101 meV [88, 90]), one obtains  $E_{\text{ad}}(-420 \text{ mV}) + E_{\text{diff}}(-420 \text{ mV}) = 0.64 \pm 0.12 \text{ eV}$ , which is comparable to the result of  $E_{\text{ad}} + E_{\text{diff}} = 0.76 \text{ eV}$ , we determined for Cu(111) in UHV measurements [200, 201] and to EMT calculations by Stoltze ( $E_{\text{ad}} + E_{\text{diff}} = 0.767 \text{ eV}$  [81], see also Table 7). Using (3.27), the pre-exponential factor for terrace diffusion is determined to  $v_0 = 1.5 \times 10^{16 \pm 2} \text{ s}^{-1}$ . Similar to what is found for Ag(111) in 0.05M  $\text{H}_2\text{SO}_4 + 0.1 \text{ mM CuSO}_4$  (but for a different process) [60], this value is considerably higher than the typical value for pre-exponential factors of  $10^{13} \text{ s}^{-1}$  [190].

### 5.3. Step fluctuations on Au(111) electrodes

Ordered overlayers formed by sulfate and chloride, as discussed before for Cu(111), are also known for Au(111) electrodes: In 0.1M  $\text{H}_2\text{SO}_4$ , the formation of a  $(\sqrt{3} \times \sqrt{7})$ -sulfate superstructure is observed around +785mV vs. SCE [202]. On Au(111) in 1mM HCl+0.1M  $\text{H}_2\text{SO}_4$ , a  $(\sqrt{3} \times \sqrt{3})R30^\circ$  chloride adlayer is created around +690mV vs. SCE [203]. Sulfate and chloride are specifically adsorbed on Au(111) already at lower potentials, however, no ordered superstructures are formed. The specific adsorption of sulfate or chloride is accompanied by the lifting of the *herring bone* surface reconstruction [204]. The lifting of the surface reconstruction has a decisive influence on the dominating mass transport processes. Fluctuations of B-steps on Au(111) in 0.1M  $\text{H}_2\text{SO}_4$  with no HCl

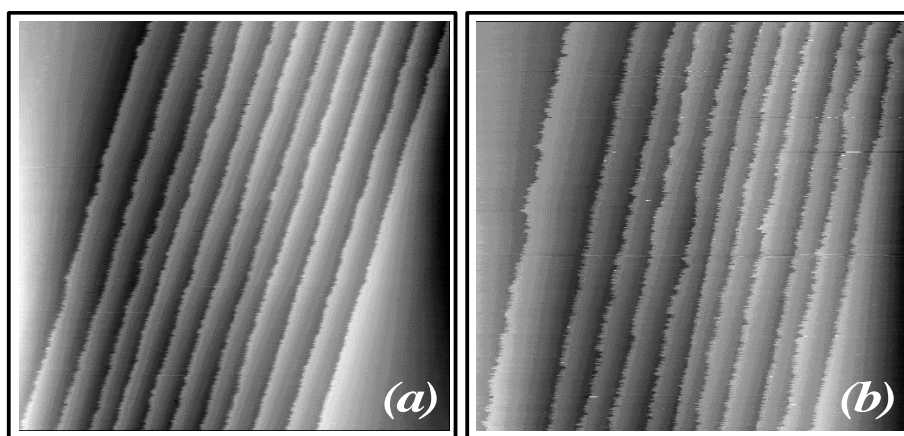


**Fig. 37.** STM images ( $150 \times 150 \text{ nm}^2$ ) of a stepped area on a Au(111) electrode in 0.1M  $\text{H}_2\text{SO}_4 + 5 \text{ mM HCl}$  at (a) 0mV and (b) +400mV vs. SCE [62].

added and with various concentrations of HCl were studied by Giesen and Kolb [62]. Fig. 37 shows STM images of B-steps oriented along  $\langle 110 \rangle$  on Au(111) in 0.1M  $H_2SO_4 + 5mM$  HCl at (a) 0mV and (b) +400mV vs. SCE. The fluctuation amplitude increases with increasing potential and so does the time correlation function  $G(t)$  (circles and squares in Fig. 38). For electrode potentials below +300mV vs. SCE,  $G(t)$  obeys a  $t^{1/2}$ -law (dashed lines in Fig. 38), whereas for electrode potentials above +300mV, the time exponent is 1/4 (solid lines). The transition in the time exponent is observed for all HCl containing electrolytes used in this study. Fig. 39 shows the value of the time correlation function at  $t_0=1s$  for +250 and +600mV vs. SCE on Au(111) in 0.1M  $H_2SO_4 + 0.5mM$  HCl as a function of the step-step distance. The time correlation function  $G(t)$  is independent of the step-step distance for all electrode potentials and for all HCl concentrations. Hence, the dominant mass transport mechanisms below +300mV is exchange of transport species between steps and terraces with fast terrace diffusion (case (iii), (3.25), (3.26)). Above +300mV, edge diffusion (case (vi), (3.29), (3.30)) takes over. The transition from one mass transport to the other occurs approximately at the electrode potential, where chloride is specifically adsorbed on Au(111) and the surface reconstruction is lifted [204]. Table 4 summarizes the time laws of  $G(t)$  found on Au(111) in the different potential ranges and for the various electrode conditions.

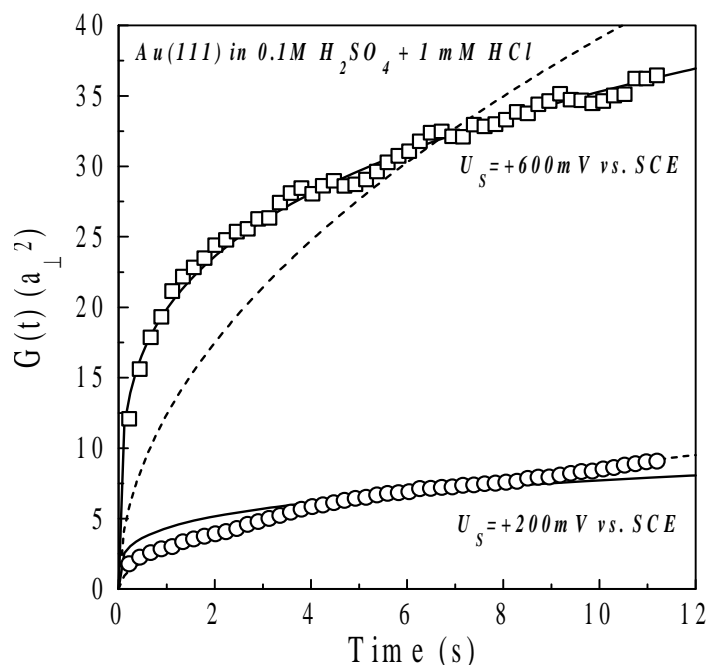


**Fig. 38.** Room temperature measurement of the time correlation function  $G(t)$  on Au(111) in 0.1M  $H_2SO_4 + 1mM$  HCl at +200 and +600mV vs. SCE. The solid and dashed curves are fits to a power law with time exponents 1/4 and 1/2, respectively [62].

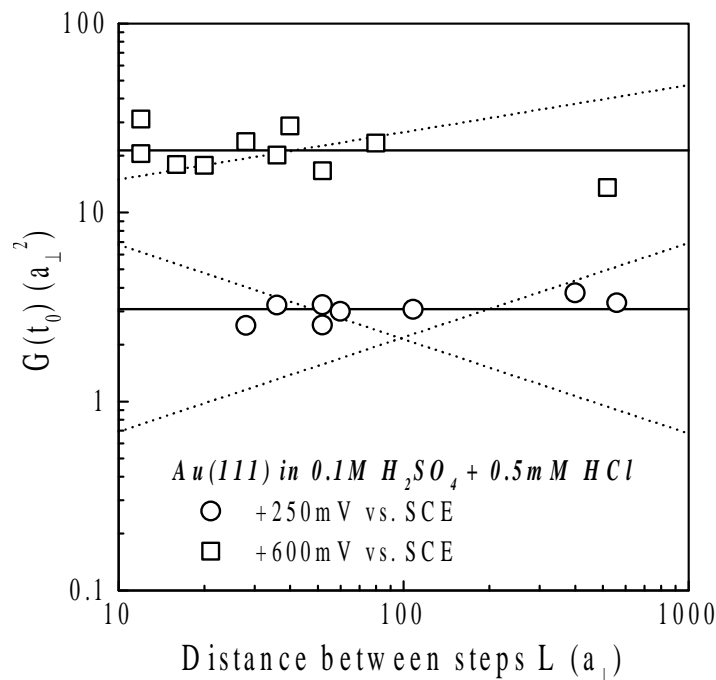


**Fig. 39.** Step-step distance dependence of  $G(t)$  at  $t_0=1s$  for  $U_S = +250$  and  $+600mV$  vs. SCE ( $T=300K$ ). The dotted lines serve as guide to the eye for possible exponents  $\delta = \pm 1/2, 1/4$  [62].

In the following, the transition from terrace diffusion at negative potentials to edge diffusion at positive potentials is discussed in the context of the experimental facts [62]: The specific adsorption of chloride at positive potentials most likely changes the diffusion barrier along steps and also the kink creation energy. In addition, the species which mediate the mass transport may change when chloride is specifically adsorbed. Gold adatoms, specifically adsorbed chloride anions at the steps, or a  $Au-Cl^-$  complex, may serve as the diffusing species in the potential range above  $+300mV$ . A possible change of the species mediating the mass transport, as the potential varies, may have a dramatic effect on the subtle energy balance, such that edge diffusion becomes more favorable than terrace diffusion for positive potentials.

The kink formation energy, as well as the kink mobility, may also be different for steps on a reconstructed surface (at negative potentials) compared to steps on the unreconstructed surface (at positive potentials). This difference in the kink formation energy may also contribute significantly to the change in the energetics on the  $Au(111)$  surface, and hence, to the transition in the dominant mass transport. The reconstruction lines cross the steps perpendicularly and are not influenced by the existence of kink sites, which is also observed for  $Au(111)$  in UHV, as nicely demonstrated in an STM study by Repain et al. [205]: Kink sites at the step edges correspond to sites, where the reconstruction lines cross the step. The

	0.1M H <sub>2</sub> SO <sub>4</sub>			0.1M H <sub>2</sub> SO <sub>4</sub> +1mM HCl		
Electrode potential mV vs. SCE	<+300	+300<U<+789	+789	<+300	+300<U<+690	+690
Specific adsorbed anion	none	SO <sub>4</sub> <sup>2-</sup>	SO <sub>4</sub> <sup>2-</sup>	none	Cl <sup>-</sup>	Cl <sup>-</sup>
Time and step-step distance dependence of G(t)	t <sup>1/2</sup>	t <sup>1/4</sup>	---	t <sup>1/2</sup>	t <sup>1/4</sup>	---
Reconstruction	Herring bone	none	none	Herring bone	none	none
Superstructure	none	none	$\sqrt{3} \times \sqrt{7}$	none	none	$(\sqrt{3} \times \sqrt{3})R30^\circ$

**Table 4.**

Summary of the measured time and step-step distance dependence of G(t) on Au(111) in various electrolytes and for different electrode conditions. Note that G(t) is independent of the step-step distance L (see also Fig. 39).

creation of kink sites and, in particular, their hopping along steps may be energetically unfavorable, because the atomic configuration around them must follow the reconstruction lines. The creation and the diffusion of free adatoms on the terrace, however, could therefore be energetically more favorable than the kink creation, since no specific restrictions concerning the atomic configuration are to be fulfilled on the reconstructed terrace.

A question of concern is how adatoms are exchanged between steps and terraces? Previous STM studies on the reconstructed Ru(0001) surface after Cu deposition by Schmid et al. [206] and of the reconstructed Au(111) surface under UHV conditions by Bartelt and coworkers [207] showed that atoms are exchanged between the dislocation cores and the free adatom sea with a high rate. The adatom creation is facilitated at the reactive elbow sites of the Herring bone reconstruction, due to a local increase of bond length between Cu and Au atoms, respectively. The high atom exchange rate at the dislocation cores, however, is accompanied by a high mobility of dislocation lines, which so far no has not been reported for Au(111) surfaces in electrolyte.

The transition from a  $t^{1/2}$  at low potentials to a  $t^{1/4}$  law at higher potentials may also be associated with the change of the atom density in the surface layer, due to the lifting of the reconstruction. In the reconstructed phase below +300mV vs. SCE, the density of surface atoms is about 4% higher than in the unreconstructed phase above +300mV vs. SCE. Meyer et al. [208] studied the mobility of Ni adatoms on Ru(0001) in UHV and showed that the energy barrier for adatom diffusion on the surface *decreases* with *increasing* density of atoms in the surface layer. For the case of Ag diffusion on Ag(111), Ratsch et al. [209] demonstrated in their calculations that the diffusion barrier increases with increasing lattice constant. A similar trend may be expected for Au adatom diffusion on Au(111) in electrolyte: In the dense reconstructed phase, the diffusion barrier on the surface may be smaller compared to the less dense unreconstructed phase. This faster terrace diffusion on the reconstructed phase at  $U_S < +300\text{mV vs. SCE}$  should favor the fluctuation process, due to exchange with the terraces with fast terrace diffusion, and hence, a  $t^{1/2}$ -law should be observed in agreement with the experimental result.

Since chloride anions in the electrolyte enhance the adatom mobility on metal electrodes [181-184], it is interesting to investigate the dependence of step fluctuations on Au(111) on the chloride concentration. Fig. 40 shows the potential dependence of the time correlation value  $G(t_0)$  at  $t_0=1\text{s}$  measured on Au(111) in 0.1M  $\text{H}_2\text{SO}_4$  with different amounts of HCl added [62]: When no HCl is added (triangles), the step fluctuations are almost potential independent and remain small. For a small amount of HCl (0.01mM), the fluctuations

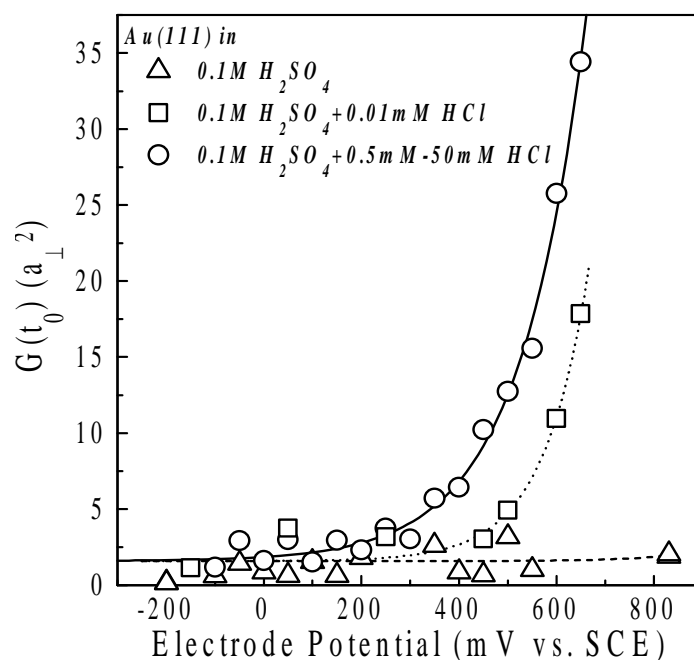


**Fig. 40.** Potential dependence of  $G(t)$  at  $t_0=1s$  for Au(111) in various electrolytes [62].

increase for electrode potentials above +300mV vs. SCE (squares). For Au(111) in chloric acid, the increase of the fluctuations is expected to shift to more negative potentials by about 60mV per decade of higher HCl concentration [210]. This shift is, indeed, observed when 0.5mM HCl is added. The increase of the fluctuations occurs now at about +200mV vs. SCE. When even more HCl is added to the electrolyte, however, no further shift to more negative electrode potentials is found. The data points measured with 0.5mM up to 50mM HCl added to the electrolyte fall onto the same curve and the fluctuations appear to be saturated (circles). This saturation is attributed to a saturation of step sites, where chloride is specifically adsorbed. When further HCl is added, chloride occupies sites on the terraces and has no further influence on the step fluctuations, because edge diffusion is the dominant mass transport mechanism in the potential range above +300mV vs. SCE [62].

A quantitative analysis of the potential dependence of  $G(t)$  yields reasonable estimates for the activation barriers involved in the dominant mass transport mechanisms [62]: In the potential range below +300mV vs. SCE, the dominant mass transport is terrace diffusion and the time dependence of  $G(t)$  is that of a  $t^{1/2}$ -law (case(iii), (3.26)). Using (3.26), the time correlation function for steps on Au(111) in 0.1M  $H_2SO_4+x$  mM HCl can be written as

$$G(t) = \sqrt{\frac{2\nu_0}{\pi}} e^{-\frac{2\varepsilon + E_{\text{ad}}^\ddagger}{2k_{\text{B}}T}} t^{1/2}, \quad (5.12)$$

where  $\varepsilon$  is the kink formation energy.  $E_{\text{ad}}^\ddagger$  is the activation energy for the creation of adatoms from step sites onto the terrace and  $\nu_0$  is the corresponding pre-exponential factor. Note that here,  $E_{\text{ad}}^\ddagger$  is the *activation* energy for adatom creation rather than a formation energy! In contrast to the cases of Ag(111) (5.3) and Cu(100) (5.10) in electrolyte, the adatom creation energy  $E_{\text{ad}}^\ddagger$  in the case of Au(111) is indeed an activation energy, and thus, equal or larger than the energy of adatom formation from kink sites. The difference in the interpretation of the energy for adatom creation becomes obvious from the scaling theory of Pimpinelli et al. [98]. In the case of Ag(111), the dominant mass transport is described by case (i), (3.23), which contains the *equilibrium concentration* of adatoms on the surface. The equilibrium concentration, however, is determined by the *formation energy* for adatoms on the terrace. In the case of Au(111) in electrolyte, the dominant mass transport is analog to case (iii), (3.26), which contains the *creation rate* of adatoms at kink sites (see also Appendix C). Hence,  $E_{\text{ad}}^\ddagger$  is an *activation energy*.

Similar to what has been discussed in Section 5.1 for Ag(111), a linear ansatz is made for the potential dependence of  $E_{\text{ad}}^\ddagger$ ,

$$E_{\text{ad}}^\ddagger(U_{\text{S}}) = E_{\text{ad}}^\ddagger(0) - \lambda_{1/2} e U_{\text{S}}, \quad (5.13)$$

where the subscript 1/2 serves as a reminder that the following analysis corresponds to the potential range where  $G(t)$  obeys a  $t^{1/2}$ -law. According to Fig. 40,  $G(t_0)$  ( $t_0=1\text{s}$ ) can be approximated by a constant  $1.6(a_{\perp}^2)$  for very low electrode potentials. Hence, inserting (5.13) in (5.12) yields

$$G(t_0) = 1.6 + \sqrt{\frac{2\nu_0}{\pi}} e^{-\frac{2\varepsilon + E_{\text{ad}}^\ddagger(0)}{2k_{\text{B}}T}} e^{\frac{\lambda_{1/2} e U_{\text{S}}}{2k_{\text{B}}T}} \left[ \text{s}^{-1/2} \right]. \quad (5.14)$$

Fitting (5.14) to the data of  $G(t_0)$  for 0.01mM (squares) and 0.5-50mM (circles) HCl added to the electrolyte in Fig. 40 for  $U_S < +300\text{mV}$  vs. SCE, and assuming  $v_0 \sim 10^{13} \text{ s}^{-1}$ , one finds [62]

$$\begin{aligned} \lambda_{1/2} &= 0.2 \pm 0.3 \\ 2\varepsilon + E_{ad}^\ddagger(0) &= 0.8 \pm 0.1\text{eV} \end{aligned} \quad \begin{array}{l} \text{(0.01mM HCl)} \\ \text{(5.15)} \end{array}$$

and

$$\begin{aligned} \lambda_{1/2} &= 0.4 \pm 0.1 \\ 2\varepsilon + E_{ad}^\ddagger(0) &= 0.7 \pm 0.1\text{eV} \end{aligned} \quad \begin{array}{l} \text{(0.5-50mM HCl),} \\ \text{(5.16)} \end{array}$$

respectively. Within the error bars, the results for 0.01mM and 0.5-50mM HCl added to the electrolyte are in agreement. The factor  $\lambda_{1/2}$  is of the order of 0.5 and may be interpreted as transfer coefficient. For Au(111) at  $U_S=0\text{mV}$  vs. SCE, the surface is stable and reconstructed and no electrolyte anions are specifically adsorbed. Therefore, the measured activation energy for the adatom creation at this potential,  $E_{ad}^\ddagger(0)$ , may be compared with typical vacuum values: A lower bound for the activation energy for adatom creation from step sites is given by the sum of the formation energy of adatoms from kink sites and the diffusion barrier on the terrace as is illustrated in Fig. 41. Using EAM calculations, Stoltze [81] finds for the formation energy of adatoms from kink sites for the unreconstructed Au surface 0.67eV/atom and for the diffusion barrier on the terrace 0.1eV. Although these energies may be different

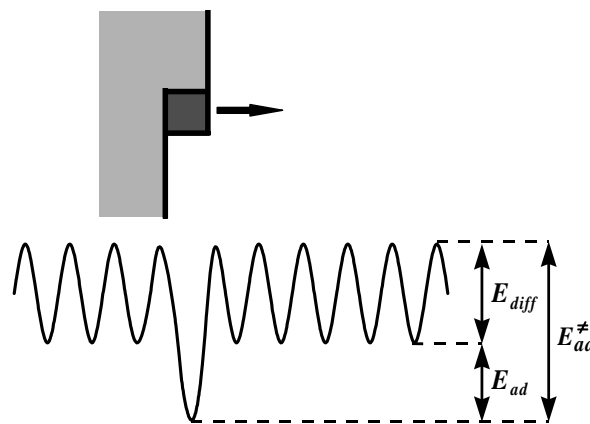


**Fig. 41.** Potential energy diagram for atom detachment from kink sites onto the terrace. The activation energy  $E_{ad}^\ddagger$  for atom detachment from kink sites onto the terrace can be approximated by the sum of the adatom formation energy  $E_{ad}$  and the diffusion barrier on the terrace  $E_{diff}$ .

for the reconstructed surface, they should be of the right order of magnitude. Hence, the energies determined for metal electrodes in electrolyte seem to be of comparable magnitude, but slightly smaller, than energies on metal surfaces in UHV for low electrode potentials.

In the potential range above +300mV vs. SCE, edge diffusion is the dominant mass transport. According to case (vi), (3.29)-(3.31),  $G(t)$  may be written as

$$G(t) = (8v_0)^{1/4} e^{-\frac{3\varepsilon + E_{st}^{ad} + E_d^k}{4k_B T}} t^{1/4}. \quad (5.17)$$

$E_{st}^{ad}$  is the formation energy of adatoms at the step edge<sup>46</sup>,  $\varepsilon$  is the kink energy,  $E_d^k$  the effective diffusion barrier along a kinked steps and  $v_0$  is the corresponding pre-exponential factor. Using  $E_d^k(U_S) = E_d^k(0) - \lambda_{1/4} e U_S$  and  $t_0 = 1s$ , one obtains

$$G(t_0) = 1.6 + (8v_0)^{1/4} e^{-\frac{3\varepsilon + E_{st}^{ad} + E_d^k(0)}{4k_B T}} e^{\frac{\lambda_{1/4} e U_S}{4k_B T}} \left[ s^{1/4} \right]. \quad (5.18)$$

Fitting (5.18) to the data in Fig. 40 for  $U_S > +300mV$  vs. SCE and assuming  $v_0 \sim 10^{13} s^{-1}$ , one finds for all electrolytes containing HCl [62] that

$$\begin{aligned} \lambda_{1/4} &= 0.6 \pm 0.1 \\ 3\varepsilon + E_{st}^{ad} + E_d^k(0) &= 0.8 \pm 0.1 eV \end{aligned} \quad (0.01-50mM \text{ HCl}) . \quad (5.19)$$

We determined the kink formation energy at -100mV vs. SCE by analyzing the spatial correlation function (3.16) to  $\varepsilon = 0.074 eV$  [62] and used this value in (5.19). In addition,  $E_d^k(0)$  can again be written as the sum of the diffusion barrier along a straight step segment  $E_d(0)$  and the kink energy  $\varepsilon$  by reducing the two-dimensional diffusion theory by Natori and Godby [128] of surface diffusion on a stepped surface to one dimension [78]. Then, one finds

$$E_{st}^{ad} + E_d(0) = 0.5 eV, \quad (5.20)$$

which is consistent with the number published by Trevor and Chidsey [211], who studied the Brownian motion (see Section 6.1.5) of Au islands on Au(111) in perchloric acid at +700mV vs. NHE and find  $E_{st}^{ad} + E_d \approx 0.5\text{eV}$ . From (5.29), one may obtain an estimate for the edge diffusion barrier at  $U_S=0$ , if the adatom formation energy at steps  $E_{st}^{ad}$  is approximated by twice the kink energy,  $E_{st}^{ad} \sim 2\varepsilon$ . Then, one finds with  $\varepsilon=0.074\text{eV}$ ,  $E_d \sim 0.3\text{-}0.4\text{eV}$ . Table 5 summarizes all quantitative results obtained to date by analyzing the step fluctuations on metal electrodes.

At the end of this section, we mention a recent work by McHardy et al. [186], who analyzed step fluctuations on Au(111) in 1mM KI + 50mM KClO<sub>4</sub> as a function of the electrode potential. In the potential range below -400 mV vs. SCE, where no iodine is adsorbed to the Au surface, they find that the step mobility is independent of the electrode potential. Between -400 and -100mV vs. SCE, where iodine is specifically adsorbed in a disordered phase, they observe a linear decrease of the step fluctuations and  $G(t)$  obeys a  $t^{1/2}$ -law, which is attributed to terrace diffusion. Since these authors performed no systematic measurement of the step-step distance dependence of  $G(t)$ , a clear identification of the dominant mass transport process is impossible. For even higher potentials, where iodine forms an ordered rectangular  $c(p \times \sqrt{3}R-30^\circ)$  adlayer, they measure a  $t^{1/4}$ -dependence of  $G(t)$ , which is interpreted as dominant edge diffusion. In this potential range, they observe a linear increase of the step mobility. Hence, the step mobility has a minimum at the phase transition from the disordered to the rectangular ordered iodine phase on the Au(111) surface.

The results by McHardy et al. [186] show, that Au(111) in contact with a iodine containing electrolyte [186] seems to behave different compared to other metal electrodes [59, 60, 62, 112, 185] investigated so far. Firstly, the step mobility depends linearly on the electrode potential, rather than exponentially, if there is any potential dependence. Secondly, it is the first system, where a minimum in the step mobility at a distinct potential has been found.

---

<sup>46</sup> In (3.29)-(3.31),  $c_{st}$  is the equilibrium adatom concentration at the step edge. Hence,  $E_{st}^{ad}$  is the adatom formation energy at steps.

Table 5.

Surface	T (K)	Electrolyte	$G(t) \propto t^{\alpha} L^{\delta}$		$E_t$ (eV)	$\nu_0$ (s <sup>-1</sup> )	$\epsilon$ (eV)	Ref.
Ag(111)	296-311	0.05M Na <sub>2</sub> SO <sub>4</sub> +0.1mM H <sub>2</sub> SO <sub>4</sub> ( $U_S < 0$ ) 0.05M H <sub>2</sub> SO <sub>4</sub> +1mM CuSO <sub>4</sub> ( $U_S > 0$ )	$U_S < 0$ $t^{1/4}$	$U_S > 0$ $t^{1/2} L^{1/2}$	$U_S = +50$ 0.54±0.11	$U_S = +50$ 6.3×10 <sup>16±4</sup>	$-800 \leq U_S \leq +60$ ~0.1	[59, 60, 185]
Cu(100)	300	0.05M H <sub>2</sub> SO <sub>4</sub>	$U_S < -490$ $t^{1/4}$	$U_S > -490$ $t^{1/2} L^{-1/2}$				[59]
Cu(111)	287-306	1mM HCl	$-470 < U_S < -120$ $t^{1/3}$		$U_S = -420$ 0.28±0.04	$U_S = -420$ 1.5×10 <sup>16±2</sup>		[112]
Au(111)	300	0.1M H <sub>2</sub> SO <sub>4</sub>	$U_S < +300$ $t^{1/2}$	$U_S > +300$ $t^{1/4}$				[62]
Au(111)	300	0.1M H <sub>2</sub> SO <sub>4</sub> +(0.01-50)mM HCl	$U_S < +300$ $t^{1/2}$	$U_S > +300$ $t^{1/4}$			$U_S = -100$ 0.074±0.002	[62]

**Table 5 (cont.).**

Surface	T (K)	Electrolyte	$\varepsilon + E_{ad}^{\neq}$ (eV)	$E^{\neq} + E_{ad}$ (eV)	$E_{st}^{ad} + E_d$ (eV)	$E_{ad} + E_{diff}$ (eV)	Ref.
Ag(111)	296-311	0.05M Na <sub>2</sub> SO <sub>4</sub> +0.1mM H <sub>2</sub> SO <sub>4</sub> ( $U_S < 0$ ) 0.05M H <sub>2</sub> SO <sub>4</sub> +1mM CuSO <sub>4</sub> ( $U_S > 0$ )		$U_S = +50$ 1.0±0.2			[59, 60, 185]
Cu(100)	300	0.05M H <sub>2</sub> SO <sub>4</sub>				$U_S = 0$ ~0.15	[59]
Cu(111)	287-306	1mM HCl				$U_S = -420$ 0.62±0.12	[112]
Au(111)	300	0.1M H <sub>2</sub> SO <sub>4</sub> +(0.01-50)mM HCl	$U_S = 0$ ~0.8±0.1		$U_S = 0$ ~0.5		[62]

**Table 5.**

Summary of the available data on various metal electrodes in electrolyte on the time dependence of  $G(t)$ , the kink energy  $\varepsilon$  and the different activation energies:  $E_i$  is the measured activation energy of the dominant mass transport and  $v_0$  is the corresponding pre-exponential factor.  $E^{\neq}$ ,  $E_{ad}^{\neq}$  and  $E_{ad}$  are the activation energy for dissolution, the activation energy of adatom creation on the terrace and the adatom formation energy from kink sites onto the terrace, respectively. The corresponding formation energy for adatom creation from kink sites to the step is denoted as  $E_{st}^{ad}$ .  $E_d$  and  $E_{diff}$  are the diffusion barrier along a straight step and on the flat terrace, respectively.  $U_S$  denotes the electrode potential at which the measurements were performed and is given in mV vs. SCE. Column 2 shows the temperature range of the experiment. Note that for the determination of the time laws summarized in column 4, the step-step distance dependence of  $G(t)$  was explicitly measured, i.e., if no L-dependence is indicated in column 4, the exponent  $\delta$  is 0.

Finally, it is emphasized that caution has to be exercised in the interpretation of mass transport mediating species on the surface of the metal electrode and related formation and diffusion energies. In the most simple case of clean metal surfaces in UHV, the mass transport mediating species are single adatoms. For (110) surfaces, the mass transport mediating species may involve the concerted motion of two adatoms as observed, e.g., on Ag(110) by Kuipers et al. [51]. However, for metal surfaces under the influence of a surrounding gas pressure - or even more pronounced -for metal electrodes in electrolyte- the mass transport mediating species may be completely different. Here, specifically adsorbed anions on the surface or at steps may also serve as diffusing species. Hence, the physical interpretation of the energies as, e.g., (5.20) is difficult.

#### **5.4. Influence of the tunneling tip**

In Section 3.4, tip-mediated diffusion processes were discussed for metal surfaces in UHV. It was argued that in most cases, the influence of the tip is negligible, if moderate tunneling parameters are used. For metal electrodes in electrolyte, the problem of tip-induced atomic motion may become more important. In particular, at large electrode potentials where the surface mobility is high, the local electric field under the tunneling tip induced by the tunneling bias may initiate atomic diffusion processes. A situation where one might actually expect tip mediated mass transport is the case of rapid metal electrode dissolution: When metal atoms dissolve into the electrolyte, the free enthalpy for dissolution is zero. For electrode potentials close to, yet slightly below, the dissolution potential, the local field under the tip may be sufficient to initiate the dissolution process locally. For the case of Ag(111) in sulfuric acid, we measured the influence of the tunneling tip on step fluctuations at various potentials [59]. Fig. 42(a) shows the value of the time correlation value  $G(t_0)$  at  $t_0=11s$  at room temperature for various tunneling currents between 1 and 3nA. The tunneling bias was held constant at -40mV with respect to the metal electrode. At negative electrode potentials, no systematic dependence of  $G(t_0)$  is observed. At an electrode potential of +50mV vs. SCE, however, the fluctuation amplitude increases with increasing tunneling current. The difference in  $G(t_0)$  at this potential exceeds the typical scattering of the data due to local variations in the kink density. Therefore, we propose that the deviation in  $G(t)$  is due to tip-surface interactions. When the tunneling current is held constant at 1nA, the fluctuation amplitude does, however, not depend on the scan rate. Fig. 42(b) shows the time correlation function as measured at +60mV vs. SCE,  $I_T=1nA$  and  $U_T=-40mV$ , for different scan rates. Within the scattering the data fall onto the same curve, in particular, the time exponent remains unaltered.

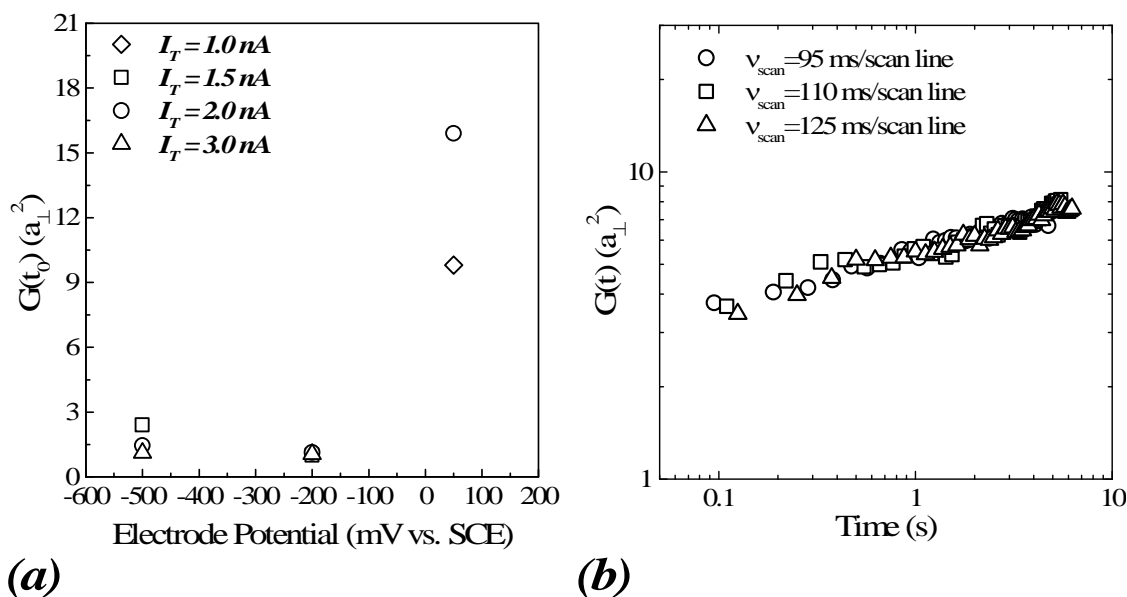


**Fig. 42.** (a) Dependence of the time correlation value  $G(t_0)$  at  $t_0=11$ s on Ag(111) on the tunneling current (measured in 0.05M  $\text{Na}_2\text{SO}_4+0.1\text{M H}_2\text{SO}_4$  for negative potentials and in 1mM  $\text{CuSO}_4+0.05\text{M H}_2\text{SO}_4$  for positive potentials). (b) Time correlation function  $G(t)$  measured on Ag(111) at +60mV vs. SCE and  $I_T=1$ nA,  $U_T=-40$ mV for different scan speeds [59].

Hence, for moderate tunneling conditions, the measured time dependence of  $G(t)$  is not affected by the tip even close to the dissolution potential of Ag.

As has been briefly discussed in Section 3, it is not quite clear whether tip-surface interactions manifest themselves in a change of the time dependence of  $G(t)$  at all. Alternatively, the tip influence may be the reason for constant contributions to  $G(t)$  at  $t=0$  as measured, e.g., on Ag(111) in 1mM  $\text{CuSO}_4+0.05\text{M H}_2\text{SO}_4$  [60] and on Au(111) in 1mM KI + 50mM  $\text{KClO}_4$  [186]. As discussed for Ag(110) in UHV by Koch et al. [138], the tip may shift step adatoms along the step edge. The same could be true for metal surfaces in liquid environment. One would, however, not expect a correlation between a contribution of such fast tip-induced diffusion processes at  $t=0$  and a later time. Tip-induced effects should therefore manifest themselves exclusively as a constant offset of  $G(t)$  at  $t=0$  rather than as a change in the time exponent. Unfortunately, Koch et al. [138] performed no detailed analysis of the consequences of the tip-surface interaction with respect to  $G(t)$  on Ag(110). The exact effect of a tip-surface interaction on  $G(t)$  is not known up to now.

### 5.5. Step-step interactions on metal electrodes

In Section 4, previous experimental studies of step-step interactions on metal surfaces in UHV were discussed. Step-step interactions may also play a significant role on metal electrodes in liquid environment. As mentioned in Section 4, dipole-dipole interactions arise

from the electronic charge distribution at step edges. A further contribution to step-step interactions are introduced by local strain fields at step edges due to lattice relaxations. Specific adsorption of anions from the electrolyte may introduce large local dipole-dipole forces at steps, due to the electronic charge transfer to the electrode surface. In addition, specific adsorption also alters the local atomic configuration at steps, and hence, may change

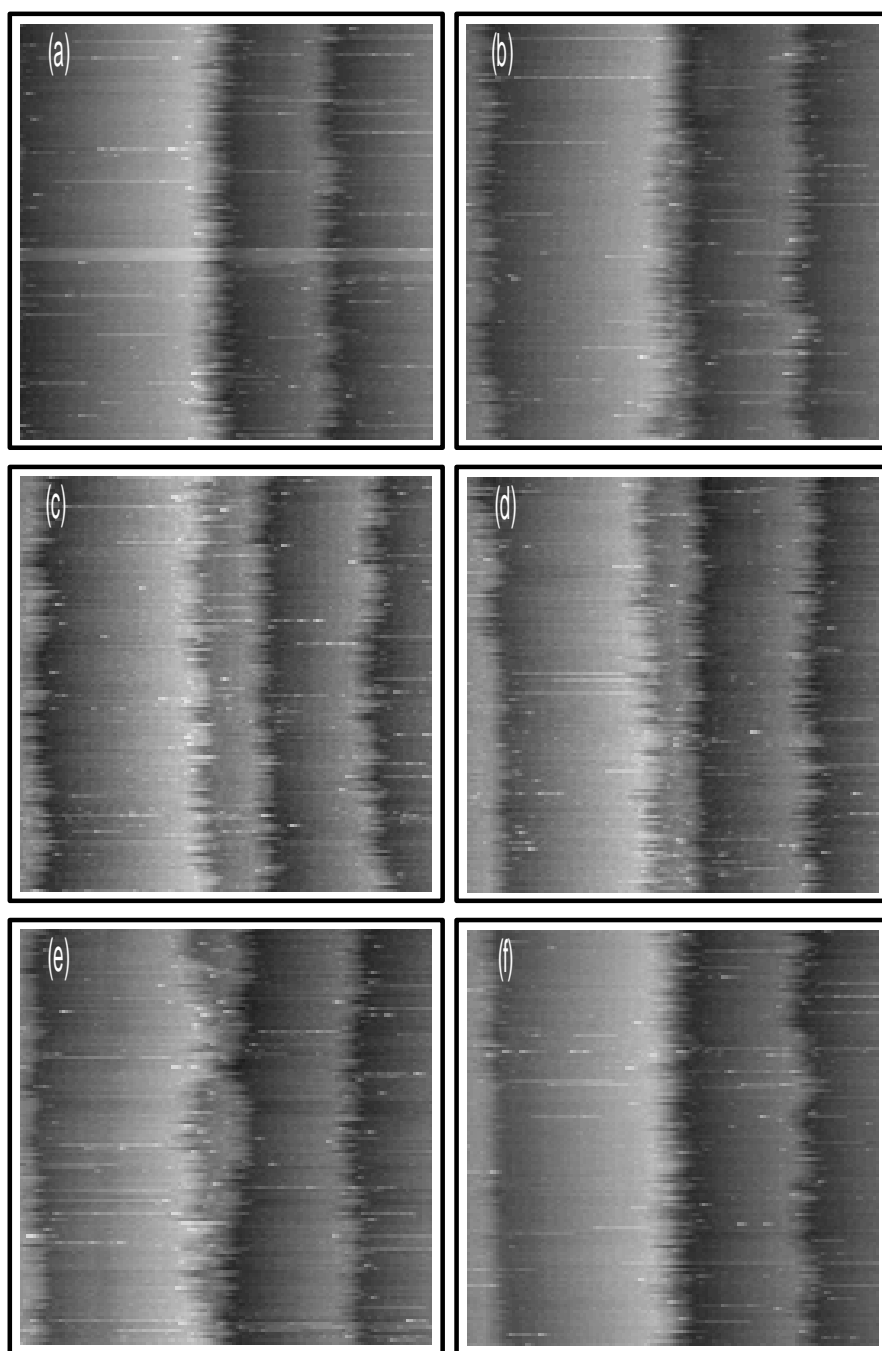


**Fig. 43.** STM images ( $20 \times 20 \text{ nm}^2$ ) of steps on a Ag(111) electrode. Initially (a), the left step is a double-layer step which separates into two monatomic high steps (b)-(d). Eventually, the steps form a double-layer step again, due to attractive step-step interactions [60].

interactions by lattice strain fields. Therefore, the observed faceting of steps on Cu surfaces in HCl, e.g., may be mediated by a change in the step-step interaction energy, as well as by a change in step energetics. Even in the case when no specific adsorption occurs, the presence of the liquid may influence the surface energetics and likewise the step-step interactions. No systematic studies on the step-step interactions on metal electrodes in liquid environment have been performed so far, however, we reported on a qualitative observation on Ag(111) electrodes [60]. Fig. 43 shows a series of room temperature STM images recorded on stepped Ag(111) in 1mM CuSO<sub>4</sub>+0.05M H<sub>2</sub>SO<sub>4</sub> at +60mV vs. SCE. Each image represents a total time span of about 2 minutes. In panel (a), a monolayer high step (right) and a double-layer high step (left) are shown. In the consequent image (b), the two steps in the double-layer high step start to split and in (c), these steps are well separated. Then in (d),(e), the steps approach again and eventually merge again into a double-layer high step (f). The oscillation between separation and approach of the steps may be attributed to a combination of short range repulsive step-step interactions and medium-range attractive interactions between steps on Ag(111) in electrolyte.

## 6. Islands on metal surfaces

In the preceding sections, steps were considered as infinitely long or as pinned between two points with a large distance. In particular, it was assumed that steps were aligned on the average along a distinct direction and deviations from the mean orientation were exclusively due to equilibrium fluctuations. Now, steps are considered to loop, and hence, form two-dimensional islands on the surface.

Two-dimensional adatom islands are generated, e.g., during epitaxial growth on a flat surface via a nucleation process. Atoms deposited on the surface perform a random walk until they form a critical nucleus, which is stable against dissociation. If desorption from the solid into the gas phase is negligible, the island density is determined by a power of the ratio of the impinging atom flux and the diffusion coefficient on the surface. The exponent depends on the size of the critical nucleus [212]. Hence, surface diffusion barriers may be determined by the analysis of the island density as a function of the deposition flux and temperature (for a recent review of such experiments see [213]). Analogous to the generation of adatom islands by atom deposition, vacancy islands are produced by the removal of atoms via ion bombardment of the surface.

Depending on the temperature and the diffusion constants on the specific surface, the shapes of the islands may be quite different: For low temperatures and slow edge diffusion, the island structures are ramified. Atoms attaching to an island edge, stick to the edge and no further hopping along the island perimeter occurs. This process gives rise to a dendritic growth shape (see Pt(111) [110, 214], Ag(111) [215]). If the temperature is high enough and the diffusion along the island edge is faster, the islands assume their equilibrium shape. The equilibrium shape of islands is temperature dependent: At low temperatures, islands on (100) and (111) surfaces of Cu and Ag are nearly quadratic and hexagonal, respectively. On highly anisotropic surfaces like the (110) plane, the equilibrium shape has a large aspect ratio (see Cu/Pd(110) [216]). At high temperatures, the island equilibrium shape becomes circular and elliptical, respectively.

The size distribution of nucleated islands depends on the surface coverage and the island density and is strongly influenced by ripening phenomena as the decay and the coalescence of islands (see [217, 218], and references therein, for a recent review see [219]). Island ripening is caused by differences in the island size: Smaller islands decay faster than large islands, because small islands have a higher vapor pressure than large islands according to the Gibbs-Thomson relation [220-222]. Island coalescence is induced by the mobility of entire islands via adatom and vacancy diffusion. The diffusion of islands is determined by a random walk of

the center of mass of the island [47]. For small 2-dimensional clusters, special mechanisms may give rise to island mobility as, e.g., the concerted motion of the atoms in the cluster [223, 224] or the motion by dislocation propagation [225].

This section focuses on two key issues: Firstly, on the equilibrium shape of islands and the quantitative analysis to determine kink and step energies. The random walk of islands is then briefly discussed because equilibrium fluctuations of the island edges give rise to equilibrium fluctuations of the island shape, as well as to the island motion. The section describes secondly the coarsening of island structures in two and three dimensions: For 2-dimensional coarsening, island decay and island coalescence are considered. Here, the focus lies on the quantitative study of the 2-dimensional island decay. Finally, the 3-dimensional coarsening via the decay of multilayer island stacks is discussed.

## **6.1. Equilibrium shape of islands**

### **6.1.1. Wulff construction**

The equilibrium shape reflects the anisotropy of the free energy  $\gamma$  of interfaces as a function of the polar and azimuthal angle and temperature. For a particular 3-dimensional crystal or a 2-dimensional island, the interface free energy is a unique function of orientation and temperature. In the macroscopic limit, crystals and islands have therefore only one equilibrium shape at a given temperature, which is independent of the particle size as long as the size is not too small. As early as 1901, Wulff established his famous construction of the equilibrium shape from the orientational dependence of the surface free energy of 3-dimensional crystals [226]. The equilibrium shape is described by a vector  $\vec{r}$  [146]:

$$\vec{r} = \lim_{V \rightarrow \infty} \left( \frac{\vec{R}}{\lambda V^{1/3}} \right). \quad (6.1)$$

Here,  $\vec{R}$  is the actual vector from the center of mass of the 3-dimensional crystal to the surface.  $\lambda$  is a scaling factor and  $V$  is the volume of the crystal<sup>47</sup>. The anisotropy of the surface free energy is described by  $\gamma = \gamma(\vec{n})$ , where  $\vec{n}$  is a unit vector (Fig. 44). When  $\gamma(\vec{n})$  is known, the equilibrium shape  $\vec{r}(\vec{m})$  in a particular direction  $\vec{m}$  ( $\vec{m}$  also being a unit vector) is

---

<sup>47</sup> Equation (6.1) includes that the crystal is macroscopically large and that all corner effects introduced by the discrete nature of the atomic lattice are negligible.

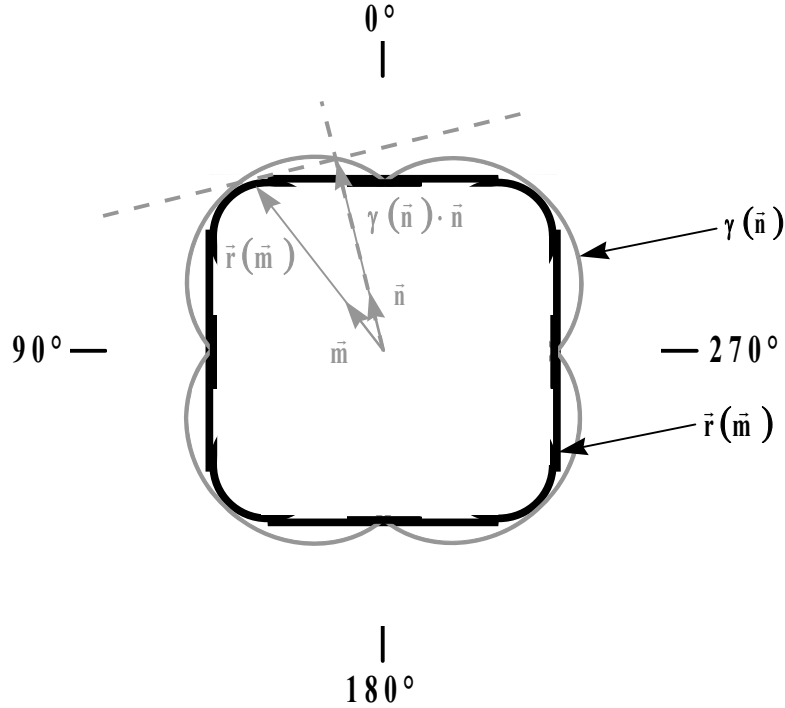


**Fig. 44.** Illustration of the Wulff construction: The equilibrium shape of a crystal (or a 2-dimensional island) is determined by the anisotropy of the interface free energy  $\gamma(\bar{n})$ . It is given by the inner envelope of the normals to all radial connection lines between the crystal center and the  $\gamma$ -plot (gray).

derived by the minimization of the surface free energy where the minimization is performed with respect to all possible vectors  $\bar{n}$ <sup>48</sup>:

$$\|\bar{r}\| = \min_{\bar{n}} \left( \frac{\gamma(\bar{n})}{\bar{m} \cdot \bar{n}} \right) = \min_{\bar{n}} \left( \|\bar{r}\| \frac{\gamma(\bar{n})}{\bar{r} \cdot \bar{n}} \right) \quad \text{with} \quad \bar{r}(\bar{m}) = \|\bar{r}(\bar{m})\| \cdot \bar{m}. \quad (6.2)$$

The equilibrium shape of crystals can mathematically be interpreted as the *Legendre-transformation* of the projected surface free energy [227]. Wulff showed that (6.2) has a geometric interpretation which is called the *Wulff construction* [226]: If the surface free energy  $\gamma(\bar{n})$  is plotted in a polar plot (called *Wulff plot* or  $\gamma$ -plot), the equilibrium crystal shape is given by the interior envelope of the family of normal planes passing through the ends of the vector  $\gamma(\bar{n}) \cdot \bar{n}$  (Fig. 44). Facets occur in the equilibrium shape of crystals when the Wulff plot has a *cusp*, i.e., when the derivative of  $\gamma(\bar{n})$  is not continuous. In Fig. 44, cusps are visible at the angles  $0^\circ$ ,  $90^\circ$ ,  $180^\circ$  and  $270^\circ$ . The existence of facets in the equilibrium

shape depends on temperature. The vanishing of a facet of a particular orientation at a particular temperature defines the roughening temperature of the distinct facet. At the roughening temperature, the cusp in  $\gamma(\bar{n})$  (and hence, the facet) vanishes. Another way of defining a rough surface is that the height correlation function diverges,

$$\lim_{x_{ij} \rightarrow \infty} \left\langle \left( h(x_{ij} + x_0) - h(x_0) \right)^2 \right\rangle \rightarrow \infty \quad (x_{ij} \text{ defined as in Fig. 1) [22].}$$

For 2-dimensional islands, the surface free energy is replaced by the step free energy. As can be seen from (3.16), the step position correlation function diverges for any temperature  $T > 0$  even when the step is nominally oriented along a direction of close packing. Accordingly, steps are always rough and the Wulff plot of the step free energy has no cusps. As a consequence, the equilibrium shape of 2-dimensional islands never reveal real facets but only quasi-straight step segments. From (6.1) and (6.2) one obtains for the special case of two vectors  $\bar{r}_i$  ( $i=1,2$ ) parallel to the respective unit vectors  $\bar{n}_i$ <sup>49</sup>

$$\frac{\gamma(\bar{r}_1)}{\gamma(\bar{r}_2)} = \frac{\|\bar{r}_1\|}{\|\bar{r}_2\|}. \quad (6.3)$$

Theoretical studies on the equilibrium shape of 3-dimensional crystals have been performed based on statistical physics [146, 228-233] and experimental studies by REM and STM [172, 173, 175, 234-239]. In all these studies, merely the *ratio* of *surface* free energies according to (6.3) were determined.

The ratio of *step* free energies may be directly determined from the equilibrium shape of 2-dimensional islands. Fig. 45 shows a series of STM images of monolayer islands on metal surfaces at different temperatures: Ag/Ag(111) at 291 and 370K, Cu/Cu(100) at 303 and 386K, Cu/Cu(111) at 300 and 355K [88]. Due to the trigonal symmetry of the fcc (111) plane, islands on Ag(111) and Cu(111) are quasi-hexagons with alternating A- and B-type step segments. When the step free energy of both step types is about equal, the A- and B-segments are of equal length.

On Cu(111), we showed that the free energy of A- and B-steps is equal within 1%, the A-step having the lower energy ( $\gamma_A/\gamma_B=0.989\pm 0.007$ ) [25, 88, 90]. Schlöber et al. [240]

<sup>48</sup> Note that  $\frac{\|\bar{r}\|}{\bar{r} \cdot \bar{n}} = \frac{1}{\cos(\angle \bar{r}, \bar{n})}$  where  $\angle \bar{r}, \bar{n}$  denotes the angle between  $\bar{r}$  and  $\bar{n}$ .

<sup>49</sup> Note that the condition  $\bar{r}_i \parallel \bar{n}_i$  is exclusively fulfilled for high-symmetry directions of the crystal surface. For example on (100) surfaces, if  $\bar{n}_i \parallel \langle 110 \rangle$  or  $\langle 100 \rangle$ ; on (111) surfaces, if  $\bar{n}_i \parallel \langle 110 \rangle$  or  $\langle 211 \rangle$ .

obtained a consistent result from independent measurements. The finding that A-steps are associated with the lower step energy is in agreement with the observation that Cu(111) vicinal surfaces with B-steps are unstable and restructure into facets consisting of A-steps (Fig. 6) [24, 25]. In ab initio calculations by Feibelman [91] for Cu(111), however, B-steps are energetically preferred and the energy difference between both step types is slightly larger (4%). Recent calculations by Vitos et al. [89] propose that A-steps should be energetically favorable ( $\gamma_A/\gamma_B=0.54$ ). The energy difference, however, is far off the experimental values. In very recent experiments, we could show that A-steps are energetically favorable also on Ag(111) ( $\gamma_A/\gamma_B=0.996\pm 0.003$ ) [88] although the energy difference is smaller than for Cu(111).

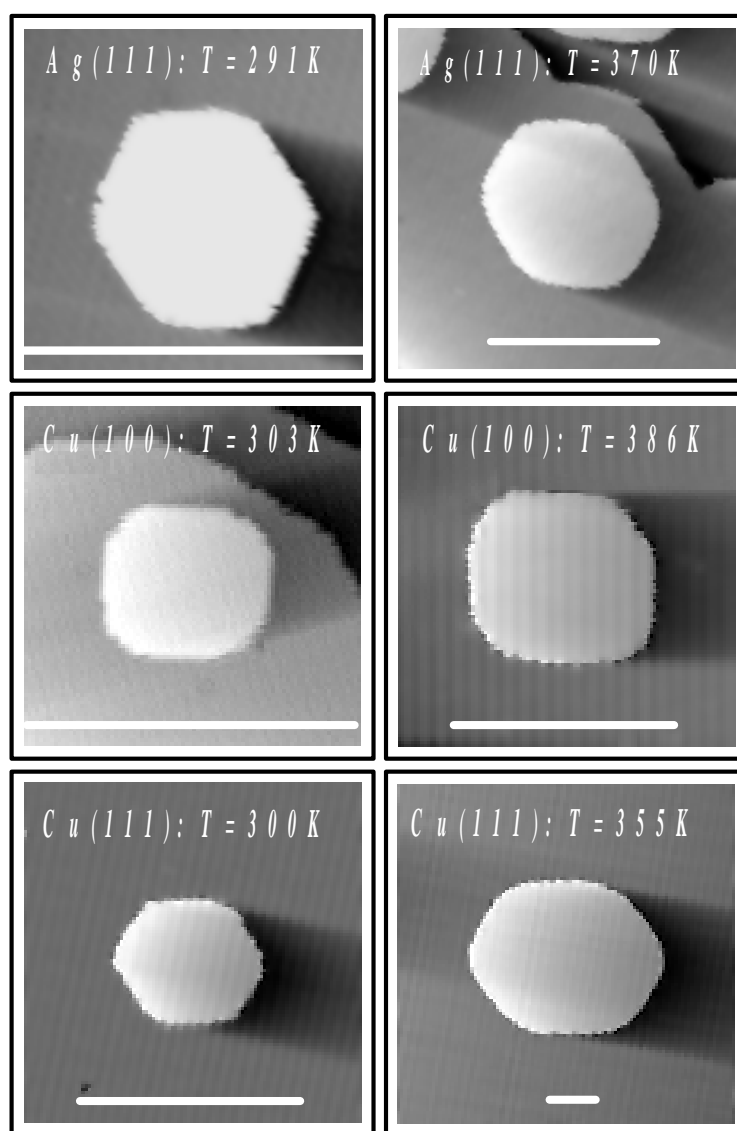


**Fig. 45.** STM images of Ag islands on Ag(111) at 291 and 370K, Cu islands on Cu(100) at 303 and 386K and on Cu(111) at 300 and 355K. The white bar in each image corresponds to a length of 30nm [88].

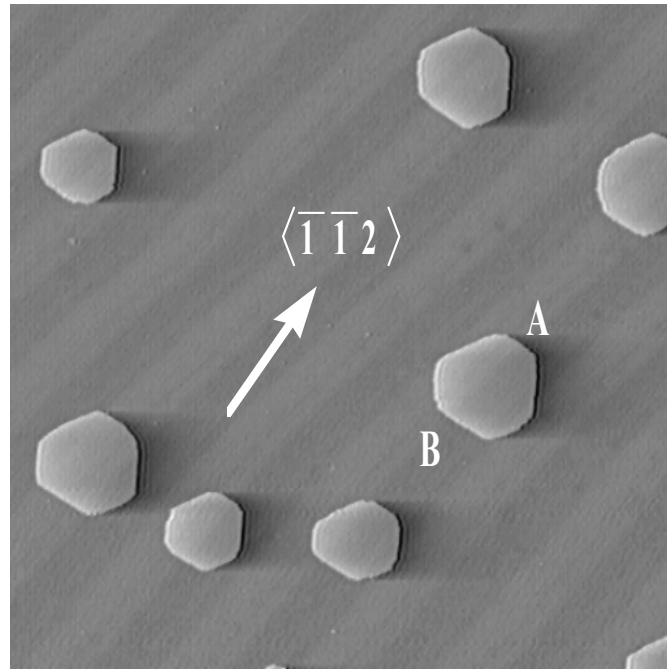


**Fig. 46.** Monatomic high Pt adatom islands on Pt(111) after deposition of 0.1ML at 425K and subsequent annealing to 700K for 60s (scan width 200nm). The islands reveal their equilibrium shape, in which the A-step segments are considerably smaller as the B-step segments. The free energy of A- and B-steps on Pt(111) differ by about 15% [243] (after Michely [242]).

On Pt(111), neighboring island edges are of considerably different length and the island shape is closer to that of a triangle [110, 241]. Fig. 46 shows an STM image of Pt islands on Pt(111) after deposition of 0.1ML at 425K and subsequent annealing to 700K as recorded by Michely and coworkers [242].

Michely and Comsa [243] found that on Pt(111) B-steps are energetically favorable by 15%, which is confirmed by several theoretical papers [82, 126, 244, 245], though the energy difference between A- and B-steps varies significantly for the various calculations (see Table 6). Best agreement between theory and experiment is achieved in *ab initio* calculations by Feibelman ( $\gamma_A/\gamma_B=1.16$ ) [126].

On (100) surfaces, the quasi-straight island edge segments consist of geometrical and energetically identical steps with equal step energy and, therefore, the islands on (100) surfaces are quasi-squares. On fcc (110) surfaces, islands have a two-fold symmetry with a large aspect ratio, due to the large difference in the step energies for steps along and perpendicular to the dense  $\langle 110 \rangle$ -direction. Only few values are available for the ratio of step free energies of steps along  $\langle 110 \rangle$  and  $\langle 100 \rangle$  on (110) surfaces. A quantitative study of the aspect ratio was published, e.g., by Morgenstern et al. for Ag(110) [246].

Table 6.

Surface	Temperature range (K)	Aspect ratio $\gamma_A/\gamma_B$	Aspect ratio $\gamma_{\langle 100 \rangle}/\gamma_{\langle 110 \rangle}$	Step energy $\gamma(0,0)$ (eV $a_{  }^{-1}$ )	$\gamma(\theta,0)/\gamma(0,0)$ ( $\theta_{100}=45^\circ, \theta_{111}=30^\circ$ )	Ref.
Cu(100) <sup>(‡)</sup>	287-448			0.22±0.02	1.24±0.01	[88]
Cu(100) <sup>(50)</sup>				0.125		[81]
Cu(111) <sup>(‡)</sup>	286-398	0.989±0.007		0.27±0.03	1.138±0.008	[88, 90]
Cu(111) <sup>(‡)</sup>	350	0.98±0.05 <sup>51</sup>				[25]
Cu(111) <sup>(‡)</sup>	260-350	0.98±0.02		0.22±0.02		[240]
Cu(111) <sup>(‡)</sup>	310			0.45±0.02		[200]
Cu(111) <sup>(50)</sup>				0.208		[81]
Cu(111) <sup>(52)</sup>		1.04		A-step: 0.27 B-step: 0.26		[91]
Cu(111) <sup>(53)</sup>				0.20		[247, 248]
Cu(111) <sup>(54)</sup>		0.54		A-step: 0.197 B-step: 0.375		[89]
Cu(110) <sup>(50)</sup>			11.3	$\langle 110 \rangle$ -step: 0.009 $\langle 100 \rangle$ -step: 0.102		[81]
Cu(110) <sup>(55)</sup>			11.2	$\langle 110 \rangle$ -step: 0.011 $\langle 100 \rangle$ -step: 0.122		[87]

<sup>‡</sup> These results are obtained from STM experiments. The others were determined from theoretical calculations.

<sup>50</sup> EMT calculations.

<sup>51</sup> In [25], a typing error occurs in equation (1). It should read  $\gamma_{100}/\gamma_{111} = I_{100}/I_{111} = 0.98 \pm 0.05$ .

<sup>52</sup> GGA first principles calculations.

<sup>53</sup> Value based on calculations by McLean at higher T [247] which are extrapolated to T=0 by Bonzel [248].

<sup>54</sup> LDA calculations.

<sup>55</sup> EAM calculations.

Table 6 (cont.).

Surface	Temperature range (K)	Aspect ratio $\gamma_A/\gamma_B$	Aspect ratio $\gamma_{\langle 100 \rangle}/\gamma_{\langle 110 \rangle}$	Step energy $\gamma(0,0)$ (eV a <sub>  </sub> <sup>-1</sup> )	$\gamma(\theta,0)/\gamma(0,0)$ ( $\theta_{100}=45^\circ, \theta_{111}=30^\circ$ )	Ref.
Ag(100) <sup>(52,54)</sup>				0.130		[121]
Ag(115) <sup>(52,54)</sup>				0.136		[121]
Ag(111) <sup>(‡)</sup>	292-406	0.996±0.003		0.25±0.03	1.136±0.009	[88]
Ag(111) <sup>(‡)</sup>	240-360			0.22±0.05		[249]
Ag(111) <sup>(50)</sup>				0.156		[81]
Ag(111) <sup>(55)</sup>		0.985		A-step: 0.188 B-step: 0.191		[82]
Ag(111) <sup>(54)</sup>		0.71		A-step: 0.155 B-step: 0.211		[89]
Ag(110) <sup>(‡)</sup>	155-255		2.9±0.4			[246]
Ag(110) <sup>(50)</sup>				$\langle 110 \rangle$ -step: 0 $\langle 100 \rangle$ -step: 0.076		[81]
Ag(110) <sup>(54)</sup>			1.14	$\langle 110 \rangle$ -step: 0.075 $\langle 100 \rangle$ -step: 0.085		[89]
Pt(111) <sup>(‡)</sup>	700-925	1.15±0.03				[243]
Pt(111) <sup>(50)</sup>				0.20		[81]
Pt(111) <sup>(55)</sup>		1.01		A-step: 0.344 B-step: 0.341		[82]
Pt(111) <sup>(54)</sup>		1.14		A-step: 0.46 B-step: 0.38		[244]

**Table 6 (cont.).**

Surface	Temperature range (K)	Aspect ratio $\gamma_A/\gamma_B$	Aspect ratio $\gamma_{\langle 100 \rangle}/\gamma_{\langle 110 \rangle}$	Step energy $\gamma(0,0)$ (eV $a_{  }^{-1}$ )	$\gamma(\theta,0)/\gamma(0,0)$ ( $\theta_{100}=45^\circ, \theta_{111}=30^\circ$ )	Ref.
Pt(111) <sup>(54)</sup>		1.02		A-step: 0.47 B-step: 0.46		[245]
Pt(111) <sup>(52)</sup>		1.16		A-step: 0.29 B-step: 0.25		[91]
Pt(111) <sup>(54)</sup>		0.41		A-step: 0.270 B-step: 0.655		[89]
Pt(111) <sup>(56)</sup>				0.37		[248, 250, 251]
Pb(111) <sup>(‡)</sup>	440-530	1.11		A-step: 0.09 B-step: 0.08		[172, 173]

**Table 6.**

Experimental (‡) and calculated values of step free energies on fcc metal surfaces in UHV. The second column shows the temperature range of experimental studies. In column 3, the ratio of the step free energies of A- and B-steps on (111) surfaces are summarized. The corresponding ratio of  $\langle 100 \rangle$  and  $\langle 110 \rangle$  oriented steps on (110) surfaces are given in column 4. Column 5 shows experimental and theoretical results of absolute step free energies of steps along the atomically dense  $\langle 110 \rangle$  steps in units of the nearest neighbor distance  $a_{||}$ . Values obtained from STM experiments on (111) surfaces correspond to an average 110 over A- and B-steps. The ratio of the step free energy of a 100% kinked step  $\gamma(\theta,0)$  and that of a quasi-straight step  $\gamma(0,0)$  at T=0 is given in column 6. For (100) and (111) surfaces,  $\theta$  is 45° and 30°, respectively.

<sup>56</sup> The value is based on papers by Tyson and Miller [250] as well as by Miedema and Dorleijn [251] at higher temperature. The extrapolation to T=0 was performed by Bonzel [248].

Experimental results for the ratios of step free energies on (111) and (110) fcc metal surfaces determined from the equilibrium shape of 2-dimensional islands are listed together with theoretical, calculated values in the 3rd and 4th column of Table 6. For (111)-surfaces, the ratio  $\gamma_A/\gamma_B$  of A- and B-steps (parallel to the dense  $\langle 110 \rangle$ -direction) is given.

We have shown recently that in the case of 2-dimensional islands, *absolute values* of the step free energy can be determined from the equilibrium shape<sup>57</sup> [88, 90], which will be explored in the following. Fig. 47 shows the equilibrium shape we measured on (a) Cu(100) and (b) Cu(111) for two different temperatures. The equilibrium shapes were obtained by averaging over 200-300 single island shapes from STM movies, where each island contained between 60000 and 200000 atoms [88, 90]. They resemble the quasi-squared and -hexagonal shape for fcc(100) and (111) surfaces. In the case of islands on the (100) plane, the radii at  $0^\circ$ ,  $90^\circ$ ,  $180^\circ$  and  $270^\circ$  ( $2n\pi/4$ ,  $n=0,1,2,\dots$ ) denote the radii of the quasi-straight island edge segments in the equilibrium shape. Steps in these segments are primarily oriented along the dense packed  $\langle 110 \rangle$ -direction with a small number of kinks. The radii of the rounded corners

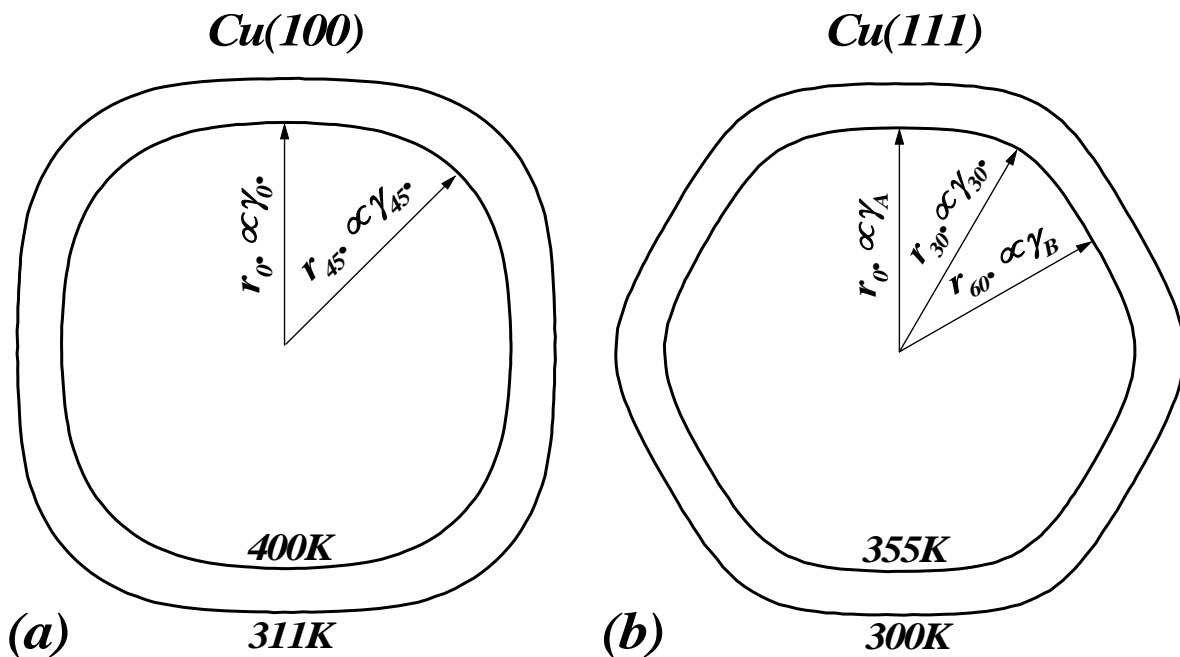


**Fig. 47.** Measured equilibrium shapes of islands on Cu(100) and (111) corresponding to an average over approximately 200-300 different islands each containing between 60000 and 200000 atoms. The inner and outer contour lines correspond to a higher and lower temperature, respectively. To illustrate the notation used in the text the radii of the quasi-straight edge segments and corners are indicated [88].

<sup>57</sup> A recent theoretical derivation by Bonzel and Emundts [252] show that absolute surface and step free energies can also be determined in the 3-dimensional case of particles on a surface from temperature dependent studies of the equilibrium crystal shape.

are at  $45^\circ$ ,  $135^\circ$ ,  $225^\circ$ , and  $315^\circ$  ( $(2n+1)\pi/4$ ,  $n=0,1,2,\dots$ ). Steps corresponding to these angles consist of 100% kinked segments along  $\langle 100 \rangle$  (compare also Fig. 32). In the case of islands on the  $(111)$  plane, quasi-straight segments occur at  $0^\circ$ ,  $120^\circ$ ,  $240^\circ$  ( $2n\pi/3$ ,  $n=0,1,2,\dots$ ) and at  $60^\circ$ ,  $180^\circ$ ,  $300^\circ$  ( $(2n+1)\pi/3$ ,  $n=0,1,2,\dots$ ), which correspond to straight A- and B-steps along  $\langle 110 \rangle$  in our experiments, respectively. Rounded corners are found at  $30^\circ$ ,  $90^\circ$ ,  $150^\circ$ ,  $210^\circ$ ,  $270^\circ$ ,  $330^\circ$  ( $(2n+1)\pi/6$ ,  $n=0,1,2,\dots$ ), which correspond to kinked step segments along  $\langle 211 \rangle$  (Fig. 32).

### 6.1.2. Island equilibrium shape in Ising-model

Analytical expressions for the equilibrium shapes of 2D-islands on a square and hexagonal lattice as a function of temperature are available for the Ising model as reported by Zia and Avron [96, 97]. In the Ising model, the energy of a step is proportional to its microscopic length. For the square lattice the energy per atom on the densely packed step is then equal to the kink energy. On the hexagonal lattice, the energy per atom on the densely packed step is twice as large as the kink energy (Fig. 48). In the following, the energy parameter in the Ising is denoted as  $J$ .

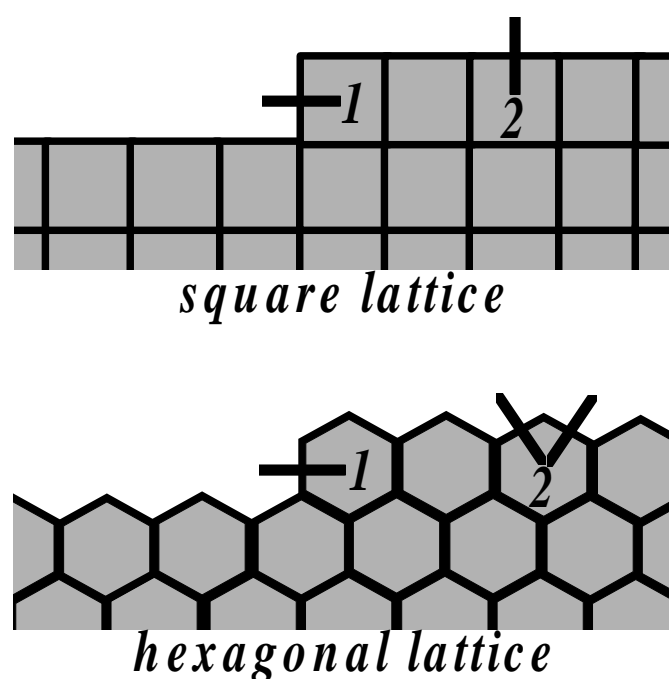


**Fig. 48.** In the Ising model for a square and a hexagonal lattice [96, 97], the energy of a step is proportional to its microscopic length. For the square lattice, the energy of a kink (1) is equal to the step energy per atom (2). In the case of a hexagonal lattice, the energy of a kink(1) is half the step energy per atom (2).

In the Ising model, the equilibrium shapes are given by the implicit expressions [96, 97]

$$\cosh\left[\frac{J(x-y)}{2k_B T}\right] \cosh\left[\frac{J(x+y)}{2k_B T}\right] = A_{\text{sq}} \quad (6.4)$$

with

$$A_{\text{sq}} = \frac{1}{2} \cosh(J/k_B T) \coth(J/k_B T) \quad (6.5)$$

for the square lattice, and

$$\cosh\left(\frac{2yJ}{k_B T}\right) + \cosh\left(\frac{(\sqrt{3}x+y)J}{k_B T}\right) + \cosh\left(\frac{(\sqrt{3}x-y)J}{k_B T}\right) = A_{\text{hex}} \quad (6.6)$$

with

$$A_{\text{hex}} = \frac{\cosh^3(2K^*) + \sinh^3(2K^*)}{\sinh(2K^*)} \quad (6.7)$$

$$\tanh(K^*) = e^{-2J/k_B T}$$

for the hexagonal lattice. The coordinates  $x$  and  $y$  are chosen such that for both lattices the nearly straight sections at low temperature are oriented parallel to the  $x$ -axis. The scaling of the cartesian coordinates is so that  $y(x=0) = \pm 1$  in the limit  $\exp(-J/k_B T) \ll 1$ , and that the size of islands described by (6.4)-(6.7) remains approximately constant with temperature.

For moderately low temperatures, i.e., in the limit  $\exp(-J/k_B T) \ll 1$ ,  $A_{\text{sq}}$  and  $A_{\text{hex}}$  can be approximated by

$$A_{\text{sq}} = \frac{1}{4} e^{\frac{J}{k_B T}}, \quad (6.8)$$

$$A_{\text{hex}} = \frac{1}{2} e^{\frac{2J}{k_B T}}. \quad (6.9)$$

In first order approximation in an expansion of powers of  $\exp(-J/k_B T)$ , the *aspect ratio* of the quasi-straight island edge segments and the corners are given by [88]

$$\frac{r(\theta = 45^\circ)}{r(\theta = 0)} \cong \sqrt{2} \frac{1 - \frac{\ln 2}{J} k_B T}{1 - \frac{2k_B T}{J} e^{-J/k_B T}} \quad (6.10)$$

$$\lim_{T \rightarrow 0} \frac{r(\theta = 45^\circ)}{r(\theta = 0^\circ)} = \sqrt{2}$$

and

$$\frac{r(\theta = 30^\circ)}{r(\theta = 0)} \cong \frac{2}{\sqrt{3}} \frac{1 - \frac{\ln 2}{2J} k_B T}{1 - \frac{k_B T}{J} e^{-J/k_B T}}, \quad (6.11)$$

$$\lim_{T \rightarrow 0} \frac{r(\theta = 30^\circ)}{r(\theta = 0^\circ)} = \frac{2}{\sqrt{3}}$$

for the square and the hexagonal lattice, respectively. Equations (6.10) and (6.11) are good approximations as long as  $2k_B T < J$  [88]. In the limit  $T=0$ , the aspect ratios are  $\sqrt{2}$  and  $2/\sqrt{3}$  for the square and the hexagonal lattice, respectively. In real systems, the aspect ratios may differ significantly from these numbers. Fig. 49 shows the measured aspect ratios  $r_{45^\circ}/r_{0^\circ}$  and  $r_{30^\circ}/r_{0^\circ}$  for Cu(100) as well as Cu(111) and Ag(111), respectively [88]. In accordance with the Ising model (6.10), (6.11), the aspect ratio of Cu islands on Cu(100) are larger than on Cu(111) and the aspect ratio for Ag islands on Ag(111) are comparable with those for Cu(111). The solid lines in Fig. 49 represent fits to the data which will be discussed in the next section. Extrapolation of the data to  $T=0$  yields  $r_{45^\circ}/r_{0^\circ}(T=0)=1.240 \pm 0.010$  for Cu(100) and  $r_{30^\circ}/r_{0^\circ}(T=0)=1.138 \pm 0.008$  for Cu(111) and  $1.136 \pm 0.009$  for Ag(111) [88, 90]. These values differ by about 12%, respectively less than 1.5% from the values obtained within the Ising model (1.41 for (100) and 1.15 for (111); (6.10), (6.11)). The Ising parameter  $J$  is determined by fitting the implicit equations (6.4) and (6.6) (using (6.5), (6.7)-(6.9)) to the experimentally determined equilibrium shapes of the islands as shown in Fig. 47. Fig. 50 shows the equilibrium shape of Cu islands on Cu(100) at 287 and 440K and of Ag islands on Ag(111) at 303 and 406K as thick black lines. The white lines are least square fits to (6.4) and

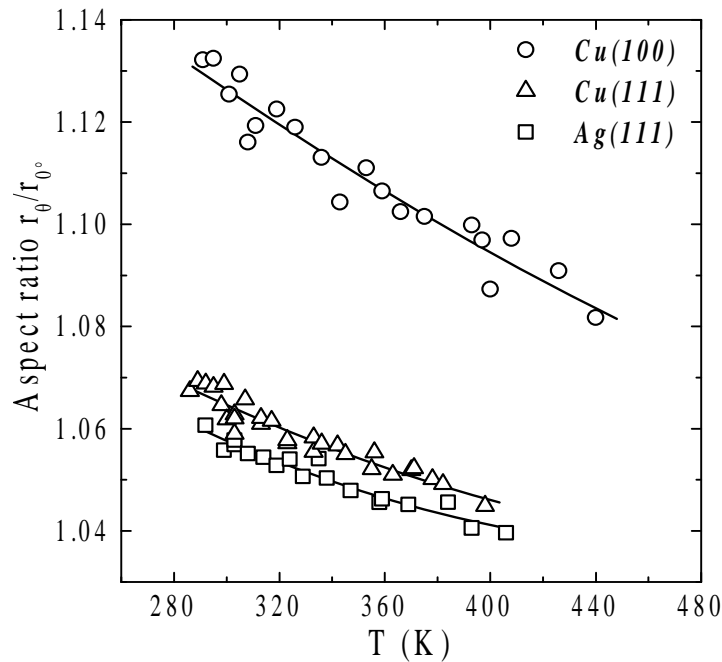


**Fig. 49.** Aspect ratios  $r_0/r_0^*$  of monolayer islands on Cu(100) (circles), Cu(111) (triangles) and Ag(111) (squares) [88]. ( $\theta=45^\circ$  and  $30^\circ$  for (100) and (111) surfaces, respectively.)

(6.6) [88]. By averaging over experimentally obtained equilibrium shapes of several thousand islands at different temperatures one determines the Ising parameter to  $J=84\pm 6\text{meV}$  for Cu(100),  $J=112\pm 7\text{meV}$  for Cu(111) and  $J=104\pm 3\text{meV}$  for Ag(111) [88, 90]<sup>58</sup>.

Breeman and coworkers [253] used the Ising model to determine the nearest-neighbor binding energy for Cu(100) from the equilibrium shape of Cu islands, as well as for studies of the equilibrium shape of islands on Cu(111) and Pt(111) [254]. These studies, however, must be interpreted rather carefully. As discussed before, the aspect ratios determined from the Ising model in the case of (100) surfaces deviates significantly from that of real systems. In the case of (111) surfaces, the Ising result for the aspect ratios is only coincidentally close to that of a real system. The Ising parameter  $J$  must not be interpreted as the kink energy but as a parameter which describes the equilibrium shape, which, in particular, becomes evident for the (100) surfaces. For Cu(100), e.g., the Ising parameter is  $J=84\pm 6\text{meV}$  [88], whereas the kink energy measured from the spatial step correlation function (3.16), (3.19) is  $\varepsilon=128\text{meV}$  [40, 41]. It is noted that (6.4) and (6.6) and the Ising parameter  $J$  may be used to compare kink

<sup>58</sup> It is emphasized at this point that reliable data on the equilibrium shape of islands and the quantitative results discussed in the following required a very large, temperature variable data set! Error bars of less than 10% were achieved only, if the numbers were determined by averaging over 200-300 individual islands at a distinct temperature and if the temperature range was sufficiently large. In all our experimental studies on the equilibrium shape of islands, we analyzed between 5000-10000 islands total, and the temperature range covered about 100-150K starting below room temperature.

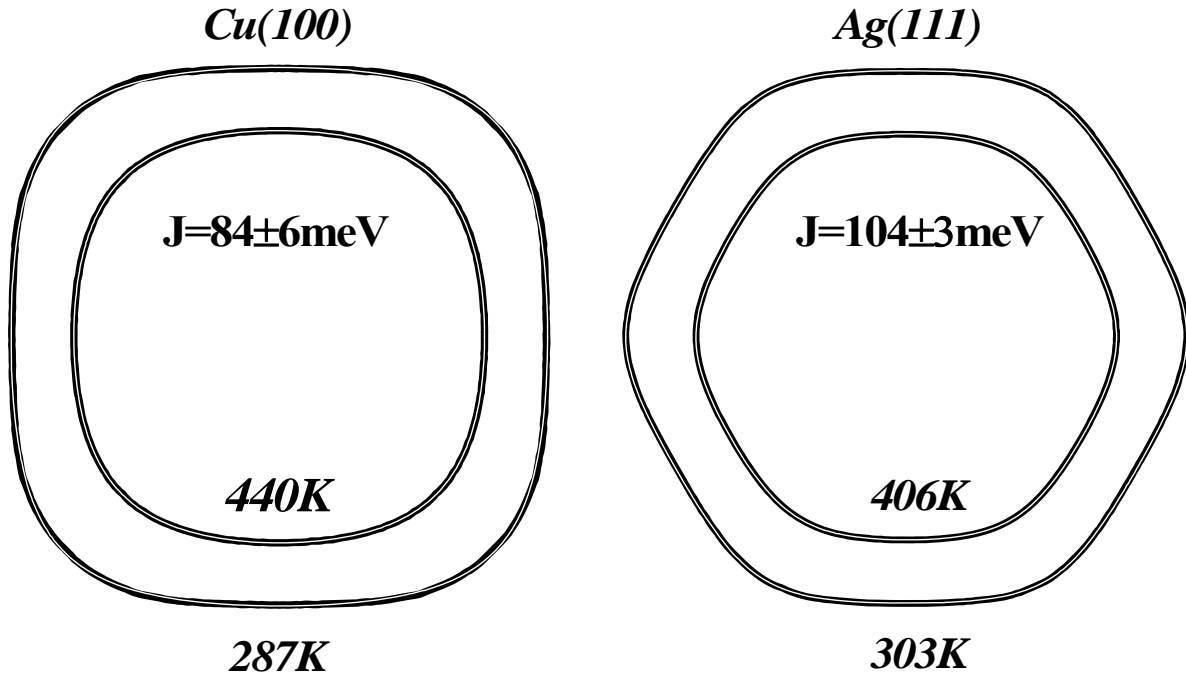


**Fig. 50.** Ising fit according to (6.6) (thin white lines) to the equilibrium shape (thick black lines) of Cu islands on Cu(100) (left hand panel) and Ag islands on Ag(111) (right hand panel) at different temperatures. From an average over various temperatures and several thousand islands one determines the Ising parameters for Cu(100) and Ag(111) to  $J=84\pm 6\text{meV}$  and  $J=104\pm 3\text{meV}$ , respectively [88]. Note, the deviation of the optimized Ising fit to the experimental equilibrium shape in particular for the (100) surface at low temperature.

energies for different systems: If the kink energies of two different systems are unknown, the Ising parameter  $J$ , however, can be determined and is about equal for both systems, the kink energies must be likewise of about the same magnitude. As is discussed in Section 7, this method can be used to obtain reasonable estimates for kink energies on metal electrodes in liquid environment, if values for the same surfaces in UHV are available.

### 6.1.3. Determination of kink and step energy by analyzing curvature of quasi-straight edge segments of islands

An interesting alternative to the determination of the kink energy from the step correlation function (Section 3.3.1) is the analysis of the curvature of the quasi-straight edge segments of islands [88]. According to (3.6)-(3.8), the chemical potential of quasi-straight sections at  $\theta=0$ , i.e.,  $x=0$  is

$$\mu = a_{\parallel} a_{\perp} \tilde{\gamma}(\theta=0) \left. \frac{\partial^2 y}{\partial x^2} \right|_{(x=0)}. \quad (6.12)$$

The chemical potential of an island is the derivative of the free energy with respect to the number of particles in the island. At  $T=0$ , one derives from (6.12) for the square and the hexagonal lattice a generalized Gibbs-Thomson relation

$$\mu(T=0) = a_{\parallel} a_{\perp} \frac{\gamma(\theta=0)}{y(x=0)}, \quad (6.13)$$

which holds also in the limit of high temperatures, where islands assume a circular shape and  $\gamma(\theta)$  is constant and according to (3.8)  $\tilde{\gamma} = \gamma$ . Then, (6.13) is the Gibbs-Thomson relation  $\mu = \Omega \gamma/r$ . One may assume that (6.13) is also a good approximation in the intermediate temperature range [88]. Combining (6.12) and (6.13) yields

$$y \frac{\partial^2 y}{\partial x^2} \tilde{\gamma} = \gamma. \quad (6.14)$$

The step stiffness  $\tilde{\gamma}$  can be expressed in terms of the diffusivity  $b^2$  (3.17), (3.18), (3.19) and therefore<sup>59</sup>

$$y \frac{\partial^2 y}{\partial x^2} k_B T \approx 2\gamma \frac{a_{\perp}^2}{a_{\parallel}} e^{-\frac{\varepsilon}{k_B T}}. \quad (6.15)$$

For islands on a (111) surface with different energies for the A- and B-steps, one obtains the same result with  $\gamma$  and  $y$  replaced by  $\gamma_{A,B}$  and  $y_{A,B}$ , respectively.

---

<sup>59</sup> In the derivation of (3.17) and (3.18) it is assumed that the energy of a kink is proportional to its length, i.e., the kink energy is equal to the step energy per atom. As will be shown in the following, the step energy is larger than the kink energy. Hence, (3.17) and (3.18) serve as an upper, respectively lower limit for the real value of the diffusivity  $b^2$ . Assuming that the diffusivity  $b^2$  is in between the limits defined by (3.17) and (3.18), the kink concentration  $P_k$  (3.19) and  $b^2$  should differ by only about 1-2% for Cu(100), Cu(111) and Ag(111) up to temperatures about 400K. Hence, (6.15) is a reasonable approximation for the studied systems and the temperature of interest.

According to (6.15), the kink energy is determined by the slope when the left-hand side of (6.15) is plotted in an Arrhenius-plot. The pre-exponential factor contains the step free energy  $\gamma$ . Fig. 51 shows the corresponding Arrhenius-plot we measured for Ag monolayer islands on Ag(111) [88]. The step curvature was obtained from both step types, such that the results correspond to an average over A- and B-steps<sup>60</sup>. From a linear fit to the data one finds a kink energy of  $\varepsilon=101\pm 5\text{meV}$  and a step energy of  $\gamma=0.17\times 10^{\pm 0.28}\text{eV a}_{\parallel}^{-1}$ . We performed the measurement of the step curvature also for Cu(100) and Cu(111) and found kink energies of  $\varepsilon=129\pm 9$  and  $117\pm 6\text{meV}$ , respectively [88, 90]. For Cu(100), the kink energy has been previously determined more accurately by analyzing the step correlation function (3.16) to  $\varepsilon=128\pm 3\text{meV}$  [40, 41], which is in excellent agreement with the result we obtain from the analysis of the island curvature. The kink energy determined for Cu(111) may be compared with theoretical calculations by Feibelman [91], who finds  $\varepsilon=92$  and  $117\text{meV}$  for A- and B-steps, respectively. The mean value of both numbers is consistent with our experimental value. The step energies on Cu(100) and Cu(111) determined from the Arrhenius-plot of the curvature are  $\gamma=0.21\times 10^{\pm 0.45}\text{eV a}_{\parallel}^{-1}$  and  $0.24\times 10^{\pm 0.38}\text{eV a}_{\parallel}^{-1}$ , respectively [88, 90]. However, the error bars in the step energies are so large that the numbers serve only as a consistency check.

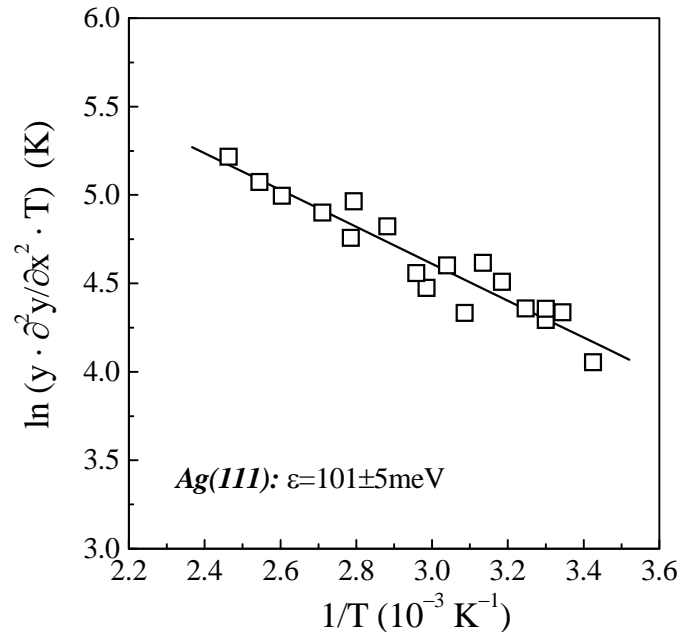


**Fig. 51.** Determination of the kink and the step free energy from the curvature of the quasi-straight island edges according to (6.15) [88].

<sup>60</sup> This is a reasonable method to analyze the data as long as the step and kink energies of A- and B-steps are about equal. This assumption is well fulfilled for Ag and Cu(111), since the islands are almost perfect hexagons.

#### 6.1.4. Determination of absolute step energies from aspect ratio of islands

The theoretical expressions for the aspect ratios as obtained within the Ising model (6.10), (6.11) can be extended to the more general problem of non-Ising systems. If  $\gamma(\theta, T)$  denotes the specific free step energy at an angle  $\theta$  and temperature  $T$ , one finds [88, 90]

$$\frac{\gamma(\theta_k, T)}{\gamma(0, T)} \left( 1 - \frac{2k_B T}{a_{\parallel} \gamma(0, 0)} e^{-\varepsilon/k_B T} \right) = \frac{\gamma(\theta_k, 0)}{\gamma(0, 0)} - \frac{\ln Z(T)}{a_k a_{\parallel} \gamma(0, 0)} k_B T. \quad (6.16)$$

Here,  $\theta_k$  denotes the angle for the hundred per cent kinked step for the square and the hexagonal lattice ( $\theta_k=45^\circ$  and  $30^\circ$ , respectively). The scaling factor  $a_k$  is introduced by the difference in the length per atom of a kinked step on the square and the hexagonal lattice ( $a_k=1/\sqrt{2}$  and  $\sqrt{3}/2$ , respectively).  $Z(T)$  is the partition function of a kinked step which considers all microscopic realizations of the step while retaining its mean orientation. Fig. 52 illustrates possible realizations on a square and a hexagonal lattice. The center path is marked by a thick black line. In the macroscopic limit of a very long kinked step the contribution of all paths except the ones adjacent to the center path (thick dashed lines) vanishes. These paths

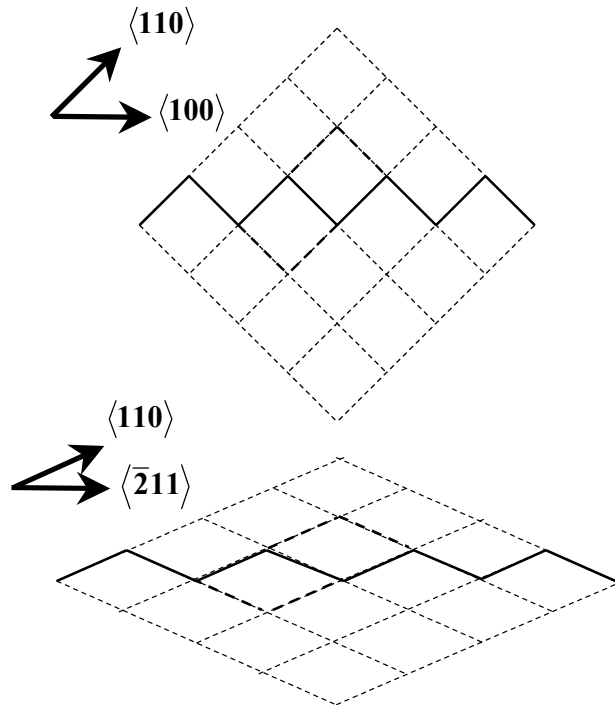


**Fig. 52.** Illustration of lowest energy (thick solid line) and adjacent energy (thick dashed lines) paths of 100% kinked steps on a square and hexagonal lattice for the determination of the partition function in (6.17). The adjacent paths are constructed from the lowest energy path by removal or addition of one atom.

next to the center path are realized by adding or removing one atom. In the Ising-model all paths of equal length (thin dashed lines) have equal energy. In reality this may not be the case, because corner effects may introduce slight energy deviations. If the energy differences are not too large, one may still consider only the paths with the largest statistical weight which are the paths adjacent to the center path. If one denotes the energy per atom between the center path and its adjacent path as  $\Delta E_b$ , the partition function  $Z(T)$  is [88]

$$Z = 2 \cosh\left(\frac{\Delta E_b}{2k_B T}\right) \cong 2 + \frac{2}{2!} \left(\frac{\Delta E_b}{2k_B T}\right)^2 + \frac{2}{4!} \left(\frac{\Delta E_b}{2k_B T}\right)^4 \dots \quad (6.17)$$

If the partition function is purely entropic ( $\Delta E_b=0$ ,  $Z=2$ ), the temperature dependence of the left-hand side of (6.16) is linear in  $T$ .

The three unknown parameters in (6.16) -  $\gamma(0,0)$ ,  $\gamma(\theta_k,0)$  and  $\Delta E_b$  - can be determined in two ways: Firstly, if  $\Delta E_b$  is negligible, a first estimate on the step energy  $\gamma(0,0)$  is obtained from the slope of the measured aspect ratios vs. temperature, neglecting the kink term on the left side of (6.16). The first estimate of  $\gamma(0,0)$  and the kink energy  $\varepsilon$  (as obtained from the equilibrium shape) are then used to calculate the term involving the kink energy. Then, the left-hand side of (6.16) is plotted once more to obtain a refined value for the step energy. This procedure is repeated until the values of the step energies  $\gamma(0,0)$  and  $\gamma(\theta_k,0)$  converge (which usually occurs after 3-4 rounds) [88, 90]. A second way to determine the three parameters  $\gamma(0,0)$ ,  $\gamma(\theta_k,0)$  and  $\Delta E_b$  is to fit (6.16) self-consistently to the measured aspect ratio directly [88]. This fit requires experimental data with sufficient low noise and measurements extended over a sufficiently wide temperature range. The solid lines in Fig. 49 are fits according to this method. For all three surfaces, the optimum fit is achieved for  $\Delta E_b \approx 0$ , i.e., the energy difference between the center path and the adjacent paths is approximately zero, which is consistent with the previous assumption that the energy difference must not be too large. For the step free energy of the quasi-straight island edge, we find<sup>61</sup>  $\gamma(0,0)=0.22\pm 0.02\text{eV } a_{\parallel}^{-1}$ ,  $0.27\pm 0.03\text{eV } a_{\parallel}^{-1}$  and  $0.25\pm 0.03\text{eV } a_{\parallel}^{-1}$  for Cu(100), Cu(111) and Ag(111), respectively [88]. For the 100% kinked step, we obtain  $\gamma(\theta,0)=0.27\pm 0.02\text{eV } a_{\parallel}^{-1}$ ,  $0.31\pm 0.03\text{eV } a_{\parallel}^{-1}$  and

<sup>61</sup> The value of  $\gamma_{a_{\parallel}}=0.31\text{eV}$  for Cu(111) published in [90] stems from the analysis of a considerable smaller though still large data set. The obvious deviation from this value to the new, more accurate one corroborates once more that reliable data is merely achieved, if a very large data base is used in experimental studies.

$\gamma(0,0)=0.28\pm 0.03\text{eV a}_{\parallel}^{-1}$  for Cu(100), Cu(111) and Ag(111), respectively [88]. The step free energies for the quasi-straight step segments are systematically larger than EMT calculations by Stoltze [81], who finds  $\gamma(0,0)=0.125, 0.208$  and  $0.156\text{eV a}_{\parallel}^{-1}$  for Cu(100), Cu(111) and Ag(111), respectively. Our values are in modest agreement with first principles calculations by Vitos et al. [89], who obtain  $\gamma(0,0)=0.200\text{eV a}_{\parallel}^{-1}$  for Cu(100) and  $0.216\text{eV a}_{\parallel}^{-1}$  for B-steps on Ag(111). Their value for B-steps on Cu(111) ( $\gamma(0,0)=0.380\text{eV a}_{\parallel}^{-1}$ ), however, is considerably larger than our result. Calculations by Feibelman [91] for Cu(111) yield  $\gamma(0,0)=0.27\text{eV a}_{\parallel}^{-1}$  and  $0.26\text{eV a}_{\parallel}^{-1}$  for A- and B-steps, respectively, which are in excellent agreement with our numbers. However, in contrast to what is observed in STM experiments [25, 88, 240], the energy of the A-step is larger than the B-step in the calculations by Feibelman. Reasonable agreement is found between our result for  $\gamma(0,0)$  on Cu(111) and measurements by Schlöber et al. [240], who analyzed island edge fluctuations on Cu(111) and find a step energy of  $\gamma(0,0)=0.22\text{eV a}_{\parallel}^{-1}$ . For the analysis, they make use of a theoretical work by Khare and Einstein [255], in which corner effects for atomic diffusion around the island perimeter are neglected and the step free energy  $\gamma$  is assumed to be isotropic. The reasonable agreement between our result and that of Schlösser et al. for Cu(111) seems to justify the approximations made in the theory of Khare and Einstein.

One may compare the step free energy  $\gamma$  determined from the equilibrium shape of islands also with values obtained in studies of the *Ostwald ripening* [222] of islands. There, the step free energy was determined by numerical integration of the diffusion equation and its fit to the decay curves of monatomic high islands. This method is discussed in detail in Section 6.2. For Ag(111), Morgenstern et al. [249] yield  $\gamma a_{\parallel} = 0.22\text{eV}$ , which is in good agreement with our result. In the case of Cu(111), however, no agreement between the results obtained from the island edge curvature and from the Ostwald ripening is achieved. From the latter, we determined the step free energy on Cu(111) to  $\gamma a_{\parallel} = 0.45\text{eV}$  [200], which is much larger than what we measure from the analysis of the curvature of the island shape. The reason for this deviation is so far not understood. Table 6 gives an overview over step energies for Cu, Ag and Pt surfaces obtained from experiment, as well as from theoretical calculations in columns 5 and 6.

### 6.1.5. Brownian motion of islands

Due to step-edge fluctuations, the center of mass of islands engage in a random walk across the surface, i.e., islands perform a Brownian motion. The Brownian motion of clusters was first observed by Masson et al. [256] for small Au crystals on a KCl substrate. More recently, de la Figuera et al. [257] published STM experiments on the vacancy island mobility on a Co covered Cu(111) surface and found that the motion of the vacancy islands is Brownian-like. For unknown reasons, these authors did not observe a mobility of vacancy islands on the clean Cu(111) surface at room temperature, which was found on Cu(111) in more recent STM studies by our group [201] and Rosenfeld and coworkers [258]. On clean Ag(111), the mobility of islands was extensively studied by Morgenstern and coworkers [47, 258]. Fig. 53(a) shows a series of STM images (30nm width) of a vacancy island located within another vacancy island on Cu(111) at 358K. Fig. 53(b) displays the trace of an adatom island on top of another adatom island on Cu(111) at 300K over a total time span of approximately 3h. Adatom and vacancy islands on Cu(111) are very mobile already at room temperature similar to what is observed on Ag(111) [47]. The mean square displacement of an island is given by the diffusion equation

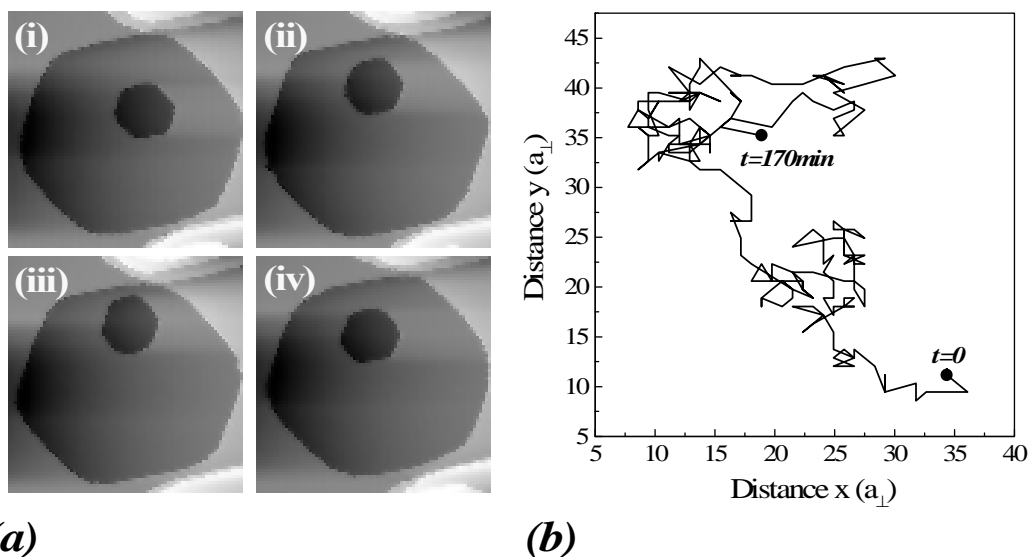


**Fig. 53.** (a) Subsequent STM images taken from a movie of a vacancy island within a vacancy island on Cu(111) at 358K. The area shown in the images is  $30 \times 30 \text{ nm}^2$  and the total time between the images (i) and (iv) is 30min. Adatom and vacancy islands undergo a Brownian motion, due to edge fluctuations. Panel (b) shows the trace of an adatom island on top of another adatom island on Cu(111) at 300K. The actual coordinate (x,y) of the upper adatom island is measured with respect to the center of mass of the lower adatom island. The black dots indicate the initial and final position of the upper island at  $t=0$  and  $t=170\text{min}$ .

$$\langle (\Delta x)^2 \rangle = 2Dt, \quad (6.18)$$

if the motion of the island is completely random [259].  $D$  is the diffusion coefficient. In temperature and island size dependent data, Morgenstern, Rosenfeld and coworkers could show that the mean square displacement of an island depends linearly on time, and hence, proved that the island motion is Brownian-like [47, 258, 260]. Khare and Einstein [255] and, in a more simple theoretical description based on a paper by Pimpinelli et al. [98], Morgenstern et al. [47] showed that  $D$  scales with the island size  $N$ , where  $N$  is the number of particles in the island:

$$D \propto N^{-\alpha}. \quad (6.19)$$

The exponent  $\alpha$  depends on the dominant mass transport mechanism causing the migration of the islands.  $\alpha$  is 3/2 for periphery diffusion,  $\alpha$  is 1 for terrace diffusion, and  $\alpha$  is 1/2 for evaporation/condensation<sup>62</sup> (analog to the cases (vi), (iv), (iii) in Section 3). The concept of universal exponents is based on the assumption that the number of adatoms  $n_p$  at the island periphery, which are responsible for the migration process, are proportional to  $\sqrt{N}$ . Furthermore, effects by the presence of kinks and island corners are neglected and  $n_p$  and  $\alpha$  are temperature independent and not influenced by the system itself. *Kinetic Monte-Carlo* simulations (KMC) by Voter [261], Sholl and Skodje [262], Bogicevic et al. [263], Heinonen et al. [264] and Müller and Selke [265], as well as thermodynamic arguments reported by Metiu and Rosenfeld [266], however, show that these assumptions are not justified. Experimentally, following Khare and Einstein, Morgenstern et al. find for Ag islands on Ag(111) at room temperature an exponent close to 1, which initially was interpreted as evidence for terrace diffusion [47]. This conclusion is contradictory to our recent analysis of equilibrium step fluctuations, where we showed that edge diffusion prevails below 450K on Ag(111) at least at short times [42]. Kürpick et al. [267] also demonstrate in their molecular dynamics simulations that edge diffusion should be the dominant process underlying vacancy island diffusion. In other experiments on Cu(100) and Ag(100) by Bartelt and coworkers and by Pai et al., non-universal exponents were found [268-272]. In recent experiments, Schlöber et al. [273, 274] measured exponents 0.7 and 0.95 for vacancy islands on Cu(111) at 318 and

---

<sup>62</sup> Sometimes, the diameter of an island  $d$  is used instead of the number of atoms  $N$  in the island to define (6.19). Then, the scaling exponent  $\alpha$  is 3, 2 and 1, if the Brownian motion of the islands is dominated by edge diffusion, terrace diffusion and evaporation/condensation, respectively.

348K, respectively. They concluded that the scaling exponents in experiments are lower than expected from the theory of Khare and Einstein [255]. Bogicevic et al. emphasized that the most critical point in experimental studies is to make sure that only *a single* mass transport mechanism contributes to the Brownian motion of islands [263]. This, however, is difficult to achieve, since the islands have a non-uniform size and undergo Ostwald ripening [220, 221, 275, 276], in which mass is exchanged between islands and mass is also lost to steps (see Section 6.2.1). Furthermore, the Brownian motion may be affected by the long-time behavior of edge fluctuations, which may be dominated by a different mass transport process than the short-time behavior: For Cu(111) and Ag(111), we showed that edge diffusion prevails at short times, whereas fast terrace diffusion dominates at long times (Section 3.3.5) [111]. Hence, a non-universal scaling exponent of the Brownian motion of islands may be indicative of the contribution of different mass transport processes to the island wandering. In summary, one might say that the theory of island migration and the interpretation of experimental results is still very controversial and a better understanding is necessary for the future.

## 6.2. Coarsening of monolayer island structures

### 6.2.1. Ostwald ripening of islands

The classical theory of Ostwald ripening was established for 3-dimensional particles in colloidal liquids by Lifshitz and Slyozov [275] and Wagner [220]. For the 2-dimensional problem of islands on surfaces, it was then derived by Chakraverty [276] and Wynblatt and Gjostein [221]. The classical Ostwald theory of island ripening is formulated for an individual circular island with radius  $r_i$  among other islands. The island is surrounded by a circular (2-dimensional) sphere with constant radius in which the adatom concentration is a mean adatom concentration field formed by the other islands.

Island configurations with fixed boundary conditions, which may be realized in experiment and solved analytically under certain assumptions, are displayed in Fig. 54: An adatom island is located in the center of a larger circular vacancy island of radius  $r_o$  (upper left panel). Analog configurations are the vacancy island within an adatom island (lower left panel), a vacancy island within a vacancy island (upper right panel) and an adatom island on top of another adatom island (lower right panel). The chemical potential of a circular island is determined by its radius  $r$  via the Gibbs-Thomson relation

$$\mu(r) = \Omega \frac{\gamma}{r}. \quad (6.20)$$

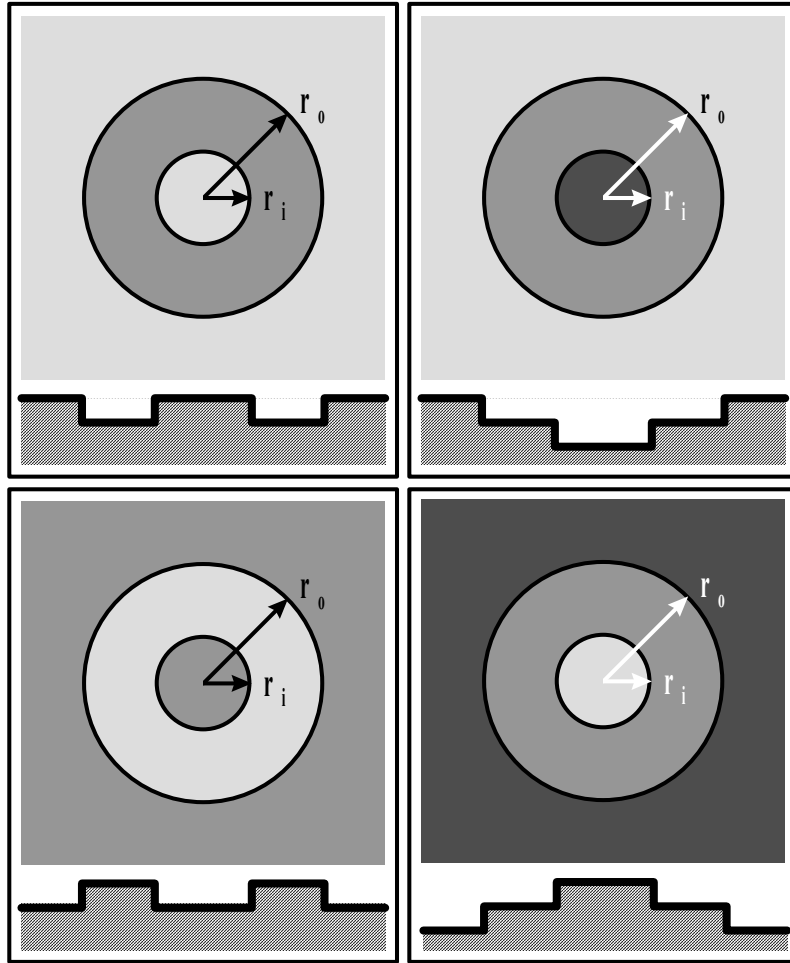


**Fig. 54.** Illustration of the island and vacancy island configurations with analytically solvable boundary conditions. Upper left: adatom island within a vacancy island; upper right: vacancy island within a vacancy island; lower left: vacancy island within an adatom island; lower right: Adatom island on top of an adatom island. The inner and outer radii are denoted as  $r_i$  and  $r_o$ , respectively.

$\gamma$  is the step line tension and equal to the step edge stiffness  $\tilde{\gamma}$  (3.19), (3.20) for a circular island and  $\Omega$  is the area of an atom<sup>63</sup>. Equation (6.20) is the high-temperature limit of (6.12) and (6.13), when the islands assume a circular shape. We showed that (6.20) holds also for hexagonal and quadratic islands, however, a *shape factor*  $\eta$  is introduced, which relates an island with side length  $s$  to an equivalent circular island with radius  $R$  with the same area [200]:

<sup>63</sup> The atomic area is given by  $\Omega = a_{\parallel} a_{\perp}$  for fcc metal surfaces,  $a_{\parallel}$  and  $a_{\perp}$  being the distance between atomic rows along and perpendicular to the dense  $\langle 110 \rangle$ -direction.

$$\mu(r) = \eta \Omega \frac{\gamma}{R}; \quad \eta = \sqrt{\frac{2\sqrt{3}}{\pi}} \text{ (hexagonal)}, \eta = \frac{2}{\sqrt{\pi}} \text{ (square)}. \quad (6.21)$$

The gradient in chemical potential between the edge of the inner and the outer island radius gives rise to a mass current between the islands (Fig. 55). In the following, the change of the island size as a function of time will be considered.

The number of atoms per time unit attaching to the perimeter of the inner island is given by

$$j_{\text{att}} = -\kappa \rho(r_i), \quad (6.22)$$

where  $\kappa$  is a rate constant.  $\rho(r_i)$  is the concentration of adatoms per atom on the terrace in close proximity to the inner island radius  $r_i$ . In equilibrium, the adatom concentration is equal to the equilibrium concentration  $\rho_{\text{eq}}(r_i)$ , and the mass current detaching from the perimeter of the island is equal in magnitude to the attaching current, however, with opposite sign:

$$-j_{\text{det}} = -\kappa \rho_{\text{eq}}(r_i) = j_{\text{att}}. \quad (6.23)$$

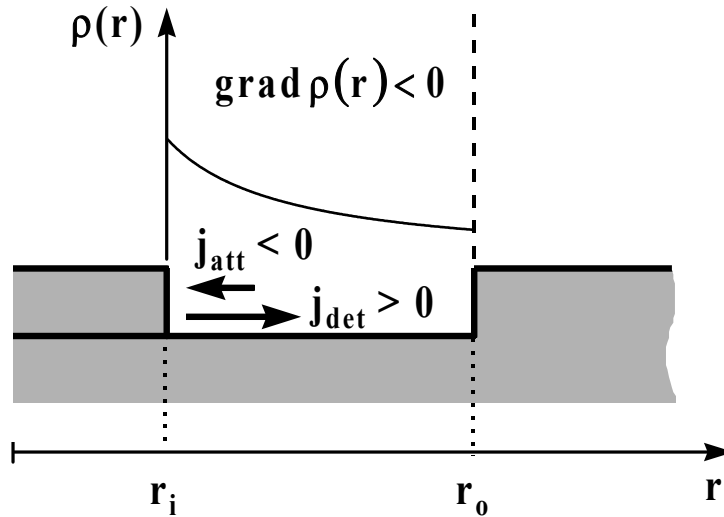


**Fig. 55.** Illustration of the notation used in this report to derive the decay equations: An adatom island with radius  $r_i$  is located in the center of a larger vacancy island with radius  $r_o$ . The radial coordinate  $r$  is measured from the center of the adatom island. The detaching mass current  $j_{\text{det}}$  is positive whereas the (smaller) attaching current  $j_{\text{att}}$  is negative. The adatom concentration  $\rho(r)$  decays as  $1/r$  from the inner to the outer island radius.

If the real concentration at the perimeter of the island deviates from the equilibrium value, the *attachment* current varies according to (6.22). The *detachment* current does not change, since the detachment is not affected by the concentration in the final state, as long as the adatom concentration is small. The net current at the island perimeter is thus

$$j_{\text{net}} = j_{\text{det}} + j_{\text{att}} = \kappa \left( \rho_{\text{eq}}(r_i) - \rho(r_i) \right). \quad (6.24)$$

The net current flow must match the flow by terrace diffusion  $j_{\text{diff}}$

$$j_{\text{net}} = j_{\text{diff}} = -v_{\text{diff}} a \text{grad} \rho(r_i), \quad (6.25)$$

where the hopping rate on the terrace is denoted as  $v_{\text{diff}} = v_0 \exp(-E_{\text{diff}}/k_B T)$ . The constant  $a$  in (6.25) is given in atomic units and is related to the atomic distance between equivalent lattice positions<sup>64</sup>. The rate constant  $\kappa$  of the attaching current (6.22) can be interpreted as the product of the hopping rate on the terrace and an additional sticking rate  $s$  at the island perimeter,  $\kappa = s v_{\text{diff}}$ . As illustrated in Fig. 56, the sticking factor  $s$  is the ratio of the sticking rate  $v_{\text{stick}} = v_0^* \exp(-(E_{\text{stick}} + E_{\text{diff}})/k_B T)$  and the diffusion rate  $v_{\text{diff}}$ .  $E_{\text{stick}}$  is the additional sticking barrier. For  $s=1$ , no additional sticking barrier is present; for  $s=0$ , the barrier is infinitely large. Equations (6.24) and (6.25) define a differential equation for the adatom

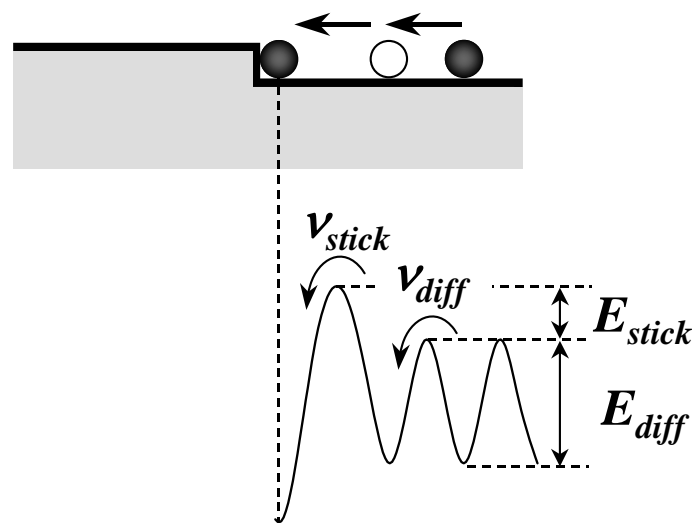


**Fig. 56.** Potential model of the additional energy barrier for sticking of an adatom at an island edge.

<sup>64</sup> For a square lattice,  $a$  is equal to the nearest neighbor distance  $a_{ij}$ . In the hexagonal case, it corresponds to the distance between 3-fold fcc hollow sites.

concentration:

$$\rho(r_i) - \frac{a}{s} \text{grad } \rho(r_i) = \rho_{\text{eq}}(r_i). \quad (6.26)$$

The adatom concentration obeys the equation for stationary diffusion which is the Laplace equation. The solution is<sup>65</sup>

$$\rho(r_i) = \ln \left| \frac{r_i}{r_o} \right| \frac{\rho_{\text{eq}}(r_i) - \rho_{\text{eq}}(r_o)}{\ln \left| \frac{r_i}{r_o} \right| - \frac{a}{sr_i}} + \rho_{\text{eq}}(r_o). \quad (6.27)$$

Hence, one finds for the net mass current

$$j_{\text{net}} = v_{\text{diff}} \frac{a}{r_i} \frac{\rho_{\text{eq}}(r_i) - \rho_{\text{eq}}(r_o)}{\ln \left| \frac{r_o}{r_i} \right| + \frac{a}{sr_i}}. \quad (6.28)$$

The reduction rate of particles N in the island with time is then given by

$$\begin{aligned} \frac{dN}{dt} &= -j_{\text{net}} \frac{2\pi r_i}{a} \\ \frac{dN}{dt} &= -2\pi v_{\text{diff}} \frac{\rho_{\text{eq}}(r_i) - \rho_{\text{eq}}(r_o)}{\ln \left| \frac{r_o}{r_i} \right| + \frac{a}{sr_i}}. \end{aligned} \quad (6.29)$$

The equilibrium concentration is  $\rho_{\text{eq}}(r_i) = \rho_{\infty} \exp(\mu(r_i)/k_B T)$  with  $\mu = \eta\gamma\Omega/r_i$  (6.21) the chemical potential and  $\rho_{\infty} = \exp(-E_{\text{ad}}/k_B T)$  the equilibrium adatom concentration on the terrace. Hence,

---

<sup>65</sup> Note, for a vacancy island, the curvature of the island perimeter is negative. Hence, the radius  $r_o$  at the outer island perimeter is interpreted as negative variable. In the case of an adatom island on top of another adatom island, the outer island perimeter is positive and for the problem of a vacancy island within a vacancy island both radii are negative.

$$\rho_{\text{eq}}(r_i) = e^{-\frac{E_{\text{ad}}}{k_B T}} e^{-\frac{\eta\gamma\Omega}{k_B T r_i}}. \quad (6.30)$$

From (6.29) then follows with  $v_{\text{diff}}=v_0 \exp(-E_{\text{diff}}/k_B T)$  and the island area  $A=N\Omega$ :

$$\frac{dA}{dt} = -2\pi v_0 \Omega e^{-\frac{E_{\text{ad}}+E_{\text{diff}}}{k_B T}} \frac{e^{-\frac{\eta\gamma\Omega}{k_B T} \left( \frac{1}{r_i} - \frac{1}{r_o} \right)}}{\ln \left| \frac{r_o}{r_i} \right| + \frac{a}{sr_i}}, \quad (6.31)$$

which allows approximations for two limiting cases:

(i) *Diffusion limited island decay*:  $s=1$

For  $s=1$ , i.e.  $\kappa=v_{\text{diff}}$ , the detachment of atoms at the island edge is fast compared to the diffusion on the terrace. With  $a/r_i \ll \ln|r_o/r_i|$  and with the additional, not necessarily fulfilled approximation  $\exp(\eta\gamma\Omega/r_{i,o}) \approx \eta\gamma\Omega/r_{i,o}$ , one obtains

$$\frac{dA}{dt} \approx -\frac{2\pi v_0 \Omega}{\ln \left| \frac{r_o}{r_i} \right|} e^{-\frac{E_{\text{ad}}+E_{\text{diff}}}{k_B T}} \frac{\eta\gamma\Omega}{k_B T} \left( \frac{1}{r_i} - \frac{1}{r_o} \right). \quad (6.32)$$

By neglecting further the time dependence of  $\ln|r_o/r_i|$ <sup>66</sup>, one has  $dA/dt \propto 1/r_i$ . With  $A=\pi r_i^2$  it follows that

$$A(t) \propto (t-t_0)^{2/3} \quad \text{or} \quad r_i(t) \propto (t-t_0)^{1/3}. \quad (6.33)$$

Hence, if the sticking probability is 1 and diffusion on the terrace is slow compared to the detachment/attachment of atoms at the inner island edge (*diffusion limited*), the time dependence of the island area scales approximately as  $t^{2/3}$ . Note that the effective exponent in (6.33) decreases if the step line tension  $\gamma$  increases. This is a consequence of the approximation  $\exp(\eta\gamma\Omega/r_{i,o}) \approx \eta\gamma\Omega/r_{i,o}$  used in (6.32). Therefore, smaller exponents may be measured in experiment, in particular when small islands are analyzed and if  $\gamma$  is large.

<sup>66</sup> Note that this approximation may be not justified since the radii of the inner and the outer island perimeter change in time and in particular the ratio of the radii may depend significantly on the time.

(ii) *Detachment limited island decay*:  $s \ll 1$

For  $s \ll 1$ , a finite energy barrier reduces the sticking probability of atoms at the island edge such that atom attachment/detachment is slow compared to terrace diffusion. Then, with the assumption  $\exp(\eta\gamma\Omega/r_{i,o}) \approx \eta\gamma\Omega/r_{i,o}$  as before one obtains

$$\frac{dA}{dt} \approx -2\pi v_0 s \Omega e^{-\frac{E_{ad} + E_{diff}}{k_B T}} \frac{\eta\gamma\Omega}{a k_B T} \left(1 - \frac{r_i}{r_o}\right), \quad (6.34)$$

i.e.,  $dA/dt \propto \text{const.}$ . The time dependence of  $A$  and  $r_i$  is therefore

$$A(t) \propto (t - t_0) \text{ or } r_i(t) \propto (t - t_0)^{1/2}. \quad (6.35)$$

Hence, if diffusion on the terrace is fast compared to the detachment/attachment of atoms at the inner island edge (*detachment limited*), the island area decays linearly in time.

It is noted that the limiting cases (6.33) and (6.35) are valid only under the following assumptions: First, the island/vacancy island should be located in the center of another vacancy island or on top of an adatom island. Second, the ratio of the outer and inner island radii must be approximately time independent. And finally, the islands must be large such that the assumption of a small line tension  $\gamma$  is justified.

Early semi-quantitative island decay studies were published by Jaklevic and Ellie [277] and Peale and Cooper [278]. These authors analyzed the time dependence of Au adatom and vacancy island decay on Au(111) around room temperature in UHV. They find that the decay is detachment limited. Since then, quite a number of quantitative experimental studies of the Ostwald ripening of islands were performed on metal [106, 200, 246, 249, 270, 271, 274, 279-284] as well as semiconductor [285, 286] surfaces. The basic problem in experimental studies of the Ostwald ripening of islands is the mean-field condition. In an early work of Theis et al. [285] it was shown that for an ensemble of adatom islands on a large flat terrace the mean-field approximation of a constant adatom concentration field does not necessarily hold. The local adatom concentration field of an island is rather determined by the nearest-neighbor islands. Their work showed that the decay of islands on Si(100) is well described by a nearest-neighbor approach, in which Voronoi polygon cells [287] are located around each island. In the Voronoi cell of a distinct island, the local adatom concentration field is exclusively

determined by the chemical potential of the nearest-neighbor islands<sup>67</sup>. Fig. 57 shows LEEM images of Si adatom islands on Si(100) at 670°C at (i) 50s and (ii) 400s after deposition [285]. The black and white regions correspond to different layers. In (iii) and (iv), the corresponding theoretically determined island distributions after 400s are displayed using a mean-field and a nearest-neighbor approach, respectively. Obviously, the island distribution is not described by the mean-field approach, whereas the nearest-neighbor model provides reasonable agreement

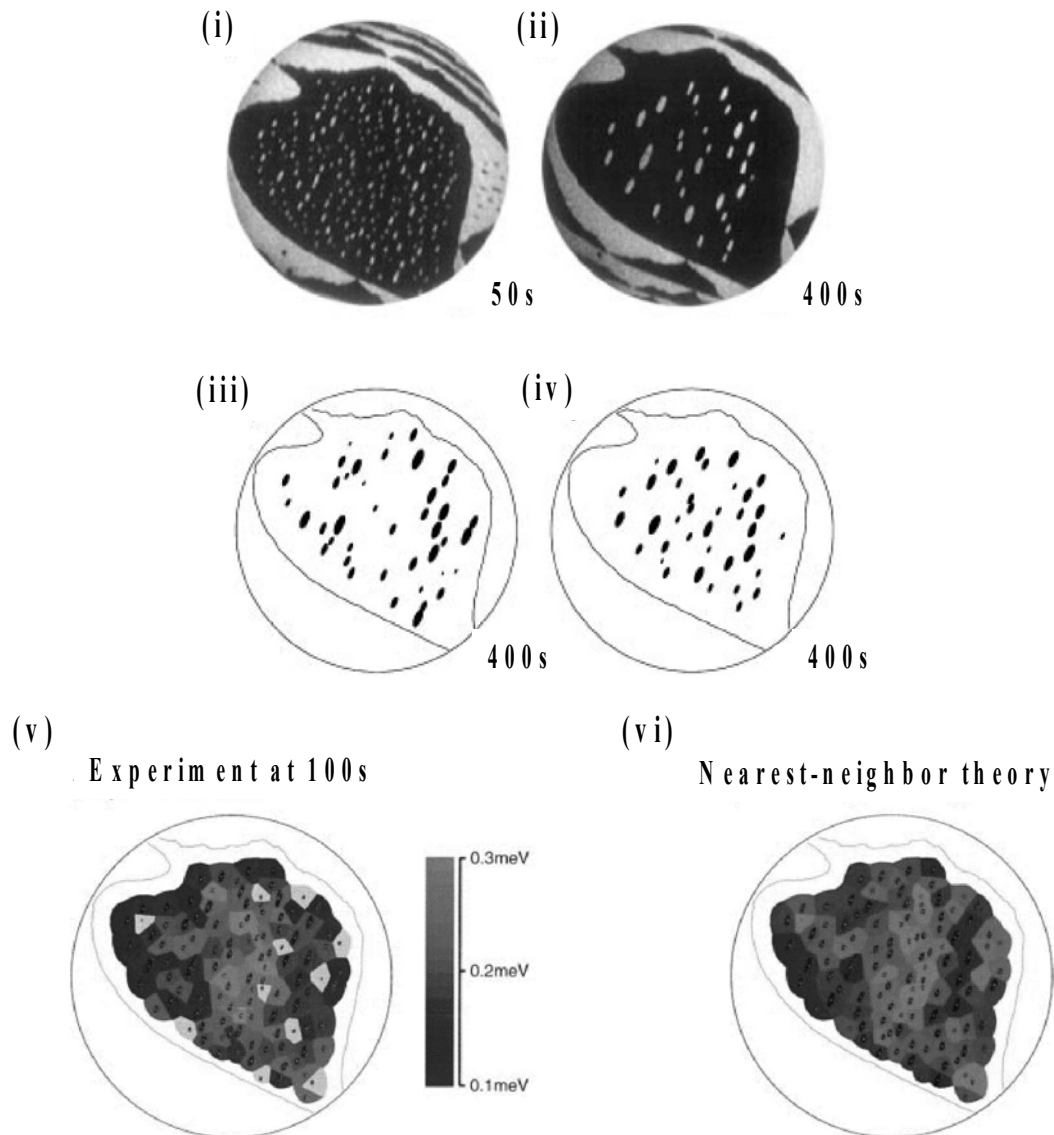


**Fig. 57.** LEEM images of Si adatom islands (bright) on a Si(100) terrace (dark) at 670°C at (i) 50s and (ii) 400s after deposition. In (iii) and (iv) simulations of the island distributions at 400s are shown using a mean-field and a nearest-neighbor approach, respectively. The chemical potential maps as determined at 100s (v) from the experimental data and (vi) as determined within the nearest-neighbor approach are displayed (after Theis et al. [285]).

<sup>67</sup> Bartelt et al. [288] showed that the Voronoi polygon tessellation is also an adequate model to describe the adatom capture of islands on Ag(100) during deposition.

between simulation and experiment. Figs. 57(v) and (vi) show the Voronoi cell constructions for the experimental island distribution as well as for the distribution obtained from the nearest-neighbor model after 100s. Different gray scales correspond to differences in the chemical potential around each island. Although local deviations between the experimentally and theoretically determined chemical potentials around the islands exist, the overall agreement is reasonable.

Morgenstern et al. [279] bypassed the problem of island interactions during decay by investigating isolated islands on Ag(111). Fig. 58 shows the radius of an island vs. time at room temperature. From this curve, they find a time exponent of the island radius of 0.27, which is smaller but close to the exponent  $1/3$  for diffusion limited decay (6.33). It was concluded that the measured exponent is smaller than  $1/3$ , because the studied islands were too small to justify the assumption  $\exp(\eta\gamma\Omega/r_{i,0}) \approx \eta\gamma\Omega/r_{i,0}$  as used in the derivation of (6.32). For small islands,  $\gamma$  becomes large and the use of the linear approximation of the exponential causes a reduction of the decay exponent. We obtained similar results for adatom islands on Cu(111), where  $r(t)$  is proportional to  $t^{0.27 \pm 0.02}$  [201]. It was also demonstrated that the influence of the local environment on the decay of an individual island may be directly visible in the decay curves [200, 201]: The top panel of Fig. 59 displays an STM image of Cu adatom islands on a stepped surface area on Cu(111) at 308K. In the panel below, the corresponding time evolution curves of the island areas are shown (numbered curves correspond to

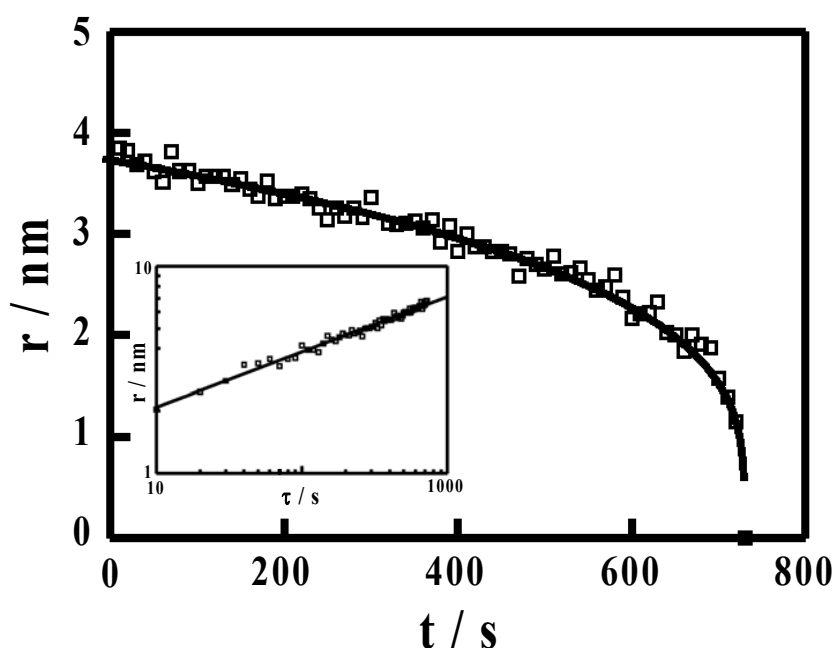


**Fig. 58.** Island radius as a function of time of an isolated Ag adatom island on Ag(111) at room temperature (after Morgenstern et al. [279]).

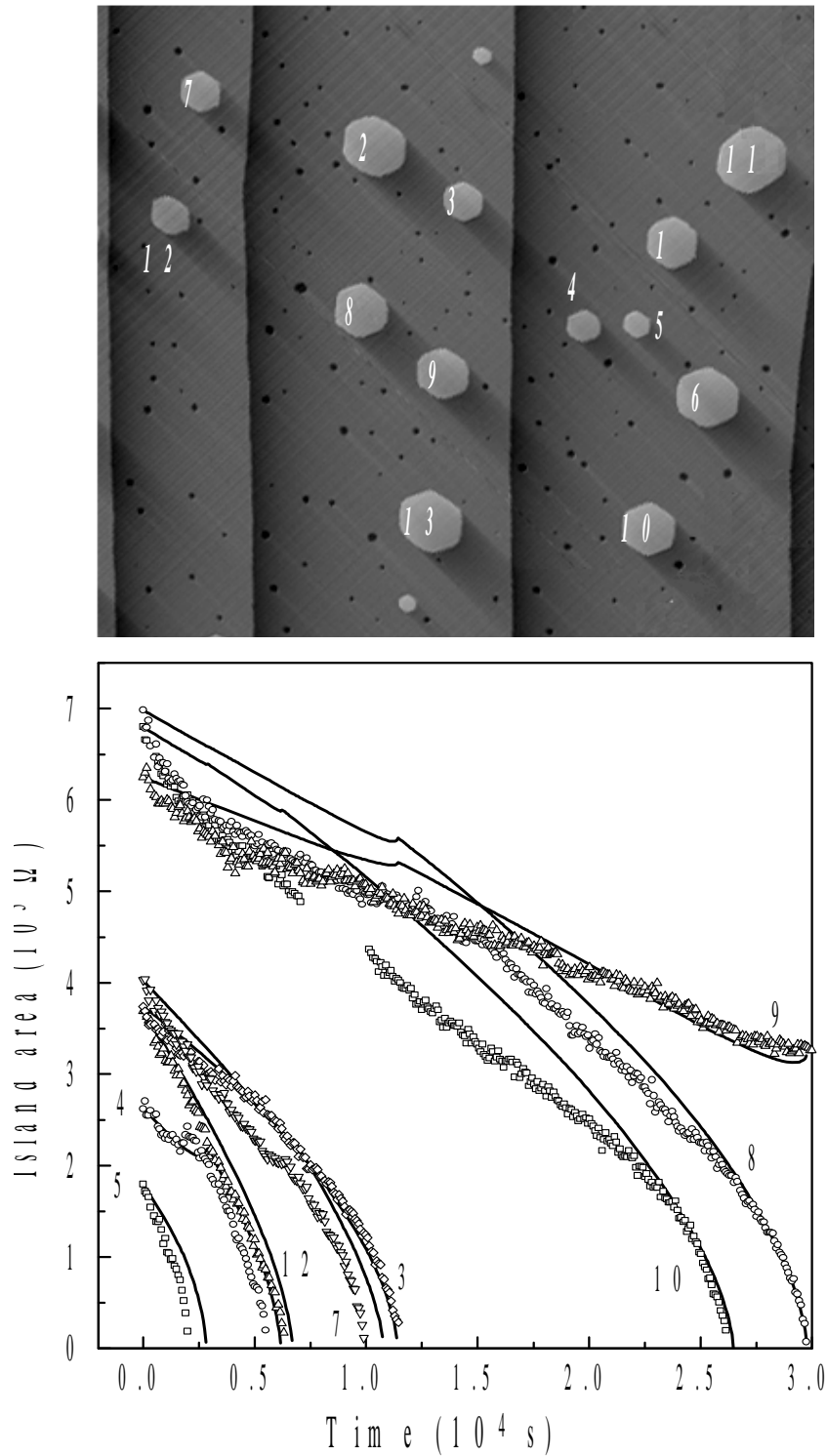


**Fig. 59.** Initial configuration of Cu adatom islands on a stepped Cu(111) surface at 308K. The scan width of the STM image in the upper panel is 300nm. The lower panel shows the corresponding decay curves (symbols). The solid curves are best fits to the data by a numerical integration of (6.32) using  $E_{\text{ad}}+E_{\text{diff}}=0.76\text{eV}$  and  $\gamma=0.45\text{eV}/a_{\parallel}$  [200].

numbered islands in the STM image) [200]. Island 4 is located on a terrace in vicinity to the smaller island 5. Atoms detaching from island 5 during decay most probably attach to island 4. When island 5 is in its final stage of decay (around 200-250s), the decay of island 4 slows down. The adatom capture by island 4 becomes finally evident in a "hiccup" of its decay curve as island 5 eventually vanishes. A similar event is observed for the islands 12 and 7. As a consequence, effective time exponents of these decay curves of the island area vary between 0.57 and 0.73 [200]. The decay curves are well described by numerical integration of (6.31), while simultaneously solving the Laplace equation in order to determine the local adatom concentration gradient on the terrace as well as the local and temporary mass flux to each island [200, 201] (solid curves in the lower panel of Fig. 59)<sup>68</sup>. Best agreement between experimental decay curves and the numerical integration is achieved if  $\gamma=0.45\text{eV } a_{\parallel}^{-1}$  is used in (6.31). The direct observation of the correlation between decaying islands was later also reported for Ag(111) by Morgenstern, Rosenfeld and coworkers. They used two different methods: First [283], they integrated (6.31) numerically and solved the Laplace equation. Second [281], they used the Voronoi polygon ansatz [285] as discussed before.

It is emphasized that even for island configurations as shown in Fig. 55, the measured time exponents deviate significantly from 1/3 and 1/2. It was found that for the diffusion limited decay of Ag adatom islands in larger vacancy islands on Ag(111), the decay exponent is smaller than 1/3 [249, 283]. Fig. 60(a) shows STM images from a similar experiment we performed for Cu(111) [201]: An adatom island is located nearly within the center of a larger vacancy island. Although the adatom island migrates within the vacancy island, it stays close to the center. In Fig. 60(b), the island radius is plotted vs. time. The corresponding time exponent of the island radius is 0.36 and the fit of the decay curve shown in Fig. 60 to (6.31) yields  $\gamma=0.50\text{eV}/a_{\parallel}$ . As an average exponent determined from various individual measurements we obtain  $0.27\pm 0.02$  and  $\gamma=0.53\text{eV}/a_{\parallel}$  [201]. The value of the step line tension is even higher than what is determined by the analysis of adatom island decay on a stepped surface ( $\gamma=0.45\text{eV}/a_{\parallel}$  [200]). Both values are much larger than the value of  $\gamma$  obtained from the equilibrium shape of islands ( $\gamma=0.27\text{eV}/a_{\parallel}$  [88]). The reason for this deviation, which is observed for Cu(111), however, not for Ag(111), is presently not understood. A possible explanation could be an electronic contribution arising from the confinement of surface states and bulk states in the first layer due to the island boundary as discussed by Jin et al. [289].

---

<sup>68</sup> Due to the choice of a special island configuration on a stepped surface as shown in Fig. 59, it could also been shown that an additional step edge barrier for atom diffusion down a step and subsequent attachment at the lower step edge has to be taken into account in order to fit the experimental decay curves properly. From this analysis, we determined also the Ehrlich-Schwoebel barrier on Cu(111) [200].

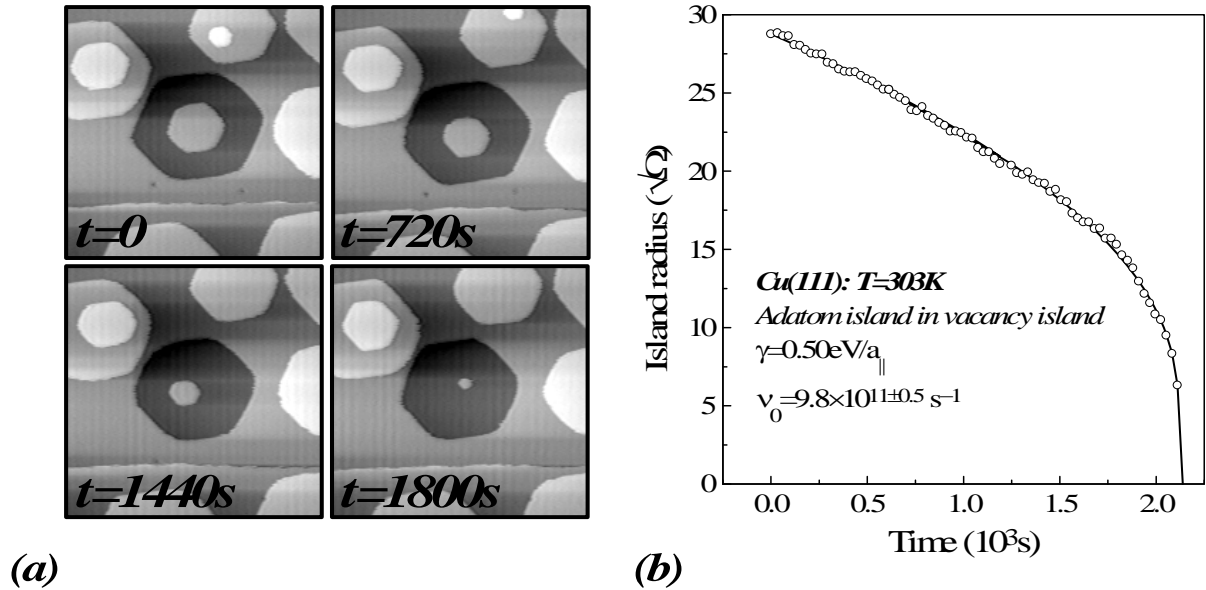


**Fig. 60.** (a) STM images of a Cu adatom island in the center of a large vacancy island on Cu(111) at 303K. The scan width is about 60nm. (b) Radius of the adatom island as a function of time. The measured time exponent of the decay curve for this individual island is  $0.36 \pm 0.01$ . The mean exponent determined from the analysis of several islands is  $0.27 \pm 0.02$  which also deviates significantly from the exponent  $1/3$  for diffusion limited decay (6.33). The solid curve represents the best fit by a numerical integration using  $E_{\text{ad}} + E_{\text{diff}} = 0.76\text{eV}$  [200]. From the best fit one obtains the step free energy to be  $\gamma = 0.50\text{eV}/a_{\parallel}$  and the pre-exponential factor for atom detachment of  $9.8 \times 10^{11} \text{s}^{-1}$  [201].

By a temperature dependent analysis of island decay curves, as shown in Fig. 59, one may determine the activation energy for the adatom island decay: Fig. 61 shows an Arrhenius-plot of the decay rate  $dA/dt$  at fixed size  $A_0 = 1600$  atoms for adatom islands on Cu(111) [200]. From the slope we find an activation energy of  $0.76 \pm 0.05\text{eV}$ . According to (6.32), this energy barrier corresponds to the sum of the adatom formation energy  $E_{\text{ad}}$  from kink sites onto the terrace and the terrace diffusion barrier  $E_{\text{diff}}$ . EMT calculations by Stoltze [81] yield  $E_{\text{ad}} + E_{\text{diff}} = 0.767\text{eV}$  in nice agreement with our experimental result. Karimi et al. [116] find a somewhat lower value ( $0.59\text{eV}$ ) using EAM calculations, however, the result is of the same order of magnitude. Similar experiments on Ag(111) by Morgenstern et al. [249] yield  $E_{\text{ad}} + E_{\text{diff}} = 0.71 \pm 0.03\text{eV}$ , also in reasonable though less perfect agreement with the theoretical value by Stoltze ( $0.619\text{eV}$ ) [81].

We have also studied decay curves of an ensemble of monolayer deep vacancy islands [201]. One may expect the decay of vacancy islands to be closer to the detachment limited decay. Adatoms have to cross the vacancy island edge and an additional attachment barrier may arise from the presence of an ES-barrier [74, 75]. Indeed, the decay curves of vacancy

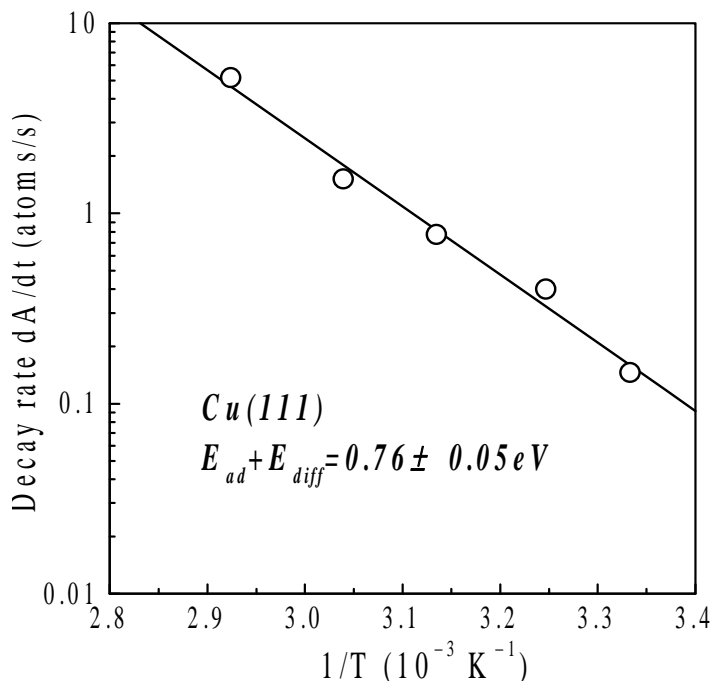


**Fig. 61.** Arrhenius-plot of the decay rate of Cu adatom islands on Cu(111) for a fixed island size of 1600 atoms. The activation energy corresponds to the sum of the adatom formation energy from kink sites onto the terrace and the diffusion barrier on the terrace  $E_{ad}+E_{diff}$  [200].

islands generally reveal the linear behavior of detachment limited decay. Fig. 62 shows STM images of vacancy islands on Cu(111) at 358K in their initial configuration and after about 1h and the corresponding decay curve of one vacancy island. The measured time exponent of the island area is  $0.9 \pm 0.1$  in agreement with (6.35). However, the extra barrier for attachment/detachment is not infinitely large as assumed in the derivation of (6.35). Therefore, a correlation of the decay of neighboring vacancy islands is observed. Fig. 63 shows decay curves for various vacancy islands on Cu(111) at 333K [201]. Obviously, the time dependence of the island area may significantly deviate from a linear curve and the vacancy island size may even increase.

On Cu(100), we found that the decay of monolayer high adatom islands is detachment limited (6.35) [106]. This result cannot be understood in the simple picture, if adatoms mediate the mass flux between islands: For a simple metal system like Cu(100), no attachment barrier for adatoms should exist at the island edge. However, energy calculations [290] based on our experimental results show that mono-vacancies see an additional energy barrier, when approaching an island edge: In Fig. 64(a), the energy potential of a mono-vacancy on the terrace is plotted as a function of its distance from a kink site at the step edge. The vacancy has to overcome an additional sticking barrier  $E_{stick}$  to attach to the step. Density functional calculations [117, 290] yield a diffusion barrier for single vacancy diffusion of

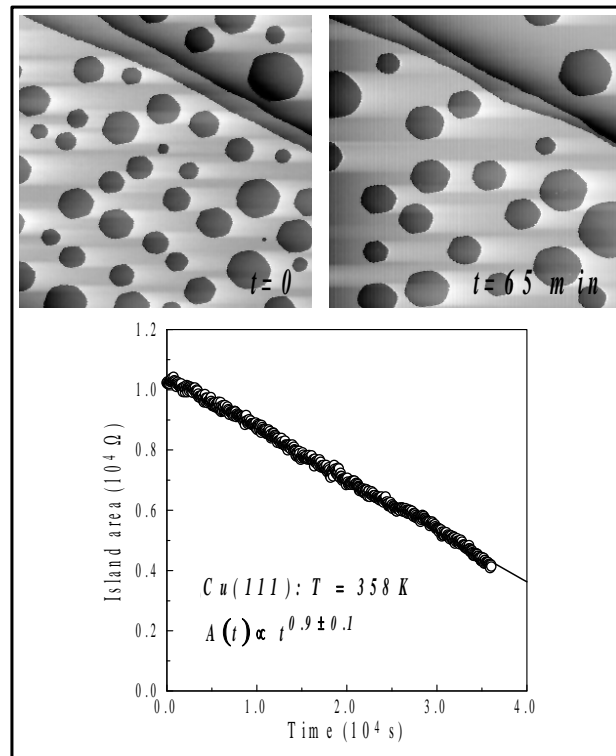


**Fig. 62.** STM images of monolayer deep vacancy islands on Cu(111) at 358K. The decay of vacancy islands on Cu(111) is detachment limited (6.34) and (6.35), which is apparent from the linear decay curve for one island as shown in the lower panel [201].

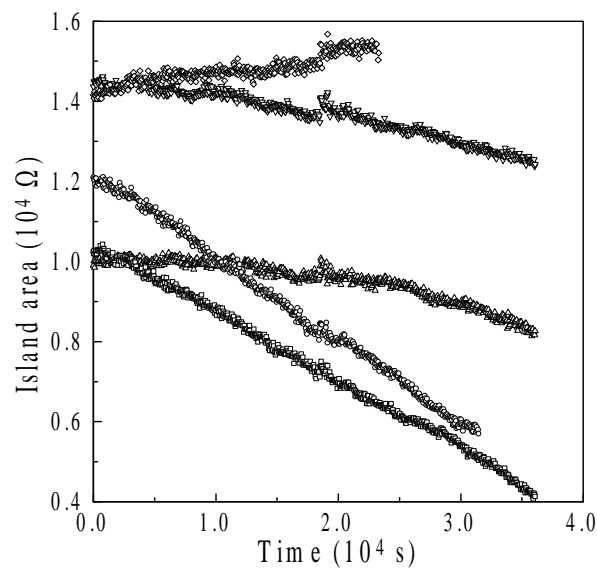


**Fig. 63.** For detachment limited decay of islands it is assumed that no interaction between neighboring island occur during the decay, i.e., all islands decay linearly with the same rate. The above data set for vacancy islands on Cu(111) at 333K shows, however, that this is not generally the case [201].

0.42eV. From the energy potential as shown in Fig. 64(a) and the energy calculations one may estimate the activation energy for the decay of Cu islands on Cu(100) to be  $E_{act}=E_{stick}+E_{diff}+E_{vac}$  where  $E_{diff}$  and  $E_{vac}$  are the energy barrier for vacancy diffusion on the terrace and the vacancy formation energy, respectively. From the first principles calculations one finds  $E_{vac} = 0.22\text{eV}$  [290]. The sticking barrier is non-zero and may be of the order of 0.1-0.2eV. Hence, the activation barrier for island decay can be estimated to be of the order of 0.70-0.85eV which is in agreement with our experimental data for the island decay on Cu(100), where we find an activation energy of  $E_{act}=0.80\pm 0.03\text{eV}$  (Fig. 64(b)) [290].

Recent results by Hoogeman et al. [284] show that mono-vacancies serve as mass transport species also on Ni(100). These authors studied the decay of monolayer deep vacancy islands on Ni(100). They find that the decay of the vacancy islands is diffusion limited. Let first be assumed that adatoms mediate the mass transport between the vacancy islands. Then, adatoms would have to cross step edges in order to fill the vacancy islands. In order to do so, the adatoms have to overcome an additional step-edge barrier [74, 75]. Hence, the vacancy island decay would be detachment rather than diffusion limited. Assuming, however, mono-vacancies are responsible for the mass exchange between the vacancy islands, no additional

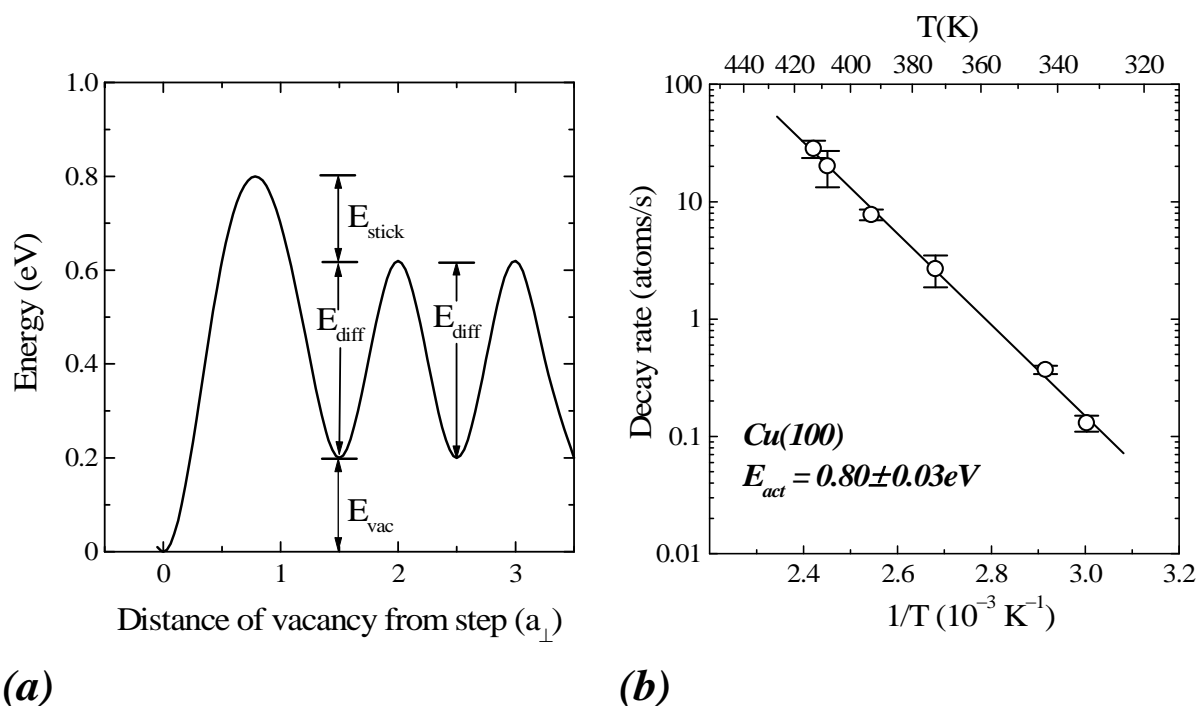


**Fig. 64.** (a) Calculation of the energy potential of a mono-vacancy as a function of its distance from a kink site at an island edge on Cu(100). To attach to the kink site, the mono-vacancy (vacancy formation energy  $E_{vac}$ ) has to overcome an additional sticking barrier  $E_{stick}$  [106, 290]. (b) Measured activation energy  $E_{act}$  for the decay of Cu adatom islands on Cu(100) [290].

sticking barrier is present and the decay of the vacancy islands should be diffusion limited as is indeed observed.

Theoretical values obtained by energy calculations or molecular dynamics simulations do not show a general trend for the preference of vacancy diffusion on (100) fcc surfaces. Table 7 summarizes experimental and theoretical data for the diffusion barrier  $E_{\text{diff}}$  for adatom and vacancy diffusion on (111) and (100) surfaces of Cu, Ag, Pt and Ni together with the pre-exponential factors: For Cu(100), the density functional calculations yield diffusion barriers for single adatom hopping and vacancy diffusion of 0.52 and 0.42eV, respectively [117, 290]. Hence, we find that vacancy diffusion is faster than adatom diffusion on Cu(100). This result supports the idea that for Cu(100), vacancies rather than adatoms mediate the mass transport between islands. Transition state theory calculations by Kürpick et al. [291-293], under consideration of vibrational states, yield a slightly lower value for vacancy diffusion (0.44eV) compared to adatom diffusion (0.48eV)<sup>69</sup> on Cu(100). They obtain a similar result for Ni(100) (vacancy: 0.55eV, adatom: 0.63eV). Embedded atom calculations and molecular dynamics simulations by Karimi et al. [116] give values of 0.36 and 0.48eV for vacancy and adatom diffusion on Cu(100), respectively. Effective medium calculations by Hansen et al. [294], Merikoski et al. [113] and Stoltze [81] propose that adatom diffusion should be energetically favorable on Cu(100) and Ni(100). The diffusion barriers for Cu and Ni reported by Stoltze, however, are very close (Cu: 0.437eV(vacancy), 0.425eV (adatom); Ni: 0.562eV (vacancy), 0.558eV (adatom)) [81]. As can be seen from Table 7, diffusion on Pt(100) and Ag(100) seems to be adatom mediated.

Only few experimental data are available for island decay on anisotropic metal surfaces: Li et al. investigated the growth shape of Cu islands on Pd(110) as a function of temperature [295]. They found a transition from 1-dimensional to 2-dimensional growth and showed that the reason for the transition is anisotropic diffusion around island corners. A similar transition may be expected for island decay on (110) surfaces and was indeed later observed by Morgenstern et al. [296] on Ag(110).

In summary, the classical Ostwald theory fails to describe experimentally observed ripening of adatom and vacancy islands, nevertheless, information about the transport kinetics may be extracted from the analysis of island decay curves. The values for  $E_{\text{ad}}$ ,  $E_{\text{vac}}$  and  $E_{\text{diff}}$  obtained from the island decay studies are generally in agreement with theory. The determination of step energies from the decay of islands remains a problem [200, 249, 286]. As a caveat it is mentioned that the values for  $\gamma$  obtained from island decay curves *must* be

---

<sup>69</sup> Both values are those obtained for the static system [291-293].

self-consistently used in (6.31), if one would like to extract further information from island decay curves. If one uses numbers for  $\gamma$  determined by the analysis of the equilibrium shape of islands or theoretical values, large errors may be introduced into the quantitative interpretation of island decay curves.

### 6.2.2. Island coalescence

On some metal surfaces, Ostwald ripening is not the dominant mechanism for coarsening. Zuo et al. [297] and Pai et al. [271] could show that island coalescence is the dominant coarsening process on Cu(100) (in agreement with helium beam scattering by Ernst et al. [298] and simulations by Barkema et al. [299]). Coalescence mediated ripening was demonstrated for Ag(100) by Wen et al. [270] and Pai et al. [271]. Recently, Hoogeman et al. [284] could show that island coalescence is also the prevailing coarsening process on Ni(100). As an example for coalescence of islands, Fig. 65 shows STM images of a coalescence event between vacancy islands on Ag(111) around room temperature by Rosenfeld and coworkers [274, 300]. Before coalescence, the vacancy islands resemble their quasi-hexagonal equilibrium shape. When the vacancy islands coalesce at  $t=0$ , a neck is formed and the chemical potential along the periphery is not constant any more. Due to the gradient in chemical potential along the vacancy island, edge rapid edge diffusion sets in and the vacancy

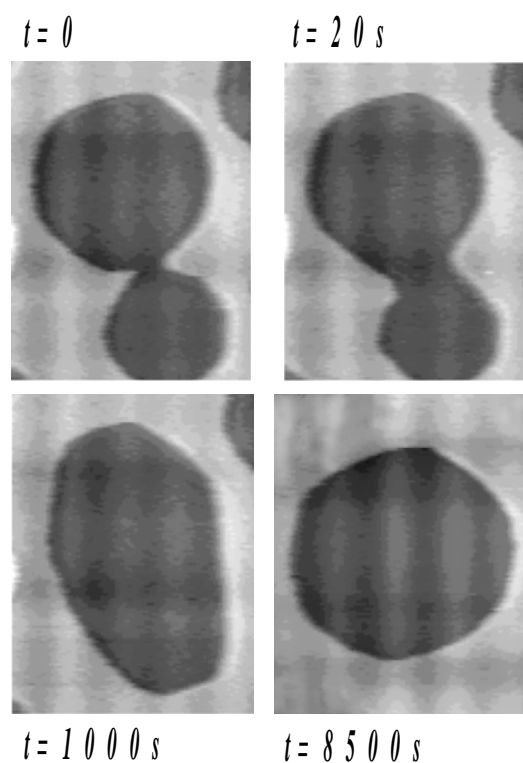


**Fig. 65.** Coalescence of two vacancy islands on Ag(111) around room temperature (after Rosenfeld et al. [274]).

island eventually approaches again the equilibrium shape. The size of the new, larger vacancy island is the sum of the areas of the initially separated islands. Rosenfeld and coworkers studied the relaxation time  $\tau$  of coalesced islands until they resemble the equilibrium shape as a function of the island diameter. The relaxation is described by an equation derived by Smoluchowski [301]. According to this equation,  $\tau$  scales with an universal exponent where the exponent depends on the dominant mass transport mechanism. The relaxation time  $\tau$  obeys a power law in the island diameter  $d$  as  $\tau \propto d^\beta$ . The problem is akin to the problem of bump decay considered in Section 3.5. For periphery diffusion, the relaxation time  $\tau(q)$  for a Fourier component of the bump is  $\tau(q) \propto q^{-4}$  (3.38) and the characteristic  $q$ -value scales as  $d^{-1}$ , where  $d$  is the linear size of the coalesced island. Hence, the relaxation time  $\tau(q)$  should scale as  $d^4$  (i.e.  $\beta=4$ ). In the case of terrace diffusion in the fast and in the slow limit  $\beta$  should be 2 and 3, respectively. For vacancy coalescence on Ag(111) at room temperature, Rosenfeld and coworkers find  $\beta=3.2\pm 0.35$  [274, 300], which would be in agreement with equilibration by slow terrace diffusion. The analysis of the equilibrium fluctuations on Ag(111) [42], however, show that edge diffusion prevails at 300K at least for short times. Hence, one would expect the reshaping exponent  $\beta$  to be about 4 as emphasized also by Rosenfeld and coworkers. A possible solution to this controversy could be the long-time behavior of edge fluctuations and bump relaxations. In Section 3.3.5, we have seen that at 314K step fluctuations on Ag(111) show a transition between periphery diffusion and fast terrace diffusion depending on the time scale. The reshaping exponent  $\beta=3.2\pm 0.35$  measured by Rosenfeld and coworkers could indicate the same transition in the relaxation time after coalescence.

### ***6.3. Coarsening of multilayer island structures***

So far, coarsening of island structures have been considered only for the case of monolayer high adatom or vacancy islands. In the following, the decay of multilayer islands and their coarsening due to ripening and coalescence processes is discussed. The driving force for coarsening is again the local gradient in chemical potential. Large lower layer islands in an island stack grow at the expense of the small upper layer islands. The interlayer mass transport during island decay may be hindered by an ES-barrier [74, 75], which is usually the case for (111) surfaces of fcc metals. Occasionally, however, the additional step-edge barrier for interlayer mass transport is bypassed and multilayer island decay is fast also on (111) surfaces [302, 303]. In the following, the normal step edge barrier limited island stack decay is discussed first. After that, several scenarios will be presented, where rapid decay events have been observed.

### 6.3.1. Barrier limited decay of multilayer islands

We consider now the decay of an adatom island on top of another adatom island or a vacancy island within a vacancy island. The situations are displayed in the right-hand panels of Fig. 54. During the decay of the top island, respectively, the inner vacancy island, atoms must cross the island edges; in the first case, the edge of the outer adatom island and, in the second case, the edge of the inner vacancy island. Both situations can be described with the same rate equations. The only difference is the sign of the chemical potential of the islands. In the case of an adatom island on top of an adatom island, both chemical potentials are positive, while in the second case of a vacancy island within a vacancy island both are negative. The decay of the multilayer island structures is described by [201, 304] (see also Section 6.2.1)

$$\frac{dA}{dt} = -2\pi v_0 e^{-\frac{E_{diff} + E_{ad}}{k_B T}} e^{\frac{\eta\gamma\Omega}{k_B T} \left( \frac{1}{r_t} - \frac{1}{r_b} \right)} \frac{1}{\ln \left| \frac{r_b}{r_t} \right| + \frac{1-s}{sr_b}}, \quad (6.36)$$

where  $r_t$  and  $r_b$  are the radii of the top and the bottom layer island, respectively. The sticking factor  $s$  is now the temperature dependent Schwoebel-factor  $s(T)$ :

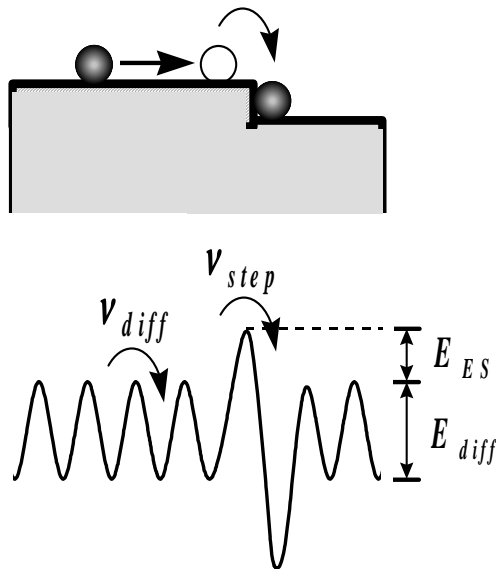


**Fig. 66.** Simple model of the additional energy barrier for atoms crossing steps (ES-barrier [74, 75]). The rates for terrace diffusion and step crossing are denoted as  $v_{diff}$  and  $v_{step}$ , respectively.

$$s(T) = \frac{v_{\text{step}}}{v_{\text{diff}}} = \frac{v_0^* e^{-\frac{E_{\text{diff}} + E_{\text{ES}}}{k_B T}}}{v_0 e^{-\frac{E_{\text{diff}}}{k_B T}}} = s_0 e^{-\frac{E_{\text{ES}}}{k_B T}}. \quad (6.37)$$

Here,  $v_{\text{step}}$  is the hopping rate across a step with additional step-edge barrier  $E_{\text{ES}}$  (Fig. 66) and  $v_0^*$  is the corresponding pre-exponential factor. Fig. 67(a) shows STM images of a multilayer island on Cu(111) at 345K in the upper panel. Below that, the decay curves of another double-layer island at the same temperature is displayed. The decay curves of a further double-layer layer at  $T=382\text{K}$  is shown in Fig. 67(b). The squares and circles represent the measured area for the second and the top layer islands, respectively. We integrated (6.36) numerically using the line tension  $\gamma=0.53\text{eV}/a_{\parallel}$ , the pre-exponential factor  $v_0=1.0 \times 10^{12 \pm 0.65} \text{ s}^{-1}$  and the sum of the adatom creation and the terrace diffusion energy  $E_{\text{ad}}+E_{\text{diff}}=0.76\text{eV}$  as previously determined from the analysis of the Ostwald ripening of adatom islands Cu(111) [200, 201]. The Schwoebel factor  $s(T)$  was adjusted such that we achieved best agreement with the experimental data [304]. Fig. 68 shows the Arrhenius-plot of the Schwoebel-factors. The ES-barrier is determined to  $0.224 \pm 0.009\text{eV}$  and the pre-factor is  $s_0=3.5 \times 10^{+0.35}$ . From (6.37) then follows the pre-exponential for step crossing  $v_0^* = 3.5 \times 10^{12 \pm 1} \text{ s}^{-1}$ . (It is noted that the difference in the ES-barrier as obtained in the previous study of island decay at a single temperature in the vicinity of straight steps ( $E_{\text{ES}}=0.19\text{eV}$ ) [200, 201] is due to the use of a "typical" pre-exponential factor of  $10^{13} \text{ s}^{-1}$  for  $v_0^*$  in the earlier study.) The experimental value of the ES-barrier seems to be lower than theoretical values for hopping across straight steps [81, 116, 305] (see also Table 7). This discrepancy can be understood, if one keeps in mind that experimental studies of multilayer island decay on (111) surfaces measure an average over A- and B-steps. Furthermore, island edges have a large number of kink sites, where the ES-barrier may be substantially reduced, as shown by Li and DePristo [306], Merikoski et al. [113], Villarba and Jónsson [125], and Jacobsen et al. [307].

The decay of multilayer island structures was also investigated by Morgenstern et al. [249] on Ag(111). From an STM study of multilayer vacancy island decay between 307 and 360K on Ag(111), using numerical integration of the rate equation (6.36), they find an ES-barrier of  $0.13 \pm 0.04\text{eV}$ . This value is in nice agreement with earlier work by Vrijmoeth et al., Meyer et al. (both  $0.15 \pm 0.03\text{eV}$  [215, 308]), Bromann et al. ( $0.12 \pm 0.02\text{eV}$  [309]), as well as by Roos and Tringides ( $0.15 \pm 0.03\text{eV}$  [310]).

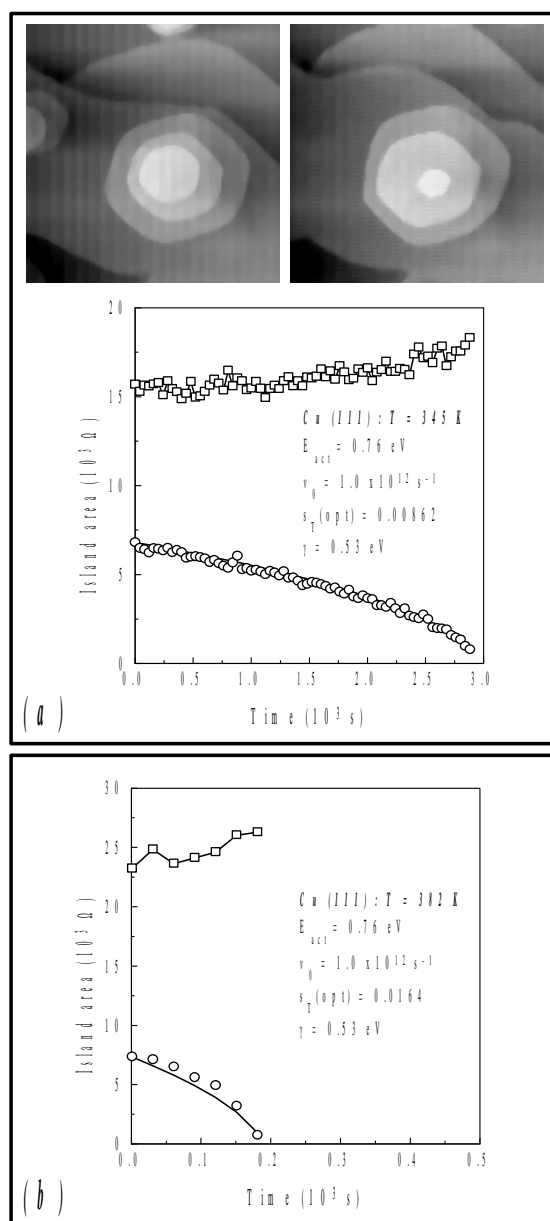


**Fig. 67.** (a) STM images ( $96 \times 96 \text{ nm}^2$ ) of a multilayer Cu island on Cu(111) at 345K. In the lower panel of (a) the areas of islands in a double-layer stack at the same temperature are plotted vs. time. (b) Island area vs. time for a double-layer island on Cu(111) at 382K [304]. For the top layer island decay (circles in (a) and (b)), atoms have to detach from the edge of the upper island, overcome the step-edge barrier and attach to the edge of the lower island. Numerical integration of (6.36) (using (6.37)) for the top layer island (lower solid curve) yields an optimum value for the Schwoebel factor  $s(T)$  (6.37). For the numerical calculation, the island size of the lower layer island was used as an input (upper solid curve and squares) as well as the values for  $E_{ad} + E_{diff} = 0.76 \text{ eV}$ ,  $\gamma = 0.53 \text{ eV}$  and  $v_0 = 1.0 \times 10^{12} \text{ s}^{-1}$  obtained from the decay of islands in a vacancy island [200, 201]. The Schwoebel factor  $s(T)$  is determined from a fit to the experimental decay curve of the top layer island [304].

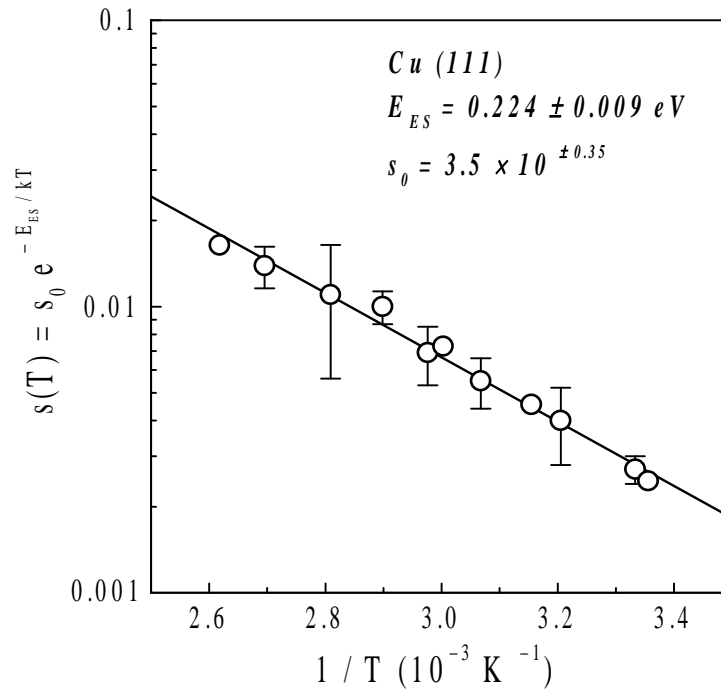


**Fig. 68.** Temperature dependence of the Schwoebel factor  $s(T)$  (6.37) as determined from studies as shown in Fig. 67. The activation energy is the ES-barrier  $E_{ES}$  as illustrated in Fig. 66 [304].

On Cu(100), we found experimental evidence that no ES-barrier is present at the step edges. We studied the decay of small islands in the vicinity of large islands in the same layer as well as the decay of small islands on top of large islands [106, 311]. Islands of the same size decay with the same rate independent of their location. Hence, the decay of small islands on top of large islands is not hindered by an additional energy barrier for crossing the lower island edge. Previous conclusions, based on growth studies on Cu(100) [312, 313] that the observed formation of multilayer mound is associated with an ES-barrier does not stand this direct test for the existence of an ES-barrier. Table 7 summarizes experimental (from STM and FIM studies) and theoretical results for the ES-barrier together with the pre-factor for (111) and (100) surfaces of Cu, Ag, Pt and Ni.

The physical origin of the additional step-edge barrier is still controversial. The most simple picture to explain the additional energy barrier for step crossing arises from the reduced (second nearest-neighbor) coordination of atoms when rolling over the step edge [346]. This simple picture, however, cannot explain substantial energy differences in the ES-barrier for crossing A- and B-steps on (111) fcc surfaces (e.g., Pt(111): A-step 0.02eV, B-step 0.35eV [109]; see also Table 7). In particular, it does not hold for more complex interlayer diffusion processes as atomic exchange at steps. The most intriguing experimental result in the previous

Table 7.

Surface	T (K)	$E_{ad}+E_{diff}$ (eV)	$E_{diff}$ (eV)	$\nu_0$ ( $s^{-1}$ )	$E_{ES}$ (eV)	$s_0 = \nu_0^*/\nu_0$	$\nu_0^*$ ( $s^{-1}$ )	Ref.
Cu(111) <sup>(‡)</sup>	300-382	0.76±0.04		$1.0 \times 10^{12 \pm 0.65}$	0.224±0.009	$3.5 \times 10^{\pm 0.35}$	$3.5 \times 10^{12 \pm 0.74}$	[200, 201, 304]
Cu(111) <sup>(‡)</sup>	55-140		0.03±0.01					[314]
Cu(111) <sup>(70)</sup>		0.767	0.053		0.312 (hop) 0.397 (ex)			[81]
Cu(111) <sup>(71)</sup>			0.026	$3.1 \times 10^{11}$ <sup>(72)</sup>				[95]
Cu(111) <sup>(71)</sup>		0.59	0.028 (ad, hop) 1.12 (ad, ex) 0.58 (vac)		0.49 (hop) 0.084 (ex)			[116]
Cu(111) <sup>(70)</sup>			0.093 (ad, hop)		0.325 (hop) 0.174 (ex)			[305]
Cu(100) <sup>(‡)</sup>	270-460		0.48	$3.5 \times 10^{12}$ <sup>(72)</sup>				[316]
Cu(100) <sup>(‡)</sup>	270-420		0.40	$9.1 \times 10^{12}$				[317]
Cu(100) <sup>(‡)</sup>	120-250		0.28±0.06	$6.5 \times 10^{11}$				[298]
Cu(100) <sup>(‡)</sup>	50-200		0.39±0.06 <sup>(73)</sup>					[318]
Cu(100) <sup>(‡)</sup>	180-265		0.36±0.03					[319]
Cu(100) <sup>(‡)</sup>	343-413				~0			[106]
Cu(100) <sup>(74)</sup>			0.38	$5 \times 10^{11}$				[320, 321]
Cu(100) <sup>(70)</sup>		0.932 (ad) ---	0.425 (ad) 0.437 (vac)		0.147 (hop) 0.201 (ex)			[81]
Cu(100) <sup>(71)</sup>			0.38(ad) 0.72 (ad, ex)	$1.9 \times 10^{12}$ <sup>(72)</sup> ---				[95]

<sup>70</sup> EMT calculations.<sup>71</sup> EAM calculations.<sup>72</sup> Value obtained using the relation:  $\nu_0 = 4dD_0/za_0^2$ ,  $a_0$  being the lattice constant,  $d$  the dimensionality of the diffusion process and  $z$  the number of nearest neighbors [315].<sup>73</sup> The pre-exponential factor was assumed to be  $\nu = 10^{13} s^{-1}$ .<sup>74</sup> KMC simulations.

Table 7 (cont.).

Surface	T (K)	$E_{ad}+E_{diff}$ (eV)	$E_{diff}$ (eV)	$\nu_0$ ( $s^{-1}$ )	$E_{ES}$ (eV)	$s_0 = \nu_0^*/\nu_0$	$\nu_0^*$ ( $s^{-1}$ )	Ref.
Cu(100) <sup>(71)</sup>		0.83	0.48 (ad, hop) 0.80 (ad, ex) 0.36 (vac)		0.29 0.03 (ex)			[116]
Cu(100) <sup>(75)</sup>	260-450 600		0.51/0.48 (ad) <sup>(76)</sup> 0.44 (vac)	$4.9 \times 10^{11}$ <sup>(72)</sup> /--- $3.9 \times 10^{12}$				[291-293]
Cu(100) <sup>(77)</sup>	650-980		$0.52 \pm 0.05$ (ad, hop) $0.96 \pm 0.10$ (ad, ex) $0.42 \pm 0.08$ (vac)	$2.0 \times 10^{13 \pm 0.1}$ $4.37 \times 10^{14 \pm 0.3}$ $2.7 \times 10^{13 \pm 0.3}$				[117]
Cu(100) <sup>(70)</sup>	100-400		0.40 (ad, hop) 0.21 (ad, ex)	$7 \times 10^{11}$ <sup>(72)</sup> $8 \times 10^{11}$				[294]
Cu(100) <sup>(71)</sup>		1.31	0.48 (ad, hop)					[118]
Cu(100) <sup>(78)</sup>			0.66 (ad, hop)	$5.5 \times 10^{12}$ <sup>(72)</sup>				[322]
Cu(100) <sup>(79)</sup>			$0.43 \pm 0.02$ (ad, hop) $0.70 \pm 0.04$ (ad, ex)	$5.2 \times 10^{12 \pm 0.2}$ <sup>(72)</sup> $9.7 \times 10^{13 \pm 0.3}$				[323]
Cu(100) <sup>(79, 80)</sup>			0.69 (ad, hop) 0.97 (ad, ex)					[324]
Cu(100) <sup>(71)</sup>		1.13	0.68 (ad, hop)					[115]
Cu(100) <sup>(79)</sup>			0.51 (ad, hop) 0.77 (ad, ex)					[325]

<sup>75</sup> Vibrational density of states calculations based on EAM potentials.<sup>76</sup> Values calculated without/with effects due to lattice vibrations.<sup>77</sup> GGA first principles calculations.<sup>78</sup> MD/MC-CEM calculations.<sup>79</sup> MD simulations.<sup>80</sup> DFT calculations.

Table 7 (cont.).

Surface	T (K)	$E_{ad}+E_{diff}$ (eV)	$E_{diff}$ (eV)	$\nu_0$ (s <sup>-1</sup> )	$E_{ES}$ (eV)	$s_0 = \nu_0^*/\nu_0$	$\nu_0^*$ (s <sup>-1</sup> )	Ref.
Cu(100) <sup>(81)</sup>			0.46(ad, hop) 0.18 (ad, ex)					[325]
Cu(100) <sup>(79)</sup>		0.688	0.399 (ad, hop) 0.996 (ad, ex) 0.482 (vac)		0.179 (hop) 0.232 (ex)			[113]
Cu(11n) <sup>(79)</sup>		0.76	0.399 (ad, hop) 0.473 (vac)		0.179 (hop) 0.232 (ex)			[113, 119]
Cu(113) <sup>(71)</sup>			0.26	$1.9 \times 10^{12}$ <sup>(72)</sup>				[95]
Cu(117) <sup>(71)</sup>			0.49					[83]
Ag(111) <sup>(‡)</sup>	300				0.15±0.03			[215, 308]
Ag(111) <sup>(‡)</sup>	65-120		0.097±0.010	$2 \times 10^{11}$				[326]
Ag(111) <sup>(‡)</sup>	70-130				0.12±0.02		$1.0 \times 10^{13 \pm 1}$	[309]
Ag(111) <sup>(‡)</sup>	307-360	0.71±0.03		$1.0 \times 10^{12 \pm 0.6}$	0.13±0.04	$0.25 \times 10^{+0.5}$	$0.25 \times 10^{12 \pm 0.8}$	[249]
Ag(111) <sup>(‡)</sup>	50-300				0.15±0.03	$2.3 \times 10^{2 \pm 0.2}$		[310]
Ag(111) <sup>(71)</sup>			0.058					[327]
Ag(111) <sup>(71)</sup>			0.059	$4.0 \times 10^{11}$ <sup>(72)</sup>				[95]
Ag(111) <sup>(78)</sup>			0.097	$7 \times 10^{11}$ <sup>(72)</sup>				[328]
Ag(111) <sup>(70)</sup>		0.619	0.064		0.295 (hop) 0.391 (ex)			[81]
Ag(111) <sup>(78)</sup>					A-step: 0.44 (hop) A-step: 0.31 (ex) B-step: 0.43 (hop) B-step: 0.06 (ex)			[306]
Ag(111) <sup>(77)</sup>			0.14±0.02					[329]
Ag(111) <sup>(70)</sup>			0.067					[122]

<sup>81</sup> CEM calculations.

Table 7 (cont.).

Surface	T (K)	$E_{ad}+E_{diff}$ (eV)	$E_{diff}$ (eV)	$\nu_0$ ( $s^{-1}$ )	$E_{ES}$ (eV)	$s_0 = \nu_0^*/\nu_0$	$\nu_0^*$ ( $s^{-1}$ )	Ref.
Ag(111) <sup>(80)</sup>			0.081					[209]
Ag(111) <sup>(80)</sup>			0.082 0.106 (tensile stress)	$8.2 \times 10^{12}$ $2.5 \times 10^{12}$				[330]
Ag(100) <sup>(‡)</sup>	295		0.40±0.04	$3 \times 10^{13} s^{-1}$				[272, 331]
Ag(100) <sup>(‡)</sup>	295-370		0.38 <sup>(73)</sup>		0.030±0.005			[218, 332]
Ag(100) <sup>(71)</sup>			0.48 (ad) 0.75 (ad, ex)	$1.4 \times 10^{12}$ <sup>(72)</sup> ---				[95]
Ag(100) <sup>(70)</sup>		0.729 (ad) ---	0.365 (ad) 0.417 (vac)		0.085 (hop) 0.194 (ex)			[81]
Ag(100) <sup>(74)</sup>			0.35	$10^{12}$				[320]
Ag(100) <sup>(77)</sup>			0.50±0.03					[329]
Ag(100) <sup>(78)</sup>			0.46 (ad, hop) 0.70 (ad, ex)					[325]
Ag(100) <sup>(78)</sup>			0.40 (ad, hop) 0.41 (ad, ex)					[325]
Ag(100) <sup>(80)</sup>			0.45 (ad, hop) 0.73 (ad, ex)		0.1 (hop) ~0 (ex)			[120]
Ag(100) <sup>(75)</sup>	160 600		0.48/0.46 (ad) <sup>(82)</sup> 0.47 (vac)	$3.6 \times 10^{11}$ <sup>(72)</sup> /--- $1.7 \times 10^{14}$				[291-293]
Ag(100) <sup>(79)</sup>		0.577	0.367 (ad, hop) 0.614 (ad, ex) 0.412 (vac)		0.114 (hop) 0.149 (ex)			[113]
Ag(100) <sup>(71)</sup>		1.21	0.48 (ad, hop)					[118]
Ag(115) <sup>(80)</sup>						0±0.05		[121]
Ag(1,1,17) <sup>(‡)</sup>			0.40±0.03 <sup>(83)</sup>					[333]

<sup>82</sup> Values calculated without/with effects due to lattice vibrations.<sup>83</sup> The pre-exponential factor was assumed to be  $\nu = 10^{12 \pm 1} s^{-1}$ .

Table 7 (cont.).

Surface	T (K)	$E_{ad}+E_{diff}$ (eV)	$E_{diff}$ (eV)	$\nu_0$ ( $s^{-1}$ )	$E_{ES}$ (eV)	$s_0 = \nu_0^*/\nu_0$	$\nu_0^*$ ( $s^{-1}$ )	Ref.
Pt(111) <sup>(‡)</sup>			0.25±0.02					[334]
Pt(111) <sup>(‡)</sup>	300				0.165			[308]
Pt(111) <sup>(‡)</sup>	23-160		0.26	$5 \times 10^{12}$				[335]
Pt(111) <sup>(‡)</sup>	120-140		0.26±0.003	$5 \times 10^{12 \pm 0.15}$	0.06±0.01			[108, 336]
Pt(111) <sup>(‡, 84)</sup>			0.07 (ad, hop)					[127]
Pt(111) <sup>(71)</sup>			0.007	$8.7 \times 10^{10}$ <sup>(72)</sup>				[95]
Pt(111) <sup>(70,74)</sup>		0.82	0.13					[123, 337]
Pt(111) <sup>(70)</sup>		0.965 (ad) ---	0.159 (ad) 0.688 (vac)		0.204 (hop) 0.311 (ex)			[81]
Pt(111) <sup>(79,81)</sup>			0.18 (ad, hop: rigid) 0.038 (ad, hop: relaxed)					[338]
Pt(111) <sup>(78)</sup>					B-step: 0.04 (ex)			[306]
Pt(111) <sup>(85)</sup>			0.08 (ad, hop)		A-step: 0.22 (ad, hop) <sup>(86)</sup> B-step: 0.10 (ad, ex)			[125, 339]
Pt(111) <sup>(70)</sup>			0.16 (ad, hop)		A-step: 0.41 (ad, hop) B-step: 0.37 (ad, ex)			[307]
Pt(111) <sup>(80)</sup>			0.33 (ad, hop)					[244]
Pt(111) <sup>(87)</sup>			0.29 (ad, hop)		A-step: 0.24 (hop) A-step: 0.02 (ex) B-step: 0.51 (hop) B-step: 0.35 (ex)			[109]
Pt(100) <sup>(‡)</sup>	170-195		0.47±0.01 (ad, ex)	$1.7 \times 10^{12}$ <sup>(72)</sup>				[340, 341]
Pt(100) <sup>(‡, 84)</sup>			0.82 (ad, hop)					[127]

<sup>84</sup> Diffusion coefficients measured using FIM. Activation energies calculated using Morse potentials.

<sup>85</sup> Simulations based on EAM potentials.

<sup>86</sup> At kink sites, the step edge barrier is considerably lower, at both A- and B-steps, 0.08 and 0.06eV, respectively [125].

<sup>87</sup> LDA first principles calculations.

Table 7 (cont.).

Surface	T (K)	$E_{ad}+E_{diff}$ (eV)	$E_{diff}$ (eV)	$\nu_0$ ( $s^{-1}$ )	$E_{ES}$ (eV)	$s_0 = \nu_0^*/\nu_0$	$\nu_0^*$ ( $s^{-1}$ )	Ref.
Pt(100) <sup>(71)</sup>			0.44 (ad) 0.31 (ad, ex)	$1.0 \times 10^{12}$ <sup>(72)</sup> ---				[95]
Pt(100) <sup>(70)</sup>		1.124 (ad) ---	0.689 (ad) 0.773 (vac)					[81]
Pt(100) <sup>(85)</sup>			0.54 (ad, ex)					[125]
Pt(100) <sup>(71)</sup>			0.63 (ad, ex)	$10^{13}$				[342]
Pt(113) <sup>(‡)</sup>			0.69±0.02	$(10^9)$ <sup>(72)</sup>				[127]
Pt(115) <sup>(79)</sup>	1340		0.72 <sup>(88)</sup>	$3.1 \times 10^8$ <sup>(72)</sup>				[343]
Ni(111) <sup>(71)</sup>			0.056 (ad, hop) 1.41 (vac)		A-step: 0.52 (hop) B-step: 0.161 (hop)			[344]
Ni(111) <sup>(71)</sup>			0.062 (ad, hop)					[342]
Ni(100) <sup>(‡)</sup>	225		0.63					[345]
Ni(100) <sup>(71)</sup>			0.63 (ad, hop) 0.93 (ad, ex)	$2.6 \times 10^{12}$ ---				[95]
Ni(100) <sup>(78)</sup>			0.61 (ad, hop)	$5.5 \times 10^{11}$ <sup>(72)</sup>				[322]
Ni(100) <sup>(71)</sup>			0.63 (ad, hop) 1.16 (vac)		0.28 (ex)			[344]
Ni(100) <sup>(70)</sup>		1.307 (ad) ---	0.558 (ad) 0.562 (vac)					[81]
Ni(100) <sup>(74)</sup>			0.43	$10^{12}$				[320]
Ni(100) <sup>(78)</sup>			0.67 (ad, hop) 0.47 (ad, ex)					[325]
Ni(100) <sup>(78)</sup>			0.60 (ad, hop) 1.00 (ad, ex)					[325]

<sup>88</sup> For the derivation of this value from the diffusion coefficient the pre-exponential factor is assumed to be  $10^{13} s^{-1}$ .

**Table 7 (cont.).**

Surface	T (K)	$E_{ad}+E_{diff}$ (eV)	$E_{diff}$ (eV)	$v_0$ ( $s^{-1}$ )	$E_{ES}$ (eV)	$s_0 = v_0^*/v_0$	$v_0^*$ ( $s^{-1}$ )	Ref.
Ni(100) <sup>(75)</sup>	600		0.63 (ad. hop) 0.55 (vac)	$5.5 \times 10^{11}$ <sup>(72)</sup>				[291, 293]
Ni(100) <sup>(79)</sup>		1.05	0.631(ad, hop) 0.844 (ad, ex) 0.655 (vac)		0.289 (hop) 0.113 (ex)			[113]
Ni(100) <sup>(71)</sup>		1.67	0.63					[118]

**Table 7:**

Diffusion barrier on the terrace  $E_{diff}$ , sum of  $E_{diff}$  and the adatom creation energies from kinks onto the terrace  $E_{ad}$ ,  $E_{diff}+E_{ad}$ , and ES-barrier  $E_{ES}$  determined from experiment ( $\ddagger$ ) and theory for fcc (111)- and (100)-surfaces in UHV.  $v_0$  and  $v_0^*$  are the pre-exponential factors for terrace diffusion and hopping across steps.  $s_0$  is the Schwoebel factor, which denotes the ratio between  $v_0$  and  $v_0^*$ .

years was the observation of a "denuded zone" on Pt(111) and Ir(111) surfaces in FIM diffusion studies by Kyuno and Ehrlich [347] and Wang and Ehrlich [348]. These studies showed that the ES-barrier is not just an additional energy barrier seen by an adatom sitting on the upper terrace next to the step edge (Fig. 69(a)). Rather, the barrier for edge crossing seems to be a steady increase of the potential energy of an atom on the terrace over a range over several atomic spacings (Fig. 69(b)). Memmel and Bertel [349] connected the increase of potential energy to the emptying of surface states close to step edges. As has been shown by low temperature STM studies, defects, steps and island edges may serve as almost perfect potential barriers where electrons in surface states are reflected and standing electron waves are observed [350-352]. Standing waves near steps have recently also been reported for room temperature investigations by Silva and Leibsle [353]. Further evidence for the correlation between surface states and the ES-barrier seemed to be found by our discovery of a rapid interlayer transport mechanism, which bypasses the ES-barrier [302, 303]. In the following section, this rapid interlayer mass transport will be discussed.

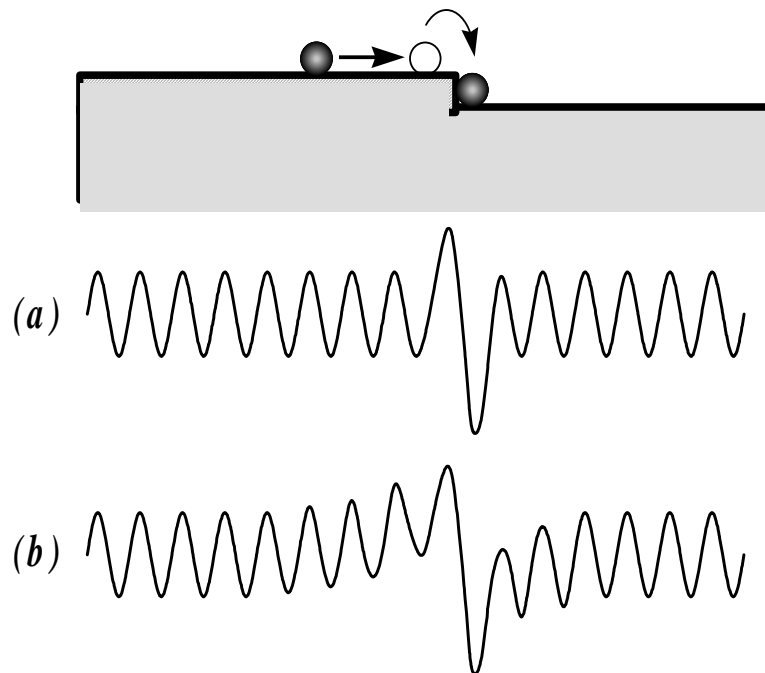


**Fig. 69.** (a) The simplest energy potential model for the step edge barrier assumes the diffusion barrier on the terrace to remain constant to the step edge. An atom sitting next to the step edge has to overcome an additional energy barrier to attach to the lower step edge. (b) A more complex model for the ES barrier proposes that the potential increase starts already several lattice sites away from the step edge. An analog variation in the potential energy may also occur for detachment of atoms from the lower step edge onto the lower terrace. A smooth increase of the potential energy over several atomic distances was found by Kyuno and Ehrlich [108] on Pt(111).

### 6.3.2. Rapid interlayer transport mechanism

In STM studies of the multilayer island decay on Cu(111), we found that the decay is hindered by the ES-barrier as long as the edges of upper and lower islands remain in a certain distance [302, 303]. When the distance decreases below a critical width  $w_c$ , the decay rate of the upper island increases by several order of magnitudes. Fig. 70 shows (a) STM images of a double-layer island at (I) 3200s, (II) 4600, (III) 4700 and (IV) 4800s after Cu deposition on Cu(111) at 314K. In (b) the corresponding areas of upper and lower island are plotted vs. time [302]. Initially, the upper island is located in the center of the lower island. Then, the decay of the upper island is barrier limited [304] with a decay rate of  $-0.02\text{atoms/s}$ . In (II), the upper island approaches the lower island edge and the decay rate increases dramatically. For a short time, the upper island retracts from the lower island edge again in (III) and the rapid decay is interrupted. Eventually (IV), the upper island comes close to the lower island edge and the decay rate increases to  $-2.48\text{atoms/s}$  until the upper island vanishes. We observed rapid decay events on Cu(111) for various island configurations [302], for multilayer islands on Ag(111) [354, 355] and during coalescence of islands [356].

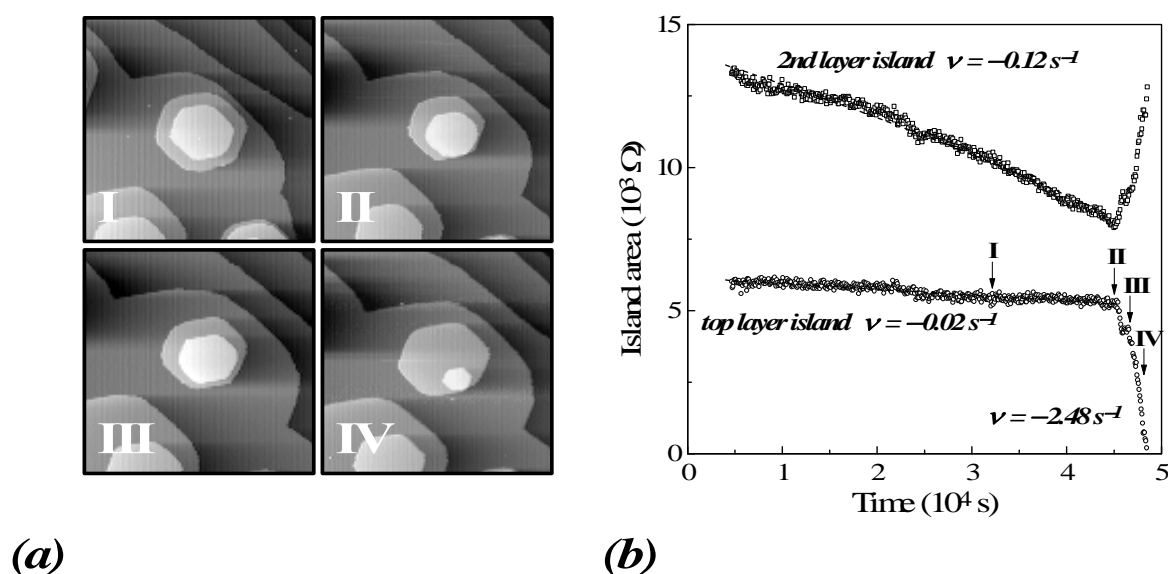


**Fig. 70.** (a) STM images ( $90 \times 90 \text{ nm}^2$ ) of a rapid decay event during multilayer Cu island decay on Cu(111) at 314K: In (I) the top layer island is approximately in the center of the lower layer island and undergoes the barrier limited decay as discussed in Section 6.3.1. Due to its Brownian motion, the upper island approaches the lower island edge in (II) and decreases rapidly. Temporarily, the upper island retracts from the lower island edge in (III) and the decay slows down. Eventually (IV), the upper island comes close to the edge of the lower island again and resumes the rapid decay. (b) Plot of the island areas of upper and lower island vs. time. [302]

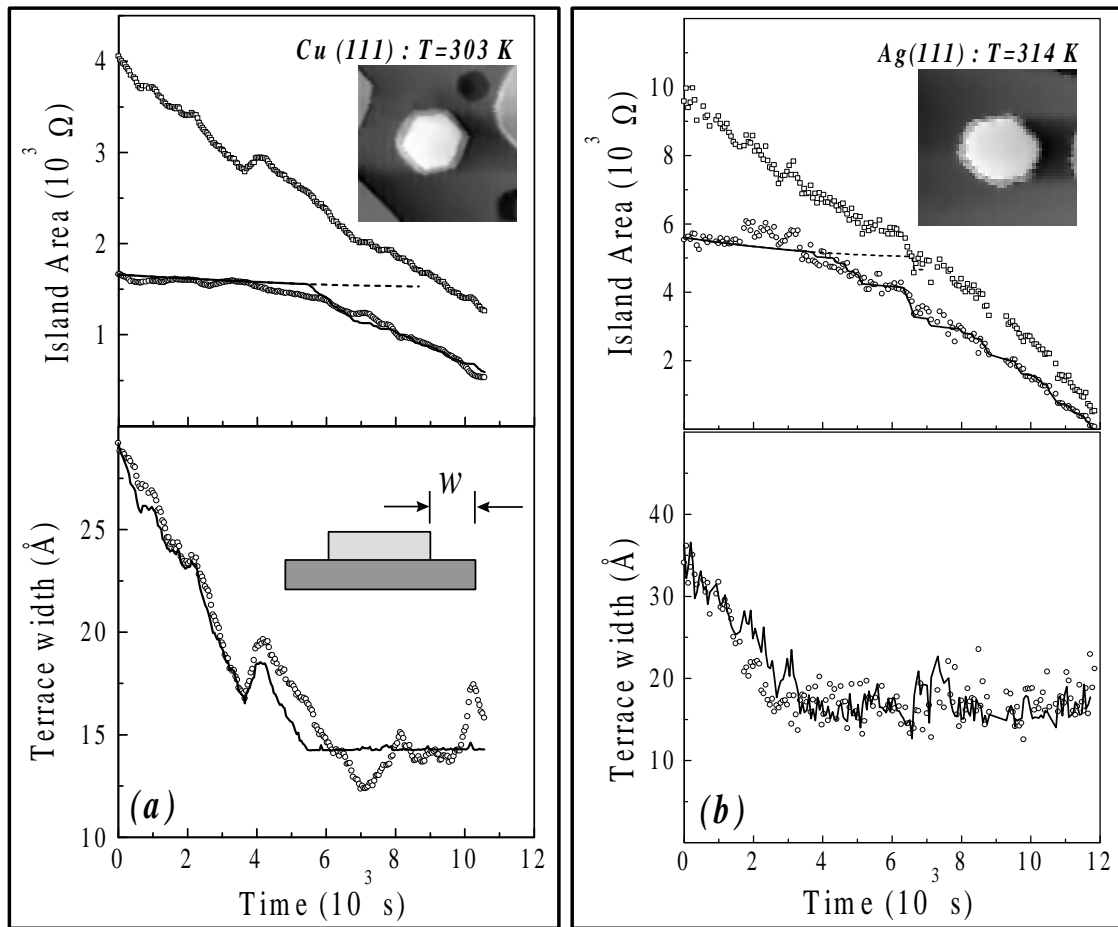


**Fig. 71.** Island areas (upper panels) and terrace width  $w$  (lower panels) between island edges (see inset) of homoepitaxial double-layer islands on (a) Cu(111) at 303K [303] and (b) Ag(111) at 314K [355] vs. time. The dashed curves correspond to a numerical calculation of the decay rate equation (6.36) using a constant ES-barrier for all island edge distances  $w$ . The solid curves in the upper as well as in the lower panels are calculated under the assumption of a vanishing ES-barrier for  $w$  smaller than a critical terrace width  $w_c$ . The critical width is  $w_c=14.5\text{\AA}$  and  $15.2\text{\AA}$  for Cu(111) and Ag(111), respectively.

As a consequence of the rapid decay mechanism, the late stage of the decay of an entire multilayer island stack is controlled by the lowest layer island [302, 303]. During rapid mound decay, the distance between the island edges remains constant with time. Fig. 71 shows the areas and the terrace width  $w$  (as indicated in the inset image) between island edges in double-layer islands on (a) Cu(111) at 303K [303] and (b) Ag(111) at 314K [355] vs. time. For both Cu(111) and Ag(111), the decay of the top islands is initially hindered by the ES-barrier, while the lower layer islands undergo the faster diffusion limited decay [200, 279]. Therefore, the width between the island edges shrinks in time. When the width is about  $14\text{\AA}$  in the case of Cu(111) and  $16\text{\AA}$  in the case of Ag(111), the decay of the top islands is

accelerated and adjusts to the decay rate of the bottom island. For both Cu(111) and Ag(111), the critical widths of 14 and 16Å, respectively, correspond to a distance of about 6 dense packed atomic rows along  $\langle 110 \rangle$ . Then, the width remains constant (save for fluctuations) until the top islands vanish. By numerical solution of the rate equations (6.36) and (6.37), we showed that the decay of the top islands cannot be described by a constant ES-barrier (dashed curves in Fig. 71(a) and (b))<sup>89</sup>. Agreement between the numerical calculation and experiment for Cu(111) is achieved, if the ES-barrier is assumed to be 0.224eV [304] as long as the width between the island edges is larger than a critical width  $w_c=14\text{Å}$  and zero otherwise (solid curves in Fig. 71(a)). In the case of Ag(111), the experimental data can be fitted by the numerical calculation, if the ES-barrier is assumed to be 0.13eV [249] for terrace widths larger than 16Å and zero for smaller terrace widths. Obviously, the decay curves of the upper islands for Cu(111) and Ag(111) are well described, if one assumes that the ES-barrier vanishes below a critical terrace width  $w_c$ .

In a first interpretation of the results for Cu(111), we related the vanishing of the ES-barrier below  $w_c=14\text{Å}$  to the occupation of the surface state on Cu(111) [303]. On Cu(111), the image potential surface state obeys a parabolic dispersion  $E(k)-E_F=(8.25\text{Å}^2\text{eV})k^2-0.389\text{eV}$ , as measured in angle-resolved photoemission studies by Kevan [358]. The island edges serve as perfect potential barriers as was demonstrated by Li et al. [352] for Ag(111). Thus, the electron wave function must have a node at the steps. When the distance between the island edges decreases, the energy of the ground state of the surface wave function increases, and is eventually shifted above the Fermi level. Using the dispersion as measured by Kevan, one finds that the ground state is shifted beyond the Fermi level, when the island edge distance is smaller than 14.5Å [303]. The consistency between this result and the experimentally obtained critical island edge distance was interpreted as a correlation between the presence of an additional energy barrier for step crossing and the occupation of an image surface potential state [303]. This interpretation was also confirmed by the temperature dependence of the critical width in the case of Cu(111). One would expect that the temperature dependence of the critical width would be that of the dispersion of the surface state. The temperature dependence of the surface state on Cu(111) was measured by Paniago et al. [357] in angle-resolved photoemission studies to  $E(k)-E_F=0.45\text{eV}-T\cdot 0.18\times 10^{-3}\text{eV}$  (if T is given in units K). Fig. 72 shows the measured critical width between island edges in an island stack on Cu(111) as solid circles [303]. The solid line is the calculated temperature

---

<sup>89</sup> The theoretical curves were calculated using experimental data for the sum of the adatom formation energy and the diffusion barrier on the terrace  $E_{ad}+E_{diff}$ , the pre-exponential factors for terrace diffusion  $v_0$  and hopping

dependence of the critical width assuming a temperature dependence of the surface state as in [357]. The data points are well described by the theoretical curve in the case of Cu(111). For Ag(111), however, the energy dispersion of the surface state for Ag(111) [357, 359] would result in a critical width of  $w_c \approx 60 \text{ \AA}$  around room temperature. Furthermore, the critical terrace width should be temperature dependent according to the studies by Paniago et al. [357], who find that  $E(k) - E_F = 0.075 \text{ eV} - T \cdot 0.17 \times 10^{-3} \text{ eV}$  (when T is given in units K). Fig. 72 shows also experimental data we obtained in recent STM investigations for the critical terrace width for Ag(111) as open squares [355]. The dashed curve corresponds to the calculated critical terrace width based on the temperature dependence of the surface state [357]. Obviously, the critical width found in our experiment is significantly smaller ( $\sim 16 \text{ \AA}$ ) than  $60 \text{ \AA}$  and shows no

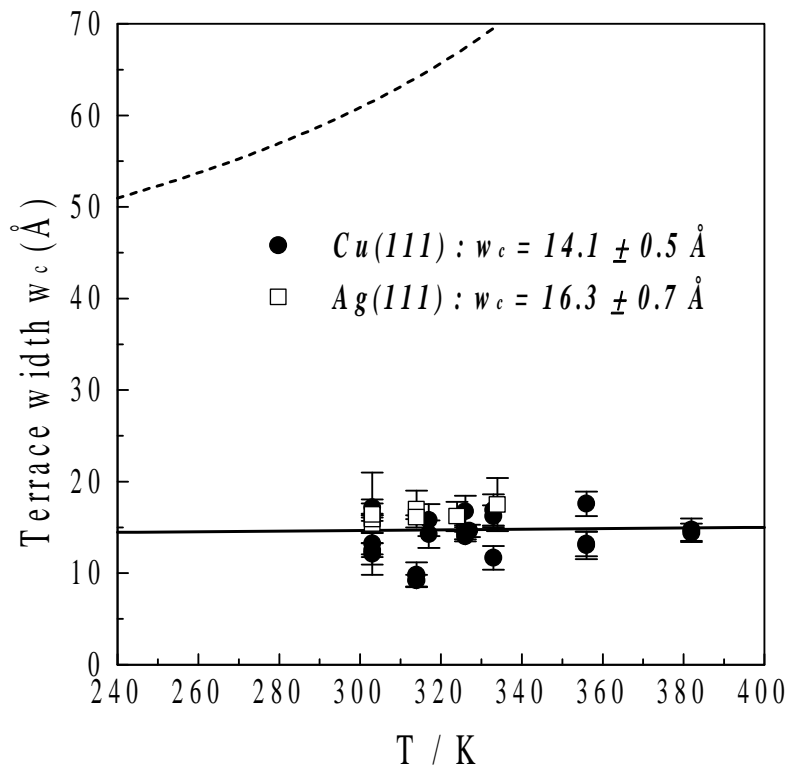


**Fig. 72.** Temperature dependence of the critical terrace width during multilayer mound decay on Cu(111) (solid circles) [303] and Ag(111) (open squares) [355]. The solid and the dashed curves represent the temperature dependence of the critical distance between island edges, below which the surface energy band is shifted above the Fermi level for Cu(111) and Ag(111), respectively. The curves were calculated assuming that the island edges serve as perfect potential barriers for the surface electron wave function and are based on angle-resolved photoemission studies by Paniago et al. [357] of the temperature variation of the surface energy band for Cu(111) and Ag(111). The values for the critical width, shown in the view graph, correspond to the average over all data points assuming that  $w_c$  is independent of the temperature.

---

across steps  $v_0^*$ , the step-edge barrier  $E_{ES}$  and the step energy  $\gamma$  [200, 249, 279, 304] (see also Table 7).

measurable temperature dependence, in contrast to the theoretical prediction. Hence, on the one hand, the data for Ag(111) seems to confirm the result that the ES-barrier vanishes below a critical distance. On the other hand, however, they are in contradiction to the interpretation of a possible correlation between the step-edge barrier and the occupation of surface states. The good agreement between the experimental data for Cu(111) and the calculated critical width based on the electron confinement may therefore be only coincidental.

Another reasonable explanation for the onset of rapid island decay for small distances between island edges may be a strong influence of overlapping lattice relaxation fields at step edges. The step-edge barrier as well as the detachment barrier for adatoms from the island edge and the diffusion barrier on the terrace may be considerably changed for small distances between island edges. Very recent STM studies on Ni(100) by Hoogeman et al. [284] corroborate the possible importance of strain fields for the diffusion barriers. They showed that vacancy islands snap together over a distance of 20-30Å rather than approach each other by their Brownian motion and coalesce<sup>90</sup>. The snapping of vacancy islands, however, was exclusively observed for vacancy islands oriented diagonally to each other, i.e., the snapping process occurred, if a vacancy island corner was within 20-30Å distance from another vacancy island's ledge. Hoogeman et al. concluded that the exchange barrier of mono-vacancies between the island edges may be reduced, due to the elastic strain fields built up for small distances. Theoretical work corroborates this idea: Schroeder and Wolf [360] showed that diffusion barriers alter significantly under strain fields. Ratsch et al. [209] demonstrated in their calculations that diffusion barriers depend on the interatomic distance, which was earlier experimentally demonstrated for Ni on Ru(0001) by Meyer et al. [208]. Since local strain fields may alter the interatomic distances considerably, the diffusion rate may be significantly enhanced. So far, it is not understood, however, whether the concept of a possible influence of strain fields on exchange and diffusion barriers is pertinent also to the rapid decay events. Therefore, detailed energy potential calculations including lattice relaxations are desirable.

In a recent work, we considered the possibility [355] that the vanishing of the step-edge barrier is not a necessary condition to describe rapid mound decay: We performed numerical calculations of the decay rate equation (6.36) and showed that all rapid multilayer island decay events can be described, if one assumes that the rapid decay process sets in, when the distance between the upper and the lower island edge is below one atomic row. Such a close

---

<sup>90</sup> We observed similar events for Cu and Ag island stacks on Cu(111) and Ag(111). The edges of adatom islands within the stack seem to snap together once in a while and form temporarily necks between the island edges.

contact between the island edges may frequently occur, due to the island edge fluctuations, and hence, due to the Brownian motion of islands. From a temperature dependent analysis of rapid island decays on Cu(111) and Ag(111), we find an activation energy of the rapid decay process of  $0.69 \pm 0.04$  eV and  $0.62 \pm 0.05$  eV [355], respectively. Both values are significantly smaller than the activation energy for normal diffusion limited decay, which are  $E_{\text{ad}} + E_{\text{diff}} = 0.76$  eV [200] and 0.71 eV [249]. A possible microscopic process, which could cause a lower activation barrier for multilayer island decay, involves a concerted motion of a kink atom in the upper island and atoms next to a adjacent kink of the lower island [355] and was first proposed by Bartelt in 1997 [361]. In order to decide whether an exchange process of kink atoms in the upper layer island adjacent to kink sites in the lower layer island or a vanishing of the ES-barrier cause rapid decay events, detailed energy calculations would be necessary.

## 7. Islands on metal electrodes in liquid environment

As was already emphasized in Section 5, basic theoretical principles for the surface in equilibrium can also be applied to metal electrodes in contact with a liquid. In the last section, ripening phenomena after homoepitaxial growth, e.g., island decay and coalescence on metal surfaces in UHV were discussed. Similar phenomena have also been observed on metal surfaces in liquid environment. The ripening of island structures on metal electrodes, however, have not yet been as intensively studied as in UHV. The interest in studies of growth phenomena on metal electrodes and the influence of defects on this growth focusses, in particular, on the physics of the UPD, where a monolayer is deposited on the substrate prior to bulk deposition. This is because of the strong interaction between the electrolyte metal cations and the first atomic layer of a chemically different metal electrode. UPD as well as the bulk deposition of metals on the atomic scale was studied quite extensively for various systems [210, 362-391]. Furthermore, many efforts were launched to manufacture nanostructures in a controlled manner on surfaces in the electrochemical cell [371, 392-404]. However, so far little quantitative information is available on activation barriers for atomic transport. Twomey et al. investigated the electrochemically induced facetting of Pt(111) in 1M H<sub>2</sub>SO<sub>4</sub>. From the temperature dependence of smooth zones on rough terraces, a diffusion barrier on the (111) plane of  $0.2 \pm 0.05$  eV at +230mV vs. RHE was estimated [11]. Semi-quantitative studies during cluster deposition and dissolution on polycrystalline copper rods in perchloric acid were presented by Zhang and Stimming [405], who analyzed local microscopic current densities and corrosion rates [406]. A theoretical analysis based on these experimental results was later published by Schmickler and Stimming [371], who simulated the ripening of isolated clusters of different sizes. Nichols et al. [368] studied Cu cluster sizes on Au(111) and (100) electrodes as a function of time and the island density as a function of the overpotential. A similar study was also performed by Li et al. [396] for Cu and Ag clusters on graphite. Milchev [407] investigated nucleation depletion zones around large clusters, which arise from the decrease of the surface adatom concentration around large 3-dimensional islands. However, no further quantitative results on diffusion lengths were obtained. The selective dissolution from Ag-Au alloys in perchloric acid was studied by Oppenheim et al. [408], who observed Brownian motion of vacancy islands and coalescence events similar to what is studied quantitatively in UHV. Trevor and Chidsey [211] then analyzed semi-quantitatively the motion of Au islands on Au(111) in perchloric acid at +700mV vs. NHE and find that the diffusion coefficient obeys a power law in the island radius with an exponent -3, which is evidence for edge diffusion mediated island motion (see Section 6.1.5).

Furthermore, they give an estimate for the sum of the adatom formation energy  $E_{ad}^{st}$  at steps and the edge diffusion barrier  $E_d$  of  $E_{ad}^{st} + E_d \sim 0.5\text{eV}$  [211]. Although qualitative observations of diffusion and ripening processes on metal electrodes in liquid environment were reported for more than a decade now, quantitative investigations are still scarce. In the following, semi-quantitative STM studies of the Ostwald ripening of mono- and multilayer islands as well as the analysis of island equilibrium shapes on metal electrodes are presented.

Talking about diffusion and ripening processes on metal electrodes in electrolyte one has to consider that, in contrast to surfaces in UHV, the solid is in equilibrium with the adjacent liquid phase and a rapid exchange of atoms can occur, if the electrode potential is changed. In other words, whereas evaporation from the solid into the gas phase is negligible in UHV studies at low temperatures, the possibility of metal dissolution into the electrolyte or deposition from the electrolyte must always be taken into account. During the ripening of surface structures after electrodeposition, mass exchange with the liquid may, in fact, become important as will be discussed in the following. It is emphasized at this point that the studies presented here deal exclusively with the ripening after cluster formation which, however, may be affected by deposition and nucleation processes.

In one of the first studies of the kind, Dakkouri et al. [409] analyzed the Ostwald ripening and coalescence of Au islands on Au(100). The monatomic high islands are formed during the lifting of the quasi-hexagonal reconstruction of the gold (100) face [179, 180, 204]. Fig. 73 shows STM images of the Au(100) surface in 0.05M  $\text{H}_2\text{SO}_4$  [409]. In the first image (a), the top scan lines were recorded at 0mV vs. SCE where the surface is still reconstructed. Marked by an arrow is the scan line, where the potential was increased to +400mV and immediately monatomic high islands were formed, due to the lifting of the reconstruction<sup>91</sup>, which reveal the square symmetry of the substrate. In the following images, the electrode potential was held constant and the island density was measured over a period of about 80min. Analog to what is found for metal surfaces in UHV, Ostwald ripening of the islands occurs. In the lower right corners of (c) and (d) as well as of (e) and (f) coalescence events between two islands, respectively between an island and a step edge are visible.

Dakkouri et al. [409] studied also the island migration velocity on Au(111) in 0.05M  $\text{H}_2\text{SO}_4$  at +540mV vs. SCE as a function of the island size and found that the speed is inversely proportional to the island diameter. Hence, the size exponent  $\alpha$  from the theory of

---

<sup>91</sup> In the reconstructed phase, the surface atom density is 4% higher than in the unreconstructed phase. Hence, when the reconstruction is lifted, additional terrace adatoms are formed which nucleate as monolayer high islands.

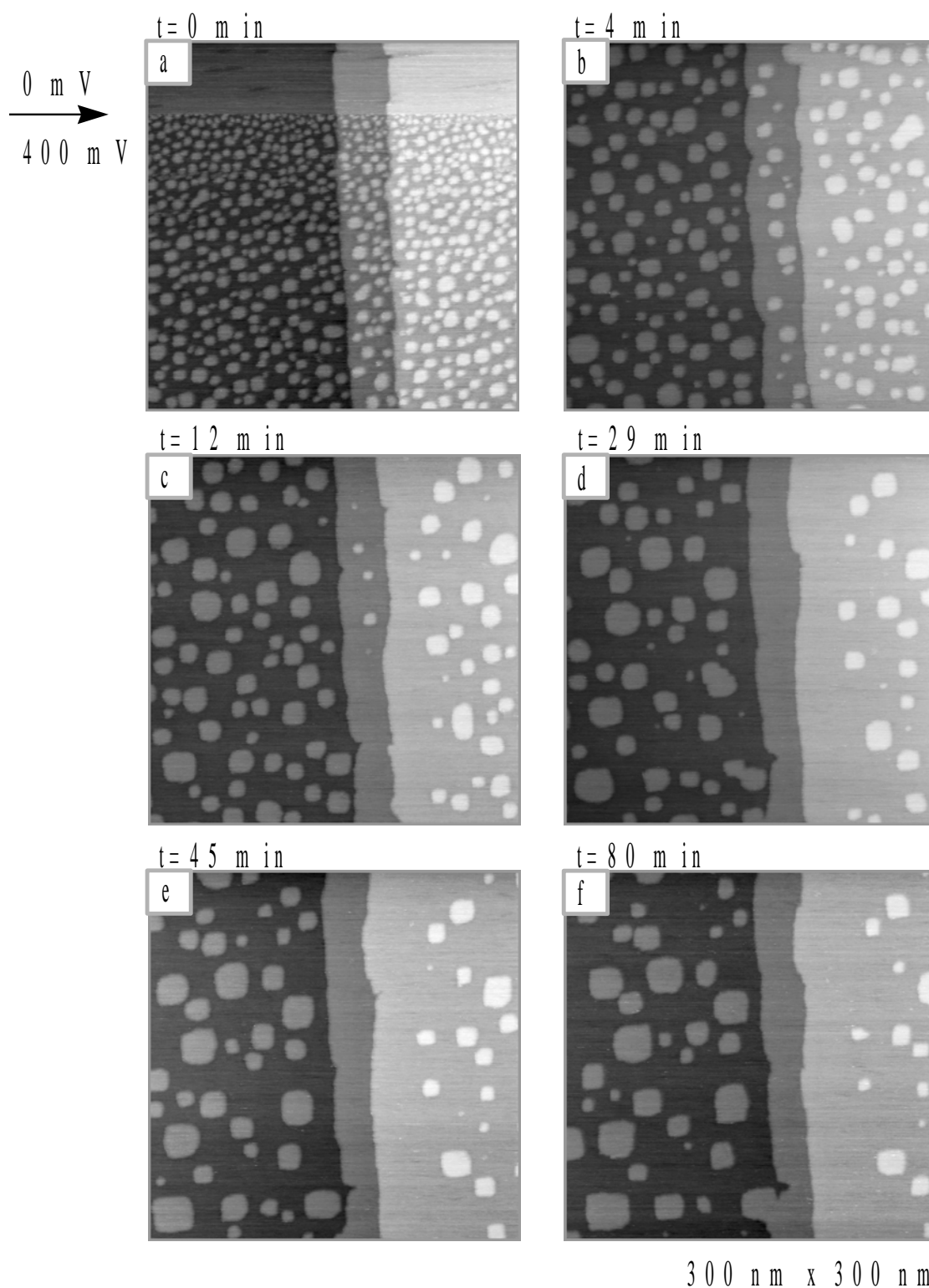


**Fig. 73.** STM images of Au(100) in 0.05M H<sub>2</sub>SO<sub>4</sub> after a potential step from 0mV to +400mV vs. SCE (as marked by an arrow in image (a)). The surface reconstruction of Au(100) in sulfuric acid [204] is lifted when the electrode potential is increased to +400mV. The lifting of the surface reconstruction is accompanied by the formation of nearly squared monolayer high islands. Subsequent island coarsening is due to Ostwald ripening and coalescence (after Dakkouri et al. [409]).

Brownian motion of islands (see Section 6.1.5) is equal to  $1/2$ , which is evidence for terrace diffusion mediated island migration. This conclusion is, however, questionable as was already discussed in the previous section. There, it was mentioned that the experimentally measured diffusion exponents may significantly deviate from the theoretically expected exponent for a given dominant mass transport process. In fact, a further experimental observation by Dakkouri et al. [409] corroborates the hypothesis that the island migration is mediated by edge rather than terrace diffusion. The authors analyzed the influence of additional chloride in the solution on the island migration on Au(111). They found that the Brownian motion is not significantly affected by chloride. In contrast to this, Ostwald ripening which involves terrace diffusion is much faster when chloride is added. One may therefore conclude that island migration involves no terrace diffusion, but is driven by edge diffusion in agreement with the studies by Trevor and Chidsey [211] on Au(111) in perchloric acid, where edge diffusion mediated island motion was observed.

The experimental observation that the Brownian motion of Au(111) is not affected by additional chloride in 0.05M  $H_2SO_4$  is, however, in contradiction to the measurements of step fluctuations on Au(111) in 0.1M  $H_2SO_4$  with different amounts of chloride added [62] (Section 5.3). When chloride is added to the solution, the step fluctuations increase compared to sulfuric acid without chloride (Fig. 40). Hence, one would expect that also the fluctuations of island edges (and hence, the Brownian motion) would increase, when chloride is added to the electrolyte. This contradiction is not solved yet.

A study of the ripening of Cu islands on Ag(111) in sulfuric acid was published by Kolb et al. [401]: Fig. 74 shows (a) a time sequence of STM images of Cu monolayer islands on Ag(111) in 0.05M  $H_2SO_4$ +1mM  $CuSO_4$  at +10mV<sup>92</sup> vs.  $Cu/Cu^{2+}$ . In (b), the areas of the numbered islands 1-4 are plotted vs. time. The size of the islands is normalized with respect to their initial size at  $t=0$ . Similar to what is observed in UHV for Ag by Morgenstern et al. [274, 281, 283], for Ni by Hoogeman et al. [284] and for Cu islands by our group (Fig. 59) [200, 201], the decay curves are rounded and the decay of neighboring islands is correlated. Larger islands initially grow at the expense of smaller islands. The larger islands start to decrease in size, when the smaller ones have disappeared. Although Dakkouri et al. did not study the decay exponents one may conclude from the shape of the decay curves and the strong correlation between neighboring islands that the decay of monolayer high Cu islands on Ag(111) in sulfuric acid is diffusion limited at +10mV vs.  $Cu/Cu^{2+}$ . In the same study, Kolb et al. could show that the decay of isolated Cu monolayer islands on Ag(111) is linear at +40mV

and +60mV vs.  $\text{Cu}/\text{Cu}^{2+}$ , and the decay rate increases with increasing overpotential (Fig. 75) [401]. The linearity of the decay curves is evidence for a detachment limited decay of monolayer high Cu-islands for larger overpotentials.

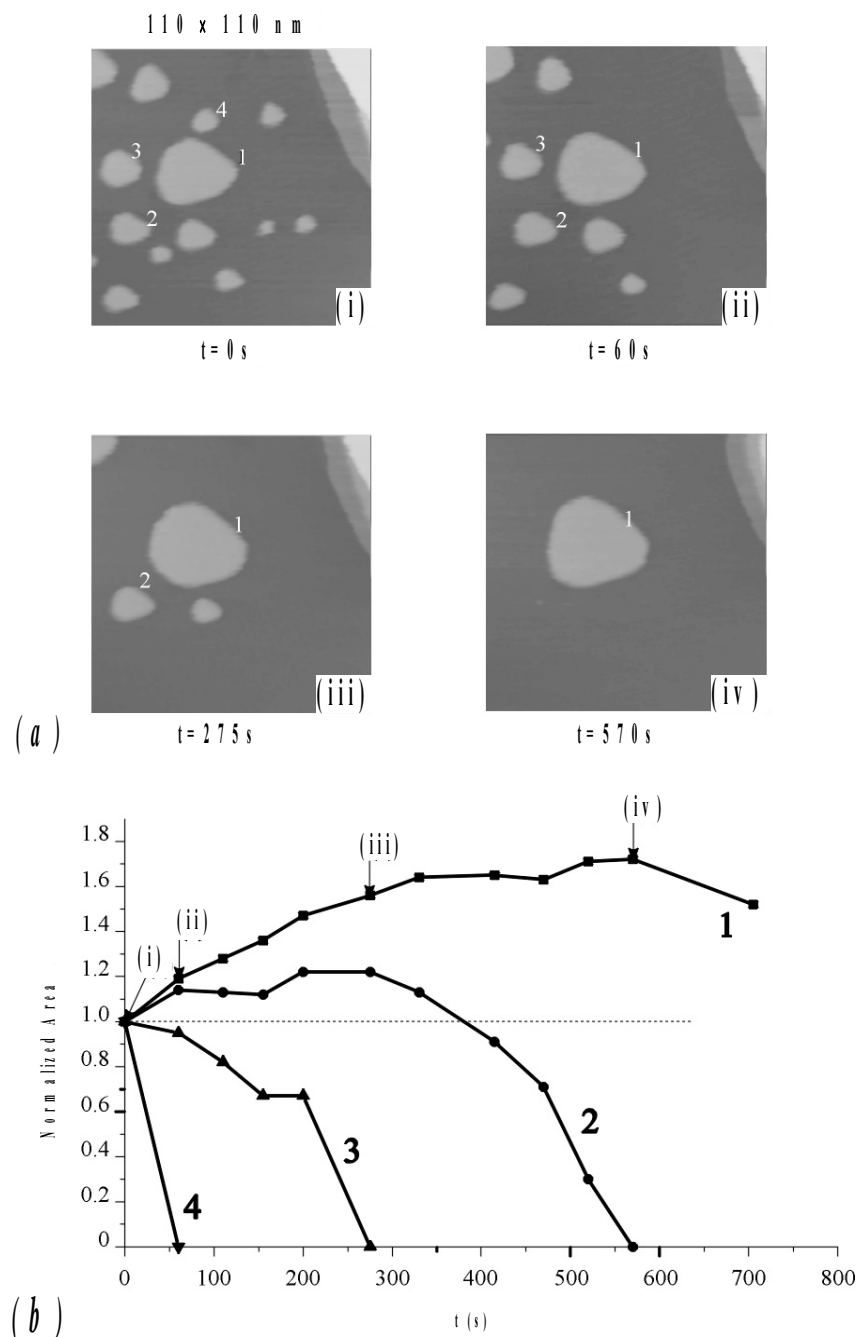


**Fig. 74.** Ostwald ripening of monolayer high Cu islands on Ag(111) in 0.05M  $\text{H}_2\text{SO}_4$ +1mM  $\text{CuSO}_4$  at +10mV vs.  $\text{Cu}/\text{Cu}^{2+}$ . (a) Series of STM images from a time sequence over 570s. Note that the shape of the islands bear a trigonal rather than a hexagonal symmetry, in contrast to Cu-islands on Cu(111) in UHV. (b) Area of the numbered islands in (a) as a function of time (after Kolb et al. [401]).

<sup>92</sup> At this potential, the system is sufficiently close to the Nernst potential of Cu (0mV vs.  $\text{Cu}/\text{Cu}^{2+}$ ) to prevent anodic dissolution within about one hour [401].

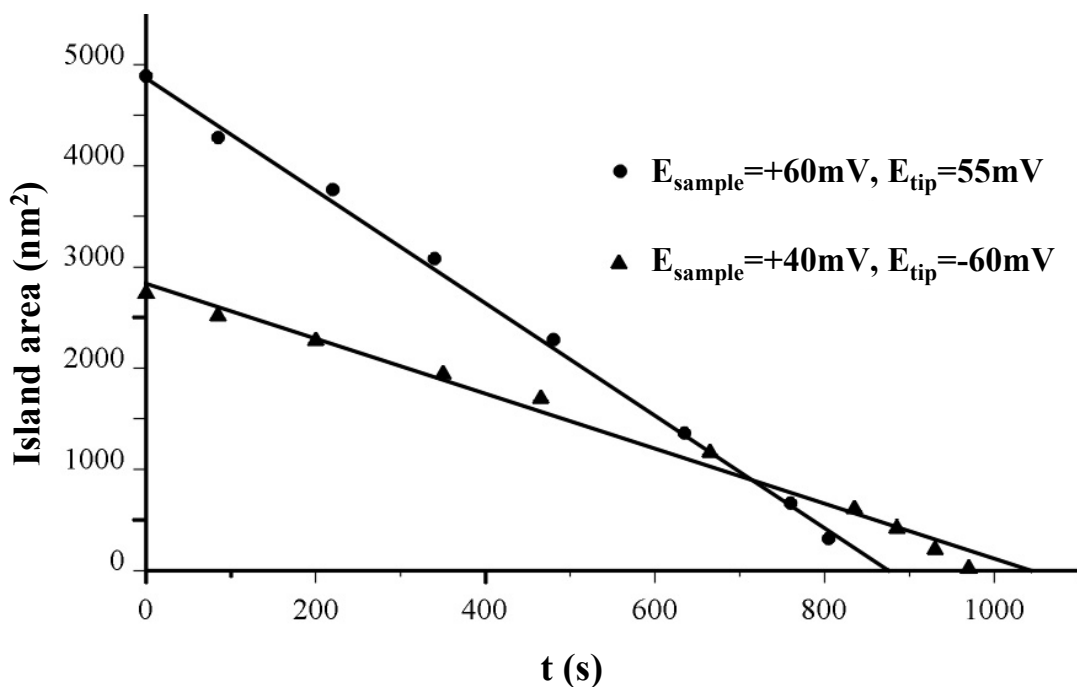


**Fig. 75.** Area of isolated monolayer high Cu islands on Ag(111) in 0.05M  $\text{H}_2\text{SO}_4$ +1mM  $\text{CuSO}_4$  at +40 and +60mV vs.  $\text{Cu}/\text{Cu}^{2+}$ . At these potentials, the island decay is detachment limited and the decay rate increases with increasing overpotential (after Kolb et al. [401]).

Kolb et al. [401] studied also the anodic dissolution of multilayer Cu islands. Fig. 76 shows (a) STM images of an initially four-layer high island stack at different times and (b) the corresponding decay curves at +30mV vs.  $\text{Cu}/\text{Cu}^{2+}$ . The decay occurs layer-by-layer, i.e., the top island decays and the island beneath grows at the expense of the top island. Lower layer islands start to decay, when the upper islands vanish. Therefore, the decay of the islands in a multilayer stack is not described by a linear curve which is in contrast to the detachment limited decay of monolayer high islands in the course of anodic dissolution shown in Fig. 75. Kolb et al. concluded that the island decay involves atomic hopping over the island edges giving rise to a net mass flux from upper to lower islands. They inferred further that the increase in size of lower layer islands must be at least partially counterbalanced by dissolving Cu atoms from the island edges into the electrolyte because the initial increase in size of the lower islands in the stack remains smaller than the total loss of the upper islands.

Further evidence for island decay by dissolution into the electrolyte was recently found by Broekmann et al. [56]. These authors studied the decay of multilayer island stacks on a Cu(111) electrode in 10mM HCl as a function of the electrode potential. For low electrode potentials, where no chloride is specifically adsorbed on the metal surface, the diffusivity is low and islands remain constant in size. At higher potentials, the diffusivity increases and

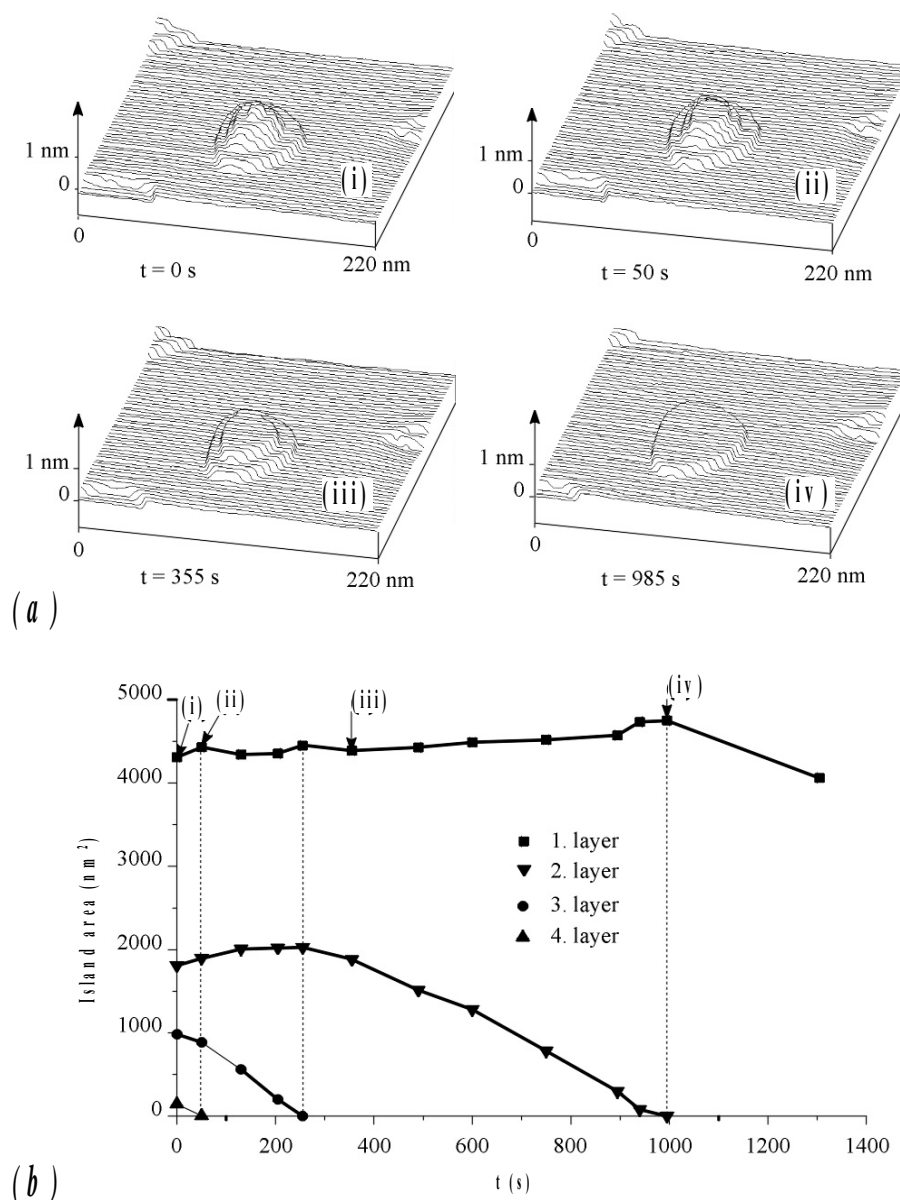


**Fig. 76.** Multilayer Cu island decay on Ag(111) in 0.05M  $\text{H}_2\text{SO}_4$ +1mM  $\text{CuSO}_4$  at +30mV vs.  $\text{Cu}/\text{Cu}^{2+}$  (after Kolb et al. [401]).

multilayer island stacks decay within several minutes. Fig. 77 shows STM images of a Cu multilayer island on Cu(111) in 10mM HCl at (a) -580mV vs.  $\text{Hg}/\text{Hg}_2\text{SO}_4$  (corresponding to about -170mV vs. SCE) and (b) -510mV vs.  $\text{Hg}/\text{Hg}_2\text{SO}_4$  (corresponding to about -100mV vs. SCE) at room temperature [56]. As seen from Fig. 77(a), the multilayer island stack decays layer-by-layer. A different situation is, however, observed at a more positive potential as demonstrated in Fig. 77(b). Here, the islands in the different layers seem to decay simultaneously. The difference in the island decay process for lower and higher potentials becomes obvious from the inspection of the corresponding decay curves (Fig. 78) [56]. For lower potentials (Fig. 78(a)), the decay curves are obviously curved and interaction occurs

between the islands, i.e., the island decay is diffusion limited (6.32) and (6.33). In the other potential range (Fig. 78(b)), the island decay is linear in time, and hence, the decay is detachment limited (6.34) and (6.35). Based on these results, Broekmann et al. proposed the existence of two different mass transport regimes. In the lower potential range, the decay of the islands is mediated by detachment of atoms from the edges of the smaller islands and subsequent hopping across the edge of the island below, where the diffusion on the terrace must be slow. This interpretation and the observation of a diffusion limited decay for lower potentials are in agreement with our analysis of the time dependence of step fluctuations on Cu(111) in 1mM HCl (Fig. 35) [112]. We found that the time correlation function obeys a  $t^{1/3}$ -law below -120mV vs. SCE, which is evidence for diffusion limited mass transport (3.27) on the terrace in this potential range. Furthermore, Broekmann et al. argued that for higher potentials simultaneous decay of the entire stack is possible only for direct detachment of atoms from the island edges into the electrolyte. The linearity of the decay curves in that

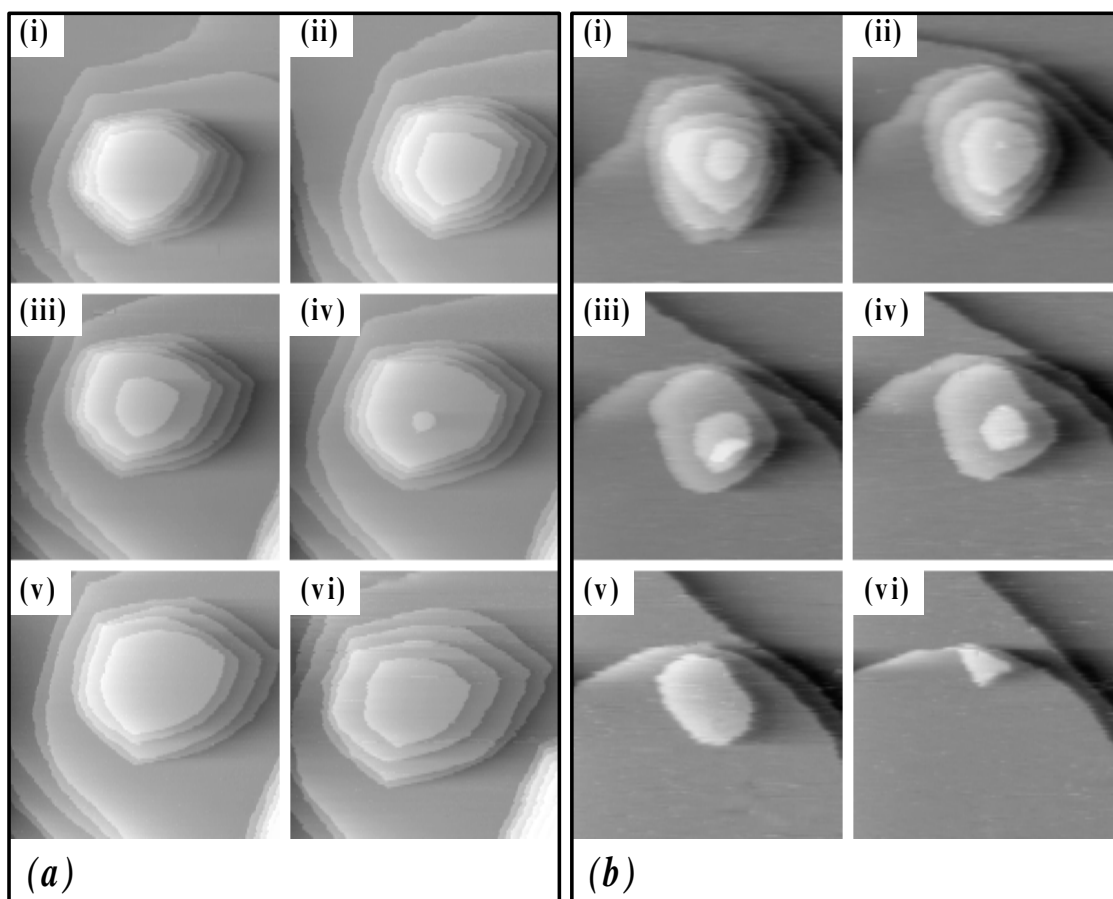


**Fig. 77.** Time sequence of STM images of a multilayer Cu island on Cu(111) in 10mM HCl (a) at -580mV and (b) at -510mV vs. Hg/Hg<sub>2</sub>SO<sub>4</sub>. The total time span covered by the images is about 36min and 10min, respectively (after Broekmann et al. [56]).

potential range confirms this conclusion because detachment of atoms from the island edge into the electrolyte is most probably slower than diffusion of  $\text{Cu}^{2+}$ -ions in the electrolyte, and hence, should be the time determining step during decay. One may emphasize, however, that the linearity of the island decay curves is a priori merely evidence for a detachment limited decay mechanism. A variation in the electrode potential changes the subtle balance between detachment barriers, diffusion energies and the activation energy for hopping across the lower island edge and thus may lead to a transition in the dominant mass transport process. Such a transition would be similar to what is observed in the potential dependent studies on step fluctuations on metal electrodes [59-62] and in theoretical calculations by Haftel and Einstein [189].

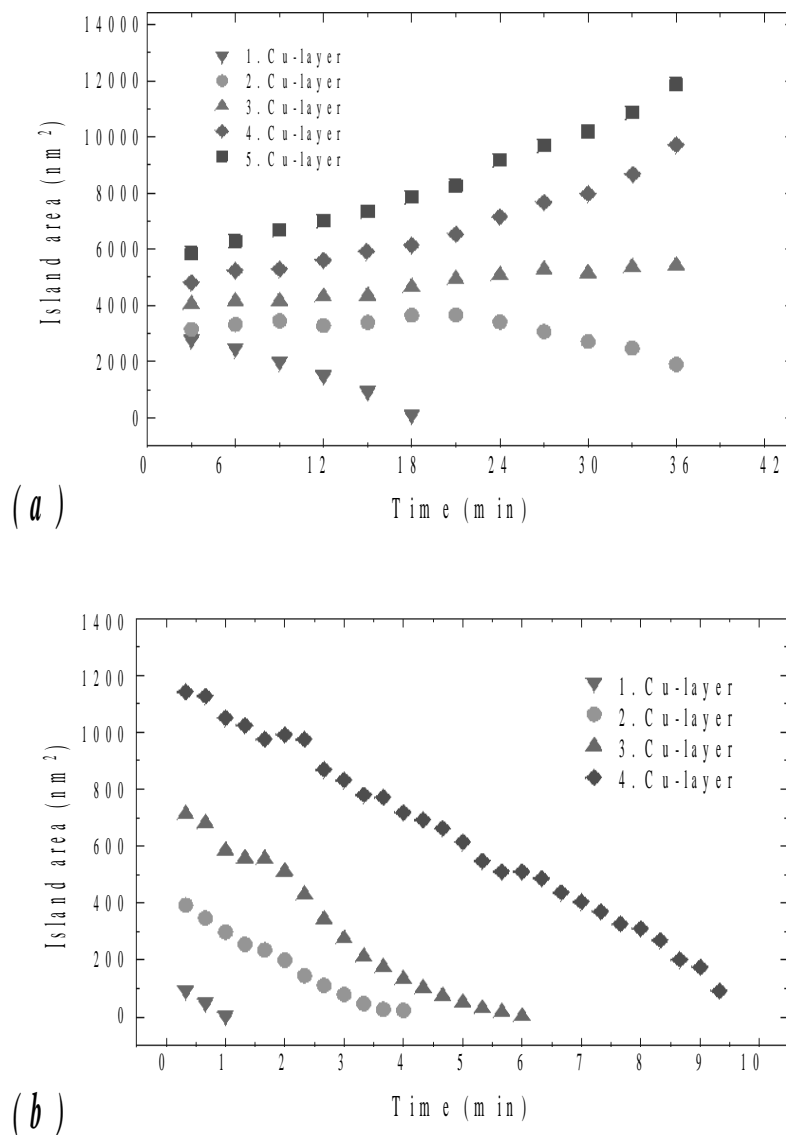


**Fig. 78.** Island area vs. time for the island stacks shown in Fig. 77. Cu(111) in 10mM HCl at (a) -580mV and (b) -510mV vs. Hg/Hg<sub>2</sub>SO<sub>4</sub> (after Broekmann et al. [56]).

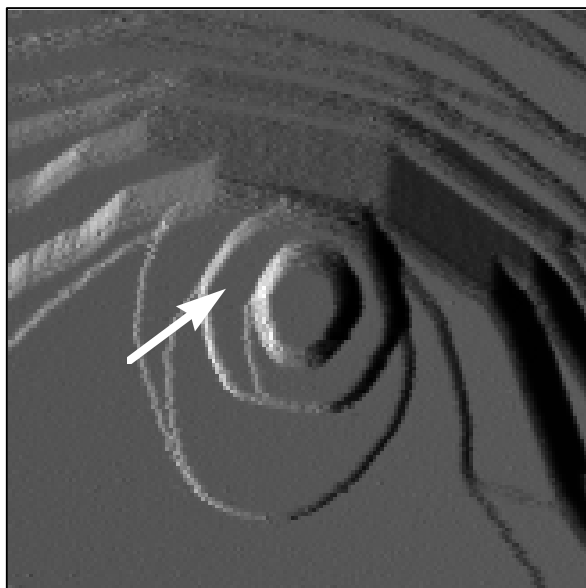


**Fig. 79.** STM image of an Ag adatom multilayer island on Ag(111) in 0.05M H<sub>2</sub>SO<sub>4</sub>+1mM CuSO<sub>4</sub> at +60mV vs. SCE. The lower layer islands (marked by an arrow) are in equilibrium. From the equilibrium shape, the Ising parameter J (6.4)-(6.9) can be determined [59].

Finally, a study of the equilibrium shape of Ag islands on Ag(111) [59] is mentioned, where we estimated the kink energy on Ag(111) in electrolyte. Fig. 79 shows a multilayer silver island on Ag(111) at +60mV vs. SCE in 0.05M H<sub>2</sub>SO<sub>4</sub>+1mM CuSO<sub>4</sub>. The top layer islands do not reveal the equilibrium shape, which is an almost perfect hexagon. The lower layer islands (marked by an arrow), however, are in equilibrium. The island shape was analyzed according to the Ising model (6.6) and (6.7), from which we determined the Ising parameter J at +60mV to be about  $J=0.1\text{eV}^{93}$ . This value is consistent with the Ising parameter measured on Ag(111) in UHV ( $J=104\pm 3\text{meV}$ , Fig. 50) [88]. The agreement between the Ising parameters for Ag(111) in electrolyte at this potential and in UHV justifies the conclusion that the kink and step energies for both systems should be approximately the same (compare also Section 6.1.3). Hence, we find that on Ag(111) in 0.05M H<sub>2</sub>SO<sub>4</sub>+1mM CuSO<sub>4</sub> at +60mV vs. SCE the kink energy is about  $\varepsilon=100\text{meV}$  [88].

<sup>93</sup> In [59], we interpreted the Ising parameter J as the kink energy  $\varepsilon$ . Later, we showed that J is not related to the kink energy [88] as discussed in Section 6.1.2. In particular on (100) surfaces, the Ising parameter is much smaller than the kink energy. Only in the case of (111) surfaces, J is coincidentally about the same size as the kink energy.

## 8. Conclusion

The investigation of step and island dynamics on metal surfaces in equilibrium and non-equilibrium has contributed enormously to the understanding of surface structures, growth phenomena and stability of nano-structures. These studies are the only ones available today, which provide with quantitative information about atomic diffusion processes in cases, where the motion of single atoms is not directly visible as, e.g., on metal surfaces at high temperatures or on metal electrodes in contact with an electrolyte.

The equilibrium fluctuations of steps on surfaces in UHV are widely understood and the method to determine kink energies and diffusion parameters by analyzing the step correlation functions for spatial as well as for time information is well established. Concern has been raised by some researchers in how far the experimental results are partially due to tip artefacts. It was shown, however, that careful studies as a function of the tunneling resistance and the scan frequency can unambiguously determine whether and even how much the results are affected by tip-surface interactions. In the by far prevailing number of cases no tip effects were found. Interesting open questions concern the influence of geometrical kinks on the time correlation function and the kind of information, which can be extracted from the analysis of equilibrium fluctuations of steps oriented along a low-symmetry crystal direction. Furthermore, systematic studies of the influence of adsorbates on the step fluctuations are still lacking. Investigations of the influence of adsorbates on the step dynamics are very important as model studies for metal electrodes in contact with an electrolyte and for the role of surfactants in epitaxial growth. It was demonstrated, e.g., for Cu(111) that the mass transport kinetics on the surface in contact with an electrolyte may differ considerable from UHV, if anions are specifically adsorbed: Whereas in UHV edge diffusion is the mediating transport mechanism on Cu(111) below 500K, terrace exchange with slow surface diffusion prevails, when the surface is brought into chloric acid. It would be interesting whether similar mass transport processes could be initiated on metal surfaces in UHV, if the substrate is covered by adsorbates.

Three key problems remain unsolved in the theory of surface coarsening: The first problem is the physical explanation for the unusually large values of the step free energy obtained from the analysis of the decay of monolayer high islands. A possible reason could be a deviation of the chemical potential from that in the Gibbs-Thomson equation for small islands. Here, a better understanding of the consequences of approximations in the theory for the two limiting cases - diffusion and detachment limited decay - is desirable. Unfortunately, simulations of

island decay using realistic energy parameters, which may contribute to the solution of this unsolved problem, are still lacking.

A second major question is in which way coarsening exponents measured, e.g., during island diffusion and coalescence yield information on the dominant mass transport mechanism. In contrast to theoretical studies, where universal exponents are proposed, experimental studies and simulations show that a large variety of exponents may be measured. As a consequence, direct conclusions about the dominant mass transport processes from the Brownian motion of islands are still difficult, if not impossible. It would be interesting to study theoretically in how far the non-universal exponents found in experiment are due to the contribution of different mass transport mechanisms in the short- and in the long-time regime.

The third key problem is related to the physical origin of the step-edge barrier. Our previous interpretation that the existence of an ES-barrier is correlated with the occupation of surface states, does not hold in the light of the most recent experiments. In addition, the rapid decay mechanism can be explained by an exchange process at kink sites rather than by a vanishing of the ES-barrier. Here, theoretical calculations would be in particular helpful.

For metal surfaces in electrolytes, it was demonstrated that activation energies of atomic processes can be measured from either the potential or the temperature dependence of step fluctuations in equilibrium. The main problem for metal surfaces in aqueous electrolytes is the restriction of the experiments to a small temperature range, which in general reduces the accuracy of measured activation energies and pre-exponential factors. Non-aqueous electrolytes have not been considered, so far, however, their use in analogous experiments would be of great interest.

The analysis of island dynamics on metal electrodes in contact with a liquid is still at the beginning. Nevertheless, preliminary, semi-quantitative experiments are very promising. In order to systematically study island dynamics and extract quantitative information about diffusion barriers or step energies, the experimentalists have to learn how to create vacancy and adatom islands (in hetero- as well as in homoepitaxy) in a controlled manner to provide for a sufficiently large data base.

The experimental results achieved so far confirm the idea that activation and formation energies on metal electrodes in liquid environment are similar to the energies on metal surfaces in UHV, at least for electrode potentials far below the potential of rapid metal dissolution. Although it may be a great challenge to extend experiments at the solid/liquid interface and obtain sufficient large data sets to match the high quality standard common in UHV experiments as well as the standards of statistical significant experiments, the expected

results would be worth the effort. Such experiments would serve to lay the foundation for a quantitative understanding of dynamical processes at the solid-liquid interface.

## Acknowledgement

I gratefully acknowledge the contribution of all former and present collaborators in the STM group in Jülich to the work presented in this review, namely Sascha Baier, Josef Frohn, James B. Hannon, Rainer Jentjens, Christian Klünker, Mathias Poengen, Georg Schulze Icking-Konert, Frank Schmitz, Dietmar Stapel, Christoph Steimer and J. Franciscus Wolf.

I further appreciate fruitful collaborations and discussions with Ted L. Einstein and Ellen D. Williams (both University of Maryland, College Park) and Norman C. Bartelt (Sandia National Labs, Livermore).

My gratitude goes also to Dieter M. Kolb (University of Ulm, Germany) for helpful discussions on the field of electrochemistry. I further appreciate the collaboration with his group in Ulm and their experimental contributions. I acknowledge, in particular, the help of Michael Dietterle, Ludwig Kibler, Markus Kleinert and Rudolf Randler.

I am deeply indebted to Harald Ibach (Research Center Jülich, Germany) for his steady support over the last years and for his comments on the article. My special thank goes also to Sascha Baier (Research Center Jülich, Germany) for the critical reading of the manuscript and to Andreas Otto (University of Düsseldorf, Germany) for his support during the last two years.

Many people have contributed to this review by giving me kindly permission to use their data and sending me electronic files: Norman C. Bartelt, Peter Broekmann, Erminald Bertel, Michael Dietterle, Ted L. Einstein, Dieter M. Kolb, Thomas Michely, Karina Morgenstern, Rudolf Randler, Georg Rosenfeld, Krishna Swamy, Klaus Wandelt, Jörg Ziegler.

## Appendix A

### *Determination of miscut angles and mean step separations for vicinal surfaces of fcc metals*

Here, useful formulas for the determination of the miscut angle and mean terrace widths of several vicinal surfaces of fcc metals are given.

#### *A.1. Vicinal surfaces with Miller indices (11n)*

(11n) surfaces are vicinal to the (001) plane, with a miscut angle  $\theta$  along the dense  $[\bar{1}\bar{1}0]$ -direction and an azimuth  $\Phi=0$ . From the scalar product of the surface normal vectors  $[11n]$  and  $[001]$  one obtains

$$\cos\theta = \frac{n}{\sqrt{2+n^2}} ; \tan\theta = \frac{\sqrt{2}}{n} . \quad (\text{A.1.1})$$

From Fig. 80, one finds that the miscut angle  $\theta$  can be expressed in terms of the terrace width and the step height  $h$ , which is equal to the distance between adjacent (001) crystal planes<sup>94</sup> :

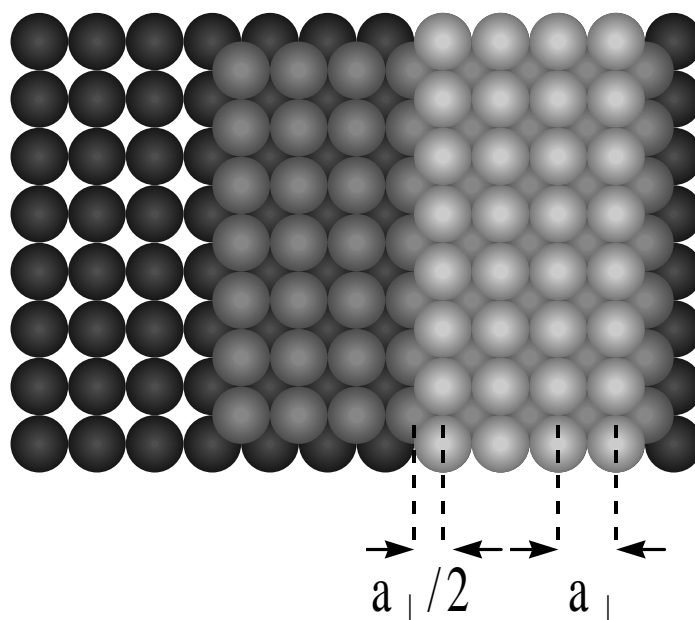


**Fig. 80.** Model of a stepped fcc (100) surface. The distance between dense atomic rows along  $\langle 110 \rangle$  is  $a_{\perp}$ . The lower atomic row at the step edge contributes a distance of  $a_{\perp}/2$  to the lower terrace width.

<sup>94</sup> The distance between crystallographic planes (hkl) is given by the Laue equation:  $d_{hkl} = a_0 / \sqrt{h^2 + k^2 + l^2}$ . Note, that for the face centered (001) plane the distance between adjacent planes is given by  $d_{002}$ !

$$\tan\theta = \frac{a_0}{2w} = \frac{a_{\perp}}{w}, \quad (\text{A.1.2})$$

where  $a_{\perp}$  is the distance between atomic rows perpendicular to the step orientation (Fig. 80). For (001) planes of fcc metals,  $a_{\perp}$  is equal to the nearest neighbor distance  $a_0/2$ . Using (A.1.1) and (A.1.2), one finds for the terrace width  $w$

$$w = a_{\perp} \frac{n}{2}. \quad (\text{A.1.3})$$

Steps on (11n) vicinals form (111)-microfacets with the underlying (001)-terrace. As shown in Fig. 80, the microfacet is formed by a closed packed atomic row in the upper and lower terrace. The contribution of the upper atomic row in the microfacet to the width of the upper terrace is that of a complete row whereas the contribution of the lower row in the microfacet to the lower terrace is that of half an atomic row. Hence, the mean terrace width consists of an integer number of atomic rows plus half a row. Vicinal surfaces to (001) with equidistant steps, i.e., constant value of  $w$ , therefore have an uneven Miller index  $n$ .

#### A.2. Vicinal surfaces with Miller indices $(n, n, n \pm m)$

Surfaces with  $(n, n, n \pm m)$  orientation are vicinal to the (111) plane. In the case of  $(n, n, n + m)$ , the surfaces consist of parallel A-steps ( $\{100\}$ -microfacet).  $(n, n, n - m)$ -vicinal surfaces reveal B-steps ( $\{111\}$ -microfacet). The azimuth is  $\Phi = 0$  and the miscut angle  $\theta$  is given by

$$\tan\theta = \frac{m\sqrt{2}}{3n \pm m}. \quad (\text{A.2.1})$$

The mean terrace width  $w$  is then

$$w = a_{\perp} \frac{2}{3m} (3n \pm m), \quad (\text{A.2.2})$$

where  $a_{\perp} = \frac{a_0}{2} \sqrt{\frac{3}{2}}$ ,  $a_0$  the lattice constant.

## Appendix B

### Derivation of (3.5) and (3.6)

According to (3.3), the free energy of a step pinned between two points A and B is given by

$$f = \int_A^B \gamma ds = \int_A^B \gamma \left( \frac{\partial x}{\partial y} \right) \sqrt{1 + \left( \frac{\partial x}{\partial y} \right)^2} dy, \quad (\text{B.1})$$

where  $ds$  is a small step segment along the step profile and  $\gamma$  is the line tension. A variation in the step position  $\delta x$  is accompanied by a variation in the step free energy  $\delta f$ :

$$\begin{aligned} \delta f &= \int_A^B \delta \left[ \gamma(x') \sqrt{1 + (x')^2} \right] dy \\ &= \int_A^B \frac{\partial}{\partial x'} \left[ \gamma(x') \sqrt{1 + (x')^2} \right] \delta x' dy = \int_A^B \frac{\partial}{\partial x'} \left[ \gamma(x') \sqrt{1 + (x')^2} \right] \frac{\partial}{\partial y} (\delta x) dy \end{aligned} \quad (\text{B.2})$$

Here, the abbreviation  $x' \equiv \frac{\partial x}{\partial y}$  is used. Partial integration of (B.2) yields

$$\begin{aligned} \delta f &= \int_A^B \frac{\partial}{\partial x'} \left[ \gamma(x') \sqrt{1 + (x')^2} \right] \frac{\partial}{\partial y} (\delta x) dy \\ &= (\delta x) \frac{\partial}{\partial x'} \left[ \gamma(x') \sqrt{1 + (x')^2} \right] \Big|_A^B - \int_A^B \frac{\partial}{\partial y} \left[ \frac{\partial}{\partial x'} \left[ \gamma(x') \sqrt{1 + (x')^2} \right] \right] (\delta x) dy \end{aligned} \quad (\text{B.3})$$

If the variation  $\delta x$  vanishes at the end points A and B of the step, one finds

$$\delta f = - \int_A^B \frac{\partial}{\partial y} \left[ \frac{\partial}{\partial x'} \left[ \gamma(x') \sqrt{1 + (x')^2} \right] \right] \delta x dy. \quad (\text{B.4})$$

Comparison with

$$\delta f = \frac{1}{\Omega} \int_A^B \mu \delta x dy, \quad (\text{B.5})$$

yields

$$\mu = -\Omega \frac{\partial}{\partial y} \left[ \frac{\partial}{\partial x'} \left[ \gamma(x') \sqrt{1+(x')^2} \right] \right], \quad (\text{B.6})$$

which is the same expression as in (3.5).

$x'$  is now expressed as  $x' = \tan \theta$  (see also Fig. 9). Then, one obtains the following substitutions:

$$1+(x')^2 = \frac{\partial}{\partial \theta} x' ; \quad \frac{\partial}{\partial x'} \gamma(x') = \frac{\partial}{\partial \theta} \gamma(\theta) \frac{1}{1+(x')^2} ; \quad \frac{\partial}{\partial y} = \frac{\partial^2 x}{\partial y^2} \frac{\partial}{\partial x'}. \quad (\text{B.7})$$

Using (B.7), (B.6) becomes

$$\mu = -\Omega \frac{\partial^2 x / \partial y^2}{\left[ 1 + (\partial x / \partial y)^2 \right]^{3/2}} \left( \gamma + \frac{\partial^2 \gamma}{\partial \theta^2} \right), \quad (\text{B.8})$$

which is the same as (3.6) with  $K = -\partial^2 x / \partial y^2 \left[ 1 + (\partial x / \partial y)^2 \right]^{-3/2}$ .

## Appendix C

### *Formulation of time correlation function in experimentally relevant quantities for mass transport cases (iii), (iv) and (vi)*

#### *C.1. Case (iii): Exchange of atoms with terrace, fast terrace diffusion*

Neglecting the noise term, the Langevin equation is [72]

$$\frac{\partial x}{\partial t} = \frac{a_{\perp}^2 a_{\parallel} v_a \tilde{\gamma}}{k_B T} \frac{\partial^2 x}{\partial y^2} . \quad (\text{C.1})$$

Here,  $v_a$  is the detachment/attachment rate of adatoms between the step and the terrace<sup>95</sup>.

With (3.19)-(3.20), one then obtains for the time correlation function  $G(t)$

$$\frac{G(t)}{a_{\perp}^2} = P_k \sqrt{\frac{2}{\pi}} v_a^{1/2} t^{1/2} . \quad (\text{C.2})$$

#### *C.2. Case (iv): Exchange of atoms with terrace, slow terrace diffusion*

The Langevin equation for this case is given by [99]

$$\frac{\partial x}{\partial t} = - \frac{4D_t c_t \tilde{\gamma} \Omega^2}{k_B T} \int_{-\infty}^{\infty} \frac{\partial^2 x}{\partial y'^2} \Big|_{y'} \times \frac{b^2 - (y - y')^2}{(b^2 - (y - y')^2)^2} dy' , \quad (\text{C.3})$$

from which follows

$$G(t) = \frac{4}{\sqrt{3}\Gamma\left(\frac{1}{3}\right)} \left(\frac{k_B T}{\tilde{\gamma}}\right)^{2/3} (2D_t c_t \Omega^2)^{1/3} t^{1/3} . \quad (\text{C.4})$$

Using (3.19) and (3.20) and  $\Omega = a_{\perp} a_{\parallel}$ , one obtains

$$\frac{G(t)}{a_{\perp}^2} \approx 1.086 P_k^{2/3} (D_t c_t)^{1/3} t^{1/3} . \quad (\text{C.5})$$

<sup>95</sup> Note that  $v_a$  is related to the hopping coefficient  $\Gamma_a$  in (3.26) via  $\Gamma_a = v_a P_k$ .

### C.3 Case(vi): Atom hopping alongside steps

The Langevin equation for dominant edge diffusion is given by [50, 72]

$$\frac{\partial x}{\partial t} = -\frac{2^{3/4}}{\Gamma\left(\frac{1}{4}\right)} \Omega^2 a_{\parallel} \frac{\tilde{\gamma}}{k_B T} c_{st} D_{st} \frac{\partial^4 x}{\partial y^4}, \quad (\text{C.6})$$

which can be rewritten with (3.19) and (3.20) as

$$\frac{\partial x}{\partial t} = -\frac{2^{3/4}}{\Gamma\left(\frac{1}{4}\right)} \frac{a_{\parallel}^4}{P_k} c_{st} D_{st} \frac{\partial^4 x}{\partial y^4}. \quad (\text{C.7})$$

For  $G(t)$  then follows:

$$\frac{G(t)}{a_{\perp}^2} \approx 0.464 P_k^{3/4} (c_{st} D_{st})^{1/4} t^{1/4}. \quad (\text{C.8})$$

In (C.2), (C.5) and (C.8), the kink concentration  $P_k$ , the adatom concentration at steps  $c_{st}$  and on the surface  $c_s$  are dimensionless and are given by  $P_k = 2e^{-\epsilon/k_B T}$ ,  $c_{st} = e^{-E_{st}^{ad}/k_B T}$  ( $E_{st}^{ad}$  the adatom creation energy at steps) and  $c_t = e^{-E_{ad}/k_B T}$  ( $E_{ad}$  being the creation energy for adatoms on the surface). The detachment/attachment rate  $v_a = v_0 e^{-E_{ad}^{\neq}/k_B T}$  ( $E_{ad}^{\neq}$  being the activation energy for adatom creation from kink sites onto the terrace) is given in units  $s^{-1}$ . The tracer diffusion constants along steps ( $D_{st} = D_0 e^{-E_d^k/k_B T}$ ;  $E_d^k$  being the diffusion barrier along a kinked step) and on the terrace ( $D_t = D_0 e^{-E_{diff}/k_B T}$ ;  $E_{diff}$  being the diffusion barrier on the terrace) have also units  $s^{-1}$ . No further length units are introduced, if the time correlation function  $G(t)$  is plotted in units of  $a_{\perp}^2$ . For the other cases, the same procedure applies as long as the step-step distance  $L$  is given in atomic units  $a_{\perp}$ .

**References:**

- [1] H. Ibach, *Electron Energy Loss Spectroscopy - The Technology of High Performance*, Springer-Verlag, Heidelberg 1991.
- [2] H. Ibach, *Surf. Sci.* 299/300 (1994) 116.
- [3] R. G. Greenler, *J. Chem. Phys.* 44 (1966) 310.
- [4] A. M. Bradshaw, J. Pritchard, *Surf. Sci.* 17 (1969) 372.
- [5] P. Dumas, M. K. Weldon, Y. J. Chabal, G. P. Williams, *Surf. Rev. Lett.* 6 (1999) 225 (and references therein).
- [6] E. Bauer, *Rep. Prog. Phys.* 57 (1994) 895.
- [7] E. Bauer, *Surf. Sci.* 299/300 (1994) 102 (and references therein).
- [8] G. Binnig, H. Rohrer, C. Gerber, *Appl. Phys. Lett.* 40 (1982) 178.
- [9] G. Binnig, C. F. Quate, C. Gerber, *Phys. Rev. Lett.* 56 (1986) 930.
- [10] P. W. Atkins, *Physical Chemistry*, Oxford University Press, Oxford Melbourne Tokyo 1998.
- [11] T. Twomey, Y. Uchida, G. Lehmpfuhl, D. M. Kolb, *Z. Phys. Chem.* 160 (1988) 1.
- [12] J. Canullo, Y. Uchida, G. Lehmpfuhl, T. Twomey, D. M. Kolb, *Surf. Sci.* 188 (1987) 350.
- [13] A. T. Bell, M. L. Haller, *ACS Symposium Series, Vol. 137*, American Chemical Society, Washington, D.C. 1980.
- [14] C. L. Angell, in J. R. Ferraro, L. H. Basile (Eds.): *Fourier Transform Infrared Spectroscopy-Techniques Using Fourier Transform Interferometry, Vol. 3*, Academic, New York 1982.
- [15] G. L. Richmond, in H. D. Abruna (Ed.): *Electrochemical Interfaces*, VCH, New York 1991.
- [16] H. Winick, S. Doniach, *Synchrotron Radiation Research*, Plenum, New York 1980.
- [17] R. Sonnenfeld, P. K. Hansma, *Science* 232 (1986) 211.
- [18] H. Liu, F. F. Fan, C. W. Lin, A. J. Bard, *J. Am. Chem. Soc.* 108 (1986) 3838.
- [19] H.-C. Jeong, E. D. Williams, *Surf. Sci. Rep.* 34 (1999) 171.
- [20] E. W. Müller, *Z. Phys.* 131 (1951) 136.
- [21] L. Kuipers, R. W. M. Loos, H. Neerings, J. t. Horst, G. J. Ruwiel, A. P. d. Jongh, J. W. M. Frenken, *Rev. Sci. Instrum.* 66 (1995) 4557.
- [22] J. Lapujoulade, *Surf. Sci. Rep.* 20 (1994) 191.
- [23] A. Bartolini, F. Ercolessi, E. Tosatti, *Phys. Rev. Lett.* 63 (1989) 872.

- [24] T. Klas, R. Fink, G. Krausch, R. Platzter, J. Voigt, R. Wesche, G. Schatz, *Europhys. Lett.* 7 (1988) 151.
- [25] M. Giesen, U. Linke, H. Ibach, *Surf. Sci.* 389 (1997) 264.
- [26] M. Giesen, unpublished (1997) .
- [27] I. Bönicke, W. Kirstein, S. Spinzig, F. Thieme, *Surf. Sci.* 313 (1994) 231.
- [28] M. Giesen, G. S. Icking-Konert, *Surf. Rev. Lett.* 6 (1999) 27.
- [29] C. Benndorf, L. Meyer, *J. Vac. Sci. Technol. A8* (1990) 2677.
- [30] E. Hahn, H. Schief, V. Marsico, A. Fricke, K. Kern, *Phys. Rev. Lett.* 72 (1994) 3378.
- [31] M. Yoon, S. G. J. Mochrie, D. M. Zehner, G. M. Watson, D. Gibbs, *Surf. Sci.* 338 (1995) 225.
- [32] Q. Shen, J. P. Chang, G. Navrotsky, J. M. Blakely, *Phys. Rev. Lett.* 64 (1990) 451.
- [33] H. M. v. Pinxteren, B. Pluis, J. W. M. Frenken, *Phys. Rev.* B49 (1994) 13798.
- [34] H. P. Bonzel, U. Breuer, B. Voigtländer, *Surf. Sci.* 272 (1992) 10.
- [35] Y. Kuk, F. M. Chua, P. J. Silverman, J. A. Meyer, *Phys. Rev.* B41 (1990) 12393.
- [36] J. Wintterlin, R. Schuster, D. J. Coulman, G. Ertl, R. J. Behm, *J. Vac. Sci. Technol. B9* (1990) 902.
- [37] J. F. Wolf, B. Vicenzi, H. Ibach, *Surf. Sci.* 249 (1991) 233.
- [38] M. Poensgen, J. F. Wolf, J. Frohn, M. Giesen, H. Ibach, *Surf. Sci.* 274 (1992) 430.
- [39] M. Giesen, J. Frohn, M. Poensgen, J. F. Wolf, H. Ibach, *J. Vac. Sci. Technol. A10* (1992) 2597.
- [40] M. Giesen-Seibert, F. Schmitz, R. Jentjens, H. Ibach, *Surf. Sci.* 329 (1995) 47.
- [41] M. Giesen-Seibert, H. Ibach, *Surf. Sci.* 316 (1994) 205.
- [42] M. Giesen, in preparation (2000) .
- [43] W. Feller, *An Introduction to Probability Theory and its Application*, Wiley, New York 1950.
- [44] J. C. Girard, S. Gauthier, S. Rousset, W. Sacks, S. d. Cheveigné, J. Klein, *Surf. Sci.* 301 (1994) 245.
- [45] L. Masson, L. Barbier, J. Cousty, *Surf. Sci.* 317 (1994) L1115.
- [46] L. Masson, L. Barbier, J. Cousty, B. Salanon, *Surf. Sci.* 324 (1994) L378.
- [47] K. Morgenstern, G. Rosenfeld, B. Poelsema, G. Comsa, *Phys. Rev. Lett.* 74 (1995) 2058.
- [48] M. Dietterle, T. Will, D. M. Kolb, *Surf. Sci.* 327 (1995) L495.
- [49] J. W. M. Frenken, R. J. Hamers, J. E. Demuth, *J. Vac. Sci. Technol. A8* (1989) 293.
- [50] M. Giesen, G. S. Icking-Konert, *Surf. Sci.* 412/413 (1998) 645.

- [51] L. Kuipers, M. S. Hoogeman, J. W. M. Frenken, *Phys. Rev. Lett.* 71 (1993) 3517.
- [52] L. Kuipers, M. S. Hoogeman, J. W. M. Frenken, H. v. Beijeren, *Phys. Rev. B* 52 (1995) 11387.
- [53] S. Speller, W. Heiland, A. Biedermann, E. Platzgummer, C. Nagl, M. Schmid, P. Varga, *Surf. Sci.* 331-333 (1995) 1056.
- [54] J. Li, R. Berndt, W.-D. Schneider, *Phys. Rev. Lett.* 76 (1996) 1888.
- [55] T.P.Moffat, in P. C. Andricacos, S. G. Corcoran, J.-L. Delplancke, T. P. Moffat, P. C. Searson (Eds.): *Electrochemical Synthesis and Modification of Materials, Vol. 451*, Pittsburgh 1997, p. 75.
- [56] P. Broekmann, M. Wilms, M. Kruft, C. Stuhlmann, K. Wandelt, *J. Electroanal. Chem.* 467 (1999) 307.
- [57] M. Kruft, B. Wohlmann, C. Stuhlmann, K. Wandelt, *Surf. Sci.* 377-379 (1997) 601.
- [58] M. Wilms, P. Broekmann, M. Kruft, C. Stuhlmann, K. Wandelt, *Appl. Phys. A* 66 (1998) 473.
- [59] M. Giesen, R. Randler, S. Baier, H. Ibach, D. M. Kolb, *Electrochim. Acta* 45 (1999) 533.
- [60] M. Giesen, M. Dietterle, D. Stapel, H. Ibach, D. M. Kolb, *Surf. Sci.* 384 (1997) 168.
- [61] M. Giesen, M. Dietterle, D. Stapel, H. Ibach, D. M. Kolb, *Proc. Mat. Res. Soc.* 451 (1997) 9.
- [62] M. Giesen, D. M. Kolb, *Surf. Sci.* submitted (2000) .
- [63] E. Ising, *Z. Phys.* 31 (1925) 253.
- [64] W. W. Mullins, *J. Appl. Phys.* 30 (1959) 77.
- [65] W. W. Mullins, in N. A. Gjostein, R. W. Roberts (Eds.): *Metal Surfaces: Structure, Energetics and Kinetics*, American Society of Metals, Metals Park, Ohio 1963, p. 17.
- [66] W. W. Mullins, *J. Appl. Phys.* 28 (1957) 333.
- [67] N. C. Bartelt, T. L. Einstein, E. D. Williams, *Surf. Sci.* 240 (1990) L591.
- [68] M. E. Fisher, *J. Stat. Phys.* 34 (1984) 667.
- [69] M. E. Fisher, D. S. Fisher, *Phys. Rev. B* 25 (1982) 3192.
- [70] G. Forgacs, R. Lipowsky, T. M. Nieuwenhuizen, in C. Domb, J. L. Lebowitz (Eds.): *Phase Transitions and Critical Phenomena C, Vol. 15*, Academic Press 1992.
- [71] M. Kardar, *Turk. J. Phys.* 18 (1994) 221.
- [72] N. C. Bartelt, J. L. Goldberg, T. L. Einstein, E. D. Williams, *Surf. Sci.* 273 (1992) 252.
- [73] B. Blagojevic, P. M. Duxbury, in P. M. Duxbury, T. J. Pence (Eds.): *Dynamics of Crystal Surfaces and Interfaces*, Plenum Press, New York 1997, p. 1.

- [74] G. Ehrlich, F. G. Hudda, *J. Chem. Phys.* 44 (1966) 1039.
- [75] R. L. Schwoebel, E. J. Shipsey, *J. Appl. Phys.* 37 (1966) 3682.
- [76] S. V. Khare, T. L. Einstein, *Phys. Rev. B* 57 (1998) 4782.
- [77] M. Giesen-Seibert, R. Jentjens, M. Poensgen, H. Ibach, *Phys. Rev. Lett.* 71 (1993) 3521.
- [78] M. Giesen, G. S. Icking-Konert, D. Stapel, H. Ibach, *Surf. Sci.* 366 (1996) 229.
- [79] L. Barbier, L. Masson, J. Cousty, B. Salanon, *Surf. Sci.* 345 (1996) 197.
- [80] M. Giesen-Seibert, R. Jentjens, M. Poensgen, H. Ibach, *Phys. Rev. Lett.* 73 (1994) 911.
- [81] P. Stoltze, *J. Phys. Condens. Matter* 6 (1994) 9495.
- [82] R. C. Nelson, T. L. Einstein, S. V. Khare, P. J. Rous, *Surf. Sci.* 295 (1993) 462.
- [83] Z.-J. Tian, T. S. Rahman, *Phys. Rev. B* 47 (1993) 9751.
- [84] M. S. Hoogeman, D. C. Schlösser, J. B. Sanders, L. Kuipers, J. W. M. Frenken, *Phys. Rev. B* 53 (1996) R13299.
- [85] M. F. Chang, M. S. Hoogeman, M. A. J. Klik, J. W. M. Frenken, *Surf. Sci.* 432 (1999) 21.
- [86] S. V. Khare, T. L. Einstein, *Surf. Sci.* 314 (1994) L857.
- [87] C.-L. Liu, J. B. Adams, *Surf. Sci.* 294 (1993) 211.
- [88] M. Giesen, H. Ibach, G. S. Icking-Konert, C. Steimer, in preparation (2000) .
- [89] L. Vitos, H. L. Skriver, J. Kollár, *Surf. Sci.* 425 (1999) 212.
- [90] G. S. Icking-Konert, M. Giesen, H. Ibach, *Phys. Rev. Lett.* 83 (1999) 3880.
- [91] P. J. Feibelman, *Phys. Rev. B* 60 (1999) 11118.
- [92] M. S. Hoogeman, D. C. Schlößer, J. B. Sanders, L. Kuipers, J. W. M. Frenken, *Phys. Rev. B* 53 (1996) R13299.
- [93] J. S. Ozcomert, W. W. Pai, N. C. Bartelt, J. E. Reutt-Robey, *Surf. Sci.* 293 (1993) 183.
- [94] W. W. Pai, N. C. Bartelt, J. E. Reutt-Robey, *Phys. Rev. B* 53 (1996) 15991.
- [95] C. L. Liu, J. M. Cohen, J. B. Adams, A. F. Voter, *Surf. Sci.* 253 (1991) 334.
- [96] R. K. P. Zia, J. E. Avron, *Phys. Rev. B* 25 (1982) 2042.
- [97] R. K. P. Zia, *J. Stat. Phys.* 45 (1986) 801.
- [98] A. Pimpinelli, J. Villain, D. E. Wolf, J. J. Métois, J. C. Heyraud, I. Elkinani, G. Uimin, *Surf. Sci.* 295 (1993) 143.
- [99] N. C. Bartelt, T. L. Einstein, E. D. Williams, *Surf. Sci.* 312 (1994) 411.
- [100] T. Ihle, C. Misbah, O. Pierre-Louis, *Phys. Rev. B* 58 (1998) 2289.
- [101] F. Mugele, A. Rettenberger, J. Boneberg, P. Leiderer, *Surf. Sci.* 377-379 (1997) 62.

- [102] T. L. Einstein, S. V. Khare, in P. M. Duxbury, T. J. Pence (Eds.): *Dynamics of Crystal Surfaces and Interfaces*, Plenum Press, New York 1997, p. 83.
- [103] M. I. Larsson, M. Tringides, H. Frischat, J. Wollschläger, Surf. Sci. 387 (1997) 142.
- [104] M. Bisani, W. Selke, Surf. Sci. 437 (1999) 137.
- [105] E. LeGoff, L. Barbier, L. Masson, B. Salanon, Surf. Sci. 432 (1999) 139.
- [106] J. B. Hannon, C. Klünker, M. Giesen, H. Ibach, N. C. Bartelt, J. C. Hamilton, Phys. Rev. Lett. 79 (1997) 2506.
- [107] M. Kalff, G. Comsa, T. Michely, Phys. Rev. Lett. 81 (1998) 1255 and ref. [36] of Kyuno and Ehrlich Phys. Rev. Lett. 81 (1998) 5592.
- [108] K. Kyuno, G. Ehrlich, Phys. Rev. Lett. 81 (1998) 5592.
- [109] P. J. Feibelman, Phys. Rev. Lett. 81 (1998) 168.
- [110] M. Bott, T. Michely, G. Comsa, Surf. Sci. 272 (1992) 161.
- [111] M. Giesen, Surf. Sci. 442/443 (1999) 543.
- [112] S. Baier, M. Giesen, in preparation (2000) .
- [113] J. Merikoski, I. Vattulainen, J. Heinonen, T. Ala-Nissila, Surf. Sci. 387 (1997) 167.
- [114] C.-L. Liu, Surf. Sci. 316 (1994) 294.
- [115] M. Breeman, G. T. Barkema, D. O. Boerma, Surf. Sci. 303 (1994) 25.
- [116] M. Karimi, T. Tomkowski, G. Vidali, O. Biham, Phys. Rev. B52 (1995) 5364.
- [117] G. Boisvert, L. J. Lewis, Phys. Rev. B56 (1997) 7643.
- [118] H. Mehl, O. Biham, I. Furman, M. Karimi, Phys. Rev. B60 (1999) 2106.
- [119] J. Merikoski, T. Ala-Nissila, Phys. Rev. B52 (1995) R8715.
- [120] B. D. Yu, M. Scheffler, Phys. Rev. Lett. 77 (1996) 1095.
- [121] B. D. Yu, M. Scheffler, Phys. Rev. B55 (1997) 13916.
- [122] H. Brune, H. Röder, K. Bromann, K. Kern, J. Jacobsen, P. Stoltze, K. Jacobsen, J. Norskov, Surf. Sci. 349 (1996) L115.
- [123] S. Liu, Z. Zhang, G. Comsa, H. Metiu, Phys. Rev. Lett. 71 (1993) 2967.
- [124] M. C. Bartelt, J. W. Evans, Surf. Sci. 314 (1994) L829.
- [125] M. Villarba, H. Jónsson, Surf. Sci. 317 (1994) 15.
- [126] P. J. Feibelman, Phys. Rev. B 60 (1999) 4972.
- [127] D. W. Basset, P. R. Weber, Surf. Sci. 70 (1978) 520.
- [128] A. Natori, R. W. Godby, Phys. Rev. B47 (1993) 15816.
- [129] C. Kittel, *Einführung in die Festkörperphysik*, R. Oldenbourg Verlag, München Wien 1988.
- [130] D. M. Eigler, E. K. Schweizer, Nature 344 (1990) 524.

- [131] D. M. Eigler, C. P. Lutz, W. E. Rudge, *Nature* 352 (1991) 600.
- [132] B. Neu, G. Meyer, K.-H. Rieder, *Mod. Phys. Lett. B* 9 (1995) 963.
- [133] G. Meyer, S. Zöphel, K.-H. Rieder, *Phys. Rev. Lett.* 77 (1996) 2113.
- [134] L. Bartels, G. Meyer, K.-H. Rieder, *Phys. Rev. Lett.* 79 (1997) 697.
- [135] P. Avouris, *Acc. Chem. Res.* 18 (1995) 95.
- [136] F. Thibaudau, J. Cousty, *Ultramicroscopy* 42-44 (1992) 511.
- [137] F. Mugele, A. Rettenberger, J. Boneberg, P. Leiderer, *Surf. Sci.* 400 (1998) 80.
- [138] R. Koch, J. J. Schulz, K.-H. Rieder, *Europhys. Lett.* 48 (1999) 554.
- [139] N. C. Bartelt, J. L. Goldberg, T. L. Einstein, E. D. Williams, J. C. Heyraud, J. J. Métois, *Phys. Rev. B* 48 (1993) 15453.
- [140] P. Nozières, in C. Godrèche (Ed.): *Solids far from equilibrium*, Cambridge University Press, Cambridge 1991, p. 1.
- [141] T. Yamamoto, Y. Akutsu, N. Akutsu, *J. Phys. Soc. Jpn.* 63 (1994) 915.
- [142] Y. Akutsu, N. Akutsu, T. Yamamoto, *J. Phys. Soc. Jpn.* 63 (1994) 2032.
- [143] K. Sudoh, T. Yoshinobu, H. Iwasaki, N. Akutsu, Y. Akutsu, T. Yamamoto, *J. Phys. Soc. Jpn.* 65 (1996) 988.
- [144] H.-C. Jeong, J. D. Weeks, *Surf. Sci.* 432 (1999) 101.
- [145] C. Herring, in W. E. Kingston (Ed.): *The Physics of Powder Metallurgy*, McGraw-Hill, New York 1951, p. 143.
- [146] M. Wortis, in R. Vanselow, R. Howe (Eds.): *Chemistry and Physics of Solid Surfaces, Vol. 7*, Springer, New York 1988, p. 367.
- [147] S. T. Chui, J. D. Weeks, *Phys. Rev. B* 14 (1976) 4976.
- [148] H. v. Beijeren, I. Nolden, in W. Schommers, P. v. Blanckenhagen (Eds.): *Structure and Dynamics of Surfaces II*.
- [149] E. H. Conrad, *Prog. Surf. Sci.* 39 (1992) 65.
- [150] V. I. Marchenko, A. Y. Parshin, *Sov. Phys. JETP* 52 (1981) 129.
- [151] A. C. Redfield, A. Zangwill, *Phys. Rev. B* 46 (1992) 4289.
- [152] W. W. Pai, J. S. Ozcomert, N. C. Bartelt, T. L. Einstein, *Surf. Sci.* 307-309 (1994) 747.
- [153] J. Villain, D. R. Grempel, J. Lapujoulade, *Journal Physics F* 15 (1985) 809.
- [154] X.-S. Wang, J. L. Goldberg, N. C. Bartelt, T. L. Einstein, E. D. Williams, *Phys. Rev. Lett.* 65 (1990) 2430.
- [155] E. E. Gruber, W. W. Mullins, *J. Phys. Chem. Solids* 28 (1967) 875.
- [156] O. Pierre-Louis, C. Misbah, *Phys. Rev. B* 58 (1998) 2259.

- [157] B. Joós, T. L. Einstein, N. C. Bartelt, *Phys. Rev. B* 43 (1991) 8153.
- [158] M. L. Mehta, *Random Matrices*, Academic, New York 1991.
- [159] T. Guhr, A. Müller-Groeling, H. A. Weidenmüller, *Phys. Rep.* 299 (1998) 189.
- [160] T. L. Einstein, O. Pierre-Louis, *Surf. Sci.* 424 (1999) L299.
- [161] M. Giesen, T. L. Einstein, *Surf. Sci.* 449 (2000) 191.
- [162] B. Sutherland, *J. Math. Phys.* 12 (1971) 246.
- [163] B. Sutherland, *J. Math. Phys.* 12 (1971) 251.
- [164] B. Sutherland, *Phys. Rev. A* 4 (1971) 2019.
- [165] M. Giesen, *Surf. Sci.* 370 (1997) 55.
- [166] H. L. Richards, S. D. Cohen, T. L. Einstein, M. Giesen, *Surf. Sci.* in press (2000) .
- [167] S. Rousset, S. Gauthier, O. Siboulet, J. C. Girard, S. d. Cheveigné, M. Huerta-Garnica, W. Sacks, M. Belin, J. Klein, *Ultramicroscopy* 42-44 (1992) 515.
- [168] F. Fabre, D. Gorse, J. Lapujoulade, B. Salanon, *Europhys. Lett.* 3 (1987) 737.
- [169] J. Frohn, M. Giesen, M. Poensgen, J. F. Wolf, H. Ibach, *Phys. Rev. Lett.* 67 (1991) 3543.
- [170] J. W. M. Frenken, P. Stoltze, *Phys. Rev. Lett.* 82 (1999) 3500.
- [171] M. S. Hoogeman, M. A. J. Klik, D. C. Schlößer, L. Kuipers, J. W. M. Frenken, *Phys. Rev. Lett.* 82 (1999) 1728.
- [172] K. Arenhold, S. Surnev, H. P. Bonzel, P. Wynblatt, *Surf. Sci.* 424 (1999) 271.
- [173] K. Arenhold, S. Surnev, H. P. Bonzel, P. Wynblatt, *Surf. Sci.* 441 (1999) 223.
- [174] K. Swamy, E. Bertel, I. Vilfan, *Surf. Sci.* 425 (1999) L369.
- [175] K. Arenhold, S. Surnev, P. Coenen, H. P. Bonzel, P. Wynblatt, *Surf. Sci.* 417 (1998) L1160.
- [176] K. S. Liang, E. B. Sirota, K. L. D'Amico, G. J. Hughes, S. K. Sinha, *Phys. Rev. Lett.* 59 (1987) 2447.
- [177] B. Salanon, F. Fabre, J. Lapujoulade, W. Selke, *Phys. Rev. B* 38 (1988) 7385.
- [178] F. Fabre, D. Gorse, B. Salanon, J. Lapujoulade, *J. Phys. (Paris)* 48 (1987) 1017.
- [179] H. Ibach, *Surf. Sci. Rep.* 29 (1997) 193.
- [180] H. Ibach, *Surf. Sci. Rep.* 35 (1999) 71.
- [181] J. L. Stickney, I. Villegas, C. B. Ehlers, *J. Am. Chem. Soc.* 111 (1989) 6473.
- [182] G. J. Cali, G. M. Berry, M. E. Bothwell, M. P. Soriaga, *J. Electroanal. Chem.* 297 (1991) 523.
- [183] L. B. Goetting, B. M. Huang, T. E. Lister, J. L. Stickney, *Electrochim. Acta* 40 (1995) 143.

- [184] A. S. Dakkouri, *Solid State Ionics* 94 (1997) 99.
- [185] S. Baier, M. Giesen, in preparation (2000) .
- [186] R. McHardy, W. H. Haiss, R. J. Nichols, *Phys. Chem. Chem. Phys.* 2 (2000) 1439.
- [187] M. I. Haftel, T. L. Einstein, *Proc. Mat. Res. Soc.* preprint (1999) .
- [188] M. I. Haftel, *Phys. Rev. B* 48 (1993) 2611.
- [189] M. I. Haftel, M. Rosen, S. G. Corcoran, *Proc. Mat. Res. Soc.* 451 (1997) 31.
- [190] G. L. Kellogg, *Surf. Sci. Rep.* 21 (1994) 1.
- [191] H. Ibach, W. Erley, H. Wagner, *Surf. Sci.* 92 (1980) 29.
- [192] M. Wilms, P. Broekmann, C. Stuhlmann, K. Wandelt, *Surf. Sci.* 416 (1998) 121.
- [193] M. R. Vogt, A. Lachenwitzer, O. M. Magnussen, R. J. Behm, *Surf. Sci.* 399 (1998) 49.
- [194] T. P. Moffat, in P. C. Andricacos, S. G. Corcoran, J.-L. Delplancke, T. P. Moffat, P. C. Searson (Eds.): *Electrochemical Synthesis and Modification of Materials, Vol. 451*, Materials Research Society, Pittsburgh 1997, p. 75.
- [195] C. Stuhlmann, B. Wohlmann, M. Kruff, K. Wandelt, in A. Wieckowski, K. Itaya (Eds.): *Electrode Processes*, The Electrochemical Society, Pennington, NJ 1996, p. 203.
- [196] B. Wohlmann, Z. Park, M. Kruff, C. Stuhlmann, K. Wandelt, *Colloids Surf.* A134 (1998) 15.
- [197] C. B. Ehlers, I. Villegas, J. L. Stickney, *J. Electroanal. Chem.* 284 (1990) 403.
- [198] I. Villegas, C. B. Ehlers, J. L. Stickney, *J. Electrochem. Soc.* 137 (1990) 3143.
- [199] D. W. Suggs, A. J. Bard, *J. Phys. Chem.* 99 (1995) 8349.
- [200] G. S. Icking-Konert, M. Giesen, H. Ibach, *Surf. Sci.* 398 (1998) 37.
- [201] G. S. Icking-Konert, PhD Thesis, RWTH Aachen, unpublished (1998) .
- [202] O. M. Magnussen, J. Hageböck, J. Hotlos, R. J. Behm, *Faraday Discuss. Chem. Soc.* 94 (1992) 329.
- [203] B. M. Ocko, O. M. Magnussen, J. X. Wang, R. R. Adzic, T. Wandlowski, *Physica B* 221 (1996) 238.
- [204] D. M. Kolb, *Prog. Surf. Sci.* 51 (1996) 109.
- [205] V. Repain, J. M. Berrior, S. Rousset, J. Lecoeur, *Europhys. Lett.* 47 (1999) 435.
- [206] A. K. Schmid, N. C. Bartelt, J. C. Hamilton, C. B. Carter, R. Q. Hwang, *Phys. Rev. Lett.* 78 (1997) 3507.
- [207] N. C. Bartelt, private communication (1999) .
- [208] J. A. Meyer, P. Schmid, R. J. Behm, *Phys. Rev. Lett.* 74 (1995) 3864.
- [209] C. Ratsch, A. P. Seitsonen, M. Scheffler, *Phys. Rev. B* 55 (1997) 6750.

- [210] Z. Shi, S. Wu, J. Lipkowski, *Electrochim. Acta* 40 (1995) 9.
- [211] D. J. Trevor, C. E. D. Chidsey, *J. Vac. Sci. Technol. B9* (1990) 964.
- [212] J. A. Venables, *Phil. Mag.* 27 (1973) 697.
- [213] H. Brune, *Surf. Sci. Rep.* 31 (1998) 121.
- [214] M. Hohage, M. Bott, M. Morgenstern, Z. Zhang, T. Michely, G. Comsa, *Phys. Rev. Lett.* 76 (1996) 2366.
- [215] J. Vrijmoeth, H. A. v. d. Vegt, J. A. Mayer, E. Vlieg, R. J. Behm, *Phys. Rev. Lett.* 72 (1994) 3843.
- [216] J. P. Bucher, E. Hahn, P. Fernandez, C. Massobrio, K. Kern, *Europhys. Lett.* 27 (1994) 473.
- [217] M. C. Bartelt, J. W. Evans, *Phys. Rev. B* 54 (1996) R17359.
- [218] C.-M. Zhang, M. C. Bartelt, J.-M. Wen, C. J. Jenks, J. W. Evans, P. A. Thiel, *Surf. Sci.* 406 (1998) 178.
- [219] P. Jensen, *Rev. Mod. Phys.* 71 (1999) 1695.
- [220] C. Wagner, *Z. Elektrochem.* 65 (1961) 581.
- [221] P. Wynblatt, N. A. Gjostein, in J. O. McCaldin, G. Somorjai (Eds.): *Progress in Solid State Chemistry, Vol. 9*, Pergamon Press, Oxford 1975, p. 21.
- [222] M. Zinke-Allmang, L. C. Feldman, M. H. Grabow, *Surf. Sci. Rep.* 16 (1992) 377.
- [223] S. C. Wang, G. Ehrlich, *Phys. Rev. Lett.* 79 (1997) 4234.
- [224] S. C. Wang, U. Kürpick, G. Ehrlich, *Phys. Rev. Lett.* 81 (1998) 4923.
- [225] J. C. Hamilton, M. S. Daw, S. M. Foiles, *Phys. Rev. Lett.* 74 (1995) 2760.
- [226] G. Wulff, *Z. Kristallgr. Mineral.* 34 (1901) 449.
- [227] A. F. Andreev, *Sov. Phys. JETP* 53 (1981) 1063.
- [228] W. K. Burton, N. Cabrera, F. C. Frank, *Phil. Trans. Roy. Soc. Lond.* A243 (1951) 299.
- [229] C. Rottman, M. Wortis, *Phys. Rev. B* 24 (1981) 6274.
- [230] C. Jayaprakash, C. Rottman, W. F. Saam, *Phys. Rev. B* 30 (1984) 6549.
- [231] C. Jayaprakash, W. F. Saam, *Phys. Rev. B* 30 (1984) 3916.
- [232] C. Rottman, M. Wortis, *Phys. Rev. B* 29 (1984) 328.
- [233] C. Rottman, M. Wortis, *Phys. Rep.* 103 (1984) 59.
- [234] J. C. Heyraud, J. J. Métois, *Acta. Met.* 28 (1980) 1789.
- [235] J. C. Heyraud, J. J. Métois, *Surf. Sci.* 128 (1983) 334.
- [236] J. C. Heyraud, J. J. Métois, *Surf. Sci.* 177 (1986) 213.
- [237] J. M. Bermond, J. J. Métois, X. Egéa, F. Floret, *Surf. Sci.* 330 (1995) 48.
- [238] J. M. Bermond, J. J. Métois, J. C. Heyraud, F. Floret, *Surf. Sci.* 416 (1998) 430.

- [239] S. Surnev, K. Arenhold, P. Coenen, B. Voigtländer, H. P. Bonzel, J. Vac. Sci. Technol. A 16 (1998) 1059.
- [240] D. C. Schlößer, L. K. Verheij, G. Rosenfeld, G. Comsa, Phys. Rev. Lett. 82 (1999) 3843.
- [241] M. Kalff, G. Comsa, T. Michely, Phys. Rev. Lett. 81 (1998) 1255.
- [242] T. Michely, Habilitations thesis University of Bonn (1996) .
- [243] T. Michely, G. Comsa, Surf. Sci. 256 (1991) 217.
- [244] G. Boisvert, L. J. Lewis, M. Scheffler, Phys. Rev. B 57 (1998) 1881.
- [245] P. J. Feibelman, Phys. Rev. B52 (1995) 16845.
- [246] K. Morgenstern, E. Laegsgaard, I. Stensgaard, F. Besenbacher, Phys. Rev. Lett. 83 (1999) 1613.
- [247] M. McLean, Acta Metall. 19 (1971) 387.
- [248] H. P. Bonzel, Surf. Sci. 328 (1995) L571.
- [249] K. Morgenstern, G. Rosenfeld, E. Laegsgaard, F. Besenbacher, G. Comsa, Phys. Rev. Lett. 80 (1998) 556.
- [250] W. R. Tyson, W. A. Miller, Surf. Sci. 62 (1977) 267.
- [251] A. R. Miedema, J. W. F. Dorleijn, Surf. Sci. 95 (1980) 447.
- [252] H. P. Bonzel, A. Emundts, preprint (1999) .
- [253] M. Breeman, G. T. Barkema, D. O. Boerma, Surf. Sci. 323 (1995) 71.
- [254] G. T. Barkema, M. E. J. Newman, M. Breeman, Phys. Rev. B50 (1994) 7946.
- [255] S. V. Khare, T. L. Einstein, Phys. Rev. B 54 (1996) 11752.
- [256] A. Masson, J. J. Métois, R. Kern, Surf. Sci. 27 (1971) 463.
- [257] J. d. I. Figuera, J. E. Prieto, C. Ocal, R. Miranda, Solid State Commun. 89 (1994) 815.
- [258] G. Rosenfeld, Habilitations thesis, University of Bonn, Germany , unpublished (1998) .
- [259] L. E. Reichl, *A Modern Course in Statistical Physics*, Edward Arnold, London, Melbourne, Auckland 1991.
- [260] K. Morgenstern, PhD theses, University Bonn, unpublished (1996) .
- [261] A. F. Voter, Phys. Rev. B34 (1986) 6819.
- [262] D. S. Sholl, R. Skodje, Phys. Rev. Lett. 75 (1995) 3158.
- [263] A. Bogicevic, S. Liu, J. Jacobsen, B. Lundqvist, H. Metiu, Phys. Rev. B 57 (1998) R9459.
- [264] J. Heinonen, I. Koponen, J. Merikoski, T. Ala-Nissila, Phys. Rev. Lett. 82 (1999) 2733.

- [265] T. Müller, W. Selke, Eur. Phys. J. B10 (1999) 549.
- [266] H. Metiu, G. Rosenfeld, Surf. Sci. 373 (1997) L357.
- [267] U. Kürpick, P. Kürpick, T. S. Rahman, Surf. Sci. 383 (1997) L713.
- [268] H. C. Kang, P. A. Thiel, J. W. Evans, J. Chem. Phys. 93 (1990) 9018.
- [269] J.-M. Wen, S.-L. Chang, J. W. Brunett, J. W. Evans, P. A. Thiel, Phys. Rev. Lett. 73 (1994) 2591.
- [270] J. M. Wen, J. W. Evans, M. C. Bartelt, J. W. Burnett, P. A. Thiel, Phys. Rev. Lett. 76 (1996) 652.
- [271] W. W. Pai, A. K. Swan, Z. Zhang, J. F. Wendelken, Phys. Rev. Lett. 79 (1997) 3210.
- [272] L. Bardotti, M. C. Bartelt, C. J. Jenks, C. R. Stoldt, J.-M. Wen, C.-M. Zhang, P. A. Thiel, J. W. Evans, Langmuir 14 (1998) 1487.
- [273] D. C. Schlößer, PhD thesis, University Bonn, unpublished (1997) .
- [274] G. Rosenfeld, K. Morgenstern, M. Esser, G. Comsa, Appl. Phys. A69 (1999) 489.
- [275] L. M. Lifshitz, V. V. Slyozov, J. Phys. Chem. Solids 19 (1961) 35.
- [276] B. K. Chakraverty, J. Phys. Chem. Solids 28 (1967) 2401.
- [277] R. C. Jaklevic, L. Ellie, Phys. Rev. Lett. 60 (1988) 120.
- [278] D. R. Peale, B. H. Cooper, J. Vac. Sci. Technol. A10 (1992) 2210.
- [279] K. Morgenstern, G. Rosenfeld, G. Comsa, Phys. Rev. Lett. 76 (1996) 2113.
- [280] K. Morgenstern, E. Laegsgaard, I. Stensgaard, F. Besenbacher, M. Böhringer, W.-D. Schneider, R. Berndt, F. Mauri, A. D. Vita, R. Car, Appl. Phys. A69 (1999) 559.
- [281] K. Morgenstern, G. Rosenfeld, G. Comsa, Surf. Sci. 441 (1999) 289.
- [282] G. Rosenfeld, K. Morgenstern, G. Comsa, in M. C. Tringides, M. Scheffler (Eds.): *Surface Diffusion: Atomistic and Collective Processes*, Plenum Press, New York 1997.
- [283] G. Rosenfeld, K. Morgenstern, I. Beckmann, W. Wulfhekel, E. Laegsgaard, F. Besenbacher, G. Comsa, Surf. Sci. 402-404 (1998) 401.
- [284] M. S. Hoogeman, M. A. J. Klik, R. v. Gastel, J. W. M. Frenken, J. Phys. Cond. Matt. 11 (1999) 4349.
- [285] W. Theis, N. C. Bartelt, R. M. Tromp, Phys. Rev. Lett. 75 (1995) 3328.
- [286] N. C. Bartelt, W. Theis, R. M. Tromp, Phys. Rev. B 54 (1996) 11741.
- [287] I. K. Crain, Comput. Geosci. 4 (1978) 131.
- [288] M. C. Bartelt, C. R. Stoldt, C. J. Jenks, P. A. Thiel, J. W. Evans, Phys. Rev. B59 (1999) 3125.
- [289] K.-J. Jin, G. D. Mahan, H. Metiu, Z. Zhang, Phys. Rev. Lett. 80 (1998) 1026.

- [290] C. Klünker, J. B. Hannon, M. Giesen, H. Ibach, G. Boisvert, L. J. Lewis, *Phys. Rev. B* 58 (1998) R7556.
- [291] U. Kürpick, T. S. Rahman, *Surf. Sci.* 383 (1997) 137.
- [292] U. Kürpick, A. Kara, T. S. Rahman, *Phys. Rev. Lett.* 78 (1997) 1086.
- [293] U. Kürpick, T. S. Rahman, *Phys. Rev. B* 59 (1999) 11014.
- [294] L. B. Hansen, P. Stoltze, K. W. Jacobsen, J. K. Norskov, *Surf. Sci.* 289 (1993) 68.
- [295] Y. Li, M. C. Bartelt, J. W. Evans, N. Waelchli, E. Kampshoff, K. Kern, *Phys. Rev. B* 56 (1997) 12539.
- [296] K. Morgenstern, E. Laegsgaard, I. Stensgaard, F. Besenbacher, *Phys. Rev. Lett.* 83 (1999) 1613.
- [297] J.-K. Zuo, J. F. Wendelken, H. Dürr, C.-L. Liu, *Phys. Rev. Lett.* 72 (1994) 3064.
- [298] H.-J. Ernst, F. Fabre, J. Lapujoulade, *Phys. Rev. B* 46 (1992) 1929.
- [299] G. T. Barkema, O. Biham, M. Breeman, D. O. Boerma, G. Vidali, *Surf. Sci.* 306 (1994) L569.
- [300] M. Eßer, K. Morgenstern, G. Rosenfeld, G. Comsa, *Surf. Sci.* 402-404 (1998) 341.
- [301] M. V. Smoluchowski, *Phys. Z. Sowjetunion* 17 (1916) 585.
- [302] M. Giesen, G. S. Icking-Konert, H. Ibach, *Phys. Rev. Lett.* 80 (1998) 552.
- [303] M. Giesen, G. S. Icking-Konert, H. Ibach, *Phys. Rev. Lett.* 82 (1999) 3101.
- [304] M. Giesen, G. S. Icking-Konert, H. Ibach, *Surf. Sci.* 431 (1999) 109.
- [305] P. Stoltze, J. K. Norskov, *Phys. Rev. B* 48 (1993) 5607.
- [306] Y. Li, A. E. DePristo, *Surf. Sci.* 319 (1994) 141.
- [307] J. Jacobsen, K. W. Jacobsen, P. Stoltze, J. K. Norskov, *Phys. Rev. Lett.* 74 (1995) 2295.
- [308] J. A. Meyer, J. Vrijmoeth, H. A. v. d. Vegt, E. Vlieg, R. J. Behm, *Phys. Rev. B* 51 (1995) 14790.
- [309] K. Bromann, *Phys. Rev. Lett.* 75 (1995) 677.
- [310] K. R. Roos, M. C. Tringides, *Surf. Rev. Lett.* 5 (1998) 833.
- [311] C. Klünker, PhD thesis, RWTH Aachen, published as report of the Research Center Jülich Jül-3529 (1998) .
- [312] H.-J. Ernst, F. Fabre, R. Folkerts, J. Lapujoulade, *Phys. Rev. Lett.* 72 (1994) 112.
- [313] J.-K. Zuo, J. F. Wendelken, *Phys. Rev. Lett.* 78 (1997) 2791.
- [314] W. Wulfhekel, N. N. Lipkin, J. Kliewer, G. Rosenfeld, L. C. Jorritsma, B. Poelsema, G. Comsa, *Surf. Sci.* 348 (1996) 227.
- [315] V. P. Zhdanov, *Surf. Sci.* 214 (1989) 289.

- [316] J. J. d. Miguel, A. Cebollada, J. M. Gallego, J. Ferrón, S. Ferrer, *J. Cryst. Growth* 88 (1988) 442.
- [317] J. J. d. Miguel, A. Sánchez, A. Cebollada, J. M. Gallego, J. Ferrón, S. Ferrer, *Surf. Sci.* 189/190 (1987) 1062.
- [318] M. Breeman, D. O. Boerma, *Surf. Sci.* 269/270 (1992) 224.
- [319] H. Dürr, J. F. Wendelken, J.-K. Zuo, *Surf. Sci.* 328 (1995) L527.
- [320] M. C. Bartelt, L. S. Perkins, J. W. Evans, *Surf. Sci.* 344 (1995) L1193.
- [321] M. C. Bartelt, J. W. Evans, *Surf. Sci.* 423 (1999) 189.
- [322] D. E. Sanders, A. E. DePristo, *Surf. Sci.* 260 (1992) 116.
- [323] G. A. Evangelakis, N. I. Papanicolaou, *Surf. Sci.* 347 (1996) 376.
- [324] C. Lee, G. T. Barkema, M. Breeman, A. Pasquarello, R. Car, *Surf. Sci.* 306 (1994) L575.
- [325] L. S. Perkins, A. E. DePristo, *Surf. Sci.* 325 (1995) 169.
- [326] H. Brune, H. Röder, C. Boragno, K. Kern, *Phys. Rev. Lett.* 73 (1994) 1955.
- [327] W. K. Rilling, C. M. Gilmore, T. D. Andreadis, J. A. Sprague, *Can. J. Phys.* 68 (1990) 1035.
- [328] D. E. Sanders, A. E. DePristo, *Surf. Sci.* 264 (1992) L169.
- [329] G. Boisvert, L. J. Lewis, M. J. Puska, R. M. Nieminen, *Phys. Rev.* B52 (1995) 9078.
- [330] C. Ratsch, M. Scheffler, *Phys. Rev. B* 58 (1998) 13163.
- [331] L. Bardotti, C. R. Stoldt, C. J. Jenks, M. C. Bartelt, J. W. Evans, P. A. Thiel, *Phys. Rev. B* 57 (1998) 12544.
- [332] C.-M. Zhang, M. C. Bartelt, J.-M. Wen, C. J. Jenks, J. W. Evans, P. A. Thiel, *J. Cryst. Growth* 174 (1997) 851.
- [333] M. H. Langelaar, M. Breeman, D. O. Boerma, *Surf. Sci.* 352-354 (1996) 597.
- [334] P. J. Feibelman, J. S. Nelson, G. L. Kellogg, *Phys. Rev.* B49 (1994) 10548.
- [335] M. Bott, M. Hohage, M. Morgenstern, T. Michely, G. Comsa, *Phys. Rev. Lett.* 76 (1996) 1304.
- [336] K. Kyuno, A. Götzhäuser, G. Ehrlich, *Surf. Sci.* 397 (1998) 191.
- [337] S. Liu, Z. Zhang, J. Norskov, H. Metiu, *Surf. Sci.* 321 (1994) 161.
- [338] R. Wang, K. A. Fichthorn, *Surf. Sci.* 301 (1994) 253.
- [339] M. Villarba, H. Jónsson, *Phys. Rev.* B49 (1994) 2208.
- [340] G. L. Kellogg, P. J. Feibelman, *Phys. Rev. Lett.* 64 (1990) 3143.
- [341] G. L. Kellogg, *Surf. Sci.* 246 (1991) 31.
- [342] J. M. Cohen, A. F. Voter, *Surf. Sci.* 313 (1994) 439.

- [343] K. D. Hammonds, R. M. Lynden-Bell, *Surf. Sci.* 278 (1992) 437.
- [344] C.-L. Liu, J. B. Adams, *Surf. Sci.* 294 (1993) 197.
- [345] R. T. Tung, W. R. Graham, *Surf. Sci.* 97 (1980) 73.
- [346] B. D. Yu, M. Scheffler, *Phys. Rev. B* 56 (1997) R15569.
- [347] K. Kyuno, G. Ehrlich, *Surf. Sci.* 394 (1997) L179.
- [348] S. C. Wang, G. Ehrlich, *Phys. Rev. Lett.* 70 (1993) 41.
- [349] N. Memmel, E. Bertel, *Phys. Rev. Lett.* 75 (1995) 485.
- [350] D. M. Eigler, P. S. Weiss, E. K. Schweizer, N. D. Lang, *Phys. Rev. Lett.* 66 (1990) 1189.
- [351] Y. Hasegawa, P. Avouris, *Phys. Rev. Lett.* 71 (1993) 1071.
- [352] J. Li, W.-D. Schneider, R. Berndt, S. Crampin, *Phys. Rev. Lett.* 80 (1998) 3332.
- [353] S. L. Silva, F. M. Leibsle, *Surf. Sci.* 441 (1999) L904.
- [354] G. Rosenfeld, private communication (1998) .
- [355] M. Giesen, H. Ibach, *Surf. Sci. Lett.*, submitted (2000) .
- [356] M. Giesen, *Surf. Sci.* 441 (1999) 391.
- [357] R. Paniago, R. Matzdorf, G. Meister, A. Goldmann, *Surf. Sci.* 336 (1995) 113.
- [358] S. D. Kevan, *Phys. Rev. Lett.* 50 (1983) 526.
- [359] S. D. Kevan, R. H. Gaylord, *Phys. Rev. B* 36 (1987) 5809.
- [360] M. Schroeder, D. E. Wolf, *Surf. Sci.* 375 (1997) 129.
- [361] N. C. Bartelt, private communication (1997) .
- [362] R. Sonnenfeld, B. C. Schardt, *Appl. Phys. Lett.* 49 (1986) 1172.
- [363] J. Schneir, V. Elings, P. K. Hansma, *J. Electrochem. Soc.* 135 (1988) 2774.
- [364] R. Christoph, H. Siegenthaler, H. Rohrer, H. Wiese, *Electrochim. Acta* 34 (1989) 1011.
- [365] K. Uosaki, H. Kita, *J. Vac. Sci. Technol. A* 8 (1989) 520.
- [366] R. J. Nichols, D. M. Kolb, R. J. Behm, *J. Electroanal. Chem.* 313 (1991) 109.
- [367] N. Batina, D. M. Kolb, R. J. Nichols, *Langmuir* 8 (1992) 2572.
- [368] R. J. Nichols, W. Beckmann, H. Meyer, N. Batina, D. M. Kolb, *J. Electroanal. Chem.* 330 (1992) 381.
- [369] S. G. Corcoran, G. S. Chakarova, K. Sieradzki, *Phys. Rev. Lett.* 71 (1993) 1585.
- [370] M. H. Hölzle, D. M. Kolb, *Ber. Bunsenges. Phys. Chem.* 98 (1994) 330.
- [371] W. Schmickler, U. Stimming, *J. Electroanal. Chem.* 366 (1994) 203.
- [372] T. Will, M. Dietterle, D. M. Kolb, in A. A. Gewirth, H. Siegenthaler (Eds.): *Nanoscale Probes of the Solid/Liquid Interface, Vol. E288*, Kluwer, Dordrecht 1995, p. 137.

- [373] M. Dietterle, T. Will, D. M. Kolb, *Surf. Sci.* 342 (1995) 29.
- [374] W. J. Lorenz, G. Staikov, *Surf. Sci.* 335 (1995) 32.
- [375] F. A. Möller, O. M. Magnussen, R. J. Behm, *Phys. Rev.* B51 (1995) 2484.
- [376] M. H. Hölzle, V. Zwing, D. M. Kolb, *Electrochim. Acta* 40 (1995) 1237.
- [377] F. Möller, O. M. Magnussen, R. J. Behm, *Electrochim. Acta* 40 (1995) 1259.
- [378] J. Hotlos, O. M. Magnussen, R. J. Behm, *Surf. Sci.* 335 (1995) 129.
- [379] U. Schmidt, S. Vinzelberg, G. Staikov, *Surf. Sci.* 348 (1996) 261.
- [380] F. A. Möller, O. M. Magnussen, R. J. Behm, *Phys. Rev. Lett.* 77 (1996) 3165.
- [381] F. A. Möller, O. M. Magnussen, R. J. Behm, *Phys. Rev. Lett.* 77 (1996) 5249.
- [382] M. Dietterle, T. Will, D. M. Kolb, *Surf. Sci.* 396 (1998) 189.
- [383] T. P. Moffat, *J. Phys. Chem.* B102 (1998) 10020.
- [384] R. Randler, M. Dietterle, D. M. Kolb, *Z. Phys. Chem.* 208 (1999) 43.
- [385] K. A. Friedrich, K.-P. Geyzers, A. Marmann, U. Stimming, R. Vogel, *Z. Phys. Chem.* 208 (1999) 137.
- [386] G. Staikov, W. J. Lorenz, *Z. Phys. Chem.* 208 (1999) 17.
- [387] F. A. Möller, O. M. Magnussen, R. J. Behm, *Z. Phys. Chem.* 208 (1999) 57.
- [388] O. M. Magnussen, R. J. Behm, *J. Electroanal. Chem.* 467 (1999) 258.
- [389] L. A. Kibler, M. Kleinert, D. M. Kolb, *J. Electroanal. Chem.* 467 (1999) 249.
- [390] M. S. Zei, K. Wu, M. Eiswirth, G. Ertl, *Electrochim. Acta* 45 (1999) 809.
- [391] B. M. Ocko, I. K. Robinson, M. Weinert, R. J. Randler, D. M. Kolb, *Phys. Rev. Lett.* 83 (1999) 780.
- [392] O. E. Hüsser, D. H. Craston, A. J. Bard, *J. Vac. Sci. Technol.* B6 (1988) 1873.
- [393] D. Mandler, A. J. Bard, *J. Electrochem. Soc.* 137 (1990) 1079.
- [394] R. M. Penner, M. J. Heben, N. S. Lewis, C. F. Quate, *Appl. Phys. Lett.* 58 (1991) 1389.
- [395] W. Li, J. A. Virtanen, R. M. Penner, *Appl. Phys. Lett.* 60 (1992) 1181.
- [396] W. Li, J. A. Virtanen, R. M. Penner, *J. Phys. Chem.* 96 (1992) 6529.
- [397] R. Ullmann, T. Will, D. M. Kolb, *Chem. Phys. Lett.* 209 (1993) 238.
- [398] T. P. Moffat, H. Yang, *J. Electrochem. Soc.* 142 (1995) L220.
- [399] N. Breuer, U. Stimming, R. Vogel, *Electrochim. Acta* 40 (1995) 1401.
- [400] J. Divisek, B. Steffen, U. Stimming, W. Schmickler, *J. Electroanal. Chem.* 440 (1997) 169.
- [401] D. M. Kolb, R. Ullmann, J. C. Ziegler, *Electrochim. Acta* 43 (1998) 2751.
- [402] G. E. Engelmann, J. C. Ziegler, D. M. Kolb, *Surf. Sci.* 401 (1998) L420.

- [403] J. C. Ziegler, G. E. Engelmann, D. M. Kolb, *Z. Phys. Chem.* 208 (1999) 151.
- [404] J. C. Ziegler, R. I. Wielgosz, D. M. Kolb, *Electrochim. Acta* 45 (1999) 827.
- [405] X. G. Zhang, U. Stimming, *J. Electroanal. Chem.* 291 (1990) 273.
- [406] X. G. Zhang, U. Stimming, *Corrosion Science* 30 (1990) 951.
- [407] A. Milchev, *J. Electroanal. Chem.* 312 (1991) 267.
- [408] I. C. Oppenheim, D. J. Trevor, C. E. D. Chidsey, P. L. Trevor, K. Sieradzki, *Science* 254 (1991) 687.
- [409] A. S. Dakkouri, R. Randler, D. M. Kolb, in C. Korzeniewski, B. E. Conway (Eds.): *Proceedings of the symposium on: The Electrochemical Double Layer, Vol. 97-17*, The Electrochemical Society, Pennington, NJ 1997.